STUDY OF SOLAR ACTIVITY AND ITS IMPACT ON TERRESTRIAL ENVIRONMENT

THESIS FOR THE DEGREE OF

Doctor of Philosophy

IN

PHYSICS

Investigator

Nipa Jishnu Bhatt

Supervisor

Dr Rajmal Jain

Physical Research Laboratory

Navrangpura, Ahmedabad-380009

Gujarat, India

Submitted to

SAURASHTRA UNIVERSITY

Rajkot - 360005

Gujarat, India

July, 2011

DECLARATION

I hereby declare that the work presented in this thesis is the result of the original work carried out by me, under the supervision of Dr Rajmal Jain (Physical Research Laboratory, Navrangpura, Ahmedabad-380009, Gujarat, India). This work has not been submitted for the award of any degree, diploma, associateship, fellowship, etc. of any other University or Institute.

Nipa Jishnu Bhatt

Place: Ahmedabad
Date : 4 July, 2011

Certificate from the Supervisor

This is to certify that the thesis entitled **"Study of Solar Activity and its Impact on Terrestrial Environment"** is submitted for the degree of Doctor of Philosophy in Physics of Saurashtra University, Rajkot, Gujarat, India by Ms Nipa Jishnu Bhatt (Registration No.: 3906). This thesis embodies the work carried out by her under my supervision and is a significant contribution in the field of Solar Physics.

This thesis has not been submitted for the award of any degree, diploma, associateship, fellowship, etc. of any other University or Institute.

Supervisor,

Dr. Rajmal Jain
Physical Research Laboratory,
Navrangpura,
Ahmedabad-380009
Gujarat, India
Place: Ahmedabad
Date: July, 2011

Dedicated to

My Parents,

Jishnu,

Birva

&

The sacred Memory of

Indu Aunty

who I dearly miss

Acknowledgements

I take this opportunity to express my sincere thanks to my supervisor, Dr. Rajmal Jain, for introducing me to the wonderful world of Solar Physics. I would like to heartily appreciate his expertise, constant guidance, enthusiasm and patience which led me to complete this work. I sincerely acknowledge Physical Research Laboratory (PRL), Ahmedabad for allowing me to use the library facilities for the research work. I am heartily thankful to Brian. R. Dennis, GSFC, NASA, USA whose significant comments and suggestions throughout the RHESSI data analysis led to many improvements in my work. I sincerely acknowledge and appreciate his extremely supportive attitude for helping me learn RHESSI data analysis right from the beginning and suggesting me the related literature. I am also indebted to Dr Nat Gopalswamy, GSFC, NASA, for his guidance regarding the CME work. I heartily acknowledge all the teachers at 2nd SPD summer school at New Hampshire who were a source of inspiration for my research work. I am also grateful to Markus. J. Aschwanden, Lockheed Martin Advanced Technology Center, USA, for his illuminating suggestions for flare spectral fits. I am thankful to Gordan Holman, GSFC, NASA, USA for his valuable suggestions regarding the thermal model calculations of multi-thermal emission measure. I thank Kim Tolbert for her invaluable and immediate help with the RHESSI software. I thank Raghunandan Sharma and Vishal Joshi for helping me while I was in the initial stage of data analysis. I acknowledge the moral support of Ms. Jayshree Trivedi, PRL. I extend my thanks to K J Shah, Arun and Sharad for their kind cooperation. I sincerely acknowledge the open data policy of various missions such as SOXS, GOES, RHESSI and SOHO. I acknowledge the NGDC website from which the sunspot and geomagnetic data have been acquired. I acknowledge the WDC for Geomagnetism, Kyoto website from which the geomagnetic data have been acquired.

I would like to thank all my past and present colleagues at C U Shah Science College, Ahmedabad for their constant support and encouragement

throughout my journey. I am specially thankful to Dr. P. R. Vyas and Dr. Shailesh Patel for their kind cooperation. I am grateful to all my friends, especially Subhash and Chandresh for sharing the good and bad moments throughout all these years. Special thanks go to my relatives and cousins who were equally enthusiastic about my research work as I was. Without their strong and emotional support, this work would not have been completed. I am thankful to my dear sister, Ushma for her constant love and moral support.

I am forever thankful to my dear parents, my husband and my daughter, whom I owe more than words can express.

List of Publications

1. **Prediction of the Maximum Amplitude and Timing of Sunspot Cycle 24**
   2009, Solar Physics, **260**, 225
   Nipa J Bhatt, Rajmal Jain & Malini Aggarwal

2. **Predicting Maximum Sunspot Number in Solar Cycle 24**
   2009, J. Astrophys. Astr. 30, 71
   Nipa J Bhatt, Rajmal Jain & Malini Aggarwal

3. **Solar X-ray Spectrometer (SOXS) mission: Observations and new Results**
   2006**,** Proceedings of ILWS workshop, Goa
   http://cdaw.gsfc.nasa.gov/publications/ilws_goa2006/054_Jain.pdf
   R. Jain, **N. J. Bhatt** and L. Bharti

4. **Study of Microflares through SOXS Mission**
   2006, J. Astrophys. Astr. **27,** 339
   Rajmal Jain, Vishal Joshi, Yoichiro Hanaoka, T. Sakurai & **Nipa Upadhyay (Bhatt)**

Glossary of acronyms

The most frequently used notations and abbreviations are listed below.

AR	Active region
α	Spectral index (multi-thermal)
β	Proton spectral index
CME	Coronal Mass Ejection
DEM	Differential Emission Measure
Dst	Disturbance storm time
EM	Emission Measure
F_{12}	Photon Flux at 12 keV
F_{20}	Photon Flux at 20 keV
F_{50}	Photon Flux at 50 keV
γ	Photon spectral index
GOES	Geostationary Operational Environmental satellites
HXR	Hard X-ray
IDL	Interactive Data Language
keV	kilo electron volt
LASCO	Large Angle Spectroscopic Coronagraphs
MK	mega-Kelvin
MeV	mega electron volt
nT	nano-Tesla
NASA	National Aeronautics and Space Administration
NOAA	National Oceanic and Atmospheric Administration
OSPEX	Object Spectral Executive (SSW software)
R_s	Solar radius
RHESSI	Reuven Ramaty High-Energy Solar Spectroscopic Imager
SEPs	Solar energetic particles
Si	Silicon
SXR	Soft X-ray
SWPC	Space Weather Prediction Center
SOHO	Solar and Heliospheric Observatory
SOXS	Solar X-ray Spectrometer

Contents

1 Introduction

1.1 Our Sun: Structure 1
1.1.1 The Solar Interior 1
1.1.2 The Photosphere 4
1.1.3 The Chromosphere 7
1.1.4 The Transition region 8
1.1.5 The Corona 8
1.2 Sunspot Cycle 10
1.3 Solar Flares 13
1.3.1 Solar Flares in Soft X-rays 18
1.3.2 Solar Flares in Hard X-rays 19
1.3.3 Flare classification 24
1.4 Coronal Mass Ejections (CMEs) 24
1.5 Solar Energetic Particles (SEPs) 28
1.6 Earth's Magnetosphere and Geomagnetic Activity: A brief Overview 29
1.7 Open Issues 34
1.8 Organisation of the Thesis 38

2 Instruments

2.1 SOXS 39
2.1.1 The Solid-state Detectors 40
2.1.1.1 Collimator and Filter 43
2.1.1.2 Onboard Radioactive Source 46
2.1.2 SUN ASPECT SYSTEM – SOXS SUN TRACKING MECHANISM (SSTM) 47
2.1.3 Electronics 49
2.1.3.1 SLD Front-End Electronics (SFE) 49
2.1.3.2 SLD Processing Electronics 50
2.1.3.3 Flare Triggering Logic 50
2.1.3.4 SOXS Common Electronics (SCE) 51

2.2 RHESSI 52
2.2.1 RHESSI Spectrometer – The Germanium detectors 52
2.2.2 Data handling for Spectral Analysis 55
2.3 GOES 57
2.4 SOHO 58
2.4.1 SOHO/EIT 59
2.4.2 SOHO/LASCO 59
2.5 Magnetic Sensors (Dst Index) 61
2.6 Magnetic sensors (aa index) 62

3 Data Acquisition and Analysis Techniques
3.1 Flare Location, Class and Active region 63
3.2 SOXS 65
3.2.1 Data Format 65
3.2.2 Analysis techniques 67
3.2.2.1 Response of the Detectors 67
3.2.2.2 OSPEX (Object Spectral Executive) 75
3.2.2.3 Spectral Analysis 75
3.3 RHESSI 80
3.3.1 Creation of spectrum and Spectral Response Matrix (SRM) files 80
3.3.2 Spectral Analysis 82
3.4 Disturbance Storm Time (Dst) index 83
3.5 CME 84
3.6 Proton Data 86
3.7 Geomagnetic activity index (*aa*) 86
3.8 Sunspot Number Data 87

4 X-ray Emission from Solar Flares
4.1 X- ray Emission 89
4.1.1 Soft X-ray Line Emission 90
4.1.2 X-ray Emission Mechanism 92

4.1.2.1 Free-Free Emission (Bremsstrahlung) 92
4.1.2.2 Thermal and Non-thermal Contributions 92
4.2 Dataset 93
4.3 Spectral Analysis and Results 96
4.3.1 Spectral Analysis of 6 January 2004 Flare (SOXS) 96
4.3.2 Spectral Analysis of 6 January 2004 Flare (RHESSI) 102
4.4 Spectral Analysis of other flares 106
4.5 Estimation of thermal and non-thermal energy 131
4.5.1 Estimation of thermal energy 131
4.5.2 Estimation of non-thermal energy 139
4.6 Relationship of flare parameters 145
4.6.1 Spectral index α versus Temperature T (Multi-hermal) 145
4.6.2 Photon flux F_{12} versus spectral index α 147
4.6.3 Emission Measure versus Temperature 147
4.6.4 Photon Flux versus Emission Measure 150
4.6.4.1 Photon flux F_{12} versus Emission Measure (Multi-thermal) 150
4.6.4.2 Photon Flux F_{20} versus Emission Measure (Isothermal) 151
4.6.5 Photon flux F_{20} versus Temperature (isothermal) 151
4.6.6 Spectral Index γ versus multi-thermal Emission Measure 154
4.7 Conduction and radiation power 156
4.8 Discussion and Conclusion 158

5 Investigating Solar Variables Affecting Terrestrial Environment
5.1 Solar Activity and its Impact on Earth's Environment: A Brief Overview of Previous Studies 163
5.1.1 Flare-CME relationship 165
5.1.2 Flare-SEP relationship 167

5.2 The Data 168
5.2.1 Flare Selection Procedure 168
5.2.2 Dataset 172
5.3 Exploring the Flare-CME relationship: Observations, Analysis and Results 175
5.4 Investigation of Flare-SEP relationship: Observations, Analysis and Results 180
5.4.1 Flare Spectral Analysis 184
5.4.2 SEP Spectral Analysis 200
5.5 Discussion and Conclusion 216

6 Prediction of Sunspot Cycle 24
6.1 Sunspot cycle Prediction: A brief overview 218
6.2 Data 219
6.3 Analysis and Results 219
6.3.1 Defining the Sunspot Minimum Year of Cycle 2 219
6.3.2 Prediction of the Maximum Annual Mean Sunspot Number 222
6.3.3 Prediction of the Ascending Period of Cycle 24 224
6.3.4 Prediction of the annual mean geomagnetic activity for the solar maximum year 225
6.4 Discussion and Conclusion 226
7 Discussion and Future Prospects 229
References 236
Appendix A: Plots of Flare and SEP spectra

List of Figures

1.1 Basic overview of the solar structure. The three major structural areas, i.e. the core, radiative zone and the convective zone are shown in the upper hemisphere while the lower hemisphere shows the three atmospheres, i.e. photosphere, chromosphere and the corona. (Image: SOHO (Solar and Heliospheric Observatory) 2

1.2 Sunspot image (top) with umbra (dark portion) and penumbral filaments. The image of planet-sized sunspot was taken by the Swedish Solar Telescope (SST) on 15 July, 2002. The penumbral filaments' newly revealed dark cores are seen to be thousands of kilometers long but only about 100 km wide (Scharmer *et al*., 2002). The bottom figure shows faculae which are the bright regions surrounding the sunspots (Image: Big Bear Solar Observatory) 5

1.3 A highly magnified portion of the solar surface taken by Hinode's Solar Optical Telescope. Hot gases from the solar interior are transported by convection and results in granulation, seen in this image. The lighter areas reveal where gases are rising from the interior, while the darker "intergranular lanes" reveal where cooler gases are descending back down. (Image: Hinode JAXA/NASA/PPARC) 7

1.4 (a): The monthly averaged daily International Sunspot Numbers from 1610 to April 2011 (Image: Hathaway, D. H., MSFC, NASA (b): The butterfly diagram of sunspots for the period 1875 to mid 2011 (approx) (Image: NASA) 12

1.5 A schematic profile of the temporal evolution of the flare intensity at several wavelengths (taken from Benz, 1993) 15

1.6 The standard 2D X-type reconnection model (Tsuneta 1997) 17

1.7 This image, from the soft X-ray (SXR) telescope onboard YOHKOH, shows X-ray flare emission of the solar corona on May 8, 1992. The effective wavelength is about 10 Å, or 1 keV, and the resolution is about 10 arc sec (Image: YOHKOH) 19

1.8 A halo coronal mass ejection (Image: SOHO/LASCO) 26

1.9 llustration of Earth's magnetosphere (in blue) immersed in the solar wind. The orbit of the Cluster satellites is depicted in red. Earth's cusps are located near the poles. They are magnetic field features of the magnetosphere associated with regions through which plasma from the Sun can have direct access to the upper atmosphere (Image: ESA) 30

2.1 The block scheme of the SLD payload 40

2.2 The detector package (see text) mounted on the SOXS Sun tracking mechanism (SSTM). The collimators are seen projecting outside. The FOV is 3.4°. The detector package moves in the line of sight of the Sun within an accuracy of about 0.1°. The SSTM has only one drive motor for correction in right ascension and declination 45

2.3 The effective area of the Si and CZT detectors of the SLED package. The Si and CZT have 0.025 and 0.25 mm Be windows respectively in front of the detector heads. Additional filters were mounted on the head to reject the background significantly 46

2.4 In-orbit calibration test with thermoelectric cooler (TEC) ON and OFF, however maintaining the temperature between –15 °C and –25 °C. The 22.2 keV line from onboard radioactive source (mounted inside the collimator) is seen unambiguously in both detectors. However, an anomaly of 14 channel shift in CZT detector may be noticed as soon as TEC is turn ON 48

2.5 The operation logic of the SLD payload. The temporal resolution during flare mode is100 ms 51

2.6 A cutaway of the Spectrometer showing the location of the germanium detectors (by number). (Lin *et al*. 2002) 53

2.7 Schematic cross-section of one RHESSI germanium detector, showing the electric field lines, with the field line marking the segment boundary in bold dashes (from Smith *et al*. 2002) 54

2.8 Optical components of the Lyot Coronagraph: Objective lens O1, internal occulter D1, Field lens F1, Lyot stop A3, Lyot spot, objective lens O2, and focal plane. (Image: NASA) 61

3.1 Hα image(top) of the Sun (25-August-2005). The figure shows the active region 10803 on east limb of the Sun. The bottom figure shows the GOES X ray flux as a function of time. The peak intensity (M-class X-ray flare) on 25-August-2005 between 3:00 and 6:00 UT is circled in black. (Image: Solar monitor) 64

3.2 Schematics of SOXS/GSAT-2 command and data acquisition at Master Control Facility (MCF) at Hasan. The data is then uplinked to INSAT with 64 kbps from where it comes to PRL through space-net. Finally the SOXS data is stored in the SOXS lab at PRL and then processed for next level. The processed data is uplinked to SOXS URL 66

3.3 Photo-peak effective area of Si (top) and CZT (bottom) detectors are plotted as a function of energy. It may be noted that Si has best efficiency up to 15 while CZT reveals up to 3 keV. However, for bright flares (<M5.0 intensity) Si may collect photons up to 25 keV and CZT up to 40 keV 68

3.4 Response matrix for Si (top) and CZT (bottom) detectors. The probability of photon conversion to electron and hole by the detector is also plotted as a function of energy 71

3.5 The temporal evolution of the solar flare observed on 25 August 2005 by Si detector (left panel) on its fixed energy bands L1 (6-7), L2 (7-10), L3 (10-20) and T (4-25) keV, and by CZT detector (right panel) on its fixed energy bands L1 (6-7), L2 (7-10), L3 (10-20), M (20-30) and H (30-56) keV 72

3.6 Temporal evolution (light curve) of the 25 August 2005 solar flare (employing spectral mode data in OSPEX) in the energy ranges 4.1-12 keV (black) and 12-24.7 keV (red) observed by Si detector of the SLD/SOXS mission The temporal resolution is 3s for quiet mode and 100 ms for flare mode 73

3.7 X-ray count spectrum (top) and photon spectrum (bottom) in the energy range 4.1-21 keV of 25-August-2005 solar flare. The count flux (counts s^{-1} cm^{-2} keV^{-1}) and photon flux (photons s^{-1} cm^{-2} keV^{-1}) are shown as a function of energy 76

3.8 The count spectrum (top) and the photon spectrum of 25-August-2005 flare with model fits performed in the energy range of 4.2 - 21 keV. The count flux (counts s^{-1} cm^{-2} keV^{-1}) and photon flux (photons s^{-1} cm^{-2} keV^{-1}) is shown as a function of energy. The multi_therm_pow function (green), single power(yellow), and their total (red) fit to the observed spectrum (black) are shown 81

3.9 A typical storm time Dst measurement for the period 12-18 December 2006. The sudden storm commencement (ssc), decay phase and the recovery phase during the storm interval are also shown. 84

3.10 The A frame of a JavaScript movie of the c2eit image showing the halo CME event on 13-December-2006 (Image: SOHO LASCO CME Catalog) 85

3.11 This plot shows a background-subtracted proton spectrum of 10-November-2004 SEP event in the energy range 0.8 – 80 MeV for the interval 06:00 to 09:00 UT 87

4.1 Simulation of full disk integrated X-ray photon emission spectrum from the Sun in the energy range 0.01-10 (top) and 10-1000 (bottom) keV for quiet and M5 solar flare conditions. The pre-flare background, thermal component, and super-hot and non-thermal hard X-ray components of the solar flare are also shown by different lines. The solid thick line is total flux from all these assumptions. It may be noted that iron and iron-nickel complex lines at 6.7 and 8 keV respectively appear only when flare occurs (top), and there is a break in energy from one to other spectrum (bottom) 90

4.2 Illustration of Free-Free (Bremsstrahlung) Emission 92

4.3 X-ray spectrum of a solar flare observed by RHESSI characterizing thermal and non-thermal component. Thermal (low energy) portion is fitted with the variable thermal component while the non-thermal (high energy) portion is fitted with a single power law. 94

4.4 Light curve of the 6 January 2004 solar flare in energy range 4.1-12 (black) and 12-24.7 (red) keV energy bands of the Si detector of the SLD/SOXS mission 97

4.5 The count spectra of 6 January 2004 flare during 06:26:30-06:27:00 UT. The count flux (counts s^{-1} cm^{-2} keV^{-1}) is shown as a function of energy 98

4.6 Photon spectrum (top) for 6-January-2004 flare with model fits performed in 4.2-18.5 keV. The multi_therm_pow function (green), single power (yellow), and their total (red) fit to the observed spectrum (black) are shown. Normalized residuals (bottom) for each energy bin. 99

4.7 Temporal evolution of spectral parameters for 6-January-2004 determined from spectral fitting (SOXS). From top to bottom: (1) Emission measure of multi-thermal plasma (EM); (2) Temperature of multi-thermal plasma (T); (3) Spectral index α (multi-thermal); (4) Photon flux at 12 keV (F_{12}) and (5) spectral index γ (negative power-law). Error bars for emission measure, temperature, and α are as reported by OSPEX showing the limits. 101

4.8 RHESSI X-ray light curve of 6 January 2004 solar flare in the energy range 12-25 keV (red) and 25-100 keV (blue) using detector 4F. 102

4.9 RHESSI Count spectrum of 6-January-2004 fitted with vth+1pow function in the energy range 13-75 keV. The vth function (green), 1pow (yellow), and their total (red) fit to the observed spectrum (black) are shown. 104

4.10 Photon spectrum (top) for 6-January-2004 flare event (RHESSI) with model fits. Normalized residuals (bottom) for each energy bin 105

4.11 Time history of the fit parameters of 6 January 2004 solar flare observed by detector 4F (RHESSI). From top to bottom: (1) isothermal emission measure EM; (2) Temperature T of the isothermal component; (3) Photon flux at 20 keV (F_{20}) and (4) negative power-law index γ. Error bars are as reported by OSPEX showing the limits. 106

4.12 Light curve (top) and time history (bottom) of spectral parameters of 27-July-2005 flare (SOXS). 108

4.13 Light curve (top) and time history (bottom) of spectral parameters of 27-July-2005 flare (RHESSI). 109

4.14 Light curve (top) and time history (bottom) of spectral parameters of 31-October-2005 flare (SOXS). 110
4.15 Light curve (top) and time history (bottom) of spectral parameters of 31-October-2004 flare (RHESSI). 111
4.16 Light curve (top) and time history (bottom) of spectral parameters of 17-September-2005 flare (SOXS). 112
4.17 Light curve (top) and time history (bottom) of spectral parameters of 17-September-2005 flare (RHESSI). 113
4.18 Light curve (top) and time history (bottom) of spectral parameters of 25-August-2005 flare (SOXS). 114
4.19 Light curve (top) and time history (bottom) of spectral parameters of 25-August-2005 flare (RHESSI). 115
4.20 Light curve (top) and time history (bottom) of spectral parameters of 19-November-2003 flare (SOXS). 116
4.21 Light curve (top) and time history (bottom) of spectral parameters of 19-November-2003 flare (RHESSI). 117
4.22 Light curve (top) and time history (bottom) of spectral parameters of 3-August-2005 flare (SOXS). 118
4.23 Light curve (top) and time history (bottom) of spectral parameters of 3-August-2005 flare (RHESSI). 119
4.24 Light curve (top) and time history (bottom) of spectral parameters of 5-April-2004 flare (SOXS). 120
4.25 Light curve (top) and time history (bottom) of spectral parameters of 5-April-2004 flare (RHESSI). 121
4.26 Light curve (top) and time history (bottom) of spectral parameters of 13-November-2003 flare (SOXS). 122
4.27 Light curve (top) and time history (bottom) of spectral parameters of 13-November-2003 flare (RHESSI). 123
4.28 Light curve (top) and time history (bottom) of spectral parameters of 14-July-2004 flare (SOXS). 124
4.29 Light curve (top) and time history (bottom) of spectral parameters of 14-July-2004 flare (RHESSI). 125
4.30 Light curve (top) and time history (bottom) of spectral parameters of 7-February-2010 flare (SOXS). 126

4.31 Light curve (top) and time history (bottom) of spectral parameters of 8-February-2010 (B04:06:20) flare (SOXS). 127
4.32 Light curve (top) and time history (bottom) of spectral parameters of 8-February-2010 (04:58:26) flare (SOXS). 128
4.33 Thermal energy release as a function of time in 6-January-2004 flare event observed by SOXS and RHESS 132
4.34 Thermal energy release as a function of time in 27-July-2005 flare event observed by SOXS and RHESSI. 132
4.35 Thermal energy release as a function of time in 31-October-2004 flare event observed by SOXS and RHESSI. 133
4.36 Thermal energy release as a function of time in 17-September-2005 flare event observed by SOXS and RHESSI. 133
4.37 Thermal energy release as a function of time in 25-August-2005 flare event observed by SOXS and RHESSI. 134
4.38 Thermal energy release as a function of time in 19-November-2003 flare event observed by SOXS and RHESSI. 134
4.39 Thermal energy release as a function of time in 3-August-2005 flare event observed by SOXS and RHESSI. 135
4.40 Thermal energy release as a function of time in 5-April-2004 flare event observed by SOXS and RHESSI. 135
4.41 Thermal energy release as a function of time in 13-November-2003 flare event observed by SOXS and RHESSI. 136
4.42 Thermal energy release as a function of time in 14-July-2004 flare event observed by SOXS and RHESSI. 136
4.43 Thermal energy release as a function of time in 7-February-2010 flare event observed by SOXS. 137
4.44 Thermal energy release as a function of time in 8-February-2010 flare event observed by SOXS. 137
4.45 Thermal energy release as a function of time in 8-February-2010 flare event observed by SOXS. 138
4.46 Variation of low energy cut-off with time for 6-January-2004 obtained from RHESSI spectral fits using isothermal plus thick2 model 142

4.47 Time evolution of thermal energy determined by SOXS (pink) and RHESSI (violet), and non-thermal energy determined by RHESSI (orange) for 6-January-2004 solar flare. 142

4.48 Temporal evolution of thermal energy determined by SOXS and RHESSI and non-thermal energy determined for 5-April-2004 solar flare. 143

4.49 Scatter plot (top) of spectral index versus SOXS temperatures in the energy range 4.1-24 keV. The bottom plot (with 3 MK bin) shows the dashed line (power-law) is the best fit with r = 0.9. 146

4.50 Scatter plot (top) and binned (bottom) plot (0.5 binning for spectral index) of photon flux and spectral index α with exponential correlation of 0.8. 148

4.51 Scatter plot (top) of differential emission measure against multi-thermal temperature T and binned plot (1 MK bin) at the bottom 149

4.52 The scatter plot (top) of photon flux as a function of multi-thermal emission measure. The power-law fit (for $10*10^{49}$ cm^{-3} binning of emission measure) with a correlation coefficient of 0.96 (bottom). 150

4.53 The variation of photon flux at 20 keV with emission measure (top). The best fit showing the exponential relationship with r =0.94 after binning of emission measure (0.1×10^{49} cm^{-3}). 152

4.54 The non-thermal photon flux at 20 keV is plotted as a function of isothermal temperature (top). The results after binning of temperature (1 MK bin) are shown in bottom plot. 153

4.55 Scatter plot (top) of spectral index γ and multi-thermal emission measure. The correlationship improves drastically with the binning of emission measure (bottom). 155

4.56 Temporal variation of radiative and conductive power for 27-July-2005 flare. 157

4.57 Temporal variation of radiative and conductive power for 5-April-2004 flare. 157

5.1 Image showing the Dst-CME-flare occurrences during 27-30 May-2003. The Dst plot (top) shows that the Dst value reached -144 nT on 29-May-2003 at 24:00 UT. The middle plot shows the CME height-time

and the bottom panel shows GOES soft X-ray light curves. The following three flares are marked in circles: (i) 27-May-2003 at 22:56 UT (X1.3) (ii) 28-May-2003 at 00:17 UT (X3.6) and (iii) 29-May-2003 at 00:51 UT (X1.2) which occurred prior to the Dst event (Image: SOHO LASCO CME Catalog). 169

5.2 A frame of a JavaScript movie of the c2eit_gxray image (left) showing the flare location in the south-west quadrant (S15W46).The GOES soft X-ray light curve (right) with the time of LASCO C2 image at 12:30 UT on 18-March-2003 is shown as a vertical line(Image: SOHO LASCO CME Catalog). 170

5.3 A frame of a JavaScript movie of the LASCO C2 c2rdif_gxray image (top left) of 29-May-2003 event. It clearly shows a Halo CME prominent in the South-West quadrant. The c2eit_gxray image (top right) at the same time showing the flare location in the south-west quadrant (S06W37).The GOES soft X-ray light curve (bottom) with the time of LASCO C2 image at 01:27 UT shown as a vertical line (Image: SOHO LASCO CME Catalogue). 171

5.4 RHESSI X-ray light curve of 29-October-2003 in the energy range 12-25 keV (red) and 25-100 keV (blue) using detector 4F. 175

5.5 RHESSI Count spectrum (top) of 29-October-2003 for the time interval just before the peak is fitted with vth+1pow function in the energy range 13-100 keV. The vth function (green), 1pow (yellow), and their total (red) fit to the observed spectrum (black) are shown. The middle plot shows the photon spectrum with model fits. The fitted parameters are given in the legend (left corner). Normalized residuals for each energy bin are shown in the bottom plot. 177

5.6 The spectral index obtained from the fitted spectra for 30 flares is plotted as a function of the associated CME linear speed. The best fit is a power-law relationship with r = 0.77. 179

5.7 The spectral index plotted as a function of CME speed for 19 flare-CME pairs. The peak photon flux in 12-25 keV for these 19 flares is <11000 c $(4s)^{-1}$. The best fit is a power-law relationship with r = 0.84. 179

5.8 GOES Proton flux (top) enhancement at energies >10, >50 and >100 Mev as seen at about 3:00 UT on 13-December-2006. The bottom panel shows the 13-December-2006 flare (X3.4) event as observed by GOES. (Image: SWPC/NOAA (top) and SOHO/ LASCO-CME-CATALOGUE (bottom)). 181

5.9 The light curve (top) and temporal evolution of the spectral index γ (bottom) 13-December-2006 flare in 50-100 keV energy range. 185

5.10 The light curve (top) of 27-May-2003 and temporal evolution of the spectral index γ (bottom) in 50-100 keV energy range. 187

5.11 The light curve (top) and temporal evolution of the spectral index γ (bottom) of 29-May-2003 in 50-100 keV energy range. 188

5.12 The light curve (top) and temporal evolution of the spectral index γ (bottom) of 28-October-2003 in 50-100 keV energy range. The dark circles denote the spectral index obtained from single power law. The open circles denote the values of the spectral index (above the break energy) obtained from the broken power-law fit. 189

5.13 The light curve (top) and temporal evolution of the spectral index γ (bottom) of 29-October-2003 in 50-100 keV energy range. 190

5.14 The light curve (top) and temporal evolution of the spectral index γ (bottom) of 2-November-2003 in and 50-100 keV energy range. 191

5.15 The light curve (top) and temporal evolution of the spectral index γ (bottom) of 07-November-2004 in 50-100 keV energy range. 192

5.16 The light curve (top) temporal evolution of the spectral index γ (bottom) of 10-November-2004 in 50-100 keV energy range. 193

5.17 The light curve (top) and temporal evolution of the spectral index γ (bottom) of 15-January-2005 in 50-100 keV energy range. 194

5.18 The light curve (top) and temporal evolution of the spectral index γ (bottom) of 17-January-2005 and 50-100 keV energy range. The dark circles denote the spectral index obtained from single power law. The open circles denote the values of the spectral index (above the break energy) obtained from the broken power-law fit. 195

5.19 The light curve (top) and temporal evolution of the spectral index γ (bottom) of 20-January-2005 in 50-100 keV energy range. The dark circles denote the spectral index obtained from single power law. The open circles denote the values of the spectral index (above the break energy) obtained from the broken power-law fit. 196

5.20 The light curve (top) temporal evolution of the spectral index γ (bottom) of 13-May-2005 in 50-100 keV energy range. 197

5.21 The background-subtracted proton spectrum of 13-December-2006 in the energy range of 15-500 MeV for the interval 6:00 to 9:00 UT. 201

5.22 The temporal evolution of proton flux (top) and spectral index β (bottom) of 13-December-2006 proton event in the energy range 0.8 - 500 MeV. 202

5.23 The temporal evolution of proton flux (top) and spectral index β (bottom) of 27-May-2003 proton event in the energy range 0.8 - 40 MeV. 204

5.24 The temporal evolution of proton flux (top) and spectral index β (bottom) of 29-May-2003 proton event in the energy range 0.8 - 40 MeV. 205

5.25 The temporal evolution of proton flux (top) and spectral index β (bottom) of 28-October-2003 proton event in the energy range 0.8 - 500 MeV. 206

5.26 The temporal evolution of proton flux (top) and spectral index β (bottom) of 29-October-2003 proton event in the energy range 0.8 - 500 MeV. 207

5.27 The temporal evolution of proton flux (top) and spectral index β (bottom) of 2-November-2003 proton event in the energy range 0.8 - 165 MeV. 208

5.28 The temporal evolution of proton flux (top) and spectral index β (bottom) of 7-November-2004 proton event in the energy range 0.8 - 80 MeV. 209

5.29 The temporal evolution of proton flux (top) and spectral index β (bottom) of 10-November-2004 proton event in the energy range 0.8 - 80 MeV. 210

5.30 The temporal evolution of proton flux (top) and spectral index β (bottom) of 15-January-2005 proton event in the energy range 0.8 - 80 MeV. 211

5.31 The temporal evolution of proton flux (top) and spectral index β (bottom) of 17-January-2005 proton event in the energy range 0.8 - 165 MeV. 212

5.32 The temporal evolution of proton flux (top) and spectral index β (bottom) of 20-January-2005 proton event in the energy range 0.8 - 500 MeV. 213

5.33 The temporal evolution of proton flux (top) and spectral index β (bottom) of 13-May-2005 proton event in the energy range 0.8 - 40 MeV. 214

5.34 The proton spectral index β as a function of flare spectral index γ. The best fit with a correlation coefficient of 0.67 is obtained. Note that the 20-January-2005 event is not considered in the fit. 215

6.1 The observed annual mean *aa* index (1868 to 2009) and annual mean sunspot number (1868 to 2010). 220

6.2 The observed annual mean *aa* index and annual sunspot number for the period of 1992 – 2008. Note that the annual mean *aa* index for the period of 2004 – 2008 is 18.4. 221

6.3 Plot of $(R_{n+1})^{max}$ of the $(n+1)^{th}$ cycle as a function of $(aa_n^*)_{dsc,}$ The solid line is the best fit with a correlation coefficient of r=0.89. 222

6.4 Variation of predicted (open circle) and observed (triangle) maximum annual mean sunspot number $(R_n)^{max}$ as a function of sunspot cycle number (*n*). The predicted $(R_n)^{max}$ are connected with dashed line. 223

6.5 The ascending period (in months), $(P_n)_{asc}$ is plotted as a function of $(R_n)^{max}$ for cycles 11 to 23 (Cycle 19 is omitted). The solid line is the best fit with r = - 0.86. 224

6.6 Representation of observed values of aa^* as a function of $(R_n)^{max}$ of the same cycle. Correlation coefficient is 0.85. 226

List of Tables

1.1	The SEC X-ray Flare Classification	24
2.1	SLD Characteristics	41
2.2	Special Features of the Detectors	42
2.3	Specifications and Operating Conditions of SLED	44
2.4	Energy ranges for the Energetic Particles Sensor	60
3.1	Detector and absorber specifications	69
4.1	Physical Properties of Flares observed by SOXS and RHESSI	95
4.2	Range of Spectral parameters obtained from SOXS and RHESSI	129
4.3	Integrated Thermal Energy release Estimates	139
4.4	Thermal and non-thermal energies and their ratio for 6 January 2004 flare observed by RHESSI	143
4.5	Thermal and non-thermal energies and their ratio for 5 April 2004 flare observed by RHESSI	144
4.6	Integrated thermal and non-thermal energies and their ratio	144
5.1	Details of Flares, CMEs and geomagnetic activity	173
5.2	Details of Flares and SEP events	183
5.3	Spectral index and photon flux at 50 keV for the hardest spectrum	199

CHAPTER 1
INTRODUCTION

In this chapter, I describe the solar structure from core to the corona, and the solar activity comprising of the sunspots, solar flares, coronal mass ejections and solar energetic particles. The Earth's magnetosphere and impact of solar radiation on it causing geomagnetic activity is also described. The open issues which motivated me to undertake the study are discussed. At the end I also present the organization of the thesis.

1.1 Our Sun: Structure:

About 4.6 billion years ago, in a distant spiral arm of our galaxy, called the Milky Way, a small cloud of gas and dust began to compress under its own weight. Particles within the clouds center (core) became so densely packed that they often collided and stuck (fused) together. The fusion process released tremendous amounts of heat and light which could then combat the compressing force of gravity; eventually, the two forces reached equilibrium. The balance of fusion reactions versus gravitational collapse which occurred in this little cloud is fondly referred to as a star, and this story is about the birth and life of the closest star to the Earth, the Sun. Our Sun is a medium sized star known as a yellow dwarf. The Sun is a normal main sequence G2V star. The Sun has been fusing hydrogen into helium and hence providing us with its radiant energy for 4.5 billion years, and it is expected to continue to do so for another 3 to 4 billion years more. Our Sun is a source of light and heat for life on Earth. Thus, being the most important star for mankind, every detail of the Sun is worthy of observations and study.

1.1.1 The Solar Interior:

The solar interior is separated into four regions, namely, the core, the radiative zone, the interface layer (Tachocline), and the convection zone, by the different processes that occur there. The solar structure showing the interior and the solar atmosphere is shown in Figure 1.1.

The Core:

The Sun's core (25%) is the central region where nuclear reactions consume hydrogen to form helium. The energy released during these reactions diffuses outward by radiation (mostly γ-rays and X-rays). The temperature at the core is about 15 MK, density upto 150,000 kg m^{-3} (150 times the density of water on earth), and a pressure of about 233 billion times that of the Earth's atmosphere at sea level (one bar).

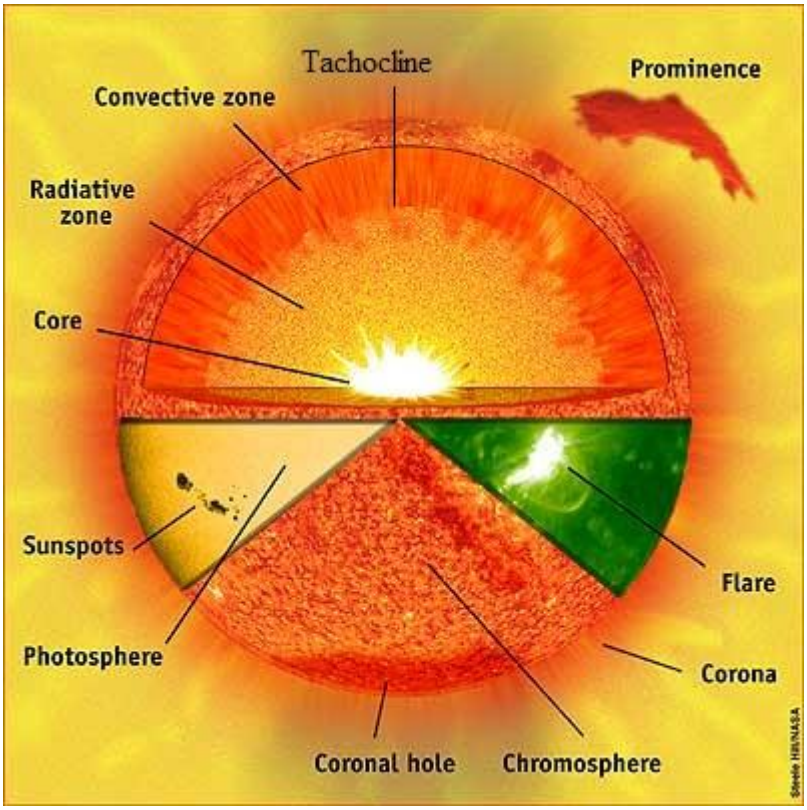

Figure 1.1: Basic overview of the solar structure. The three major structural areas, i.e. the core, radiative zone and the convective zone are shown in the upper hemisphere while the lower hemisphere shows the three atmospheres, i.e. photosphere, chromosphere and the corona. (Image: SOHO (Solar and Heliospheric Observatory)).

The Radiative zone:

The radiative zone extends outward to about 0.7 R_s from the outer edge of the core to the interface layer or the Tachocline at the base of the convection zone. Energy is transported outward in this zone through radiation. The

energy generated in the core is carried by light (photons) that bounces from particle to particle through the radiative zone.

The Interface Layer (Tachocline):

The interface layer lies between the radiative zone and the convective zone. This layer was called Tachocline by Spiegel & Zahn (1992). This thin layer has become more interesting in recent years as it is now believed that the Sun's magnetic field is generated by a magnetic dynamo in this layer. The changes in fluid flow velocities across the layer can stretch the magnetic field lines of force and make them stronger. This change in flow velocity gives this layer an alternative name-the Tachocline. There also appears to be sudden changes in chemical composition across this layer.

While the photosphere is the optical (visible) surface of the sun, the solar interior cannot be observed directly. It is possible to understand the solar interior in a better way by a systematic study of Global oscillations from the solar interior popularly known as Helioseismology. Helioseismic investigations are useful to study the internal rotation of the Sun. As determined by helioseismic studies, the tachocline is a transition layer between the solar convective envelope having differential rotation and the radiative interior where the rotation is nearly uniform. Employing the GONG and MDI data, Basu and Antia (2003) observed that in a tachocline layer, the rotation rate increases with radial distance at low latitudes, while at high latitudes the rotation rate decreases with radial distance. They further suggested the possibility of the tachocline comprising of two parts, one at low latitudes and the other at high latitudes, which are located at different depths and have different widths, but there may be no variation in position and width within each of these regions.

The Convection zone:

The convection zone is the outermost layer of the solar interior. It extends upto the visible surface of the Sun. At the base of the convection zone, the temperature is about 2 MK. This is cool enough for the heavier ions (such as carbon, nitrogen, oxygen, calcium, and iron) to hold onto some of their electrons. This makes the material more opaque so that it is harder for

radiation to get through. This traps heat that ultimately makes the fluid unstable and it starts to boil or convect. A steep temperature gradient is established and hot bubbles of gas rising through this gradient are accelerated to form convective cells. These convective motions carry heat quite rapidly to the surface.

1.1.2. The Photosphere:

The photosphere is the visible surface of the Sun and it is about a few hundred km thick. The effective temperature of the photosphere is ~ 5800 K ranging from a temperature of about 6400 K at its base to about 4400 K at the top of the photosphere. The coolest layer of the Sun is a temperature minimum region (TMR) about 500 km above the photosphere, with a temperature of about 4100 K. A number of features can be observed in the photosphere with a simple telescope. These features include the dark sunspots, the bright faculae, and granules etc.

Sunspots:

Sunspots are associated with strong magnetic fields emerging through the solar surface with magnetic field strengths of the order of 2000 to 4000 Gauss. Sunspots appear as dark spots on the surface of the Sun. Temperatures in the dark centers of sunspots drop to about 3700 K (compared to about 5700 K for the surrounding photosphere). Sunspots vary in size and shape, lasting from a few hours to several weeks and months. Sunspots usually come in groups with two sets of spots. One set will have positive or north magnetic field polarity while the other set will have negative or south magnetic field polarity. Mostly each sunspot has two regions: Umbra and penumbra. Umbra is the darker central part of the sunspot where the magnetic field is strongest. Penumbra is lighter part and filamentary around the edges where the magnetic field is weaker and more horizontal (*cf*. Figure 1.2 (top)).

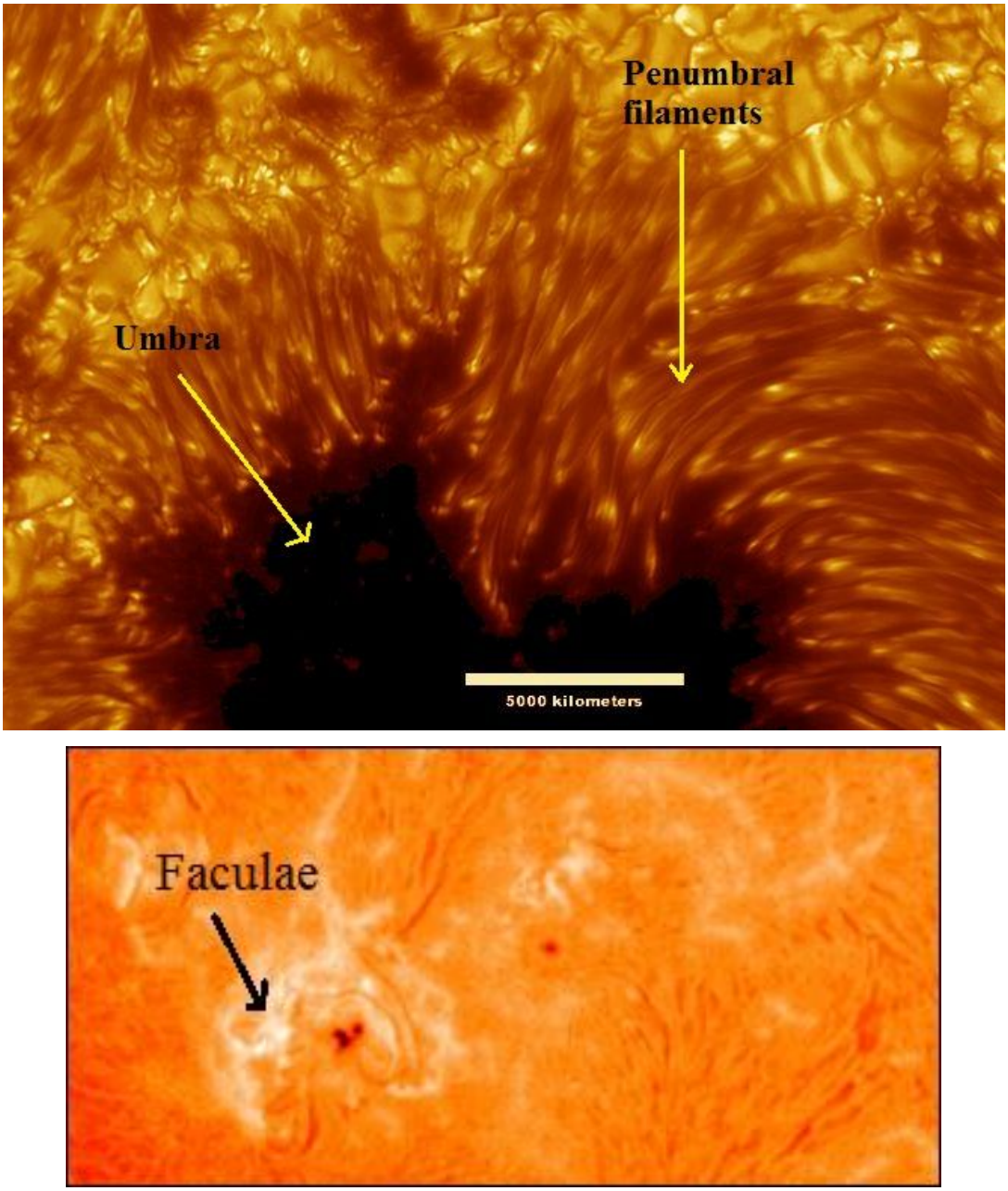

Figure 1.2: Sunspot image (top) with umbra (dark portion) and penumbral filaments. The image of planet-sized sunspot was taken by the Swedish Solar Telescope (SST) on 15 July, 2002. The penumbral filaments' newly revealed dark cores are seen to be thousands of kilometers long but only about 100 km wide (Scharmer *et al*., 2002). The bottom figure shows faculae which are the bright regions surrounding the sunspots (Image: Big Bear Solar Observatory).

Faculae:

Faculae are bright features (cf. Figure 1.2 (bottom)) seen in regions with fairly strong magnetic fields, sometimes more often in areas surrounding the sunspots. With respect to sunspots, the magnetic field is less concentrated in

facular regions. While sunspots tend to make the Sun appear darker, faculae have an opposite effect and brighten the photosphere.

Employing the data (corrected areas in micro-hemispheres) from full-disk solar images using two photometric telescopes at the San Fernando Observatory, CFDT1 and CFDT2, Chapman *et al*. (2011) analyzed facular/network and sunspot areas and their ratio covering most of cycle 22 and all of cycle 23. They observed a linear relationship of facular/network area to sunspot area and found that the average ratio of facular to spot area for cycle 22 is 45 and for cycle 23 the ratio is 42.

Granules:

Granules are the evidence of the bubbling motion of hot gases. Granules are created by the hot bubbles of gas rising from the interior and reaching the solar surface. These cellular features are the top of convection cells and cover the entire Sun except the areas covered by sunspots. In bright areas, hot gas rises up from interior and spreads out across the surface, resulting in the convection cells, or granulation. Cooler gas descends at the edge of each cell (which is the dark lane) and re-circulates back into the interior of the Sun. This motion is often referred to as overturning motion and this mechanism of energy transport is called convection. Granules are ~ 1000 km in diameter (average life time ~ 20 minutes) and supergranules are ~ 35000 km (average life time ~ day or two). Hinode's Solar Optical Telescope is the first space-borne instrument to measure the strength and direction of the sun's magnetic field in the photosphere. Figure 1.3 shows a highly magnified portion of the surface of the Sun taken by Hinode’s Solar Optical Telescope. The lighter areas reveal the gases rising from the interior, while the darker "intergranular lanes" reveal the cooler gases descending back to surface down.

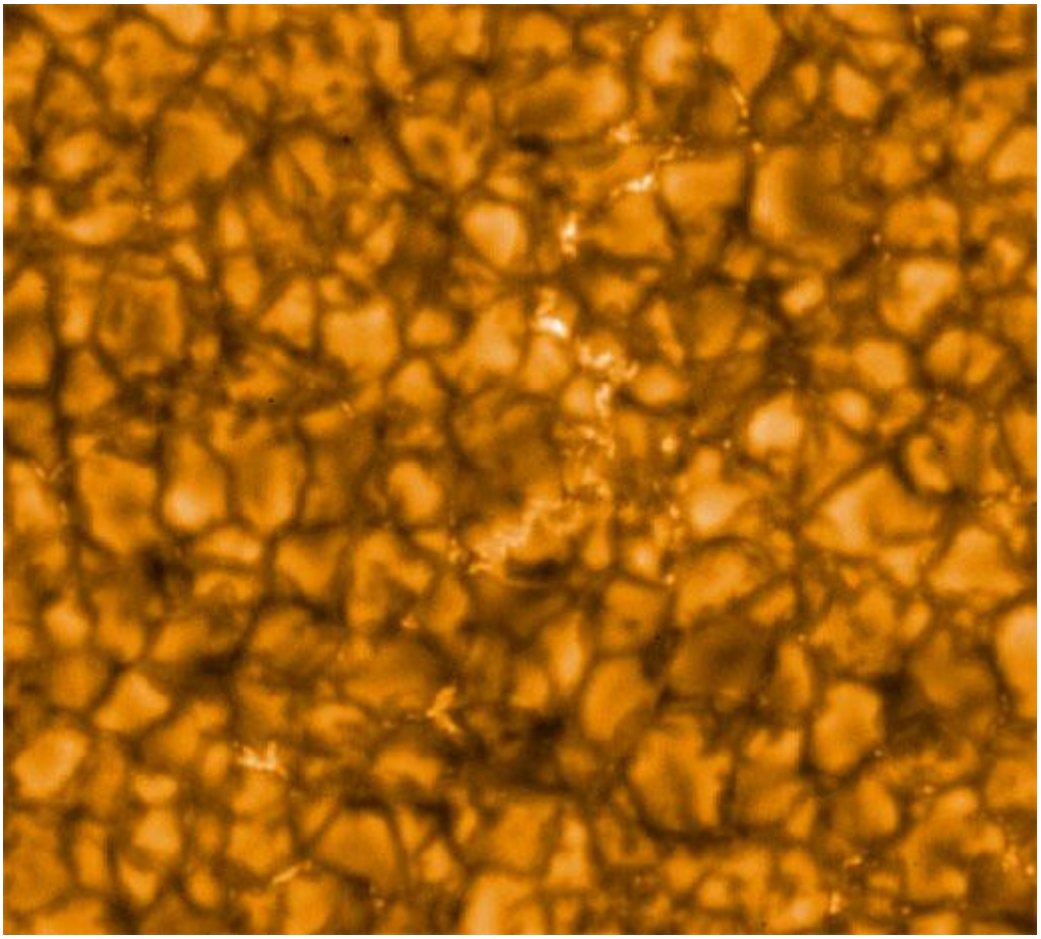

Figure 1.3: A highly magnified portion of the solar surface taken by Hinode's Solar Optical Telescope. Hot gases from the solar interior are transported by convection and results in granulation, seen in this image. The lighter areas reveal where gases are rising from the interior, while the darker "intergranular lanes" reveal where cooler gases are descending back down. (Image: Hinode JAXA/NASA/PPARC).

1.1.3 The Chromosphere:

The chromosphere lies above the photosphere. It was first discovered during a solar eclipse. It is ~ 2500 km thick layer where the temperature rises with altitude from about 4400 K to ~ 20000 K at the top of the layer. The chromosphere is most commonly observed in 6563 Å (Hα) wavelength using narrow passband Hα filters. The Hα filter isolates the red emission line of hydrogen at a wavelength of 6563 Å and rejects the rest of the spectrum. The chromosphere can also be observed at other spectral lines, for example, the violet K line of calcium with a wavelength of 3934 Å. The chromospheric features are filaments, spicules, mottles, surges and sprays.

Filaments and prominences:

A filament is a current system above a magnetic neutral line that builds up gradually over days and can remain in a quiet state for days or weeks. They can erupt prior to or during a flare or CME process (Aschwanden 2006). Filaments were first detected in Hα on the solar disk. Later on, they were also discovered in He 10830 Å and in other wavelengths. Filaments and prominences are identical. They differ in nomenclature with respect to their location on the solar disk. Filaments are observed on the disk while prominences are observed above the limb of the Sun.

1.1.4. The Transition region:

The transition region is a thin zone (~100 km) lying above the chromosphere. It separates the hot corona from the much cooler chromosphere. This thin region is produced when the heat flows down from the hot corona into the much cooler chromosphere. In the transition region, temperature changes drastically from ~ 20000 K to ~ 10^6 K with a corresponding decrease in density. Philips (2008) proposed an explanation for the structure and energy balance in the solar transition region. He suggested that the ingredients are simply cross-field diffusion of neutral atoms from cool threads extending into the corona, and the subsequent excitation, radiation, and ionization of these atoms via electron impact. The processes occur whenever chromospheric plasma is adjacent to hot coronal plasma, and when ion gyro frequencies exceed collision frequencies.

1.1.5. The Corona:

The corona is the outermost layer of the solar atmosphere with temperatures of ≥ 1 MK. The exact source of this high temperature in the solar corona (coronal heating) is still a fundamental problem in astrophysics. Jain *et al.* (2006) proposed micro and nanoflares as possible source for coronal heating based on the X-ray and simultaneous Hα observations. According to them the microflares are perhaps the result of the interaction of electrons that

accelerated during magnetic reconnection process with ambient plasma in the low lying coronal loops, and they also interact with the chromospheric material while moving down along the loops and thereby produce Hα bright kernels.

The features observed in the corona are active regions, coronal holes, helmet streamers, loop arcades, soft X-ray jets, post flare loops, cusp shaped loops, multiple arcades, sigmoid structures, flares, coronal mass ejections and solar wind. Some of the characteristic coronal features are described below:

Active regions:

Active regions span over a small fraction of the total solar surface area harboring most of the solar activity. They are located in areas of strong magnetic field concentrations and are visible as sunspot groups in optical wavelengths or magnetograms. Active regions are mainly composed of closed magnetic field lines owing to the bipolar nature of sunspot groups. Dynamic processes such as plasma heating, flares and coronal mass ejections (CMEs) occur in the active regions due to the permanent magnetic activity. Plasma heating in the chromosphere gives rise to upflows into coronal loops. Thus active regions appear as many filled loops. These loops are comparatively hotter and denser than the surrounding coronal plasma. They produce soft X-ray and EUV emission. The active regions can be seen in white in Figure 1.7 which shows the soft X-ray image observed by YOHKOH.

Coronal Holes:

The regions near the north and south poles of the Sun are generally darker than the equatorial regions. These dark regions are termed as coronal holes. These regions are associated with open magnetic field lines. Coronal holes appear dark because they flush hot coronal plasma into the solar wind and are therefore, void of plasma most of the time.

Solar Wind:

Parker (1958) derived the theoretical model of the solar wind suggesting that the gas flowing out from the Sun is not field-free but carries with it magnetic

lines of force which originate in the Sun. Solar wind is defined as the coronal plasma outflow from the Sun into the interplanetary space. The outflow of plasma blows past the planets at speeds that fluctuate between 200 km s^{-1} to 900 km s^{-1}. There are two types of solar wind: slow wind (speed ≤ 500 km s^{-1}) and fast wind (≥ 650 km s^{-1}). To drive the fast solar wind, the required energy flux density at 1 R_s is $F_E = 5 \times 10^5$ erg cm^{-2} s^{-1} (Marsch, 2006). The terminal speed beyond 10 R_S observationally is V_p = 700 - 800 km s^{-1}. The remotely inferred temperatures at 1.1 R_s are $T_e \approx T_p \approx$ 1- 2 MK, and the in-situ measured values at 1 AU are T_p = 0.3 MK, T_α = 1MK, and T_e = 0.15 MK. The three dimensional structure of the solar wind was confirmed by in situ measurements with Ulysses spacecraft.

The solar wind particles move radially outwards from the Sun, but due to solar rotation the direction of the solar wind becomes a spiral flow (Archimedes Spiral). With increasing distance from the Sun, the mean free path of the solar wind particles is very large and the solar wind can be treated as collisionless plasma (Campbell, 1997). As the electrical conductivity of the solar wind is very large, the currents generated in the solar wind hold the internal magnetic field within the solar wind. Thus, the field becomes frozen into the solar wind (at about 2.5 to 3 R_s). As the fast moving plasma overtakes the slower moving plasma, shock front of the compressed solar wind develops. Observations from recently launched STEREO mission can be used to develop three-dimensional (3-D) time-dependent models of the magnetic topology, temperature, density and velocity of the solar wind between the Sun and Earth (Kaiser *et al*. 2008).

1.2 Sunspot Cycle:

The sunspot cycle was discovered way back in early eighteenth century based on the periodic increase and decrease of sunspot groups. Schwabe (1844) discovered that the sunspot activity has a period of about 10 years. This cycle is called Schwabe cycle or the so called 11 year cycle. However, it has been observed that the sunspot cycle varies in amplitude and length. Hale *et al*. (1919) found that the polarities of the sunspot groups are opposite in Northern and Southern hemispheres when a new 11-year cycle starts

(Hale's polarity law). Also the preceding and following spots, with few exceptions, are of opposite polarity in Northern and Southern hemispheres. The original magnetic configuration is restored after a cycle of 22 years (Hale cycle). During the maximum of a sunspot cycle, the solar magnetic flux is at its peak and drops to a low level during the sunspot minimum.

According to Babcock (1961) dynamo model, when an initial poloidal field is sheared out under the influence of differential rotation, toroidal field is produced which erupts as an active region during the following cycle. According to the recent scenario, the origin of the sunspot cycle is the solar dynamo process that is driven by the internal magnetic field in the tachocline. In the tachocline, a strong magnetic field is periodically strengthened and weakened. Buoyant magnetic fluxtubes rise through the convection zone and emerge at the photosphere where they are visible as bipolar sunspot pairs. Diffusion of the erupting active region magnetic field and transport by the meridional flow then leads to the accumulation of opposite polarity fields towards the poles and the ultimate reversal of the polar fields (Hathaway, 2010).

The sunspot regions drift from higher latitudes (~ 40°) towards lower latitudes near the equator exhibiting "butterfly wings" as shown in Figure 1.4(b). The monthly averaged daily International Sunspot Numbers from 1610 to April 2011 are shown in Figure 1.4 (a) and the butterfly diagram of sunspots for the period 1875 – mid 2011 (approx) is shown in Figure 1.4 (b). The last solar maximum occurred in 2000. The noticeable variation in the maximum amplitude of sunspot cycles 1 to 23 (cf. Figure 1.4a) make the prediction of the next cycle maximum an interesting issue. Since the sunspot activity is the major determinant of space weather, its prediction is of utmost importance. Many researchers have attempted to predict the solar activity in the past using different prediction techniques. On the basis of geomagnetic activity aa indices during the descending phase of the preceding cycle, Jain (1997) predicted the sunspot maximum for cycle 23. Employing the precursor method used by him, Bhatt, Jain & Aggarwal (2009b) attempted to predict the amplitude of the current cycle 24 (chapter 6). Reviews on sunspot activity can be found in Usoskin (2008), Hathaway (2010) and references therein.

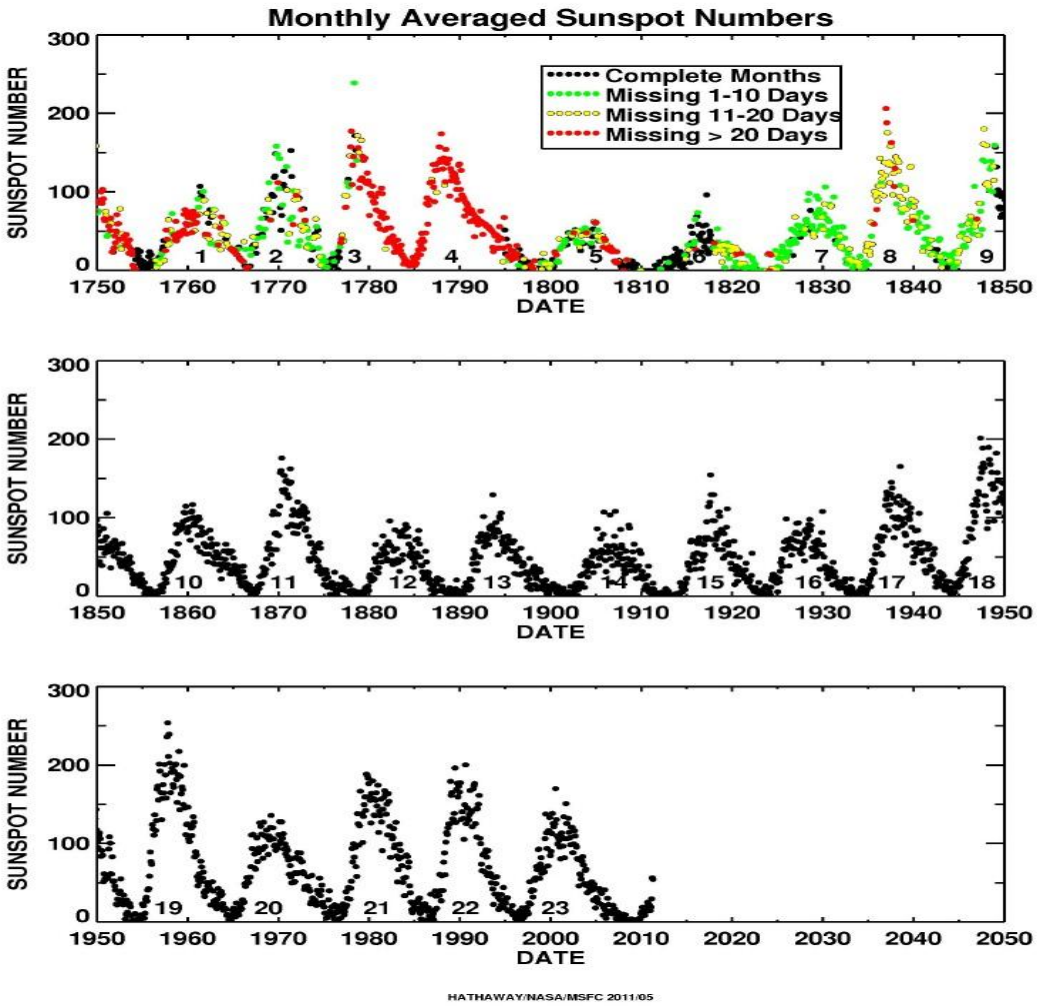

Figure 1.4 (a): The monthly averaged daily International Sunspot Numbers from 1610 to April 2011 (Image: Hathaway, D. H., MSFC, NASA).

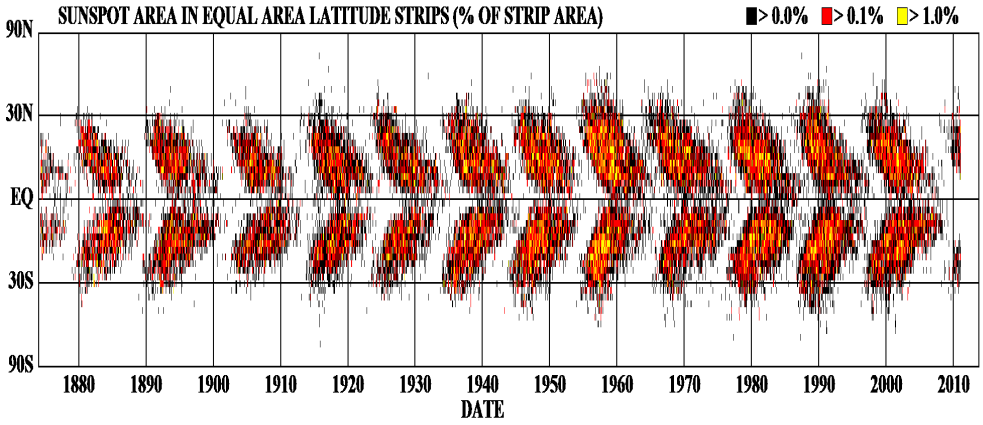

Figure 1.4 (b): The butterfly diagram of sunspots for the period 1875 to mid 2011 (approx) (Image: NASA)

1.3 Solar Flares:

Solar flares are extremely powerful events comprising of sudden, intense and rapid release of energy on the Sun emitting radiation from radio waves to X-rays and γ-rays in large flares. This radiation may be continuous emission in some parts of the spectrum, line emission in others, or a combination of both (Švestka, 1976). The first solar flare recorded in astronomical literature was on September 1, 1859. Two scientists, Richard C. Carrington and Richard Hodgson, were independently observing sunspots at the time, when they viewed a large flare in white light. Excellent reviews on solar flare and associated phenomena observations are given by Benz (2008), and Jain and Bharti (2009). The early idea of solar flares (Švestka, 1976) was formed from the observations taken at optical wavelength primarily in Hα (6563 Å). The Hα emission observations describe the shape, location and intensity of the solar flare in the chromosphere (immediately above the photosphere). Meter-wave radio emissions from flares were detected in 1942 during military radar operations and revealed the presence of non-thermal electrons in the corona (Hey, 1983). The UV/EUV radiation in the solar atmosphere originates in the chromosphere - corona transition region and in the upper atmosphere. EUV emissions have shown that the flare energy heats the plasma of coronal loops to temperatures from 1.5 MK to beyond 30 MK (Benz 2008). The soft X-rays from the Sun were first detected on 6 August, 1948 with V-2 rocket experiment performed by the U.S. Naval Laboratory (NRL, Burnight 1949). The X-rays cannot reach to the ground due to their absorption by the Earth's atmosphere, so the observations of solar X-rays are made with satellites, rockets or balloons. In the late 1950s it became possible to observe the Sun in hard X-rays (≥ 10 keV) by balloons and rockets. Peterson & Winckler (1959) discovered the first hard X-ray emission during a flare in 1958. The first observation of solar γ rays was made by Chupp *et al*. (1973) who reported preliminary observations from OSO-7 on the emission of γ ray lines associated with the solar flares on August 4 and 7, 1972. Solar flare emission is observed from the chromosphere to the corona.

The Phases of Flares:

The temporal evolution of the flare intensity at several wavelengths is presented schematically in Figure 1.5. In the preflare phase the coronal plasma in the flare region slowly heats up and is visible in soft X-rays and EUV. The magnetic energy is slowly built up in the corona. A good physical understanding of the preflare build-up and trigger mechanism is at the heart of understanding the physics of solar flares a whole. A large number of energetic electrons (up to 10^{38}) and ions (with similar total energy) are accelerated in the impulsive phase, when most of the energy is released. Some high-energy particles are trapped and produce intensive emissions in the radio band. The fast MHD plasma flows and the local restructuring of magnetic fields occurs during this phase. The thermal soft X-ray and Hα emissions finally reach their maxima after the impulsive phase. The heat is further distributed during the flash phase. In the decay phase, the coronal plasma returns nearly to its original state. In a large event, the preflare phase typically lasts a few minutes, the impulsive phase lasts upto tens of minutes, the flash phase 5 to 20 minutes and the decay phase can last for hours, depending on the power and intensity of the flare.

The Standard 2D Flare Model:

The 2D standard flare model is based on the magnetic reconnection that evolved from the concepts of Carmichael (1964), Sturrock (1966), Hirayama (1974), Kopp & Pneuman (1976). It has also been named as the CSHKP model after these scientists. Employing YOHKOH observations, this model has been elaborated further by Tsuneta (1996; 1997) and Shibata (1995).

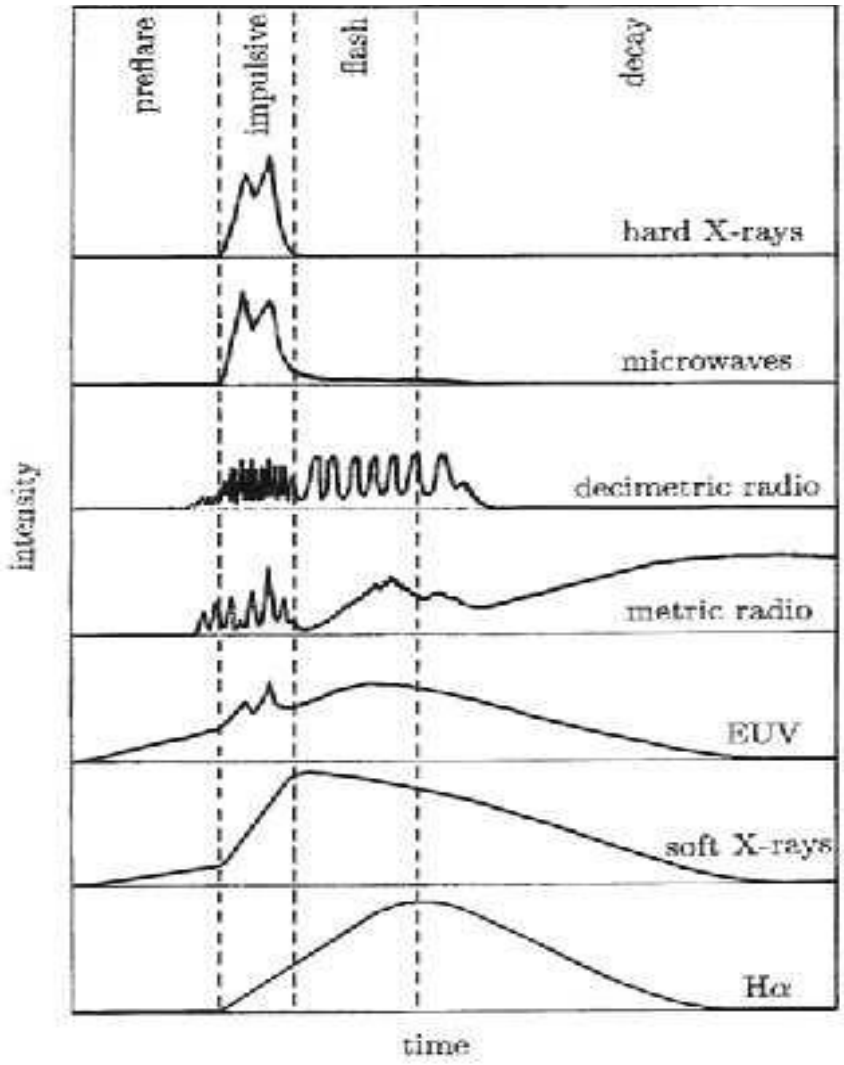

Figure 1.5: A schematic profile of the temporal evolution of the flare intensity at several wavelengths (taken from Benz, 1993)

According to the standard flare CSHKP model, the initial driver of a flare process is a rising filament (or prominence) above the neutral line. The rising filament stretches the overlying field lines. This results in the formation of the current sheet above a neutral line where they reconnect. In Petschek's reconnection model (1964), the size of the diffusion region current sheet occupies only a central compact location. As the length of the current sheet is shorter, the propagation time through the diffusion region is shorter and the reconnection process becomes faster. Most of the inflowing plasma turns around outside the compact diffusion region and slow mode MHD (magneto-hydrodynamic) shocks arise in the outflow region.

In the model of Sturrock (1966), a helmet streamer configuration was assumed to exist at the beginning of a flare, where the tearing-mode instability (induced by foot-point shearing) near the Y-type reconnection point triggers a flare, accelerating particles move in a downward direction and producing shock waves and plasmoid ejection in an upward direction.

Hirayama (1974) explains the preflare process as a rising prominence above a neutral line (between oppositely directed open magnetic field lines), which carries an electric current parallel to the neutral line and induces a magnetic collapse on both sides of a current sheet after eruption of the prominence. The magnetic collapse is accompanied by lateral inflow of plasma into the opposite sides of the current sheets. The X-type reconnection region is assumed to be the location of major magnetic energy dissipation, which heats the local coronal plasma and accelerates non-thermal particles.

These two processes produce thermal conduction fronts and precipitating particles which both heat the chromospheric footpoints of the newly reconnected field lines. As a result of this impulsive heating, chromospheric plasma evaporates and fills the newly reconnected field lines, with over-dense heated plasma, which produces soft X-ray emitting flare loops with temperatures of T_e ~ 10 – 40 MK and densities of n_e ~10^{10} - 10^{12} cm^{-3}.

Once the flare loops cool down by thermal conduction and radiative loss, they also become detectable in EUV (T_e ~ 1 – 2 MK) and Hα (T_e ~ 10^4 – 10^5 K). Kopp & Pneuman (1976) refined this scenario further and predicted a continuous rise of the Y-type reconnection point, due to the rising prominence. As a consequence, the newly reconnected field lines beneath the X or Y-type reconnection point have an increasingly larger height and a wider footpoint separation. Tsuneta (1996; 1997) and Shibata (1995) elaborated on the temperature structure, upward ejected plasmoids, slow shocks, and fast shocks in the outflow region of the X-type reconnection geometry as shown in Figure (1.6).

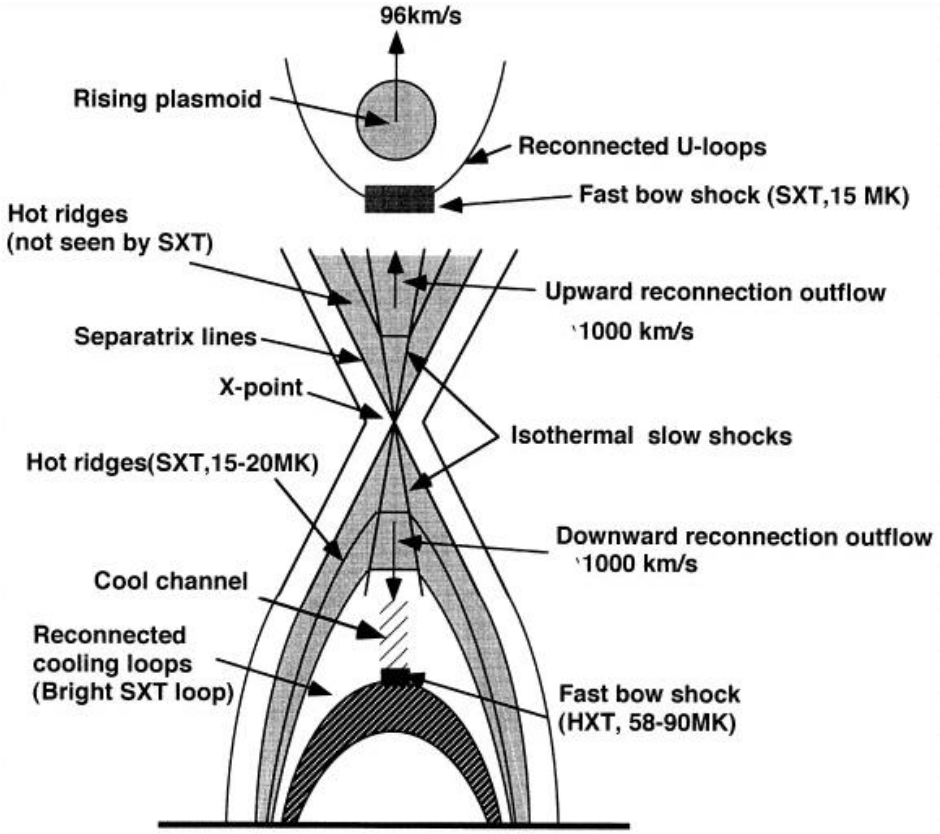

Figure 1.6: The standard 2D X-type reconnection model (Tsuneta 1997).

The heated plasma in the reconnection outflow produces hot ridges (T ~ 15 – 20 MK) along the seperatrices with the slow shocks, sandwiching the denser soft X-ray flare loops that occupy the newly reconnected relaxing field lines, which are filled with chromospheric evaporated plasma. The fast shocks in the reconnection outflows collide with the previously reconnected field lines and may produce hot thermal (as well as non-thermal) hard X-ray sources above the flare loop-tops. This model fits a lot of the observational features in hard X-rays, soft X-rays, Hα and radio wavelengths, providing a physical mechanism to explain self-consistently the processes of filament eruption, magnetic reconnection, and coronal mass ejection, but does not specify what drives the initial magnetic system to become unstable (Aschwanden 2006).

According to the general flare scenario, the accelerated electrons spiral down the magnetic field lines to the chromosphere. In the chromosphere, they suffer collisions with the ions in the ambient plasma and produce Bremsstrahlung. They loose energy through Coulomb collisions, which leads

to heating the chromospheric plasma upto several MK, which is also known as chromospheric evaporation. This hot plasma expands and fills up the coronal flare loops emitting soft X-rays. The temperature of the flare plasma decreases slowly and returns gradually to its original state due to flare plasma cooling processes.

1.3.1 Solar flares in Soft X-rays:

The soft X-rays (~ 0.1-10 keV) emitted during the solar flares are thermal radiation, released by the virtue of the intense heat and dependent upon the random thermal motions of very hot electrons. They are emitted in the solar corona. Soft X-ray (SXR) flux from an active region varies greatly with time. These variations may be fast, lasting from few minutes upto several hours, as well as gradual, lasting for hour upto days (Krieger *et al*., 1972, Parkinson, 1973). The fast variations are mostly associated with solar flares. According to Hudson *et al*. (1969) and Drake (1971) about 70% of these X-ray enhancements can be identified with Hα flares, but this percentage decreases if more sensitive X-ray detectors are used. A typical flare-associated SXR burst has a time profile roughly similar to the time development of the Hα intensity in the brightest point of the flare and similarly, is characterized by a fast rise and a much slower decay as shown in Figure 1.5 (Švestka, 1976). The SXR burst begins before the optical Hα event, reaches its peak later and ends several minutes after the optical flare is no longer visible (Thomas and Teske, 1971). Statistically, the strength of X-ray bursts increases with the increasing Hα importance of the flare. Figure 1.7 shows the image of the solar flare observed by YOHKOH in soft X-rays. The soft X-ray refers to the thermal part of the flare photon spectrum, upto ~20 keV in powerful flares. Soft X-ray line emission is discussed in Section 4.1.1.

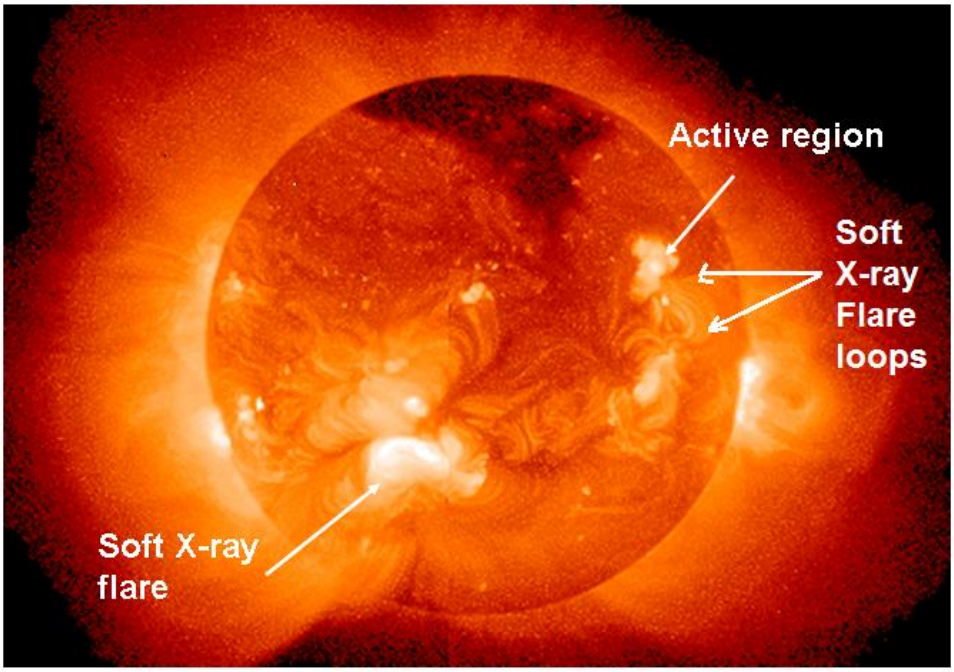

Figure 1.7: This image, from the soft X-ray (SXR) telescope onboard YOHKOH, shows X-ray flare emission of the solar corona on May 8, 1992. The effective wavelength is about 10 Å, or 1 keV, and the resolution is about 10 arc sec (Image: YOHKOH).

1.3.2 Solar Flares in Hard X-rays:

Solar flare hard X-ray (HXR) emission above ~ 20 keV is a continuum emission. The X-ray emission is associated with the physical process of Bremsstrahlung (section 4.1). This continuum is the non-thermal power-law like part of the photon spectrum. The non-thermal radiation mechanism can be described by two situations: Thick-target Bremsstrahlung and thin-target Bremsstrahlung (Brown, 1971). Here, I briefly summarize the thick target and thin target emissions.

Bremsstrahlung Cross-Section:

For Bremsstrahlung for electrons emitting HXR in the 10-100 keV range, the cross-section for a collision of an electron with energy E, producing a photon with energy ε (where $\varepsilon < E$), is given by non-relativistic Bethe-Heitler cross-section (Jackson, 1962):

$$\sigma_B(\varepsilon,E)=\frac{8\alpha}{3}r_0^2\frac{m_ec^2}{\varepsilon E}\ln\frac{1+\sqrt{1-\varepsilon/E}}{1-\sqrt{1-\varepsilon/E}}$$

Here, $\alpha=\frac{e^2}{\hbar c}=\frac{1}{137}$ is the fine structure constant; $r_0=\frac{e^2}{m_ec^2}$ is the classical electron radius; E and ε are in keV. $\sigma_B(\varepsilon,E)$ in cm^2 keV^{-1}. The term $\frac{8\alpha}{3}r_0^2m_ec^2=K_{BH}$ (cm^2 keV) is the constant in Bethe-Heitler cross-section.

$$\sigma_B(\varepsilon,E)=\frac{K_{BH}}{\varepsilon E}\ln\frac{1+\sqrt{1-\varepsilon/E}}{1-\sqrt{1-\varepsilon/E}}$$

$$\sigma_B(\varepsilon,E)=\frac{K_{BH}}{\varepsilon E}\ln\left[\left(\frac{E}{\varepsilon}\right)^{\frac{1}{2}}+\left(\frac{E}{\varepsilon}-1\right)^{\frac{1}{2}}\right] \qquad (1.1)$$

The energy loss rate by Coulomb collisions is given as

$$\frac{dE}{dt}=-\sigma_E(E)n_i\mathbf{v}(E)E \qquad (1.2)$$

where n_i is the target density and $\mathbf{v}(E)$ is the velocity of electrons. The cross-section for the Coulomb energy loss $\sigma_E(E)$ is expressed by

$$\sigma_E(E)=\frac{2\pi e^4\ln\Lambda}{E^2}=\frac{K}{E^2} \qquad (1.3)$$

where $\ln\Lambda$ is the Coulomb logarithm and $K=2\pi e^4\ln\Lambda$ which ranges from 20-30 for solar conditions.

Thick-target Bremsstrahlung:

Thick-target Bremsstrahlung occurs when the incident electrons have first been accelerated to a much higher (non-thermal) energy (in collisionless plasma) and then become collisionally stopped when they hit thermal plasma (Aschwanden 2006). Suppose that electrons with initial energy E_0 lose their energy via Coulomb collisions. The number of photons per unit energy

$v(\varepsilon, E_0)$ (photons keV^{-1}), at an energy of ε produced by an electron whose energy is E_0 is given as

$$v(\varepsilon, E_0) = \int_{t_0(E=E_0)}^{t_1(E=\varepsilon)} n_i \sigma_B(\varepsilon, E(t)) \mathbf{v}(E) dt = \int_{\varepsilon}^{E_0} \frac{\sigma_B(\varepsilon, E) dE}{E \sigma_E(E)} \qquad (1.4)$$

Since the electrons are decelerated until they are at rest in the target, the emitted photon flux $v(\varepsilon, E_0)$ is independent of n_i, the density of target ions. From this equation, the X-ray photon spectrum $I(\varepsilon)$ (photons cm^{-2} s^{-1} keV^{-1}) at the Earth's distance produced by electrons with their initial (or injection) energy distribution function $F(E_0)$ (electrons s^{-1} keV^{-1}) can be written as

$$I_{thick}(\varepsilon) = \frac{1}{4\pi R^2} \int_{\varepsilon}^{\infty} F(E_0) v(\varepsilon, E_0) dE_0$$

Substituting equation (1.4)

$$I_{thick}(\varepsilon) = \frac{1}{4\pi R^2} \int_{\varepsilon}^{\infty} F(E_0) \int_{\varepsilon}^{E_0} \frac{\sigma_B(\varepsilon, E)}{E \sigma_E(E)} dE dE_0$$

(1.5)

$$I_{thick}(\varepsilon) = \frac{1}{4\pi R^2 K} \int_{\varepsilon}^{\infty} F(E_0) \int_{\varepsilon}^{E_0} E \sigma_B(\varepsilon, E) dE dE_0$$

(1.6)

This equation implicitly defines the injection spectrum $F(E)$ by the observed photon spectrum $I_{thick}(\varepsilon)$. The implicit equations for the electron injection spectrum $F(E)$ can be transformed into Abelian integral equations whose

analytical solution was calculated by Brown (1971). He assumed the power-law function for the observed hard X-ray spectrum $I_{thick}(\varepsilon)$ as

$$I_{thick}(\varepsilon) = I_1 \frac{(\gamma - 1)}{\varepsilon_1} \left(\frac{\varepsilon}{\varepsilon_1} \right)^{-\gamma} \qquad (1.7)$$

where ε_1 is a reference energy, above which the integrated photon flux is I_1 (photons cm^{-2} s^{-1} keV^{-1}) and γ is the power-law slope. The parameters ε_1 and γ of the hard X-ray spectrum can be time-dependent. The total number of photons above lower cut-off energy ε_1 is the integral of equation (1.7),

$$I(\varepsilon \geq \varepsilon_1) = \int_{\varepsilon_1}^{\infty} I(\varepsilon) d\varepsilon = I_1 \qquad (1.8)$$

Brown (1971) solved the inversion of Eq. (1.6) and expressed the simplified form of associated electron injection spectrum $F(E)$

$$F(E) = 2.68 \times 10^{33} \gamma^2 (\gamma - 1)^3 B\left(\gamma - \frac{1}{2}, \frac{3}{2} \right) \frac{I_1}{\varepsilon_1^2} \left(\frac{\varepsilon}{\varepsilon_1} \right)^{-(\gamma+1)} \text{ (electrons keV}^{-1} \text{ s}^{-1}\text{)}$$

(1.9)

where $B(p,q)$ is the Beta function,

$$B(p,q) = \int_0^1 u^{p-1} (1-u)^{q-1} du \qquad (1.10)$$

which is calculated in Hudson *et al*. (1978) for a relevant range of spectral slopes γ and is combined in the Auxiliary function $b(\gamma)$,

$$b(\gamma) = \gamma^2 (\gamma - 1)^2 B\left(\gamma - \frac{1}{2}, \frac{3}{2} \right) \approx 0.27 \gamma^3 \qquad (1.11)$$

The beta function $B(p,q)$ is a function of photon spectral index (u is the ratio of kinetic energy E of the electron to photon energy ε).

So the power-law slope of the electron injection spectrum $(\delta = \gamma + 1)$ is steeper than γ of the photon spectrum in the thick-target model. With this

notation, the electron injection spectrum (Aschwanden 2006) may be written as,

$$F(E) = 2.68 \times 10^{33} (\gamma - 1) b(\gamma) \frac{I_1}{\varepsilon_1^2} \left(\frac{\varepsilon}{\varepsilon_1} \right)^{-(\gamma+1)} \quad \text{(electrons keV}^{-1}\text{ s}^{-1}\text{)}$$

(1.12)

The total number of electrons above cut-off energy ε_C will be

$$F(E \geq \varepsilon_C) = \int_{\varepsilon_C}^{\infty} F(E) dE = 2.68 \times 10^{33} b(\gamma) \frac{(\gamma - 1)}{\gamma} \frac{I_1}{\varepsilon_1} \left(\frac{\varepsilon_C}{\varepsilon_1} \right)^{-(\gamma)} \text{(electrons s}^{-1}\text{)}$$

(1.13)

Thin target Emission:

For the thin target case (Aschwanden 2006), the electrons are continuously accelerated. The thin target scenario is applicable to electrons injected outward through the corona and they emit X-rays as they travel upwards. Thin target scenario may also be applicable to a population of electrons which are confined in a magnetic trap and continue to emit X-rays. The hard X-ray spectrum is nearly identical to the acceleration or injection spectrum. The thin-target electron injection spectrum $F(E)$ is given in Lin & Hudson (1976) and Hudson *et al*. (1978),

$$F(E) = 1.05 \times 10^{42} C(\gamma) A \frac{1}{n_i} \varepsilon^{-(\gamma - 1/2)} \quad \text{(electrons keV}^{-1}\text{)} \qquad (1.14)$$

and the function $C(\gamma)$ is defined in terms of the beta function,

$$C(\gamma) = \frac{(\gamma - 1)}{B\left(\gamma - 1, \frac{1}{2}\right)} \approx (\gamma - 1.5)^{1.2} \qquad (1.15)$$

A given photon spectrum (e.g. with $\gamma = 3$) implies a flatter electron injection spectrum in the thin target case ($\delta = \gamma - \frac{1}{2} = 2.5$) than in the thick target case $\delta = \gamma + 1 = 4$. Unlike thick target emission, $F(E)$ in thin target emission depends on the target ion density n_i.

1.3.3 Flare Classification:

Individual solar flares differ greatly in size and intensity. The classification of solar flares in X-rays is ranked by its peak X-ray intensity in the 1 – 8 Å band as measured by the Geostationary Operational Environmental satellites (GOES), and has been presented in Table 1.1. It gives a better measure of the geophysical significance of a solar event, and it provides an objective means of classifying geophysically significant activity regardless of its location on the solar disk.

Table 1.1

The SEC X-ray Flare Classification

Classification	Peak Flux (φ) measured in (1– 8 Å) (W m^{-2})
A	$\varphi < 10^{-7}$
B	$10^{-7} \leq \varphi < 10^{-6}$
C	$10^{-6} \leq \varphi < 10^{-5}$
M	$10^{-5} \leq \varphi < 10^{-4}$
X	$10^{-4} \leq \varphi$

The classification letter designates the order of magnitude of the peak value and the number following the letter is the multiplicative factor. A C3.2 event for example, indicates an X-ray burst with 3.2×10^{-6} W m^{-2} peak flux. Solar flare forecasts are usually issued only in terms of the broad C, M, and X categories. Since X-ray bursts are observed as a full-Sun value, bursts below the X-ray background level are not discernible. The background drops to class A during the sunspot minimum period while during the solar maximum, it varies between B and C class.

1.4. Coronal Mass Ejections (CMEs):

The dynamic phenomena on the Sun known as Coronal Mass ejections (CMEs) occur as a consequence of reconnection of magnetized loops in the corona, which, however, accelerates magnetized plasma beyond the escape speed. Therefore, the CMEs are generally associated with a release of

magnetic energy in the solar corona. CMEs occur with a frequency of few events per day. CMEs carry a bulk of plasma with mass ranging from 10^{14} to 10^{16} g. As the CMEs propagate outward from the Sun into the interplanetary space, they expand in size and carry a frozen-in magnetic flux. A CME aimed towards the earth is called a Halo-CME or an Earth-directed CME event. It has been proposed that when the CME is launched in the western hemisphere of the Sun, the CME accelerated energetic particles propagate along the curved Parker spiral interplanetary magnetic field and they are likely to reach the Earth (Jain, 1986). Earth directed CMEs may cause most solar wind induced geoeffective disturbances which are responsible for large geomagnetic storms. They disrupt satellite communication systems, operation of low-earth orbiting satellites, operation of power grids on Earth and are therefore of practical importance. Figure (1.8) shows image of the halo CME captured by C2 coronagraph along with EIT instrument onboard SOHO mission on 13- December-2006.

Coronagraphs measure mainly photospheric light scattered by coronal electrons (Thomson scattering). An increase in brightness means that the integrated density along the line-of-sight is increased which provides us with a white-light image against the plane of the sky. A typical morphology of many CMEs is the three-part structure consisting of a bright leading edge (or frontal loop) and a dark cavity surrounded by a bright core. Employing the LASCO observations of CME, Chen *et al*. (1997) showed that the magnetic field geometry of a CME is that of a flux rope. They further explained that LASCO observations are consistent with a two-dimensional projection of a three-dimensional magnetic flux rope with legs that remain connected to the Sun.

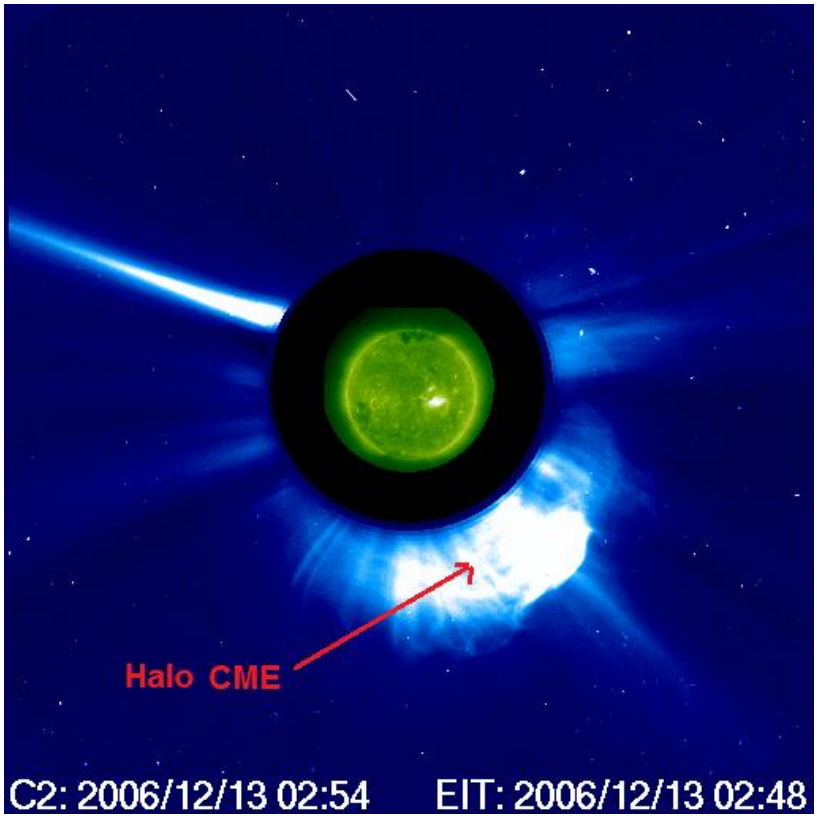

Figure 1.8: A halo coronal mass ejection (Image: SOHO/LASCO)

The density distribution in a CME is very inhomogeneous. The first determination of true mass of CMEs observed with SECCHI-COR2 on *STEREO*-A and B was made by Colaninno & Vourlidas (2009). They demonstrated that it is possible to simultaneously derive the direction and true total mass of the CME (with two viewpoints for spacecraft separations of 40º–50º) by assuming that the same mass should be observed in COR2-A and B.

Based on the velocity and acceleration profiles observed with SOHO/LASCO over the distance range of $2R_s$ to 30 R_s, it was proposed that there exist two distinct classes of CMEs (Sheeley *et al*. 1999): gradual CMEs and impulsive CMEs. When prominences and their cavities rise up from below coronal streamers, gradual CMEs are formed. They typically attain slow speeds (v ~ 400 - 600 km s^{-1}) with clear signs of gradual acceleration (3 - 40 m s^{-2}) at distances R < $30R_s$. Impulsive CMEs are often associated with flares and Moreton waves on the visible disk. They have velocities ≥ 750 - 1000 km s^{-1}. When first seen in coronagraphs, observations show that they either have a constant velocity or they decelerate at distances R ≥ $2R_s$.

Typical total energy of CMEs ranges between ~10^{29} - 10^{32} erg, comparable with the flare energy. Using the direct measurements of the mass, velocity, and dimensions of CMEs observed by LASCO on SOHO, Vourlidas *et al*. (2000) found that the potential and kinetic energies increase at the expense of the magnetic energy as the CME moves out, keeping the total energy almost constant. Jain (2010) studied the relationship between the CME velocity and plasma temperature of the solar flare employing SOXS (CZT) data and obtained a correlation of 0.82. This suggests that, when the free magnetic field energy in the active region is converted pre-dominantly to heating the flare plasma near the energy release site, the associated outgoing CMEs move faster initially. This also suggests that the source of the energy release of CME and flare events, when associated, is the same.

A closely associated phenomenon to CMEs is coronal dimming, which is interpreted in terms of an evacuation of coronal mass during the launch of a CME.

Owing to the space weather effects of CMEs, it is extremely important to understand their speed profiles, propagation direction and 3D configuration so that their arrival time can be accurately predicted. A better understanding in this context is now possible with the launch of STEREO spacecraft in 2006. The purpose of the STEREO Mission is to understand the causes and mechanisms of coronal mass ejection (CME) initiation and to follow the propagation of CMEs through the inner heliosphere to Earth (Kaiser *et al*. 2008). Mierla *et al*. (2010) suggested that the propagation direction and the 3-D structure of coronal mass ejections may be inferred using data from the SECCHI coronagraphs onboard the STEREO mission. They described different techniques that were used to model the 3-D configuration of CMEs in the coronagraph field of view (up to $15R_s$). They estimated the most probable CME propagation direction at the outer boundary of the corona (observed in coronagraph images) to within ~10°.

Various models have been proposed to understand and explain the theoretical concepts of a CME. Some of the major CME models are thermal blast model, Dynamo model, storage and release model, tether-cutting or flux cancellation model and magnetic breakout model. The thermal model proposed that a CME is driven outward by a greatly enhanced thermal

pressure produced by a flare (Dryer, 1982; Wu, 1982). The thermal blast model may not be acceptable since it is now known that many CMEs occur without a flare (Gosling 1993). Reviews on CMEs can be found in MacQueen (1980), Low (1996), Klimchuk (2001), and references therein. Reviews on CME models can be found in Vrˇsnak (2008), Chen (2011) and references therein.

1.5 Solar Energetic Particles (SEPs):

Solar energetic particles (SEPs) are accelerated particles escaping from the Sun into the interplanetary space. Some particles are originating in solar flares, while other being accelerated in transient interplanetary shocks, driven by fast CMEs. The SEP events are characterized by abrupt enhancements in the proton flux in the energy range of keV to GeV as measured by spacecraft at 1 AU. In particular, during SEP events, protons in energy range of 47 - 187 keV fed to the magnetosphere have been found to contribute substantially to enhancement of ring current leading to intense magnetic storms. On impacting the earth's magnetosphere, the SEP events can lead to a sudden disturbance of the earth's magnetic field, known as geomagnetic storms. The largest SEP event in the last 400 years appears to be related to the flare observed by Carrington in 1859 (Reames, 2004).

In major SEP events, the protons are accelerated to very high energies (~ GeV) within short time scale of seconds to minutes. This phenomenon is still not well understood.

SEP events can be classified into two types (Reames 1999): Impulsive and gradual. Gradual SEP events are long duration events. They are associated with coronal and interplanetary shocks and are proton-rich. On the other hand, impulsive SEP events are short duration events. They are believed to be associated with a solar flare and they are electron-rich and ^{3}He-rich events.

It is generally accepted that a spacecraft must be magnetically well-connected to the flare site to be able to see the escaping SEPs. Literature on SEPs can be found in Schwenn (2006) and references therein.

Measurements from IMPACT and PLASTIC instrument onboard STEREO spacecraft may be used to study the mechanisms and sites of energetic particle acceleration (Kaiser *et al*. 2008). Barnard and Lockwood (2011) studied 110 gradual SEP events for the period 1967-2006 providing estimates of event onset, duration, fluence, and peak flux for protons of energy E > 60 MeV. They further investigated the variation of gradual SEP occurrence and fluence with solar cycle phase, sunspot number and interplanetary magnetic field intensity over solar cycles 20–23. They found that there is a positive correlation between SEP occurrence and solar activity as determined by SSN and B_{mag}, while the mean fluence in individual events decreases with the same measures of solar activity. Therefore, although the number of events decreases when solar activity is low, the events that do occur at such times have higher fluence. Thus, large SEP events such as the “Carrington flare” may be more likely when the solar activity level is low.

1.6 Earth’s Magnetosphere and Geomagnetic Activity: A brief overview:

In 1959 Thomas Gold of Cornell University proposed to name the Earth’s environment as "magnetosphere", and this name is still used. He wrote: "The region above the ionosphere in which the magnetic field of the earth has a dominant control over the motions of gas and fast charged particles is known to extend out to a distance of the order of 10 earth radii; it may appropriately be called the magnetosphere" (Gold, 1959). The Earth’s magnetosphere is a bubblelike region defined by the presence of the Earth’s main magnetic field in space (Campbell, 1997). Life on Earth has developed and sustained under the protective shield of this magnetosphere. Figure 1.9 shows a simple illustration of Earth’s magnetosphere.

The Earth’s magnetic field extends upto a limited distance only which is known as magnetopause. It is the outer limit of Earth’s magnetic field (magnetosphere). It isolates the Earth’s magnetic field from interplanetary

environment and solar wind (moving plasma of ionized particles and associated magnetic fields that are expanding outward from the Sun). Magnetopause is flattened on sunward side by solar wind pressure. On the side facing the Sun, the distance to its boundary (which varies with solar wind intensity) is about 5 to 20 R_e (earth radius, 1 R_e = 6371 km) with a typical location of 11 to 12 R_e. On the anti-sunward side, the magnetopause is drawn out into a long tail which extends possibly 1000 times Earth's radius, its exact length is not known.

This extension of the magnetosphere is known as the magnetotail (or geotail). Above and below the geotail (beyond about 20 R_e) the field lines run in opposite directions and in the central portion there is a neutral sheet. The geotail lobes connect magnetically to the polar cusps at one end and to the interplanetary field at the other end. The polar cusps occur where the magnetospheric field is folded downstream by the solar wind.

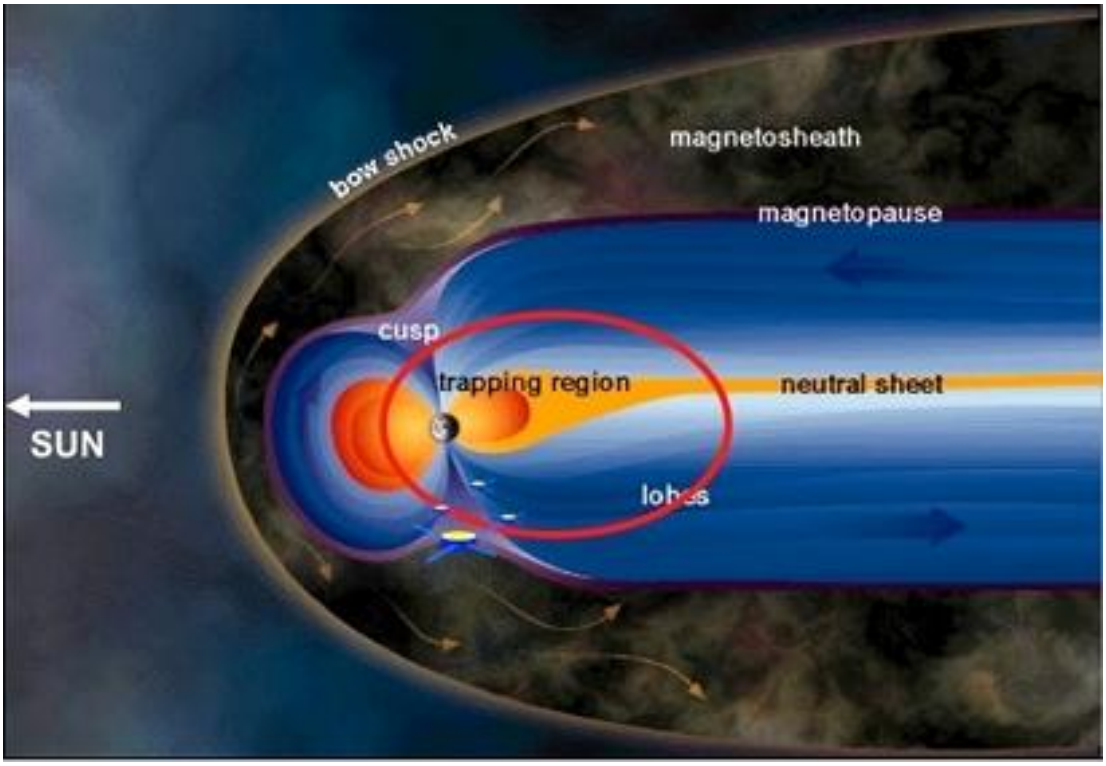

Figure 1.9: Illustration of Earth's magnetosphere (in blue) immersed in the solar wind. The orbit of the Cluster satellites is depicted in red. Earth's cusps are located near the poles. They are magnetic field features of the magnetosphere associated with regions through which plasma from the Sun can have direct access to the upper atmosphere (Image: ESA).

When the solar wind flows Earthward from the Sun, it senses an obstacle ahead of it in the form of Earth's magnetic field and develops a bow shock at about 10-15 R_e. Bow shock is an imaginary surface at which the solar wind is first deflected. Bow shock is continuously formed as solar wind particles and their frozen-in interplanetary magnetic field (IMF) encounter Earth's magnetosphere. The turbulent region (plasma) between the bow shock and the magnetopause is called magnetosheath.

The solar wind could not normally penetrate the magnetosphere, but on certain occasions, particularly after solar flares, interplanetary structures with high number density and increased wind speed cause geomagnetic storms but only when the magnetic field in the structure had a southward component ($-B_z$ IMF) antiparallel to the geomagnetic field (Kane, 2005). Dungey (1961) explained that magnetic field reconnection between the southwardly directed IMF and the geomagnetic field leads to magnetospheric energization and magnetic storms. If the IMFs are directed opposite to the Earth's field, there is magnetic erosion on the dayside magnetosphere by magnetic reconnection, and the magnetic field accumulates in the nightside magnetotail region. The magnetic reconnection in the tail leads to the plasma injection towards the earth in the nightside. Low energy particles precipitate in the high latitudes and cause aurora, while high energy protons drift to the west, and the electrons drift to the east forming a "ring current" around the Earth. This ring current causes a reduction in the geomagnetic field (storm time disturbance field Dst). Ring current is located at about 2-7 R_e. This ring current causes a decrease (depression) in the horizontal (H component) intensity of the geomagnetic field.

The geoeffectiveness of different types of CME/shock structures is explained by Koskinen & Huttunen (2006). They observed that smoothly rotating magnetic fields within CMEs are most efficient in driving storm activity seen in the inner magnetosphere due to enhanced ring current, whereas the sheath regions between the shock and the ejecta tend to favour high-latitude activity. Reviews on geomagnetic storms can be found in Gonzalez *et al*. (1994), Yermolaev & Yermolaev (2010).

Geomagnetic activity Indices:

Magnetic activity indices (e.g. Dst, AE, aa, A_p, K_p, ASY) are designed to describe variations in the geomagnetic field. A brief description of Dst index and aa index which are used in the thesis is given below.

Disturbance Storm Time Index Dst:

It has long been known that the horizontal component, H, of the geomagnetic field is depressed during periods of great magnetic disturbances and that the recovery to its average level is gradual (Broun, 1861; Adams, 1892; Moos, 1910). Comprehensive analyses of magnetic storm morphology have been made by Chapman (1935, 1952), Vestine *et al*. (1947), Sugiura and Chapman (1960), and many others (Akasofu and Chapman, 1972). These studies have shown that at equatorial and mid latitudes the decrease in H during a magnetic storm can approximately be represented by a uniform magnetic field parallel to the geomagnetic dipole axis and directed toward south. The magnitude of this axially symmetric disturbance field varies with storm-time, defined as the time measured from the storm onset. The onset of a magnetic storm is often characterized by a global sudden increase in H, which is referred to as the storm sudden commencement and denoted by ssc.

Following the ssc, the H component typically remains above its average level for a few hours; this phase is called the initial phase of the storm. Then a large global decrease in H begins, indicating the development of the main phase of the storm. The magnitude of the decrease in H represents the severity of disturbance. Although the above description gives statistical average features of magnetic storms, the variations in individual cases differ greatly from one storm to another. The disturbance field is denoted by Dst, which is axially symmetric with respect to the dipole axis, and which is regarded as a function of storm-time. If an index monitoring the Dst in H is derived continuously as a function of UT, this variation clearly indicates the occurrences of magnetic storms and their severity when they occur. Furthermore, even in the absence of distinct magnetic storms, this index continuously monitors disturbances that are smaller in magnitude than those

usually called magnetic storms, or disturbances that begin gradually without a well-defined commencement. Thus, the Dst variation so derived provides a quantitative measure of geomagnetic disturbance that can be correlated with other solar and geophysical parameters (Source: http://wdc.kugi.kyoto-u.ac.jp/dstdir/dst2/onDstindex.html).

Sugiura and Chapman (1960) assigned a numerical intensity index to individual storms by measuring the difference in daily mean values of the horizontal field at 26 mostly middle and low geomagnetic latitude observatories. Reorganizing low-latitude ground-based data to measure the intensity of the ring current, Sugiura (1964) published hourly values of the average global variation of the low-latitude H component (H, D, and Z are the vector components of the magnetic field at ground based observatories: H, horizontal; Z, vertical; and D, the dip-angle between the field vector and H) for the International Geophysical Years. This index, called Dst, has been continued since then and is presently compiled by the World Data Center for Geomagnetism in Kyoto, Japan.

Geomagnetic activity index aa:

The aa index of geomagnetic activity provides one of the longest and most important solar proxy data sets. The *aa* index was retrospectively compiled for 1868-1968 by *Mayaud* (1972) and has been continued up to the present day. The "*K* indices" from two near-antipodal stations are compiled from the range of variation of the horizontal component of the geomagnetic field in each 3-hour period and, using site-dependent scaling factors, are then combined to generate *aa*. The K indices are derived from the magnetic observations according to a standard process which includes the removal of the solar quiet time (Sq) variation. By averaging the two antipodal stations, the annual variation is reduced. Past investigations have shown that the long-term measure of geomagnetic activity, the aa index, is inhomogeneous. It shows a large (about 12 nT) centennial increase, most likely caused by related variations of solar activity (Lukianova, 2009). This increase in global geomagnetic activity, first found and quantified by the aa index, has been widely discussed in literature, and important results about the related changes

in the Sun have been obtained (Russell, 1975; Feynman and Crooker, 1978; Clilverd *et al*., 1998; Demetrescu and Dobrica, 2008).

1.7. Open Issues:

Solar flares and CMEs also release energetic particles into space and, when they move Earthward, can cause major geomagnetic storms and drive interplanetary (IP) shocks. Solar flares influence the ionosphere and radio communications at the earth. They can damage satellites and endanger spacewalking astronauts. Therefore, there is a strong need to understand the impact of solar activity on the earth, which is also an integral part of space weather. The solar variables responsible for geomagnetic activity at the earth are not well understood because of constraints on the temporal, spatial and spectral observations made in multi-wavelengths. However, recent investigations by the space missions *viz*. Hinode, SDO and STEREO show that the high energy eruptions on the sun can influence the earth strongly but the quantitative relationship between magnitude of the energetic eruptions (flares, CMEs and SEPs) and their impact on the earth has not been well known, and thereby requiring a detailed investigation.

The single temperature approximations have been widely used in the past in investigations of X-ray emissions from the solar flares. However the fact that the plasma is heated at different temperatures (multi-thermal plasma), and the emission measure varies as a function of temperature emphasizes the crucial need to study the X-ray flare spectra with high energy and temporal resolution. Similarly, the continuum spectra above 10 keV with better energy and temporal resolution are also essential to improve our current understanding on the non-thermal acceleration of electrons during impulsive phase of solar flares. The relationship between the thermal and non-thermal components of the total flare energy budget is not well understood. Indeed, the total energy in either component has generally not been determined to better than an order of magnitude. However, there are strong indications that, in many flares, the non-thermal component contains a substantial fraction of the total flare energy (Dennis *et al*. 2003, Jain *et al*. 2008), while significant energy release in soft X-ray domain (<10 keV) is also

estimated to first order. Thus, it is critically important to improve our present knowledge of the flare energy release process to determine the energy in these two components and their relationship as a function of time more precisely. In this view, I am motivated to investigate these issues in detail employing observations from “Solar X-ray Spectrometer (SOXS)” and “Reuven Ramaty High-Energy Solar Spectroscopic Imager (RHESSI)” missions (presented in Chapter 4).

The flare-CME relationship is a big issue in solar physics (Gosling 1993; Hudson *et al*. 1995; Jain *et al*., 2010). Both of these phenomena often occur in conjunction but the exact nature of the flare-CME triggers and the relationship between the cause and consequence is still open and quite puzzling. Statistical studies show that CME parameters, like the velocity or kinetic energy, are correlated with characteristics of the associated flare, e.g., the SXR peak flux or the integrated flux (Moon *et al*. 2002, 2003; Burkepile *et al*. 2004; Vrˇsnak *et al*. 2005; Chen & Zong 2009). More recently Jain *et al*. (2010) found that the velocity of CMEs increases with plasma temperature (R=0.82) of X-ray flare. They suggested the heating of the coronal plasma appears significant to release CME from the reconnection region where the flare also occurs. They proposed that initiation and velocity of CMEs perhaps depend upon the dominant process of conversion of the magnetic field energy of the active region to heating/ accelerating the coronal plasma in the reconnected loops. Their results show that flare and associated CME are two components of one energy release system, perhaps, magnetic field free energy. The above results imply that there exist close physical connections between CME kinematics and flaring processes, at least for a certain class of CME-flare pairs. However, no study has been made on the relationship between the dynamics of CMEs and the X-ray flare plasma characteristics to address the important question of whether solar flares and associated CMEs are related with early impulsive acceleration taking place during reconnection of the magnetized loops? In this context, I am motivated to study the X-ray spectral characteristics of solar flares and compare them with dynamics of the associated CMEs. In contrast to Jain *et al*., (2010) who employed SOXS data for 4-50 keV energy band, I study the X-ray emission characteristics of solar flares observed by the RHESSI mission in the energy band 13–100 keV and

compare them with dynamics of the associated CMEs. The investigation with important findings is presented in Chapter 5.

Following to pioneering work namely “A new approach for predicting proton events” by Jain (1986) suggesting a special class of flares only produce proton events, Kiplinger (1995) studied the hard X-ray spectral evolution in solar flares and their associations with energetic interplanetary proton events. He employed data from the Hard X-ray Burst Spectrometer (HXRBS) instrument onboard the Solar Maximum Mission (SMM). He found a strong association of hard X-ray progressive spectral hardening with interplanetary proton events. Saldanha *et al*. (2008) studied the progressive spectral hardening in January 2005 solar flare events and confirmed that the progressive spectral hardening in these flares are related to solar energetic particle (SEP) events. Grigis and Benz (2008) studied the spectral hardening in large solar flares and proposed that the hardening during the decay phase is caused by continuing particle acceleration with longer trapping in the accelerator before escape. Grayson *et al*. (2009) studied 37 magnetically well-connected flares (W30-W90) observed by RHESSI and found that 12 out of 18 flares with SHH behavior produced SEP events and none of 19 flares without SHH behavior produced SEPs. However, all these studies are based on temporal evolution of spectra, while no study has been carried out in detail to estimating the evolution of the spectral index (hardness parameter) over time and its relation with spectral index of the associated proton event. Therefore I studied hard X-ray spectra of the flares in greater detail in context to their relationship with the SEPs (protons). I employed the RHESSI observations for this investigation and the results are presented in Chapter 5.

The Sun and Earth are related through the impact of solar radiation on the Earth’s weather and climate. Space weather and space climate are the short-term and long-term variability in the plasma environment of the Earth and other planets. The study of solar–terrestrial environment involves the investigation of short-term as well as long-term evolution of solar and geomagnetic activities, which has applications for the forecasting of space weather and space climate. The space weather is largely affected due to explosions on the Sun *viz.* solar flares and CMEs, which, however, in turn

depend upon the magnitude of the solar activity *i e*. number of sunspots and their magnetic configuration. Owing to these space weather effects, predictions of solar and geomagnetic activity are important, and, therefore, in speculation of forthcoming sunspot cycle 24, which is in great debate, I undertook study of prediction of the amplitude of the sunspot cycle 24 and possible geomagnetic activity on the Earth during this period and published two research papers in peer reviewed international journals. I include this investigation in the thesis in Chapter 6, and below is brief description of the same.

I have predicted the annual geomagnetic activity aa index to be 20.6 ± 4.7 nT for the solar maximum year of sunspot cycle 24 (Bhatt, *et al*. 2009a). However, following the method of Svalgaard, Cliver, and Le Sager (2004) and Wilson and Hathaway (2006), the values of *aa* prior to 1957 were increased by 3 nT in the present study to compensate for change in the geographical latitudes of the magnetometers used in determining the *aa* index. I have estimated the annual mean geomagnetic activity *aa* index for the solar maximum year in cycle 24 to be 21.75 ± 3.8 which is close to the earlier predicted value of 20.6 ± 4.7. This predicted value of *aa* is lower compared to the observed 31(in 1989) and 25.4(in 2000) for cycle 22 and 23 respectively. This depicts the decreasing trend of geomagnetic activity during the sunspot maximum year of the upcoming cycle 24 as compared to previous two cycles.

Various techniques, namely, even/ odd behaviour, precursor, spectral, climatology and neural networks have been used in the past for the prediction of the solar activity. Many researchers (Ohl, 1966; Kane 1978, 2007; Thompson, 1993; Jain, 1997; Hathaway and Wilson, 2006; Wilson and Hathaway, 2009) have used the 'precursor' technique to predict the solar activity. In this view, my prediction for the amplitude of the maximum annual mean sunspot number of current solar cycle 24 to be 92.8±19.6 (Bhatt *et al*. 2009b) and the results are presented in Chapter 6.

The main objectives of my investigation are as following.

- Study of X-ray emission characteristics of solar flares employing high sensitivity and sub-keV energy resolution capabilities of the Si PIN detector of the SOXS and RHESSI missions.
- Investigation of solar flare plasma characteristics in association to CMEs and SEPs.
- Prediction of solar activity using precursor technique.

1.8 Organisation of the Thesis:

The thesis consists of seven chapters including the Introduction chapter. Chapter 2 contains the description of the instruments of which the data have been used for the investigation in this thesis while Chapter 3 contains the data acquisition and data analysis techniques. In chapter 4, I present the study of X-ray emission from solar flares observed by SOXS and RHESSI missions. I describe detailed investigation related to solar variables affecting terrestrial environment in Chapter 5, and in chapter 6 the prediction of solar activity of the current sunspot cycle 24 has been presented. Chapter 7 comprises discussions, and future scope and prospects of this work.

CHAPTER 2
INSTRUMENTS

The investigation in this thesis required observations from space-borne instruments in order to study X-ray emission in solar flares. Observations from ground-based instruments are used to study the geomagnetic activity. This chapter presents the details of space-borne instruments and ground-based instruments used for the study of solar and geomagnetic activity respectively.

A: Space-borne Instruments:

2.1 SOXS:

Solar X-ray Spectrometer (SOXS) is the first space-borne solar astronomy experiment of India. The “Solar X-ray Spectrometer (SOXS)” mission (Jain *et al.*, 2000a) was successfully launched onboard an Indian geostationary satellite namely GSAT-2 on 8 May 2003 by GSLV-D2 rocket. The SOXS aims to study the high spectral and temporal resolution X-ray spectra from solar flares. The SOXS consists of two independent payloads, viz. SOXS Low-Energy Detector (SLD) and SOXS High-Energy Detector (SHD) payloads. The SLD is comprised of two semiconductor devices, viz. silicon PIN detector for 4–25 keV (area 11.56 mm^2); and cadmium–zinc–telluride (CZT) detector for 4–56 keV energy range (area 25 mm^2). These state-of-the-art solid state detectors in SLD have superb sub-keV energy resolution and 100 ms temporal resolution characteristics, which make them most appropriate for solar flare research in the context of energy transport and acceleration time scales of particles. This section presents the details of the SLD instrumentation and its in-orbit performance. For my investigation I have employed observations from the SLD payload and the observations and results are discussed in Chapter 4.

The SLD payload consists of four subsystems, viz. SOXS Low Energy Detector (SLED) package; SOXS Sun Tracking Mechanism (SSTM), SOXS Low Energy Processing Electronics (SLE) package; and SOXS Common

Electronics (SCE) package. The SLD payload, spacecraft and mission characteristics are presented in Table 2.1 while the block scheme of the SLD payload is shown in Figure 2.1. I describe below the specifications and operations of various packages of the payload.

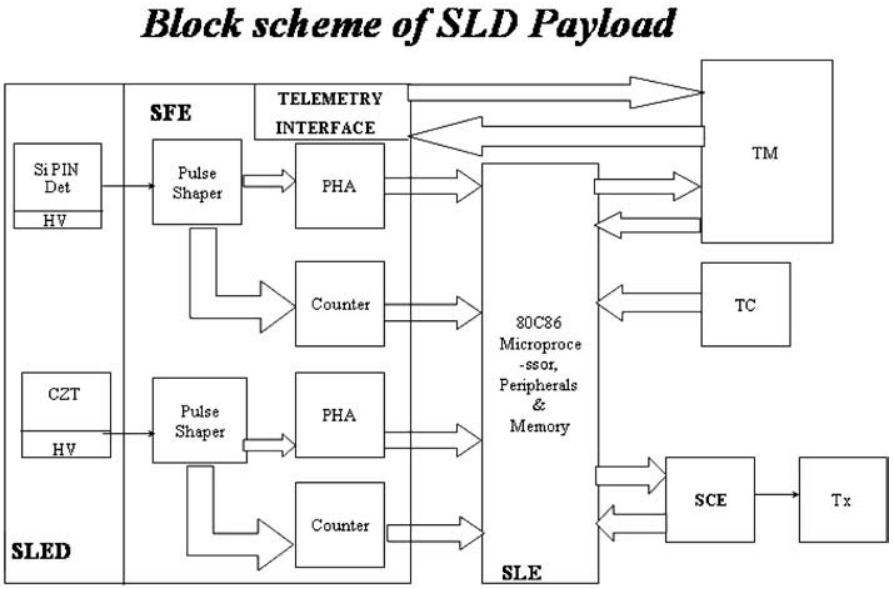

Figure 2.1: The block scheme of the SLD payload.

2.1.1 The Solid-state Detectors:

The state-of-the-art solid state detectors viz. Si PIN and CZT detectors (diodes) have been used, for the first time, for a dedicated space-borne solar astronomy experiment. These are new high performance X-ray detectors having a charge sensitive preamplifier and thermoelectric cooler system. The FET and the feedback circuit are also mounted on the cooler. These components are kept approximately at −20°C, and can be monitored by an internal temperature sensor. The detectors were developed at the Physical Research Laboratory using the hermetic TO-8 package from Amptek, USA. Special features of these detectors, which have been exploited to full potentiality to achieve the science goals, are shown in Table 2.2. In Table 2.3 specifications and operating conditions of CZT and Si detectors are presented.

Table 2.1 (SLD Characteristics)

1a. Instrument characteristics:		
Detectors:	Si PIN	CZT
Energy range:	4 - 25 keV	4 - 60 keV
Energy resolution (FWHM):	~700 eV at 5.9 keV, ~ 900 eV at 22.2 keV.	~1.5 keV at 5.9 keV ~1.8 keV at 22.2 keV
Temporal Resolution:		
Flare	100 ms	100 ms
Quiet	1 s temporal, 3 s spectral	1 s temporal, 3 s spectral
Field of view	full Sun (~3.4°)	full Sun (~3.4°)
Effective area:	~10^{-4} cm^2 at 4 keV ~10^{-2} cm^2 at 10 keV	~10^{-4} cm^2 at 4 keV ~10^{-1} cm^2 at 30 keV
Aspect system:	SOXS Sun Tracking Mechanism; Sun centered to <0.2°	
Mass:	18 kg	
Power:	20 watts	
Telemetry:	8 kbps, downlink	
On-board storage:	5 MB	
1b. Spacecraft characteristics:		
Payload:	SLD/SOXS, payload of opportunity	
Spacecraft:	GSAT-2, communication satellite	
Orbit:	Geostationary	
Altitude:	36400 km	
Nominal mission lifetime:	5 years	
1c. Mission characteristics:		
Launch Date:	8 May 2003	
Launch vehicle:	GSLV-D2	

Table 2.2

Special Features of the Detectors

- Si-PIN and CZT photodiode detectors
- Thermoelectric cooler (Peltier cooler)
- Cooled FET
- Temperature monitor
- Beryllium window
- Charge sensitive preamp
- Hermetic package (TO-8)
- Wide detection range
- Operation at near room temperature.

Various investigators have carried out the design, development and characterization of various kinds of Si and CZT detectors. Huber, Pantazis, and Jordanov (1995), Jordanov, Pantazis, and Huber (1996), and Desai, Pantazis, and Shah (1995) studied the response of high performance, thermoelectrically cooled X-ray and gamma ray detectors. They used compact Si and CZT detectors to explore their potentiality for high-resolution X-ray and gamma ray spectroscopy for future missions. The system used by them consists of a small cylindrical hybrid circuit including detector, FET and feedback components mounted on a small thermoelectric cooler. Huber, Pantazis, and Jordanov (1995) achieved energy resolution (FWHM) ~250 and 350 eV at 5.9 keV for Si PIN and CZT detectors respectively under all ideal conditions and at operating temperature of −20°C. Later, a detailed response study of CZT detectors to explore them as future spectroscopic detectors for X-ray astronomy was undertaken in a big way by several investigators over the globe (Jordanov, Pantazis, and Huber, 1996; Tousignant *et al*., 1997; Matteson *et al*., 1997; Kraft *et al*., 1998; Narita *et al*., 1997; Kuvvetli *et al*., 1999; Lachish, 1999, 2001).

A detailed design and development study on the application of XR-100CR (Si PIN) and XR-100T-CZT (CZT) detectors from Amptek, USA for the proposed

SLD payload was carried out by Jain *et al*. (2000b). A prototype model of the detector package was designed and developed at PRL, and thereafter characterization of the detectors was successfully carried out by Jain *et al*. (2002a). Later, the flight model was fabricated at Space Application Centre (SAC) of Indian Space Research Organisation (ISRO), Ahmedabad, India and pre-flight characterization was done by Jain *et al.* (2003) at Dr. Satish Dhawan Space Launching Facility, of ISRO at Shriharikota, India almost 2 weeks before the launch.

2.1.1.1 Collimator and Filter:

Si and CZT detectors have 0.025 and 0.250 mm thick Beryllium (Be) window to cut the background noise. However, in view of the application of these detectors for studying the Sun from a geostationary platform the thickness of Be window is not sufficient to cut the background significantly so as to achieve the S/N ratio >10. In this view a collimator and filter/attenuator were designed and fabricated at PRL.

The collimator is built of a 1.8 mm thick nickel sandwiched between 1.8 and 3.4 mm thick aluminum tubes. The length of the collimator is 56 and 81.5 mm for Si and CZT detectors respectively in order to achieve 3.4° FOV. In Figure 2.2 the SLED package is shown mounted on the aspect system viz. SOXS Sun Tracking Mechanism (SSTM). A 0.080 mm thick aluminum filter plus 0.15 mm thick kapton polyamide film are mounted on the Be window of the detector.

The Be window plus the aluminum and kapton films are good enough to eliminate the X-rays below 4 keV (solar and cosmic) and electrons and protons up to 300 keV and 2 MeV respectively that fall directly in the line of sight of the FOV. This enabled us to achieve S/N ratio ~100 in Si and ~50 in CZT. However, due to the 2 mm thick CZT substrate higher noise counts are observed as a function of energy.

Table 2.3

Specifications and Operating Conditions of SLED

Characteristics	**CZT**	**Si PIN**
Material	Cadmium-Telluride crystal doped with zinc	N type silicon wafer with P type material
Size	5 x 5 x 2 mm	3.6 x 3.6 x 0.3 mm
Be window thickness	0.25 mm	0.025 mm
Energy Resolution	1.2 keV at 5.9 keV	500 eV at 5.9 keV
Dark counts	$< 5 \times 10^{-3}$ cts/s at 10 keV < E < 1 MeV	$<3 \times 10^{-3}$ cts/s at 2 keV < E < 150 keV
Preamps	Amptek model A250 with current divider	Amptek model A250 with current divider
Operating Voltage	300 - 400 volts DC	100 volts DC
Temp. Monitor Sensor	1 μA/°K	1 μA/°K
Operating Temperature	-30 °C to -10 °C	-30 °C to -10 °C
Sensitivity	0.73 mV/keV	1 mV/keV
Pedigree	never flown in space	flown on Mars Pathfinder
Pre-Amps Power	± 8 volts at 25 mA	± 8 volts at 25 mA
Detector Power	+ 400 volts at 1μA	+100 volts at 1 μA
Cooler Power	2.1 volts at 0.7A	2.1 volts at 0.7A
Total Power	< 1 watt	< 1 watt

Shown in Figure 2.3 (left and right) are the effective area for Si PIN and CZT detectors folded over the efficiency of the detector and considering the above design for filter. It may be noted that almost no contribution arrives from X-rays below 4 keV where the Sun remains bright even outside of flare conditions. The design details of collimator and filter may be found in Jain *et al.* (2002b).

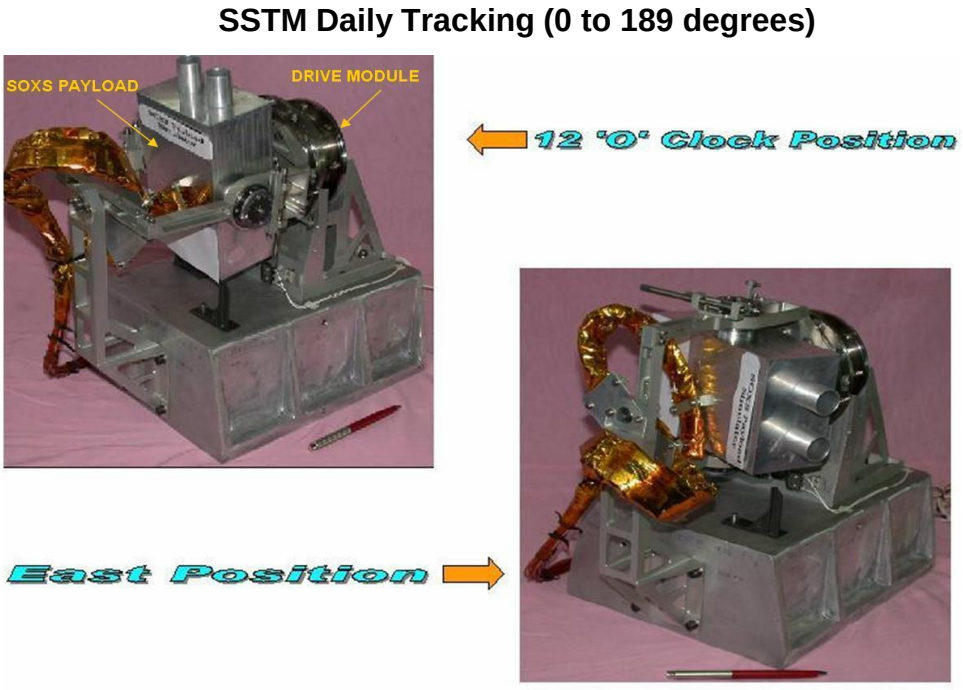

Figure 2.2: The detector package (see text) mounted on the SOXS Sun tracking mechanism (SSTM). The collimators are seen projecting outside. The FOV is 3.4°. The detector package moves in the line of sight of the Sun within an accuracy of about 0.1°. The SSTM has only one drive motor for correction in right ascension and declination.

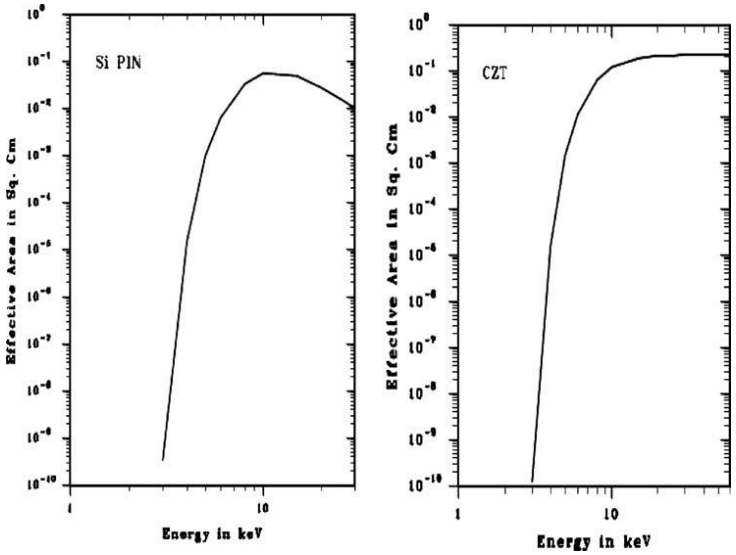

Figure 2.3: The effective area of the Si and CZT detectors of the SLED package. The Si and CZT have 0.025 and 0.25 mm Be windows respectively in front of the detector heads. Additional filters were mounted on the head to reject the background significantly.

2.1.1.2 Onboard Radioactive Source:

SLD carries a small onboard radioactive source namely Cd^{109} (5 microcuries, half life time 412 days) that emits lines at 22.2 and 25 keV, far from any line expected to occur in flare or in the detector's dynamic range by any varying background. The source is mounted on a M5 screw, which is inserted inside the collimator at an angle so as to direct the radiation on the center of the detector. The intensity of the source is further attenuated by 2 mm thick aluminum shield on the top of the source so that it forms the spectral lines after accumulating the counts over an hour or more. The 22.2 keV line is used for in-flight calibration of the Si detector by accumulating the counts for an hour. The calibration is conducted in night time as well as in the day time in the line of sight of the Sun. Similarly, for in-flight calibration of CZT detector, the 25 keV line in addition to the 22.2 keV line is used. The 22.2 keV line from the radioactive source and the 6.7 keV line from Fe XXVI emission during solar flares enable to monitor any energy band shift over the dynamic range of the detector as well as the FWHM as a function of the period elapsed from the launch.

In Figure 2.4 the results of in-flight calibration taken on 05 June 2003 during spacecraft nighttime for Si and CZT detectors are shown. It may be

noted that Si detector shows unambiguously 22.2 keV line arising from in-built Cd^{109} radioactive source irrespective to TEC ON or OFF condition. However, in the case of CZT we find shift of 14 channels as soon as we turn ON the TEC. This anomaly is due to grounding scheme adopted by us for CZT detector, and thereby it reveals both lines from Cd^{109} radioactive source at 22.2 keV and 25 keV shifted to 14 channels. In this view the dynamic energy range for CZT detector is now 4 keV to 56 keV instead of 4 keV to 60 keV.

2.1.2 SUN ASPECT SYSTEM – SOXS SUN TRACKING MECHANISM (SSTM):

The GSAT-2 is a communication satellite and SOXS is a payload of opportunity. The SLD payload is mounted on the anti-earth view (AEV) side of the spacecraft enabling the payload to look at the sky. However considering the limited FOV of 3.4°, an aspect system *viz*. SOXS Sun Tracking Mechanism (SSTM) was designed and developed at Spacecraft Mechanisms Group of ISRO Satellite Centre. The SSTM is unique in terms that it employs only a single drive module and keeps the Sun tracking in both right ascension and declination (Viswanatha, 2000). The SSTM consists of one stepper motor drive module with a gear reducer, and attached to it is a frame with the Declination Tilt Mechanism above which the detector package (SLED) is mounted. The drive module (Figure 2.2) consists of a stepper motor and a pancake type harmonic drive gear reducer. The stepper motor is a two-piece motor, and Duplex pair of angular contract ball bearings fixes on the motor to the input shaft. The motor drives the input shaft in steps of 1°. The input shaft drives the harmonic drive. The fixed gear of the harmonic drive is fixed to the outer housing and the rotating dynamic gear is mounted on a four-point contact ball bearing and the output flange is fixed on the outer side. The gear reducer has 1:157 gear reduction.

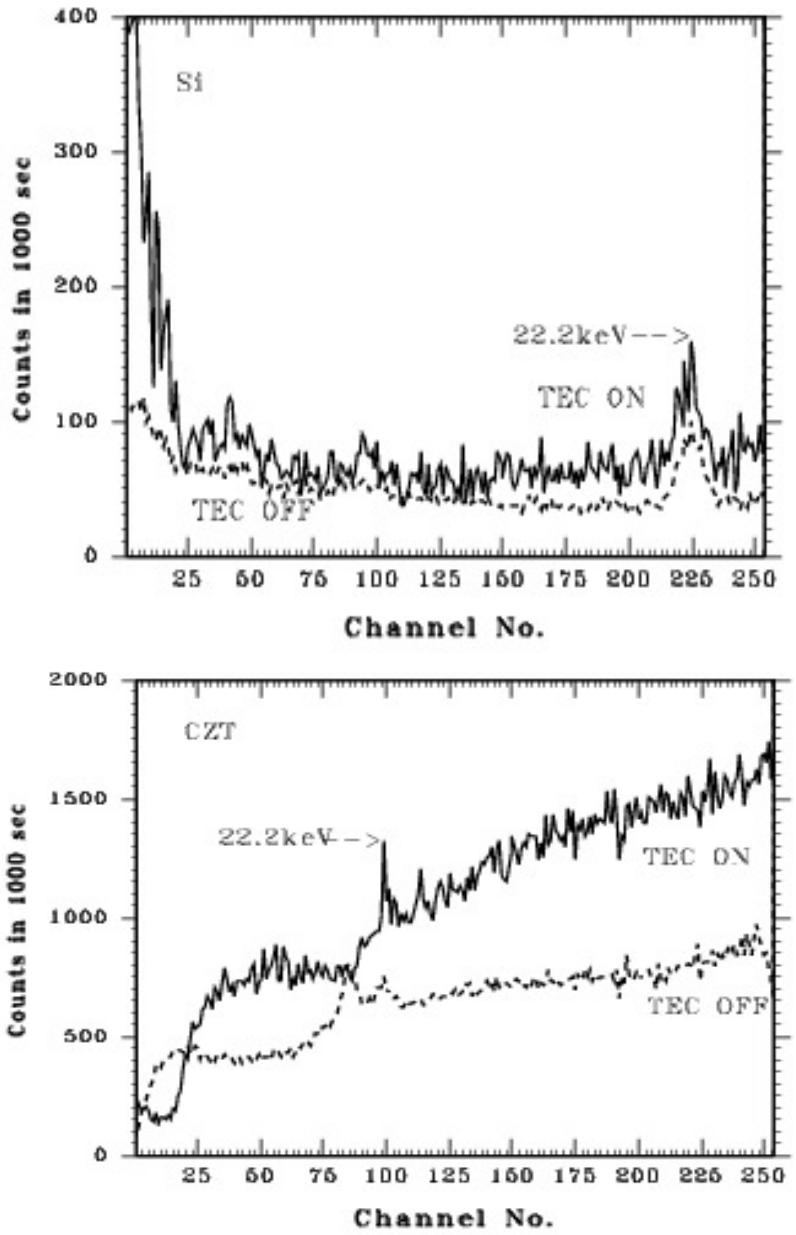

Figure 2.4: In-orbit calibration test with thermoelectric cooler (TEC) ON and OFF, however maintaining the temperature between –15 °C and –25 °C. The 22.2 keV line from onboard radioactive source (mounted inside the collimator) is seen unambiguously in both detectors. However, an anomaly of 14 channel shift in CZT detector may be noticed as soon as TEC is turn ON.

The output flange provides the interface for mounting the main frame. The motor used is SAGEM 35PP 81 04-03-01 redundant winding stepper motor of 1° step angle and the holding torque of 0.6 Nm and drive torque 0.4 Nm. The detailed design specifications may be found in the preliminary design review document prepared by Viswanatha (2000). A Sun sensor is mounted on the

payload (SLED) platform to indicate the Sun axis pointing error during payload operation. The sensor does not operate in a close-loop arrangement. The sensor's FOV is ± 15° and the accuracy is 0.1° in two axes.

2.1.3. Electronics:

2.1.3.1. SLD Front-End Electronics (SFE):

The SLD front-end electronics (SFE) aims to carry out the tasks of pulse shaping, pulse amplification, peak detection, and digital conversion of the input pulse train from the SLED package. In order to achieve these functions the front-end electronics package includes a linear pulse shaping amplifier, peak detectors, 8-bit ADC, energy window discriminators, telemetry interface for house keeping (HK) parameters, and temperature and corona (high voltage) auto-shutoff circuits. It also classifies input energy into nine (four for Si and five for CZT detectors) predefined energy window counters for light curve (temporal mode) observations and flare detection logic. The power supply circuit converts regulated DC voltages from SOXS common electronics (SCE) into required DC voltages for SFE and SLED packages. The package is designed and developed to maintain and reveal detector characteristics *viz.* sub-keV spectral energy resolution and 100 ms temporal resolution

House keeping parameters:

System health is monitored at 1 kHz telemetry rate. 16 house keeping (HK) parameters are monitored at every 16 s through LBT. These parameters provide the information such as detector temperatures, SFE DC-references and salient threshold voltages. Total events recorded in both detectors are also monitored by telemetry.

Detector Protection Circuits:

SFE includes an auto-shut off circuit, which switches off the detector bias voltage as soon as the detector temperature falls out of operating temperature range of −5°C to −30°C so as to protect the detectors from

thermal break down. Corona auto-shut off circuit switches off the detector bias when the bias current increases to 50% above the normal value.

2.1.3.2. SLD Processing Electronics:

SLD processing electronics (SLE) aims to read digital information from the SFE store into onboard memory and upload it to the ground station. The whole data processing electronics are integrated into this package. It consists of 16-bit window counters, ADC interface, real-time pulse height analysis (PHA) circuits for Si and CZT detectors, 5 MB onboard memory to store flare and HK data, on board timer (OBT) and telemetry–telecommand interfaces. This package was designed and developed at Space Astronomy and Instrumentation Division of ISRO Satellite Centre (ISAC), Bangalore (Umapathy *et al.*, 2003). Onboard 16-bit CPU controls all operations of the processing electronics. The SLD current operating mode is programmable via telecommand. SLD has following operating modes:

1. Search, quiet and flare integrated mode.
2. Survey/background mode (100 ms and 1 s).
3. Memory and electronics checkout mode.
4. Readout mode.

Search mode is normal operating mode. In this mode a search is going on for flare onset and quiet phase. Survey mode has been used to study the level of background noise of the quiet Sun. This helps to estimate correct thresholds for flare detection. Memory checkout and read out modes are usable for onboard diagnosis.

2.1.3.3 Flare Triggering Logic:

The SLD operation/observing logic is as follows:

(a) The Survey Mode observes preflare background in the line-of-sight of the Sun and thereby the threshold flux for flare trigger can be determined precisely. However, this default threshold can be modified as and when required through telecommand. This selected threshold flux is equal to 5σ, where σ is measured preflare background during the quiet Sun condition. After completion of Survey Mode during 5–7 June 2003 two default energy windows 10–20 keV for Si and 20–30 keV for CZT detectors were chosen

respectively for flare trigger logic. However, out of nine energy windows any two may be selected for flare detection through telecommand.

(b) As shown in Figure 2.5 during normal observing mode, i.e., Search Mode, the observations in these energy window counters (temporal data) are made always at a cadence of 100 ms but recorded at every 1 s.

(c) The Search Mode will turn into Flare Mode as soon as five consecutive 100 ms observations in any one out of the two energy windows show the flux ≥ threshold that is set in these windows.

(d) The Flare Mode, however, lasts only for 287.5 s, as shown in Figure 2.5, with a temporal resolution of 100 ms for energy windows (temporal) and PHA (spectral). After 287.5 s the logic returns to *Quiet Mode*, which continues for 2274 s and observations are made at a cadence of 1 and 3 s in windows and PHA respectively irrespective of new flare occurrence during this period. This design is carried out in context to limited onboard memory and telemetry rate as well as keeping in mind the most interesting period for high time resolution observations during the flare is first 5 min. After completion of quiet mode the logic returns to search mode automatically. Both Si and CZT detectors are competent to observe soft and hard X-ray micro flares.

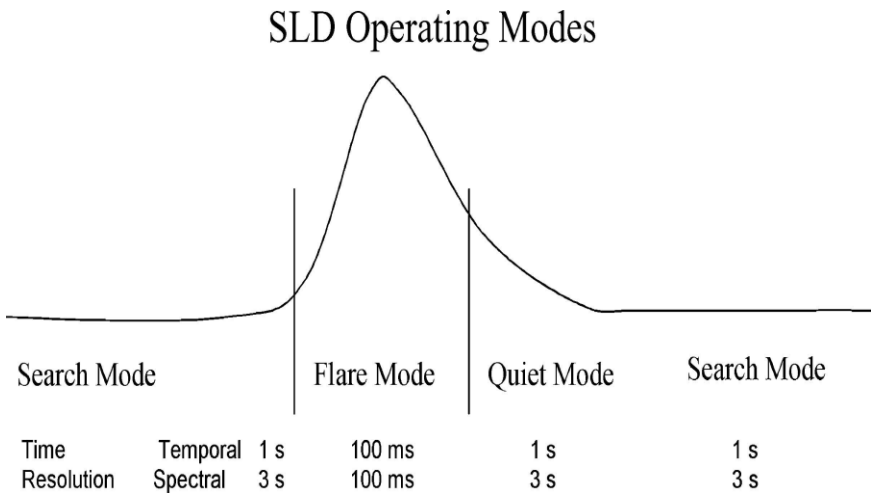

Figure 2.5*:* The operation logic of the SLD payload. The temporal resolution during flare mode is100 ms.

2.1.3.4 SOXS Common Electronics (SCE):

The SOXS common electronics (SCE) is truly common for both low energy and high-energy payloads. SCE package provides common interface to all

SOXS packages with spacecraft (S/C) bus. It minimizes the chance of damage to the mainframe bus because of any anomaly in the packages. SCE consists of low voltage DC/DC converters, high current ART converters, power electronics, telemetry/telecommand interfaces, base-band data encoder, convolution encoder, pre-modulation filter, Sun sensor and SOXS Sun tracking mechanism (SSTM) drive electronics. This package is also designed and developed at Space Astronomy and Instrumentation Division of ISAC, Bangalore (Sharma *et al*., 2000).

2.2 RHESSI:

The Reuven Ramaty High-Energy Solar Spectroscopic Imager (RHESSI) was designed to investigate particle acceleration and energy release in solar flares, through high resolution imaging and spectroscopy of hard X-ray/gamma-ray continua emitted by energetic electrons, and of gamma-ray lines produced by energetic ions. RHESSI was launched in February 2002, into a nearly-circular, 38° inclination, and low-Earth orbit, and began observations a week later. As of today, it continues to successfully operate with similar observing capabilities as at launch. RHESSI is a solar-pointed spinning spacecraft with a nominal rotation period of ~4 sec. The detailed mission overview is provided by Lin *et al*. (2002). I have used the RHESSI Spectrometer observations in chapter 4 and 5. Here, I provide a brief overview of RHESSI spectrometer.

2.2.1 RHESSI Spectrometer – The Germanium detectors:

The RHESSI spectrometer is described in detail by Smith *et al*. (2002). It is composed of nine cryogenically cooled coaxial germanium detectors (GeD). A cutaway of the Spectrometer showing the location of the germanium detectors (by number) is shown in Figure 2.6. When ultra pure germanium is at cryogenic temperatures, no electron-hole pairs are in the conduction band, but a hard X-ray or gamma – ray photon interacting in the crystal will release many energetic electrons, which lose energy by creating free pairs. If there is a high electric field (~1000 V cm^{-1}) across the crystal, the electrons and holes will be pulled to each electrode, creating a current pulse that can be amplified

and digitized by suitable electronics. Figure 2.7 shows a germanium detector. A special arrangement of the electrodes and the field lines allows a single germanium detector to be operated as two segments, a front segment and a rear segment. X-rays (primarily below ~200 keV) have shallow penetration in Ge and are measured primarily in the front segment, while higher-energy gamma rays penetrate more deeply and are measured primarily in the rear segment.

One of the unique features of the RHESSI spectrometer is its high spectral resolution which allows for the accurate measurement of even extremely steep power-law spectra. Energy resolution of the front detectors is about 1 keV (for 3-100 keV). For the rear detectors, it is around 3 keV (for higher energies upto 17 MeV). Photons from 3 keV to 17 MeV can be detected. RHESSI can also detect micro flares in the 3-10 keV range.

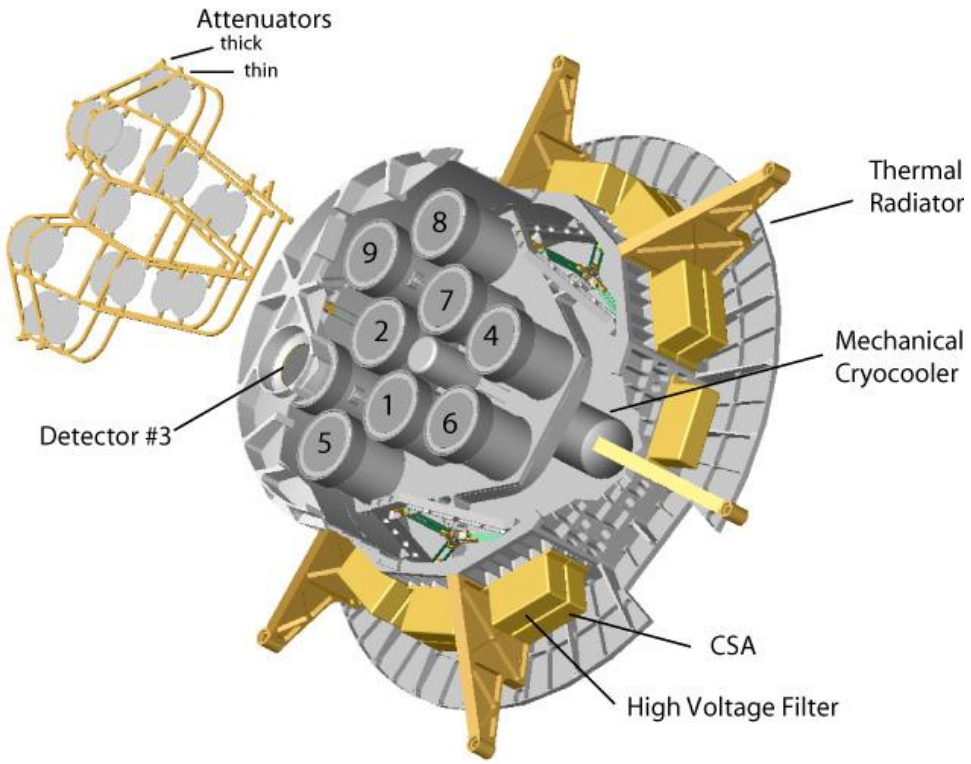

Figure 2.6: A cutaway of the Spectrometer showing the location of the germanium detectors (by number). (Lin *et al*. 2002).

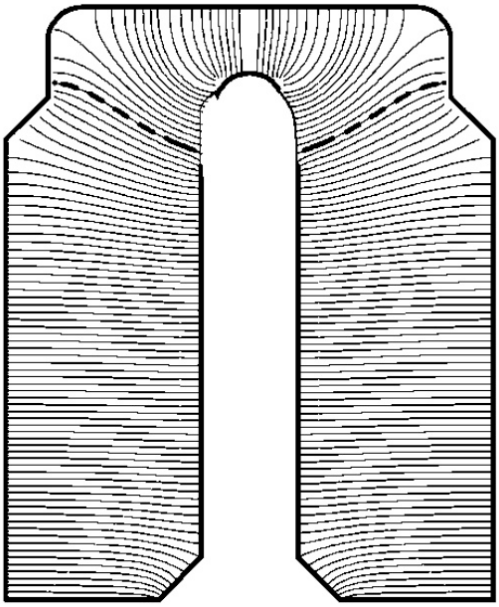

Figure 2.7: Schematic cross-section of one RHESSI germanium detector, showing the electric field lines, with the field line marking the segment boundary in bold dashes (from Smith *et al*. 2002).

Attenuators:

To the top of the spectrometer are two light weight movable frames, each holding nine aluminium discs – thin and thick attenuators – that can be moved in front of the nine GeDs to attenuate the incident SXR flux. Because flare emission is strongly dominated by lower-energy photons, attenuating the SXR flux reduces detector dead time and pulse pileup, maintaining accurate spectroscopy for higher-energy photons above ~ 6 keV even during periods with high incident SXR fluxes. The centers of the attenuators are thinned to preserve some low-energy response – the transmitted flux is reduced by 1/*e* below ~15 and ~25 keV for the thin and thick attenuators, respectively.

Consequently, the detector resolution below ~10 keV is somewhat improved in attenuator states A1 and A3 (to ~0.75 keV FWHM, compared to ~1 keV nominally), as the low-energy photons are then detected only at the center of the GeDs, where the electric fields are strongest, charge travel distance is smallest, and charge collection is fastest. Although all attenuators of a given type (thin or thick) move together, the thin and thick attenuators can be inserted independently. In practice, only three of four modes are used, in order of increasing attenuation: A0 – no attenuators (when both sets of attenuators are held out of the detector lines of sight to the Sun); A1 – thin

attenuators only (when the X-ray counting rate from a flare increases above a prescribed level); and A3 – thin and thick attenuators engaged (if the emission increases still further to another prescribed count rate level). The on-board computer automatically engages the appropriate attenuators as the detector-averaged live time drops below specified thresholds (~92% for A0, ~90% for A1). When the live time remains above 99% for ~4 minutes, the most recent attenuator is disengaged. If the now-unattenuated rates are still sufficiently high so that the live time falls below the threshold, the attenuator is reinserted, and the process repeats; the data during these successive attenuator changes should generally be omitted during spectral analysis.

Background:

The background counts are mainly due to the induced radioactivity of the detectors and due to cosmic ray and trapped particle radiation. The background count rates vary roughly sinusoidally over the orbit of the spacecraft, with the highest rates occurring when RHESSI reaches its highest geomagnetic latitude (~ 50°).

2.2.2 Data handling for Spectral Analysis:

The minimal on-board processing of the photon data maximizes the flexibility for data analysis. Since photons are precisely tagged with the energy they deposit in the germanium detectors and their arrival time, they can be accumulated in arbitrary energy and time bins to produce spectra optimized for the analyst's needs, whether to maximize sensitivity, resolution, statistics, etc. However, because of attenuation, dead time, and various other factors, the observed count spectrum is not identical to the incident photon spectrum, and any analysis must compensate for the effect of the instrument. Much of this is (or can be) done automatically via the RHESSI SSW software (Schwartz *et al*. 2002).

The spectra must also be corrected for count decimation. To prevent the on-board memory from filling too quickly during high count rates, the flight computer employs a progressive decimation scheme whereupon *M* of every *N*

counts below an energy *E* are automatically discarded, with *N* and *E* functions of the memory fill level, attenuator state, and segment (front or rear). Since the decimation scheme is exact, the original count flux can be precisely reconstructed by multiplying the measured count rate below energy *E* by *N/M* (in practice, this can be folded into the live time correction). However, because fewer count rates are observed for the same incident flux, decimation causes an increase in the Poisson noise of the derived count rate.

For a given photon energy, the photo-peak efficiency is the percentage of incident photons that are recorded as counts with that same energy, within the detector resolution; this is represented by the main diagonal of the DRM, and components of the response which affect primarily the photo-peak efficiency are termed “diagonal” components. These include: Grid transmission, Attenuator, blanket, & Be window transmission, Low-level discriminator. In flares, although the photon flux typically rises exponentially with decreasing energy, these three factors combine to yield a photo-peak efficiency that drops even faster; the measured count flux actually decreases below a peak energy (~6 keV for A0, ~10 keV for A1, and ~18 keV for A3), and the counts below this energy become quickly dominated by other than the diagonal response.

Contributions to the response that map an incident photon energy to a different measured count energy further reduce the photo-peak efficiency and are termed “off-diagonal” elements; they include: Energy resolution, K-escape, Compton scattering, Albedo & Pulse pileup. With the exception of those that are functions of the electronics, all of the above response components (specifically: grid transmission, attenuation, K-escape, Compton scattering, and albedo) assume that the incoming photons are incident along the axis, i.e. from the Sun. For such spectral analysis to be accurate and well-defined, the non-solar background must be subtracted from the data before analysis.

2.3 GOES:

In chapter 5, I have employed the proton flux data from the geostationary operational environmental satellites (GOES) Space Environment monitor (SEM). GOES have been developed for National Oceanic and Atmospheric Administration (NOAA) by the National Aeronautics and Space Administration (NASA). The (SEM) measures solar radiation in the X-ray and EUV region and the in-situ magnetic field and energetic particle environment at geosynchronous orbit, providing real-time data to the NOAA Space Weather Prediction Center (SWPC). GOES satellites provide continuous monitoring necessary for intensive data analysis. They circle the Earth in a geosynchronous orbit, which means they orbit the equatorial plane of the Earth at a speed matching the Earth's rotation. The geosynchronous plane is about 35,800 km above the Earth, high enough to allow the satellites a full-disc view of the Earth. The Space Environment Monitor (SEM) subsystem onboard GOES consists of four instruments: An energetic particles sensor (EPS), high energy proton and alpha detector (HEPAD), X-ray sensor (XRS) and two redundant three-axis magnetometers. HEPAD monitors the incident flux density of protons, alpha particles, and electrons over an extensive range of energy levels. XRS monitors the solar output. Two redundant three-axis magnetometers operate one at a time to monitor earth’s geomagnetic field strength in the vicinity of the spacecraft. The SEM instruments are capable of ground command-selectable, in-flight calibration for monitoring on-orbit performance and ensuring proper operation (GOES data book).

Energetic Particles Sensor:

The EPS/ GOES at geostationary orbit performs three integral measurements of electrons from 0.6 to more than 4.0 MeV, a seven-channel differential analysis of protons from 0.8 to 500 MeV, and a six-channel differential analysis of alpha particles from 4 to 500 MeV per nucleon. The EPS also provides all the support required by the HEPAD, which extends the EPS energy ranges to greater than 700 MeV for protons and to greater than 3400 MeV per nucleon for alphas. The EPS and HEPAD are housed within the spacecraft main body and view the space environment through apertures.

The EPS unit consists of a telescope subassembly, a dome subassembly and signal analyzer unit/data processing unit (SAU/DPU); the latter unit provides the final amplification of the telescope and dome output signals. These components are housed on a separate panel, mounted on the spacecraft's south equipment panel, providing a clear field of view towards the west.

The telescope uses two silicon surface barrier detectors that output charge pulses to charge sensitive preamplifiers within the telescope, converting them into voltage pulses; this preconditions the signals sent to the SAU/DPU. These detectors sense low energy protons in the range of 0.8 to 15 MeV and alpha particles in the range of 4 to 60 MeV. The two detectors, surrounded by tungsten shielding, are arranged in a telescope configuration: a 50-μm, 100-mm^2 front detector and a 500-μm, 200-mm^2 rear detector. Tungsten collimators define the field of view of 70° and eliminate detector edge effects. Sweeping magnets exclude electrons below about 100 keV, while a 0.145-mil aluminum foil excludes light. The outer surface of the front solid-state detector is covered with 130 $\mu g/cm^2$ of aluminum, rendering it light tight. The dome employs three sets of two 1500-μm, 25-mm^2, silicon surface barrier detectors, each with different thickness moderators covering the respective pairs' independent fields of view, thus providing three different energy thresholds. As in the telescope, the solid state detector output charge pulses are passed through charge sensitive preamplifiers, converting them into voltage pulses before being routed to the SAU/DPU. After processing, the output of the detector pairs provides data for four proton, three alpha, and three electron energy bands, ranging from 15 to 500 MeV for protons, 60 to 500 MeV for alphas, and less than 0.6 to more than 4.0 MeV for electrons. Table 2.4 shows the energy ranges for the energetic particles sensor.

2.4 SOHO:

SOHO, the Solar and Heliospheric Observatory, is a project of international cooperation between ESA and NASA to study the Sun, from its deep core to the outer corona, and the solar wind. The scientific payload of SOHO

comprises 12 complementary instruments, developed and furnished by 12 international consortia involving 29 institutes from 15 countries. In chapter 5, I have used the Extreme ultraviolet Imaging Telescope (EIT) and Large Angle and Spectrometric Coronagraph (LASCO) observations to establish the flare-CME correlationship and the dynamic and physical properties of CMEs.

2.4.1 SOHO/EIT:

The Extreme-ultraviolet Imaging Telescope (EIT) provides wide-field images of the corona and transition region on the solar disc and up to 1.5 R_s above the solar limb (Delaboudinière *et al*. 1995). Its normal incidence multilayer-coated optics selects spectral emission lines from Fe IX (171 Å), Fe XII (195 Å), Fe XV (284 Å), and He II (304 Å) to provide sensitive temperature diagnostics in the range from 6×10^4 K to 3×10^6 K. The telescope has a 45×45 arcmin field of view and 2.6 arcsec pixels which provides approximately 5-arcsec spatial resolution. The EIT probes the coronal plasma on a global scale, as well as the underlying cooler and turbulent atmosphere, providing the basis for comparative analyses with observations from both the ground and other SOHO instruments.

2.4.2 SOHO/LASCO:

The Large Angle Spectroscopic Coronagraph (LASCO) is a three coronagraph package which has been jointly developed for the Solar and Heliospheric Observatory (SOHO) mission by the Naval Research Laboratory (USA), the Laboratoire d'Astronomie Spatiale (France), the Max-Planck-Institut für Aeronomie (Germany), and the University of Birmingham (UK). LASCO comprises three coronagraphs, C1, C2, and C3, that together image the solar corona from 1.1 to 30 R_s (C1: 1.1- 3 R_s, C2: 1.5-6 R_s, and C3: 3.7 - 30 R_s) (Brueckner *et al*. 1995). The C1 coronagraph is a newly developed mirror version of the classic internally-occulted Lyot coronagraph, while the C2 and C3 coronagraphs are externally occulted instruments. However, only C2 and C3 data are used for uniformity because C1 was disabled in June 1998. A layout of the basic Lyot Coronagraph is shown in Figure 2.8.

Table 2.4 (Energy ranges for the Energetic Particles Sensor)

Particle Type	Channel Designation	Nominal Energy Range (MeV)	Detector Assembly
Proton	P1	≤0.8 to 4	Telescope
Proton	P2	4 to 9	Telescope
Proton	P3	9 to 15	Telescope
Proton	P4	15 to 40	Dome
Proton	P5	40 to 80	Dome
Proton	P6	80 to 165	Dome
Proton	P7	165 to 500	Dome
Proton	P8	350 to 420	HEPAD
Proton	P9	420 to 510	HEPAD
Proton	P10	510 to 700	HEPAD
Proton	P11	> 700	HEPAD
Alpha	A1	4 to 10	Telescope
Alpha	A2	10 to 21	Telescope
Alpha	A3	21 to 60	Telescope
Alpha	A4	60 to 150	Dome
Alpha	A5	150 to 250	Dome
Alpha	A6	300 to 500	Dome
Alpha	A7	2560 to 3400	HEPAD
Alpha	A8	> 3400	HEPAD
Electron	E1	≥ 0.6	Dome
Electron	E2	≥ 2.0	Dome
Electron	E3	≥ 4.0	Dome
“Singles”	S1 to S5	--	HEPAD

Table reproduced from GOES databook.

A solar image is formed by the objective lens O1 at the internal occulter D1. The field lens F1 forms an image of the objective lens onto the Lyot stop A3, where diffracted light from the edge of the lens is prevented from reaching the focal plane. The second objective O2 relays the solar image onto the focal plane.

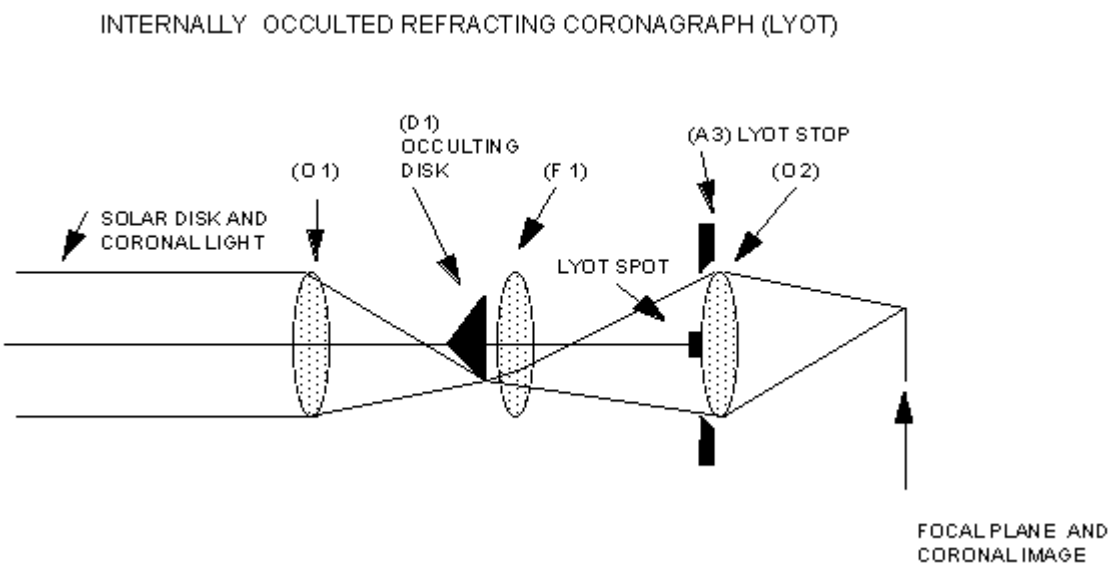

Figure 2.8: Optical components of the Lyot Coronagraph: Objective lens O1, internal occulter D1, Field lens F1, Lyot stop A3, Lyot spot, objective lens O2, and focal plane. (Image: NASA)

B: Ground-based Instruments:

2.5 Magnetic Sensors (Dst Index):

In chapter 5, I have considered the geoeffectiveness in terms of Dst index. The storm-time disturbance index Dst is calculated at the World Data Center WDC at Kyoto, Japan using hourly-mean magnetic observatory data from four standard observatories at low to mid-latitudes (Hermanus, HER; Honolulu, HON; Kakioka, KAK and San Juan, SJG).

The basic sensor package at each observatory consists of a tri-axial fluxgate magnetometer which gathers vectorial data, typically the horizontal intensity, declination, and the vertical component (H, D, Z), plus a proton magnetometer, which measures the total intensity of the field (F). The redundancy between these two measurement systems allows for consistency checks that are useful for troubleshooting. Moreover, a fluxgate sensor-electronics package is prone to deliver data that drift on an absolute scale, primarily as the result of changes in ambient temperature; proton magnetometer data also drift with temperature, but usually much less than fluxgate data. To reduce this baseline drift, the sensors and electronics are housed in well-insulated, thermostatically-controlled buildings, but even then

there remains some residual baseline drift. 'Absolute' measurements are made using a theodolite coupled to a small magnetometer; these data are used later during data processing to make final adjustments to the data baselines. To preserve sensor orientation, both the fluxgate magnetometer and the theodolite are supported by piers that are firmly anchored into the ground. This information is acquired from the following website: http://geomag.usgs.gov/operations.php#sensors.

2.6 Magnetic sensors (aa index):

To predict the amplitude of solar cycle 24 (chapter 6), I have used a precursor technique which employs geomagnetic activity index *aa*. The *aa*-index is a simple global geomagnetic activity index. It is derived from the *K* indices from two approximately antipodal observatories and has units of 1 nT. The *aa* index represents the activity level at invariant magnetic latitude of about 50°. The two observatories were Greenwich (1868 – 1925) in the northern hemisphere and Melbourne (1868 – 1919) in the southern hemisphere. Greenwich was replaced by Abinger in 1926 and by Hartland in 1957. Melbourne was substituted by Toolangui in 1920 and by Canberra in 1980. The observatories employ two sets of sensors for magnetic measurements. A tri-axial linear-core fluxgate magnetometer is used to measure the variations in the horizontal (H) and vertical (Z) components of the field. The third sensor is oriented perpendicular to these, and measures variations which are proportional to changes in the declination (D). Measurements are made at a rate of 1 Hz. A proton precession magnetometer (PPM) measures the total intensity of the field (F) at a rate of 0.1 Hz. A fluxgate sensor mounted on a theodolite is used to determine D and inclination (I). (Hartland Observatory, Monthly Magnetic Bulletin, March 2011).

In next Chapter 3 I describe data acquisition and analysis techniques.

CHAPTER 3
DATA ACQUISITION AND ANALYSIS TECHNIQUES

This chapter describes the data acquisition and analysis techniques for different types of data-set used in this thesis.

3.1. Flare Location, Class and Active region:

Solar flares occurring on the Sun are identified and characterized by their location on the Sun and magnitude in a given waveband of observations. The flare location along with active region in which it occurred, its importance in Hα as well as in X-ray waveband (GOES class) are being published in Solar & Geophysical Data (SGD) Reports, which are available at the following URL. ftp://ftp.ngdc.noaa.gov/STP/SOLAR_DATA/SGD_PDFversion/

However, the Active region numbers for February, 2010 flares are taken from SGD weekly reports published by Space Weather Prediction Center (SWPC) NOAA available at http://www.swpc.noaa.gov/ftpmenu/ as the final comprehensive SGD reports are not yet available for the period of 2010.

As an example Figure 3.1 (top) shows the Hα of the 25-August-2005 solar flare. This flare occurred in the active region 10803 located at the north-east (N09E80). Figure 3.1(bottom) shows the temporal variation of GOES X-ray flux in 1-8 Å. The black circle in the figure highlights the flare peak X-ray intensity of the order of 6.4×10^{-5} watts m^{-2} on 25- August-2005 at time of peak intensity in UT. This is therefore, an M-class solar flare (*cf*. Table1.1). These details can be obtained from the SGD reports in which they are listed as follows:

Date	GOES Class	Location	NOAA Active Region
25-AUGUST-2005	M6.4	N09E80	10803

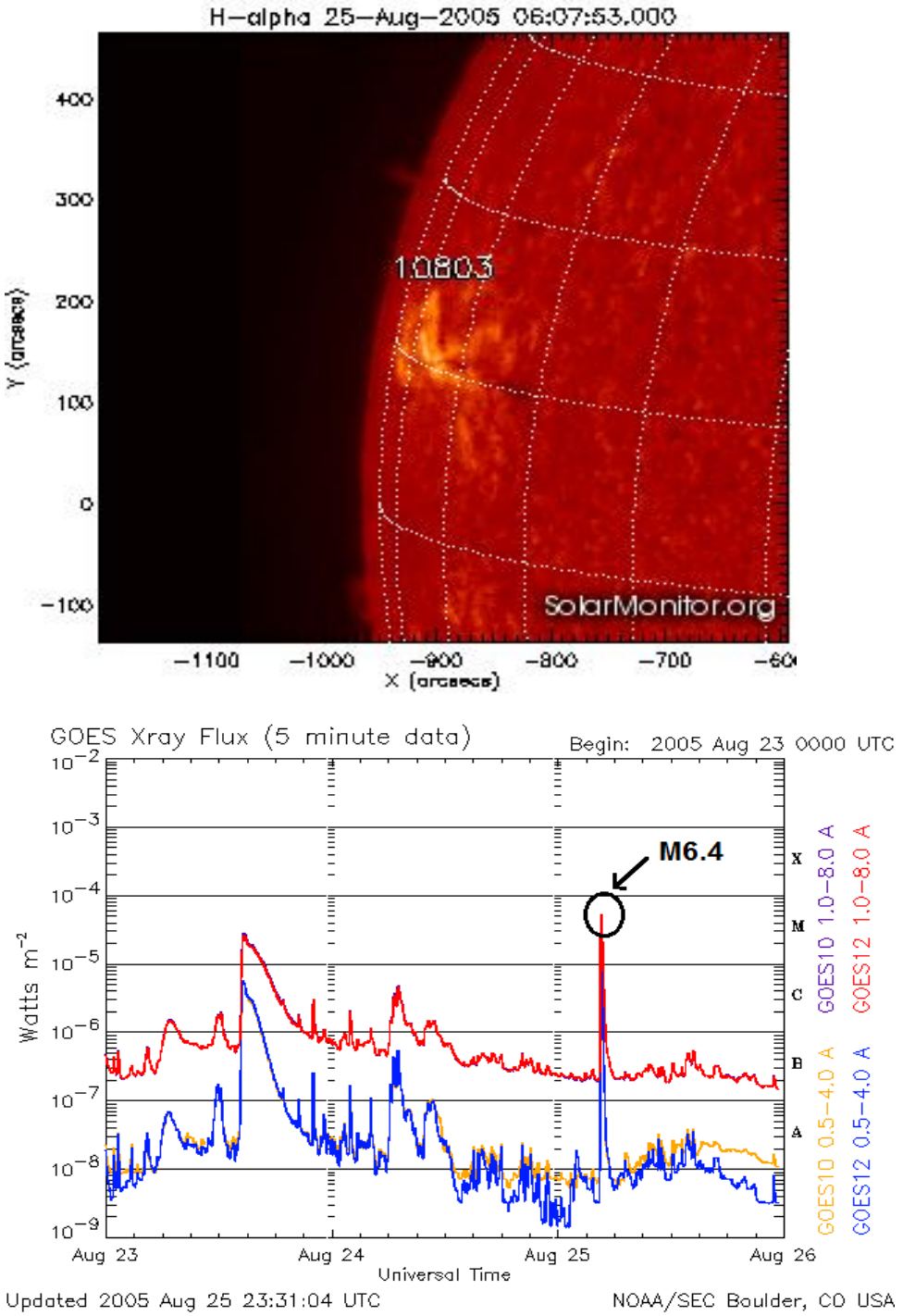

Figure 3.1: Hα image(top) of the Sun (25-August-2005). The figure shows the active region 10803 on east limb of the Sun. The bottom figure shows the GOES X ray flux as a function of time. The peak intensity (M-class X-ray flare) on 25-August-2005 between 3:00 and 6:00 UT is circled in black. (Image: Solar monitor)

3.2 SOXS:

3.2.1 Data Format:

The SOXS/ SLD data is acquired through SOXS processing electronics (SLE). The SLE has a total of 5 MB onboard memory divided into two banks each of 2.5 MB. The instrument provides “a continuous data recording and playback” mechanism. When any one bank is busy with data acquisition, the other is flushing data to telemetry at 8 kHz rate. The banks are switched every 42.69 min for data acquisition. SLD has various programmable operating modes like search mode, flare mode, background mode and memory check mode, which have been described in the previous chapter. We describe here data packaging of flare and background modes.

The flare/background data has been arranged in packets, each packet of 700 bytes length. The packet consists of

- Header (Packet ID, Time Tag, Flare Status) information.
- Pulse height analysis (real-time spectrum) information.
- Energy window counters (temporal) information.
- Padding information.

Header is of 8 bytes divided into 3 bytes for Packet ID, 1 byte for flare status and 4 bytes for time tag with 8 ms time resolution. PHA is 638 bytes – divided into 360 bytes for Si and 296 bytes for CZT detectors. Both Si and CZT PHA have 16-bit channel depth from 4 to 10 keV energy range and 8-bit channel depth above 10 keV.

Temporal data is of 54 bytes in search phase and 18 bytes in flare phase. Temporal data consists of 4 and 5 energy window counters data for Si and CZT detectors respectively.

Padding information is dummy zero or flare on-set information to complete a 700 byte packet.

The packet is constructed every 100 ms during the flare phase and 3 s during search/quiet phase. These packets are flushed continuously at 8 kHz telemetry rate. The 700 bytes data packet is further enclosed into 1248 bytes data packet in order to include

- Frame ID (sync. bytes, data ID, and frame counter).
- Data packet status.

- Derived and current PID values (Parameters at onboard & current time).
- Frames ground reception time (GRT).
- Dummy bytes.

The 1248 packet consists of house keeping parameters and flare data. Each packet has all the information regarding health and the event so that data analysis becomes easy.

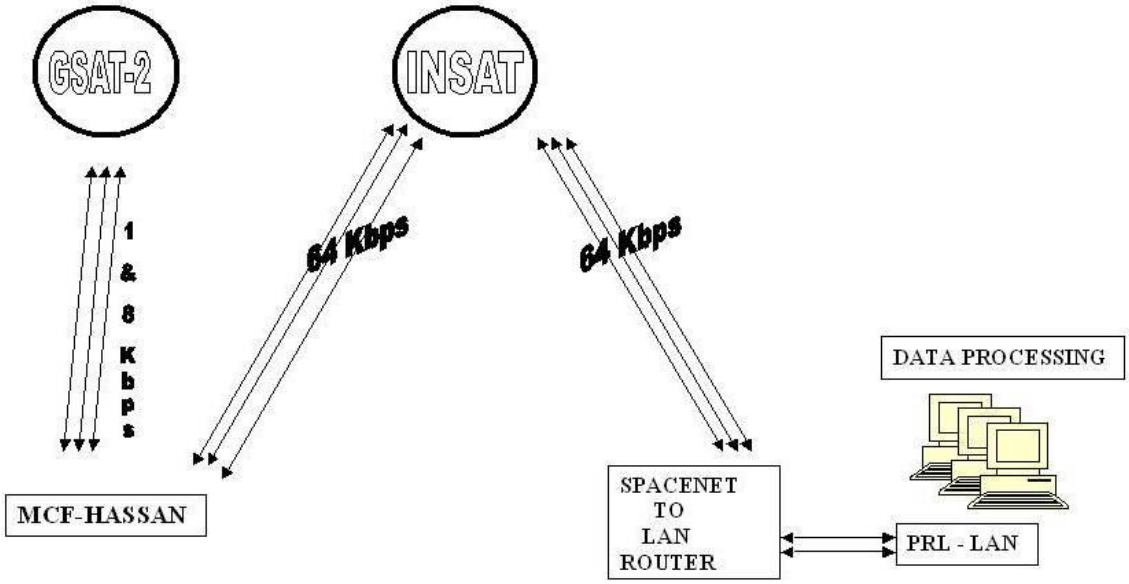

Figure 3.2: Schematics of SOXS/GSAT-2 command and data acquisition at Master Control Facility (MCF) at Hasan. The data is then uplinked to INSAT with 64 kbps from where it comes to PRL through space-net. Finally the SOXS data is stored in the SOXS lab at PRL and then processed for next level. The processed data is uplinked to SOXS URL.

In Figure 3.2 schematics of commands to spacecraft and data acquisition from Master Control Facility (MCF) of ISRO at Hasan (Karnataka), and data transfer to PRL is presented. The data at SOXS Lab at PRL is further processed for corrections and to upload to SOXS URL at http://www.prl.res.in/~soxs-data/

3.2.2 Analysis techniques:

The daily SOXS data acquired at PRL is uploaded at the SOXS website: http://www.prl.res.in/~soxs-data/. The data is stored in the form of .les files. The solar flare observations are generally recorded from 03:50 to 06:50UT.

The SLD provides data in two modes: Temporal and Spectral modes. However, the data recorded by the instrument is in the counts mode and in order to convert into the photons mode we have to de-convolute the count domain over the response of the instrument. Thus, first, I describe the response of the instrument in detail.

3.2.2.1 Response of the Detectors:

The Si and CZT detectors have dynamic energy range of 4-25 and 4-56 keV respectively, which is distributed over 256 channels employing 8-bit ADC. Therefore Si detector has channel width of 0.082 keV. The CZT ADC output shows non-functioning of first 13 channels and therefore its dynamic energy range works on 243 channels revealing channel width of 0.214 keV. The energy range of both the detectors is ≤56 keV, and therefore contribution from the Compton scattering is not significant. In fact the effective area of both the detectors permits detection of X-ray photons from the Sun below 40 keV, which is reasonably out of Compton scattering contribution.

The energy spectrum, intensity (counts/s) as a function of energy at a given time is called count spectrum. The detected count spectrum is in fact given by the convolution of the actual photon spectrum with the response matrix as shown in Equation (1). The response matrix R(I,E) of an X-ray detector allows reconstruction of the source photon spectra from the observed counts per channel in the Pulse Height Analyzer (PHA). Thus all X-ray experiments have well defined and calibrated instrumental response matrix, which can be used to reconstruct the photon spectrum.

$$C_i = \int_0^{255} \frac{dN}{dE} R(i,E)dE = \sum_j \frac{dN}{dE}(E_j)R_{ij}\Delta E_j \qquad (3.1)$$

where C_i are the detected counts in the i-th PHA channel, dN/dE is the input photon spectrum, R is the overall response matrix and j describes the binning of the photon input energy E, where the j-th bin has a width ΔE_j. In Equation

(1) the matrix $R_{ij,}$ is an overall response matrix having dimension of (cm^2 keV), indicating the efficiency of the detector folded over effective area and FWHM (energy resolution). Figure (3.3) shows the photo-peak effective area as a function of energy for Si detector and CZT detectors.

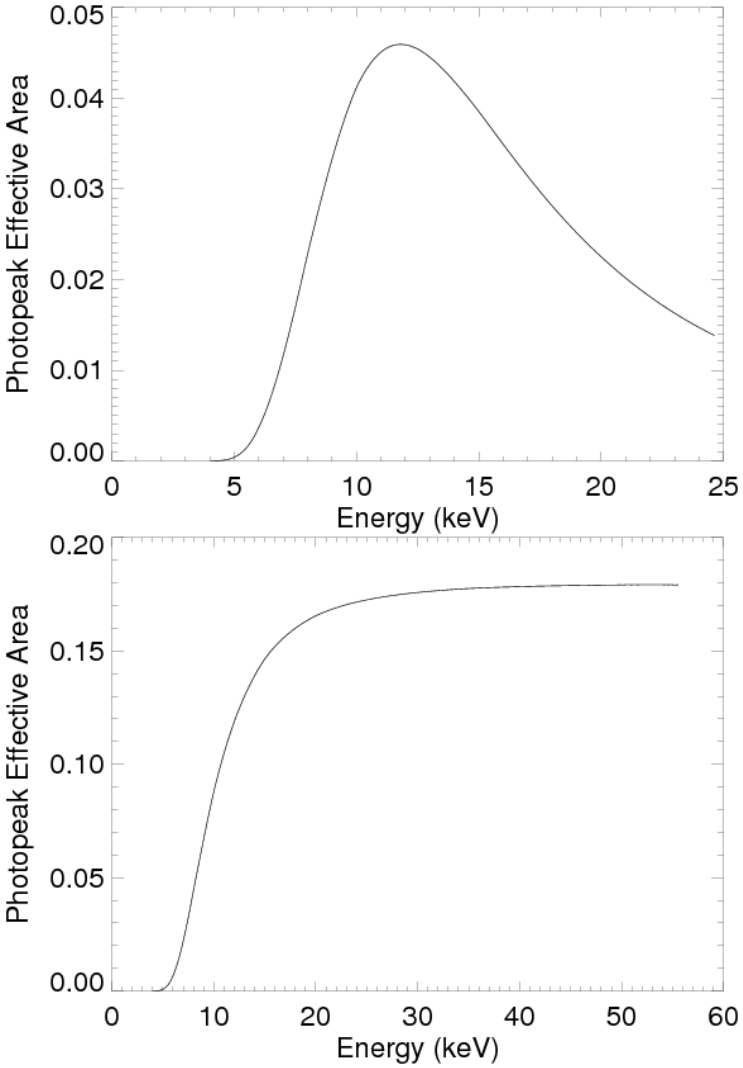

Figure 3.3: Photo-peak effective area of Si (top) and CZT (bottom) detectors are plotted as a function of energy. It may be noted that Si has best efficiency up to 15 while CZT reveals up to 3 keV. However, for bright flares (<M5.0 intensity) Si may collect photons up to 25 keV and CZT up to 40 keV.

As mentioned earlier, in our case, the effective area can be used to measure the photo-peak area of the detector employing calibration measurements. The photopeak response of the detectors is computed from the exposed geometric area through the collimator circle, the absorption from the Be, Al, and Kapton, and then the probability of single photon energy detection in Si

and CZT. A correction to the photopeak efficiency was obtained by a second order fit of the detector efficiency data which included the Be window of 1 mil for Si and 10 mil for CZT detector. We therefore group the Be window with the detector and treat the Al and Kapton separately as absorbers (*cf*. Table below (3.1)).

Table 3.1

Detector and absorber specifications

S.No.	Parameter	Detector-Si	Detector-CZT
1.	Detector Thickness (cm)	0.03	0.2
2.	Al Thickness (micron)	50+20	100+20
3.	Be Thickness (micron)	25.4 (1mil)	254 (10mil)
4.	Kp Thickness (micron)	150	150
5.	Geometric Area (cm^2)	0.091	0.18

Effective Area:

The effective area is derived using the following function.

1. **For Si Detector**

$$EA_{Si} = e^{(-\mu t)_{Al}} \times e^{(-\mu t)_{Kp}} \times \left\{1 - e^{(-\mu t)_{Si}} \times e^{(-\mu t)_{Be}}\right\} \times GA$$

2. **For CZT detector**

$$EA_{CZT} = e^{(-\mu t)_{Al}} \times e^{(-\mu t)_{Kp}} \times \left\{1 - e^{(-\mu t)_{CZT}} \times e^{(-\mu t)_{Be}}\right\} \times GA$$

where μ = Attenuation Coefficient for corresponding absorber

t = Thickness (cm), and GA is geometrical area of the detector.

The above effective area calculations have been performed in OSPEX/ SolarSoft package using ‘soxs_photopeak.pro’ and ‘soxs_czt_photopeak.pro’ programs for Si and CZT detectors respectively. The photo-peak effective area for Si and CZT detectors on linear scales are presented in Figure 3.2.

Response Matrix:

Response matrix R(i,E) equation is taken by multiplying effect of resolution broadening matrix with peak response. The construction of the matrix is of the form R[i,E] where index E refers to the energy of the incident photon and the index i refers to the output energy channel. The values of R[i] for a given E are taken from a normalized Gaussian integration where the full width at half max (FWHM) is 0.7 keV (for Si) and the centroid is taken at the center of the channel where i eq E for the square matrix we start within the construction.

Detector response is determined using programs *viz.* soxs_drm.pro and soxs_czt_drm.pro in OSPEX/ SolarSoft package for Si and CZT detectors respectively. The detector response matrix (DRM) is calculated by using the effective area and the energy resolution function (Jain *et al*., 2003), which is a Gaussian resolution function with 2.0 keV (CZT) and 0.8 keV (Si) FWHM for all energies.

The efficiency/ probability of photon conversion to electron and hole by Si and CZT detector over their respective dynamic energy range with a Gaussian shape over the PHA channels is then derived from the above response and is presented in Figure 3.4.

Temporal Mode:

The temporal mode (Si) observations reveal flux (counts s^{-1} cm^{-2} keV^{-1}) as a function of time for four fixed energy bands (6-7, 7-10, 10-20, and 4-25 keV), while for the CZT detector in five fixed energy bands *viz.* 6-7, 7-10, 10-20, 20-30 and 30-56 keV. The time resolution for temporal mode observations during quiet periods is one second but during flares it is 100 ms. In Figure (3.5) I show as an example temporal mode observations of 25 August 2005 flare at fixed energy window counters of Si and CZT detectors, which are employed to trigger the flare in the front-end electronics (*cf.* Chapter 2).

The temporal mode observations may also be created from the spectral mode data for any energy band in the dynamic range of the given detector. However, the temporal resolution would be 3s for quiet mode and 100 ms for flare mode. In Figure 3.6 an example of temporal mode observations for the same flare employing spectral mode data is presented.

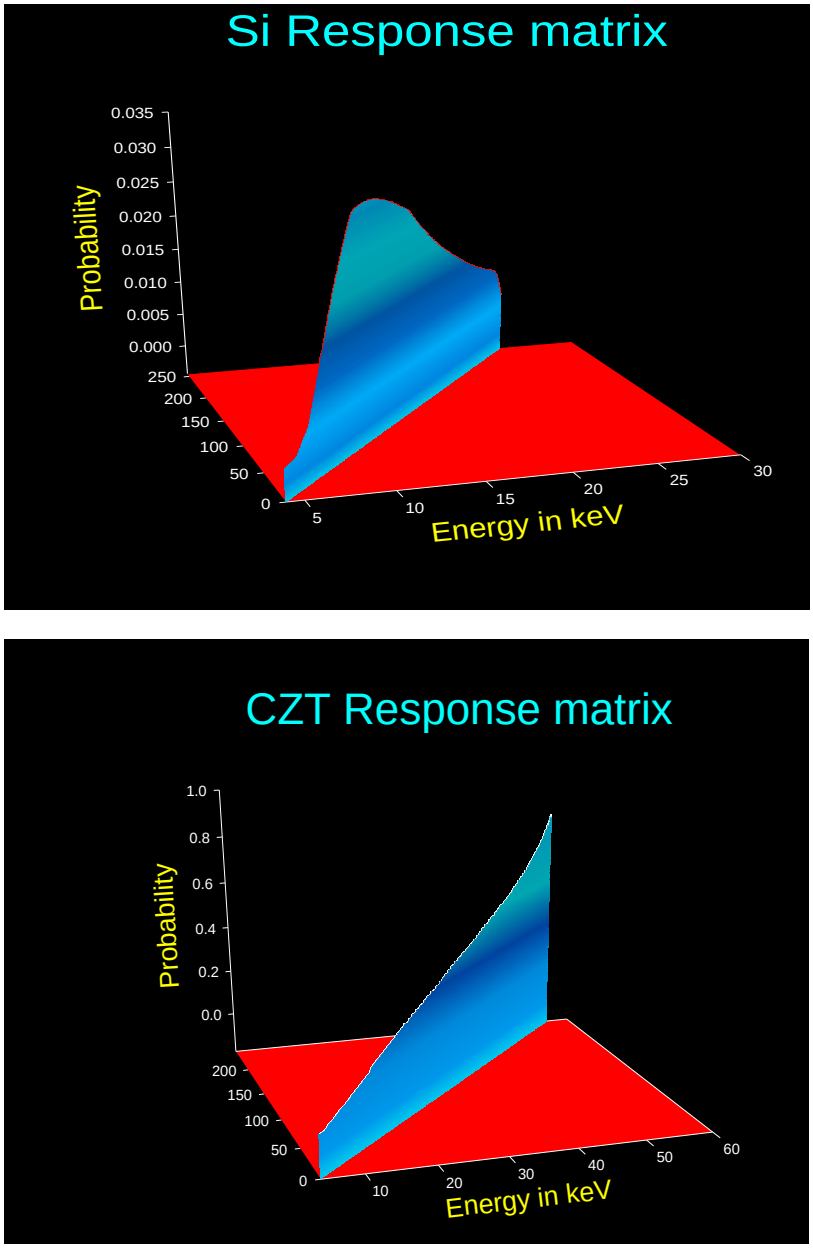

Figure 3.4: Response matrix for Si (top) and CZT (bottom) detectors. The probability of photon conversion to electron and hole by the detector is also plotted as a function of energy.

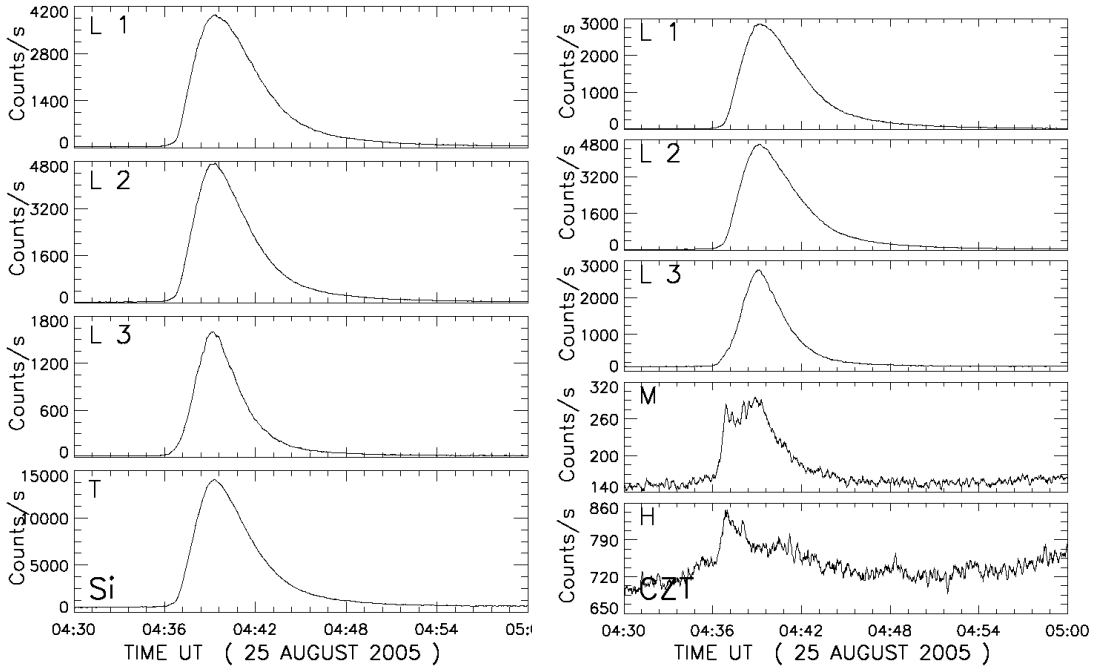

Figure 3.5: The temporal evolution of the solar flare observed on 25 August 2005 by Si detector (left panel) on its fixed energy bands L1 (6-7), L2 (7-10), L3 (10-20) and T (4-25) keV, and by CZT detector (right panel) on its fixed energy bands L1 (6-7), L2 (7-10), L3 (10-20), M (20-30) and H (30-56) keV.

Spectral Mode:

The spectral mode observation reveals the flare flux as a function of energy at a given time. The time resolution for spectral mode observations during quiet periods is three seconds but during flares it is 100 ms. Energy region 4-15 keV in solar flare X-ray spectra is of great importance for inferring the properties of the hottest parts of the thermal plasma created during a solar flare. It contains emission lines of highly ionized Ca, Fe, and Ni atoms and a continuum that falls off steeply with increasing energy. In this context SLD is the first payload which has an energy range of 4 - 25 keV to study the line emission and continuum with sub-keV spectral resolution. This is achieved by employing the Si PIN detector as described in Chapter 2 (Section 2.1)

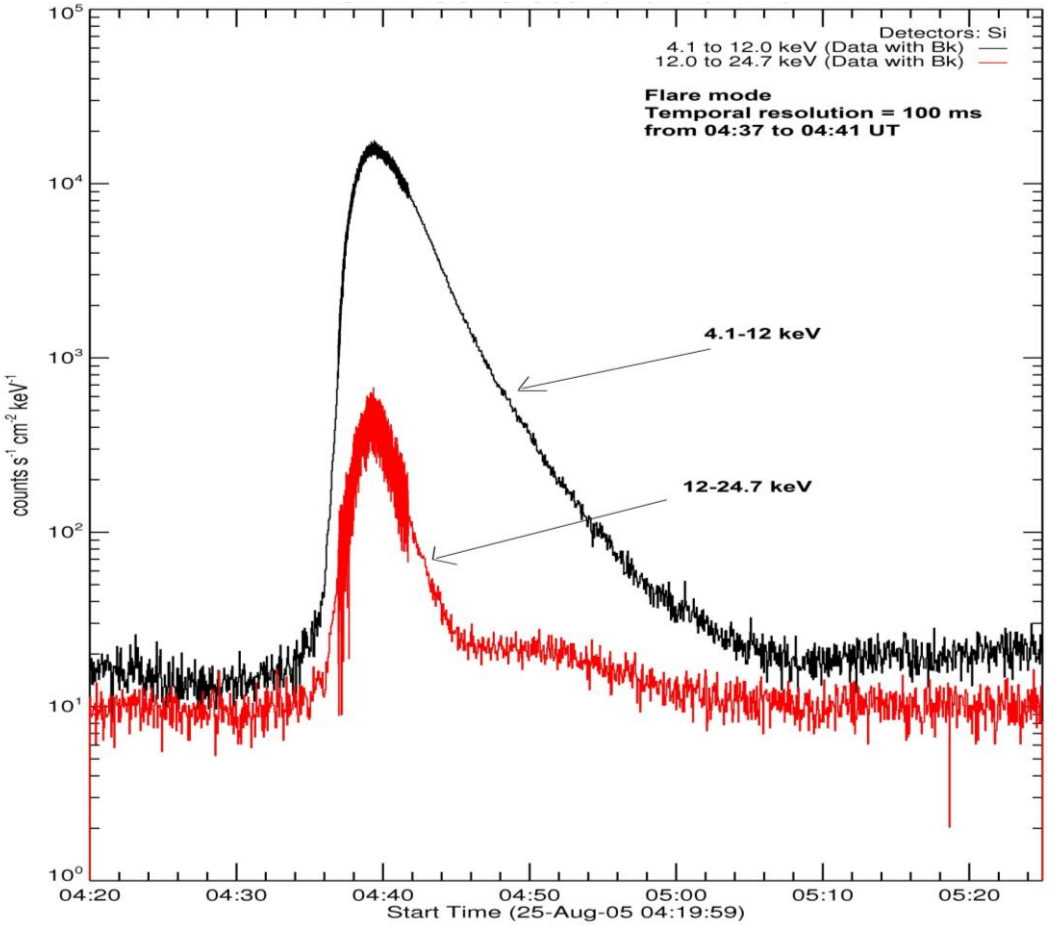

Figure 3.6: Temporal evolution (light curve) of the 25 August 2005 solar flare (employing spectral mode data in OSPEX) in the energy ranges 4.1-12 keV (black) and 12-24.7 keV (red) observed by Si detector of the SLD/SOXS mission The temporal resolution is 3s for quiet mode and 100 ms for flare mode.

The raw data for temporal and spectral mode observations are first corrected for any spurious, or false, flares as well as for the pre-flare background (Jain *et al*., 2005). The spectrum at a given time is formed by integrating the high cadence (100 ms) spectra over an interval of 30 to 100 seconds. The photon spectrum is produced by de-convolution of the count spectrum over the instrumental response as follows.

Let N_{ij} be the corrected PHA spectral data where *i* is a spectral record from 0 to *n,* and *j* is the channel number ranging from 0 to 255 for that particular spectral record. Firstly, in order to calculate the background spectra

a range of N_{ij} is selected where the Sun is quiet for a significant period (>20 minutes) between i_b and i_e on the observational interval. Here i_b and i_e are the beginning and ending spectral records for the quiet interval.

The integrated background counts spectra (IB_j) may be written as follows.

$$IB_j = \frac{\sum_{i_b}^{i_e} N_{ij}}{T_{i_e} - T_{i_b}} \qquad (3.2)$$

Now, for generating a photon spectrum of the flare for a given interval *viz.* k_b to k_e, during the flare, count spectra for this time interval is first generated as shown in relation (3).

$$IF_j = \frac{\sum_{k_b}^{k_e} N_{lj}}{T_{k_e} - T_{k_b}} \qquad (3.3)$$

However, to obtain pure flare count spectra (CF_j), the background count spectra (IB_j) are subtracted from IF_j, which gives

$$CF_j = (IF_j - IB_j) \qquad (3.4)$$

and finally the count spectra (C_i) are deconvolved over the instrumental response (R_j) to obtain the flare photon spectra (PFj) as shown in the relation (5).

$$PF_j = \frac{CF_j}{R_j} \qquad (3.5)$$

These photon spectra may be used to study the X-ray line and continuum emission. The various steps from data acquisition to data analysis were presented in detail by Jain *et al.,* (2005) employing SOXSSoft and Jain *et al.,* (2008) employing SolarSoft. Previously SOXSSoft was employed but since 2006 we have been using SolarSoft package for SOXS data analysis. In this software a subroutine namely OSPEX (Object Spectral Executive) package,

described in detail below in section 3.2.2.1, is being used by us in which instrumental response for both the detectors has also been incorporated. Therefore we may use both count spectra fitting and photon spectra fitting to measure the flare plasma codes. The former fitting is called forward while later is known as inverse fitting of the spectra. Shown in Figure 3.7 is an example of count spectra (top) and photon spectra (bottom).

3.2.2.2 OSPEX (Object Spectral Executive):

The OSPEX is a software package inside SolarSoft for X-ray spectral analysis of RHESSI, SOXS and other instruments. It is the next generation of SPEX (Spectral Executive) written by R. Schwartz in 1995. This program takes its main routine from Solarsoftware (SSW) package where the Mewe and Chianti codes are included. The instrumental response function for Si detector is included in the SolarSoft package for SOXS to enable forward fit of the count spectra. This software package allows the user to read and display the input data, separate background subtraction in different energy bands and analyze the spectra. It enables to fit the energy spectra using CHIANTI codes (Dere *et al.* 1997) for flare plasma diagnostics with the application of various thermal, multi-thermal and no-thermal functions. Detailed online documentation can be found at http://hesperia.gsfc.nasa.gov/rhessidatacenter/spectroscopy.html

3.2.2.3 Spectral Analysis:

The OSPEX subroutines have been updated to undertake detailed temporal and spectral data analysis of Si detector of SLD/SOXS mission. The preflare background selection and subtraction is done using the GUI (Graphical user interface).

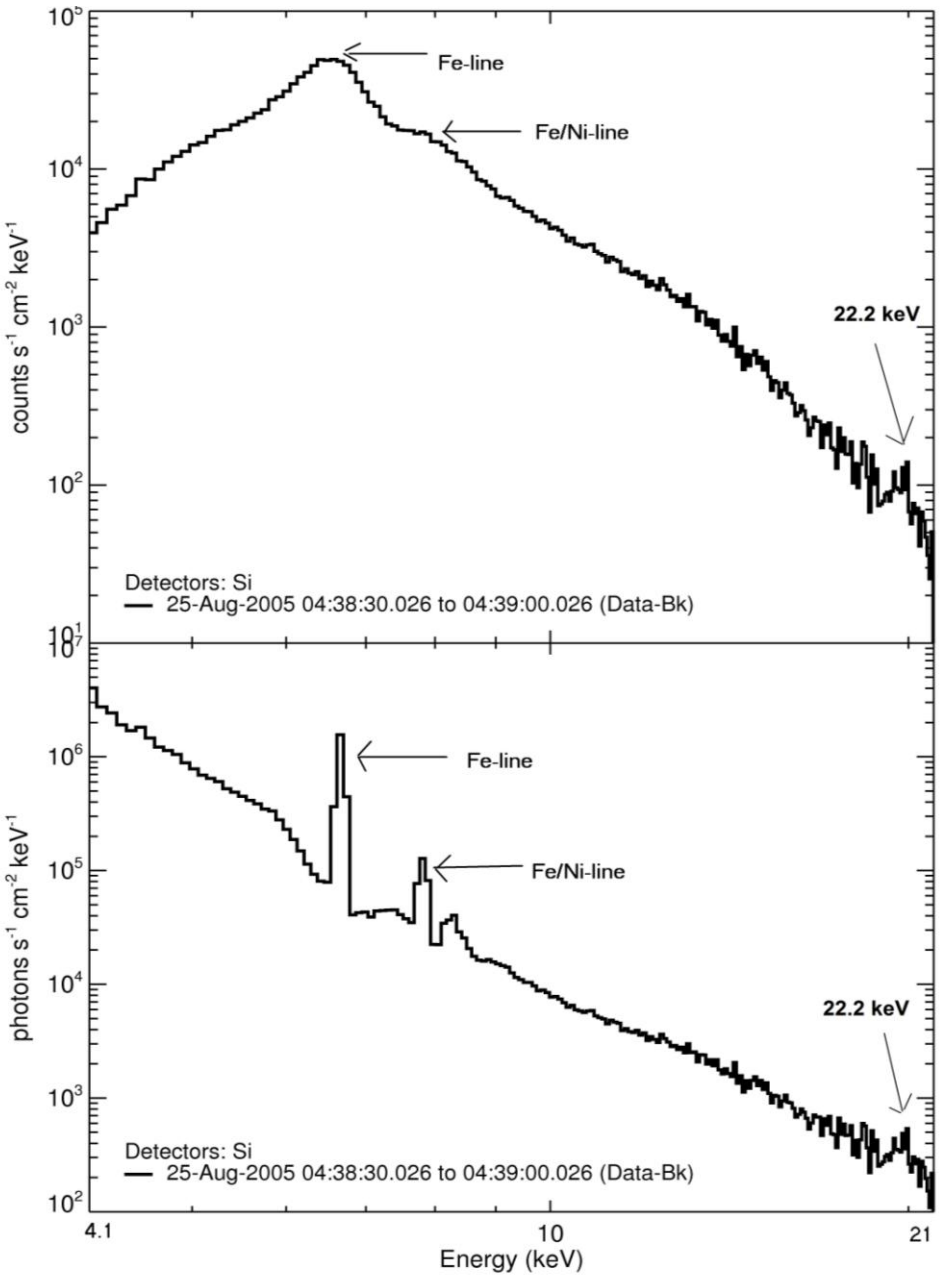

Figure 3.7: X-ray count spectrum (top) and photon spectrum (bottom) in the energy range 4.1-21 keV of 25-August-2005 solar flare. The count flux (counts s^{-1} cm^{-2} keV^{-1}) and photon flux (photons s^{-1} cm^{-2} keV^{-1}) are shown as a function of energy.

The spectral analysis is dependent upon the initial assumptions about the electron spectrum such as thermal and/ or non-thermal models, and the details of which are as follows:

Thermal models:

(i) Isothermal assumption:

In thermal Bremsstrahlung, the electron population is assumed to have Maxwellian velocity distribution in a hot plasma with temperature T and electron density n_e within the emitting volume V. Considering $n = n_i = n_e$ and neglecting factors of order unity, and $Z \approx 1$, the standard expression for the Bremsstrahlung spectrum $F(\varepsilon)$ (Brown, 1974) is given by

$$F(\varepsilon) \approx 8.1 \times 10^{-39} \int_V \frac{\exp(-\varepsilon / k_B T)}{T^{1/2}} n_e{}^2 dV \quad \text{(keV cm}^{-2}\text{ s}^{-1}\text{ keV}^{-1}\text{)} \quad (3.6)$$

$F(\varepsilon)$ is a function of photon energy $\varepsilon = h\nu$

k_B = Boltzmann constant = 1.38 x 10^{-16} erg K^{-1}.

$$\int_V n_e^2 dV = \text{emission measure} \quad (3.7)$$

Fitting this equation to the observed spectrum yields the electron temperature and emission measure of the hot flaring plasma. Thus, the best fit electron temperature and emission measure can be determined by fitting the low-energy X-ray spectrum with an isothermal model in OSPEX (section 3.3.2).

(ii) Multi-thermal assumption:

Instead of single temperature assumption, Craig and Brown (1976) considered flare plasma to be multi-thermal (multi-temperature) plasma in which the emission measure is replaced by differential emission measure (DEM), which varies as a function of temperature corresponding to a temperature range dT. The bremsstrahlung spectrum $F(\varepsilon)$ of multi-thermal plasma with temperature T

$$F(\varepsilon) \approx 8.1 \times 10^{-39} \int_T \frac{\exp(-\varepsilon / k_B T)}{T^{1/2}} \frac{dEM(T)}{dT} dT \quad \text{(keV cm}^{-2}\text{ s}^{-1}\text{ keV}^{-1}\text{)}$$

(3.8)

dEM/d*T* specifies the temperature sensitivity of the differential emission measure at temperatures between *T* and *T* + *dT* contained in the volume *V* and is expressed as

$$\left[\frac{dEM(T)}{dT}\right]dT = n_e^2(T)dV \qquad (3.9)$$

Using the multi-thermal power model, the physical parameters such as DEM (and hence density, if the volume is known) and the upper (higher) temperature value of the hot thermal (multi) plasma can be determined.

Non-thermal Models:

In non-thermal Bremsstrahlung, i.e. in the energy range of about 20-100 keV, the electron population is assumed to be non-Maxwellian. The nonthermal emission exhibits a power-law energy distribution of energetic electrons. The hard X-ray Bremsstrahlung flux exhibits a power-law spectrum of the form

$$I(\varepsilon) = A\varepsilon^{-\gamma} \qquad (3.10)$$

where *A* is the normalization (photon flux) and γ is the spectral index (slope of the spectrum) of the photon power-law. These parameters can be determined by fitting the spectrum with 1-power law model in OSPEX.

To explore the thermal and non-thermal characteristics of solar flares, I have analysed the X-ray spectra by fitting the spectra with a thermal model (Multi-thermal power model) and a non-thermal model (1power-law model). During the fitting process, the response matrix is used to convert the photon model to the model counts to compare with the input count data. The spectra are integrated for different time intervals during the flare. The details of these models are as under:

Multi_therm_pow model:

This function returns the photon spectrum seen at the Earth for a multithermal model (optically thin thermal Bremsstrahlung function, normalized to the Sun-Earth distance). The differential emission measure DEM(T) has a power-law dependence on temperature. Thermal Bremsstrahlung fluxes are computed by integrating the isothermal Bremsstrahlung from plasma in the temperature

range a(1) to a(2) with differential emission measure. This model is valid for temperatures between .086 and 8.6 keV. Fitting the count spectrum with this model yields the following spectral parameters:

a(0): Differential emission measure at T= 2 keV in units of 10^{49} cm^{-3} keV^{-1}

a(1): Minimum plasma temperature in is taken to be 0.5 keV.

a(2): Maximum plasma temperature in keV

a(3): Power law index for calculating the differential emission measure at temperature T

$$DEM(T) = a(0) \times \left(\frac{2.0}{T} \right)^{a(3)}$$

a(4): Relative abundance for Iron/Nickel, Calcium, Sulfur, Silicon

Relative to coronal abundance for Chianti

Relative to solar abundance for Mewe

Single power-law model:

Fitting the count spectrum with this model yields the following spectral parameters:

a(0): Normalization at epivot (photon flux of first power-law at epivot)

a(1): negative power-law index

a(2): epivot (keV)

Pileup modulation:

Pulse pileup occurs at high count rates (if the count rate exceeds ~1000 counts s^{-1}), when the instrument electronics are unable to separate the pulses produced by two photons arriving in a detector within a few μs of each other. As a result, the two photons are recorded as a single photon with energy equal to the sum of energies of the individual photons. The analysis software allows the correction for pile-up. Pulse pile-up function was added (wherever required) while fitting the spectra with multi-thermal and single power-law model.

Once the count spectrum is fitted, it can be de-convoluted over the instrumental response to obtain the photon spectrum which is generated using the fitted model count spectrum. Figure 3.8 shows the count spectrum (top) and the photon spectrum (bottom) of 25-August-2005 flare for the time interval 04:38:30 to 04:39:00 from the Si detector. The model fits are

performed in the energy range of 4.2 - 21 keV. The count flux (counts s^{-1} cm^{-2} keV^{-1}) and photon flux (photons s^{-1} cm^{-2} keV^{-1}) is shown as a function of energy. The multi_therm_pow function (green), single power(yellow), and their total (red) fit to the observed spectrum (black) are shown. The fits are considered acceptable if $\chi^2 \leq 3$. The resulting time-ordered fit parameters (shown as legend in lower left of Figure 3.8) are stored and can be displayed and analyzed with OSPEX. The entire OSPEX session can be saved in the form of a script and the fit results stored in the form of a FITS file.

3.3 RHESSI:

In order to study the X-ray emission from solar flares and the temporal evolution of the spectral parameters of solar flares I have employed the RHESSI data. The following data files are required for the flare analysis: (i) Level-0 data files contain full raw telemetry data in packed format. They are in the form of fits files. (ii) RHESSI observing summary data files containing various rates pre-binned to coarse energy and time resolution. These files are stored in daily fits files in the metadata/catalog directory of the RHESSI data archive. Other key files the software needs are the filedb files (for both the level-0 and Observing files) and the flare catalogue.The filedb files contain a cross-reference between time intervals and file names. These files are distributed with the SSW tree. The data is acquired from the following website: http://hesperia.gsfc.nasa.gov/hessidata/. The RHESSI data analysis software is available in SolarSoftware (SSW) IDL (Interactive Data Language) routines. It also employs OSPEX as described earlier for SOXS data analysis. The analysis is performed in following two steps.

3.3.1 Creation of spectrum and Spectral Response Matrix (SRM) files:

The RHESSI data files containing the raw time-ordered data for a particular time interval are read in RHESSI IDL routine. The following procedure is to be performed for the creation of these files:

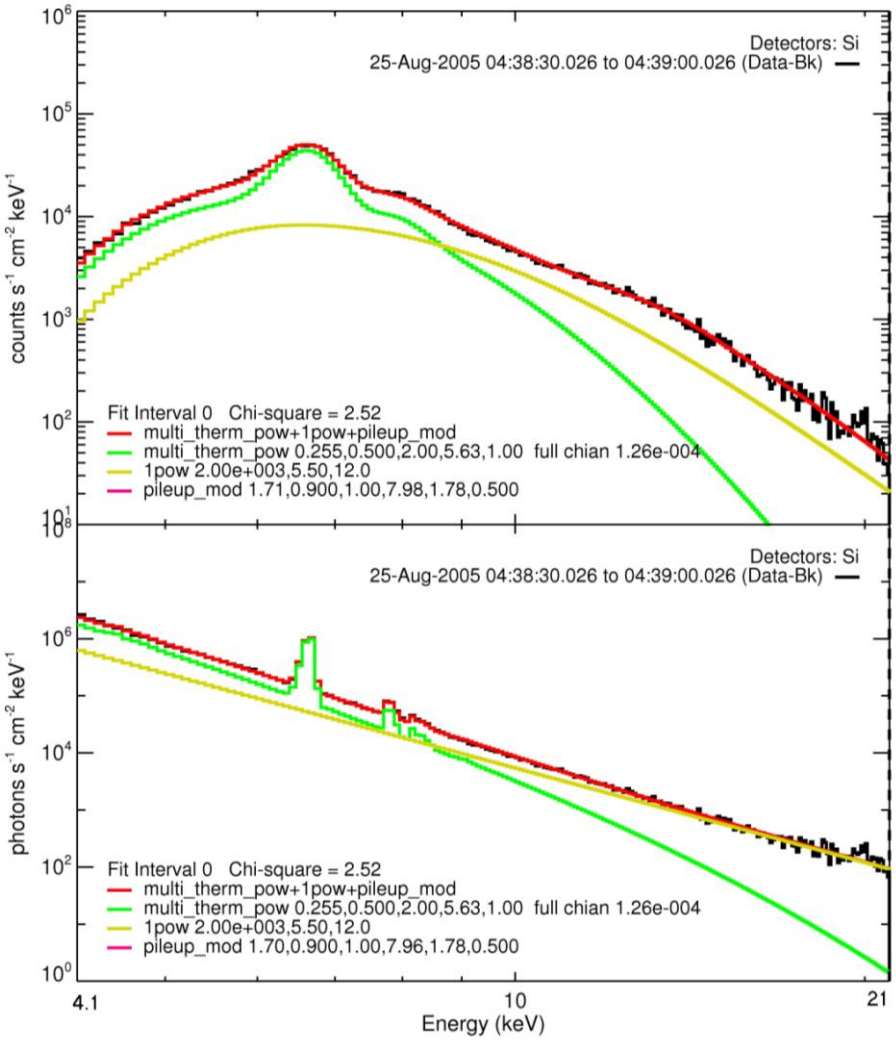

Figure 3.8: The count spectrum (top) and the photon spectrum of 25-August-2005 flare with model fits performed in the energy range of 4.2 - 21 keV. The count flux (counts s^{-1} cm^{-2} keV^{-1}) and photon flux (photons s^{-1} cm^{-2} keV^{-1}) is shown as a function of energy. The multi_therm_pow function (green), single power(yellow) and their total (red) fit to the observed spectrum (black) are shown.

(i) Selection of spectrum time interval: I choose the entire time span of the flare (with RHESSI in sunlight) with additional intervals before and after the flare to allow the background spectrum to be estimated.

(ii) Time Binning: For the energy range 12-100 keV, I used 1 keV wide bins.

(iii) Time bins: I used the time bin width of 4 seconds which is the spacecraft spin period.

(iv) Segments/ Detectors: Since I was interested in the energy range from 12-100 keV, only the data from the front detectors has been chosen. Detector 2 was deselected due to its threshold of about 25 keV and poor energy

resolution of about 9 keV. Detector 7 was generally not included for spectroscopy either because of its threshold of 7 keV and resolution of about 3 keV.

(v) Pile-up and Decimation correction: The analysis software allows the correction for pile-up. Pulse pile-up and decimation corrections were enabled.

After completion of the above mentioned procedure, the spectrum and SRM files were created to be read in by OSPEX. The spectrum file contains the count rate spectra for the chosen time interval. The SRM file contains full spectrometer response matrix (SRM) including the off-diagonal elements. The accumulated spectra and the SRM are then exported to FITS files. After exporting the data to FITS files, we proceed with external spectral analysis software (OSPEX) to produce more accurate photon spectra and compute best-fit function parameters to the spectral data.

3.3.2 Spectral Analysis:

The generated spectrum and the SRM files were read by OPSEX so that the spectral analysis can be carried out through the following steps:

(i) Background subtraction: OPSEX allows separate background for each energy band. We used GUI to select the background time interval. We selected an interval during pre-flare or post-flare night time period for the background. The “Order” was set to zero so that the same background is subtracted from all time intervals. In some flares, separate background time intervals in each energy channels had to be chosen. If the accurate determination of both pre- and post-flare background was not possible, the simplest approach was to consider the background during the night time part of the orbit since then there can be no solar emission enhancing the background. A model photon spectrum (that best fits the data for each time interval) is transformed into a count rate spectrum using the SRM and compared to the observed count spectrum.

The following functions were used to fit the spectra for the thermal and non thermal X-ray emission.

1. Variable thermal (Isothermal) plus a single power-law or a broken power-law model as found suitable.

2. Variable thermal (Isothermal) plus thick2 model.

The details of these functions are given below:

vth (isothermal component) model:

It is optically thin thermal Bremsstrahlung radiation function as differential spectrum seen at Earth in units of photons cm^{-2} s^{-1} keV^{-1}) valid for temperatures between .086 and 8.6 keV.

a(0): Emission measure (10^{49} cm^{-3})

a(1): KT, plasma temperature (keV)

a(2): Relative abundance for Iron/Nickel, Calcium, Sulfur, Silicon

Single power-law model: It is described in section 3.2.2.3

Broken power-law model:

a(0) - normalization at epivot

a(1) - negative power law index below break

a(2) - break energy (keV)

a(3) - negative power law index above break

Thick2 model:

a(0) - Total integrated electron flux, in units of 10^{35} electrons s^{-1}

a(1) - Low delta, index of the electron distribution function below the break

a(2) - Break energy (in keV). To use a single power-law electron distribution, this value can be set to a value greater than of equal to high energy cut-off or to a value lower than or equal to low energy cut-off

a(3) - High delta, index of the electron distribution function above the break

a(4) - low energy cut-off (in keV)

a(5) - high energy cut-off (in keV)

These functions enable to derive the parameters of coronal flare plasma. The fit parameters enable to quantifying the flare plasma energetics and processes responsible for the flare emission.

3.4 Disturbance Storm Time (Dst) index:

In chapter 5, I have considered geoeffectiveness based on Dst index. The Dst index values are taken from Kyoto website: http://wdc.kugi.kyoto-u.ac.jp/dstdir/index.html. Values of Dst index are final values for the period 2002 -2003 and provisional for the period 2004-2006.

Figure 3.9 shows an example of the geomagnetic storm during December 2006. The figure shows a sudden rise in the Dst index value which corresponds to the sudden storm commencement (ssc). As the intensity of the ring current increases, the value of Dst decreases sharply which corresponds to the main decay phase of the geomagnetic storm. The ring current begins to recover as soon as the IMF turns northward. Thereafter, the Dst index recovers (rises) slowly back to the no-disturbance (quiet) level.

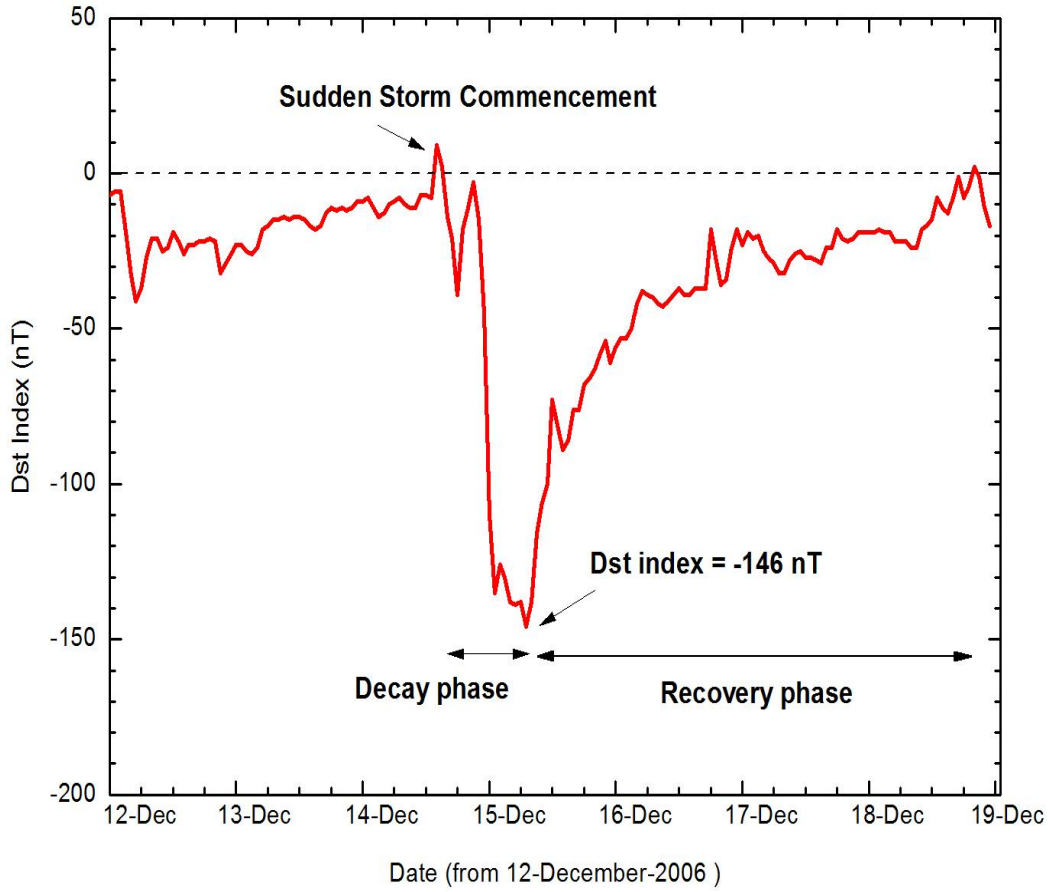

Figure 3.9: A typical storm time Dst measurement for the period 12-18 December 2006. The sudden storm commencement (ssc), decay phase and the recovery phase during the storm interval are also shown.

3.5 CME:

In chapter 5, I have explored the flare-CME relationship. I have employed the observations of CMEs made by LASCO onboard SOHO mission. The preliminary kinematics of the observed CMEs are presented in the Catalogue available at http://cdaw.gsfc.nasa.gov/CME_list/. This catalogue contains all

CMEs manually identified since 1996 from the LASCO and the kinematics used by me are from this catalogue. I have not attempted separately to measure the dynamics of the CMEs.

Shown below is the portion of the kinematics data sheet (Date and time of first C2 appearance, central position angle, angular width, linear speed, links to movies and plots) obtained from SOHO/LASCO CME catalog. The data sheet is for the 13-December-2006 CME event. The corresponding halo CME is shown below in Figure 3.10.

First C2 Appearance Date	Time [UT]	Central PA [deg]	Angular Width [deg]	Linear Speed [km/s]	Movies, plots, & links
2006/12/13	02:54:04	Halo	360	1774	C2 C3 195 PHTX DST Java Movie

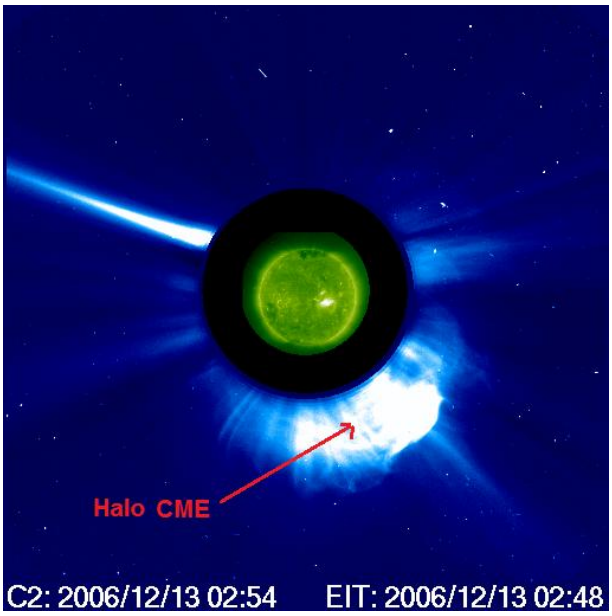

Figure 3.10: The A frame of a JavaScript movie of the c2eit image showing the halo CME event on 13-December-2006 (Image: SOHO LASCO CME Catalog).

3.6 Proton Data:

SEP events are studied in chapter 5. Proton data is taken from GOES-Space Environment Monitor available at the following website: http://spidr.ngdc.noaa.gov/spidr/

The temporal mode observations reveals proton flux (particles cm^{-2} s^{-1} sr^{-1} MeV^{-1}) as a function of time for fixed energy bands (0.8 – 4, 4 – 9, 9 – 15, 15 – 40, 40 – 80, 80 – 165 and 165 - 500 MeV). Similarly, the spectral mode observations reveal the particle flux as a function of energy at a given time. The proton spectra are fitted with a single power-law (or a double power-law as necessary) to obtain the spectral index using Origin8 software. There are only seven energy channels in which the flux can be plotted. In some events, the spectrum was observed upto 80 or 165 MeV with a break in the spectrum. In that case the spectral index above the break energy was considered. The spectral index below the break energy could not be obtained because of the spectrum was too flat with a spectral index ≤ 1. In some events, only two energy channels were left after fitting the spectrum above the break energy. In some events, the spectrum was observed upto 332.5 MeV with a break in the spectrum, in that case the spectrum was fitted with a power-law below and above the break energy and the average spectral index was considered.

Figure 3.11 shows an example of a background-subtracted proton spectrum of 10-November-2004 SEP event in the energy range 0.8 – 80 MeV for the interval 06:00 to 09:00 UT.

3.7 Geomagnetic activity index (*aa*):

The prediction of solar activity is done using geomagnetic *aa* indices in chapter 6. The *aa* index data are normalized by cross-correlation of the instruments (described in section 2.6) distributed over the globe and over time, and therefore may be considered homogeneous over the period under current study.

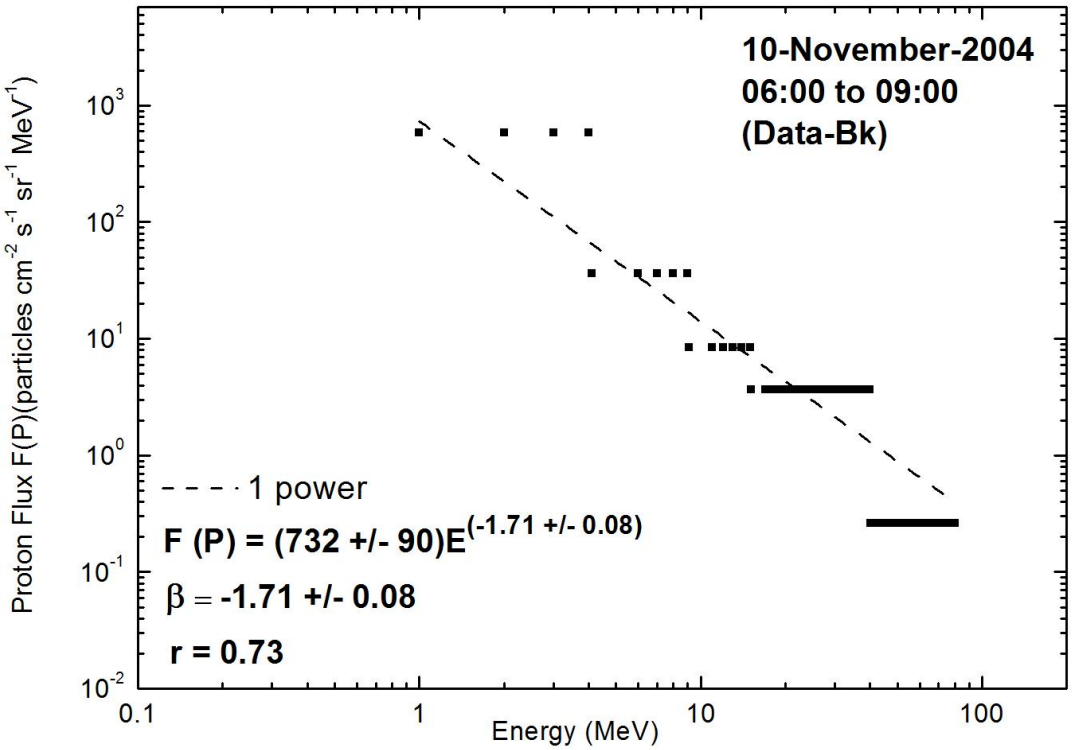

Figure 3.11: This plot shows a background-subtracted proton spectrum of 10-November-2004 SEP event in the energy range 0.8 – 80 MeV for the interval 06:00 to 09:00 UT.

The annual geomagnetic *aa* indices are obtained for the period 1868 –2007 from the website:

ftp://ftp.ngdc.noaa.gov/STP/SOLAR_DATA/RELATED_INDICES/AA_INDEX/AA_YEAR

The monthly *aa* values for 2008 (January –November) are acquired from the following website:

ftp://ftp.ngdc.noaa.gov/STP/SOLAR_DATA/RELATED_INDICES/AA_INDEX/AA_MONTH

Following the method of Svalgaard, Cliver, and Le Sager (2004) and Wilson and Hathaway (2006), the values of *aa* prior to 1957 were increased by 3 nT in the present study to compensate for change in the geographical latitudes of the magnetometers used in determining the *aa* index.

3.8 Sunspot Number Data:

The relative sunspot number (International Sunspot Number), Ri, is an index of the activity of the entire visible disc of the Sun. It is determined each day at

a given observing station without reference to preceding days using the form $R_i = K\,(10g+s)$, where *g* is the number of sunspot groups and *s* is the total number of distinct spots. The scale factor *K* (usually less than unity) depends on the observer and is intended to effect the conversion to the scale originating in the work of Wolf. The relative sunspot number R_i (international) is derived from the statistical treatment of data originating from more than twenty-five observing stations.

For the current investigation (in chapter 6), the data for the yearly sunspot numbers for the period 1868 – 2007 are taken from the following website:
ftp://ftp.ngdc.noaa.gov/STP/SOLAR_DATA/SUNSPOT_NUMBERS/INTERNATIONAL/yearly/YEARLY

However, for 2008 (monthly) is obtained from the following website: ftp://ftp.ngdc.noaa.gov/STP/SOLAR_DATA/SUNSPOT_NUMBERS/INTERNATIONAL/monthly/MONTHLY

CHAPTER 4

X-RAY EMISSION FROM SOLAR FLARES

In this chapter, I present the study of X-ray emission from solar flares (GOES M and C class) observed by “Solar X-ray Spectrometer” (SOXS) as well as “Reuven Ramaty High-Energy Spectroscopic Imager” RHESSI missions. I study temporal and spectral evolution of flare plasma. The thermal energy content in all solar flares from SOXS and RHESSI observations is also determined. I explored the relation between the thermal and non-thermal energies for various time intervals, however, for those two flares which were observed for sufficient time interval. The relationship among the spectral parameters is also investigated and presented in this chapter.

4.1 X- ray Emission:

X-ray emission from a large variety of objects is mostly in continuum. Extracting the significant parameters from the X-ray continuum spectroscopic methods requires the detectors of sufficiently high spectral and temporal resolution. In the case of X-ray emission from solar flares it is more complex because the flux at low energies (below 20 keV) is extremely high while at higher energies (above 20 keV) it starves of photons. Shown in Figure 4.1 is a simulation of full disk integrated X-ray emission carried out by Jain and Masuda for the energy range from 0.01 to 1000 keV, and described by Jain *et a*l. (2005) for the energy range 1-100 keV, and Jain (2009) for the whole energy range 0.01-1000 keV. They carried out simulation considering the following plasma parameters for quiet (pre-flare) and various components of a M5 class flare. Pre-flare background, T = 4 MK, EM = 10^{49} cm^{-3}; thermal, T = 13 MK, EM = $10^{49.5}$ cm^{-3}; super-hot, T = 40 MK, EM = 10^{47} cm^{-3}, and non-thermal spectral index γ = -3.5 (range = –2.5 to –4.5), and flux at 20 keV = 10 photons cm^{-2} s^{-1} keV^{-1}.

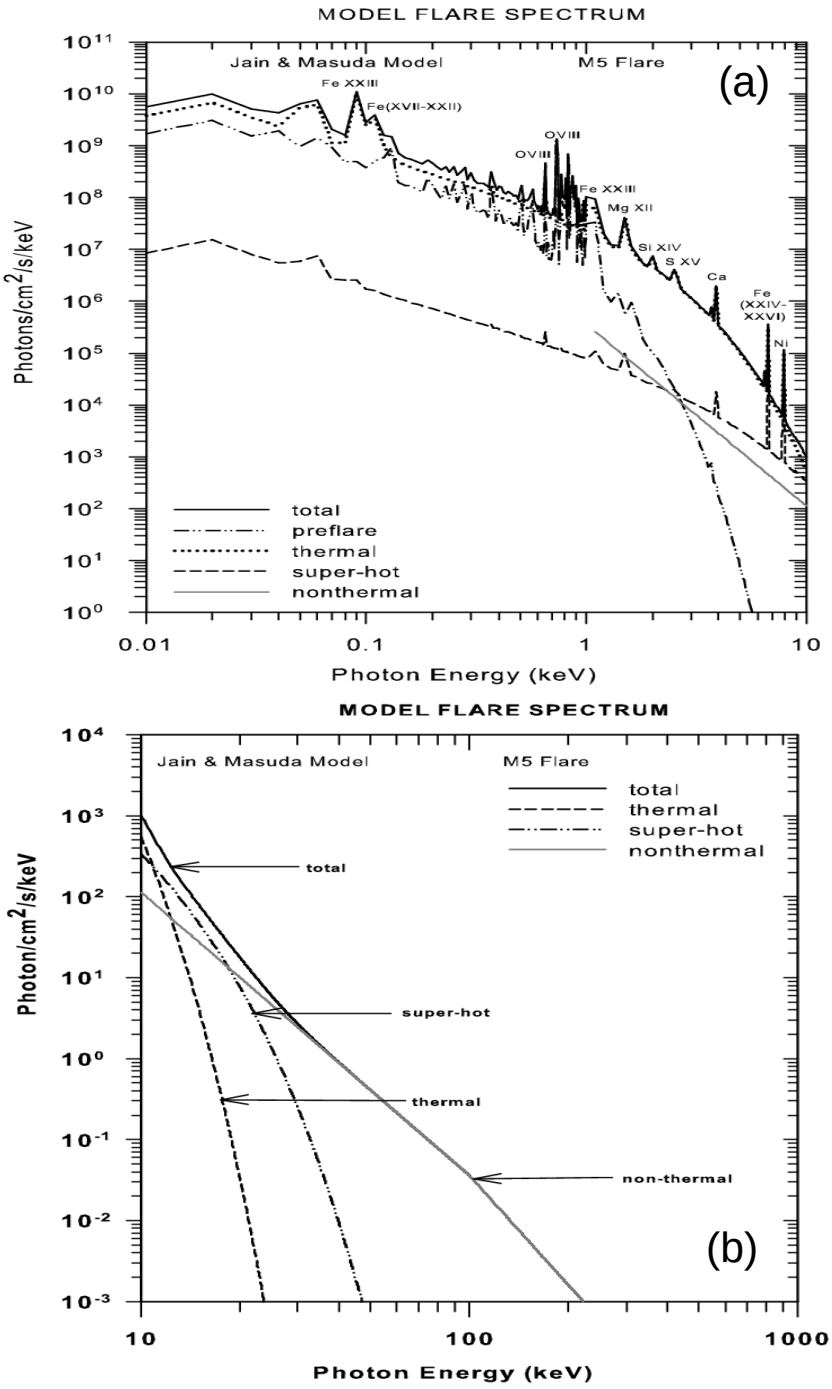

Figure 4.1: Simulation of full disk integrated X-ray photon emission spectrum from the Sun in the energy range 0.01-10 (top) and 10-1000 (bottom) keV for quiet and M5 solar flare conditions. The pre-flare background, thermal component, and super-hot and non-thermal hard X-ray components of the solar flare are also shown by different lines. The solid thick line is total flux from all these assumptions. It may be noted that iron and iron-nickel complex lines at 6.7 and 8 keV respectively appear only when flare occurs (top), and there is a break in energy from one to other spectrum (bottom).

4.1.1 Soft X-ray Line Emission:

Figure 4.1 (top) shows the prominent XUV line emission with and without solar flare in the energy range 0.01 to 10 keV. It may be noted that line emission from many prominent elements below 5 keV is visible without flare but above 5.0 keV it becomes visible only when the flare occurs. The simulation of X-ray emission from the solar flare (Figure 4.1) unambiguously indicates the possibility to determine the thermal spectrum from the measurements of the soft X-ray line and continuum emission. However, this requires high sensitivity of the instrument as well as < 1 keV (FWHM) energy resolution. It may be noted from Figure 4.1(top) that iron-line complex and Fe/Ni line complex are visible only during the flare. The Fe-line feature is due mostly to the 1s-2p transitions in He-like and H-like iron, FeXXV and FeXXVI respectively, with associated satellite lines. Another weaker line complex at ~ 8 keV made up of emission from He-like nickel and more highly excited FeXXV ions is also evident in the more intense flares (Phillips 2004, Phillips *et al*. 2004). The centroid energy and width of the iron-line complex at ~6.7 keV, the intensity of the Fe/Ni line complex at ~ 8 keV, and the line-to-continuum ratio are the functions of the plasma temperature and can be used to limit the range of possible plasma parameters. Figure 4.1 (top) shows that below 5 keV the corona is so hot that a large number of photons are emitted, mostly in the form of lines, even in the absence of the flare (Jain *et al*., 2005). This restricts to design the spectroscopy experiment from 1 keV to 20 keV in view of saturation of the detector, because of its limited counts handling capability, by low energy photons only. However realizing that the synoptic observations at energies below 10 keV may improve our current understanding on the temperature enhancement during flares of different magnitude requires optimization in design such that the detectors do not get saturated. The flare spectrum (Figure 4.1 (bottom)) also reveals break energy points between 10 - 100 keV, the first between thermal and super-hot components, and second between super-hot and non-thermal components. Precise measurements of these break energy points will improve current knowledge of the acceleration of electrons and energy release in solar flares.

4.1.2 X-ray Emission Mechanism:

4.1.2.1 Free-Free Emission (Bremsstrahlung):

When a free electron hits an ion in a Coulomb collision, an X-ray photon is emitted whose energy corresponds to the difference of energy between incoming and out coming electrons. After scattering, the electron remains free and hence the name free-free emission. This radiation mechanism is called Bremsstrahlung which is illustrated in Figure 4.2**.** In solar flares, the emission in X-ray wavelengths is mainly governed by bremsstrahlung emission.

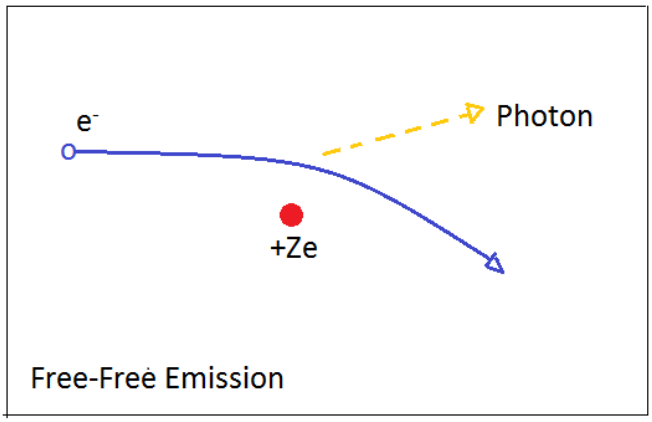

Figure 4.2: Illustration of Free-Free (Bremsstrahlung) Emission

4.1.2.2 Thermal and Non-thermal Contributions:

The single temperature approximations have been widely used in the past in investigations of X-ray emissions from the solar flares. However the fact that the plasma is heated at different temperatures (multi-thermal plasma), and the emission measure varies as a function of temperature emphasizes the crucial need to study the X-ray spectra with high energy and temporal resolution. Similarly, the continuum spectra above 10 keV with better energy and temporal resolution are essential to improve our current understanding on the non-thermal acceleration of electrons during impulsive phase of solar flares (Figure 4.1 (bottom)). The quantitative fraction of thermal and non-thermal components of the total flare energy budget has not been well understood. Indeed, the total energy in neither component has generally been determined to better than an order of magnitude. However, there are strong indications that, in many flares, the non-thermal component contains a substantial fraction of the total flare energy (Dennis *et al*. 2003, Jain *et al*. 2008), while

significant energy release in soft X-ray domain (<10 keV) is also predicted. Thus, it is critically important to improve our present knowledge of the flare energy release process to determine the energy in these two components and their relationship as a function of time more precisely.

Figure 4.3 shows the spectrum of thermal and non-thermal X-ray emission in a solar flare. The flare loops (coronal loops) are filled with hot thermal plasma emitting X-rays. The corresponding thermal bremsstrahlung spectrum extends upto about 20 keV (low energy portion) and is fitted with the variable thermal component (green line) as shown in Figure 4.3. The non-thermal (high energy portion) emission comes from the footpoints of the flare loops. The corresponding non-thermal bremsstrahlung spectrum is fitted with a single power law (yellow line) as shown in Figure 4.3.

4.2 Dataset:

In order to study the temporal evolution of spectral parameters of solar flares, I selected 10 flares of GOES importance class M which were well observed by both SOXS and RHESSI. In addition, I also considered 3 C class flares observed by SOXS. The details of the physical properties of these flares *viz*. flare location, GOES class, and active region are given in Table 4.1. For the current study, the flare X-ray emission data is employed from the Si detector of the SOXS payload. The start time (column c), peak time (column d) and end time (column e) of the selected flares observed by Si detector is determined in 4.1-12 keV energy range. The start time of the flare is taken when the flux becomes 5σ above the background flux in the Si detector, where σ is the standard deviation of the pre-flare background. The peak time is the time of maximum flux in 4.1-12 keV energy band (column f). The GOES class, flare location and active region number (obtained from SGD reports) are given in columns g, h and I respectively.

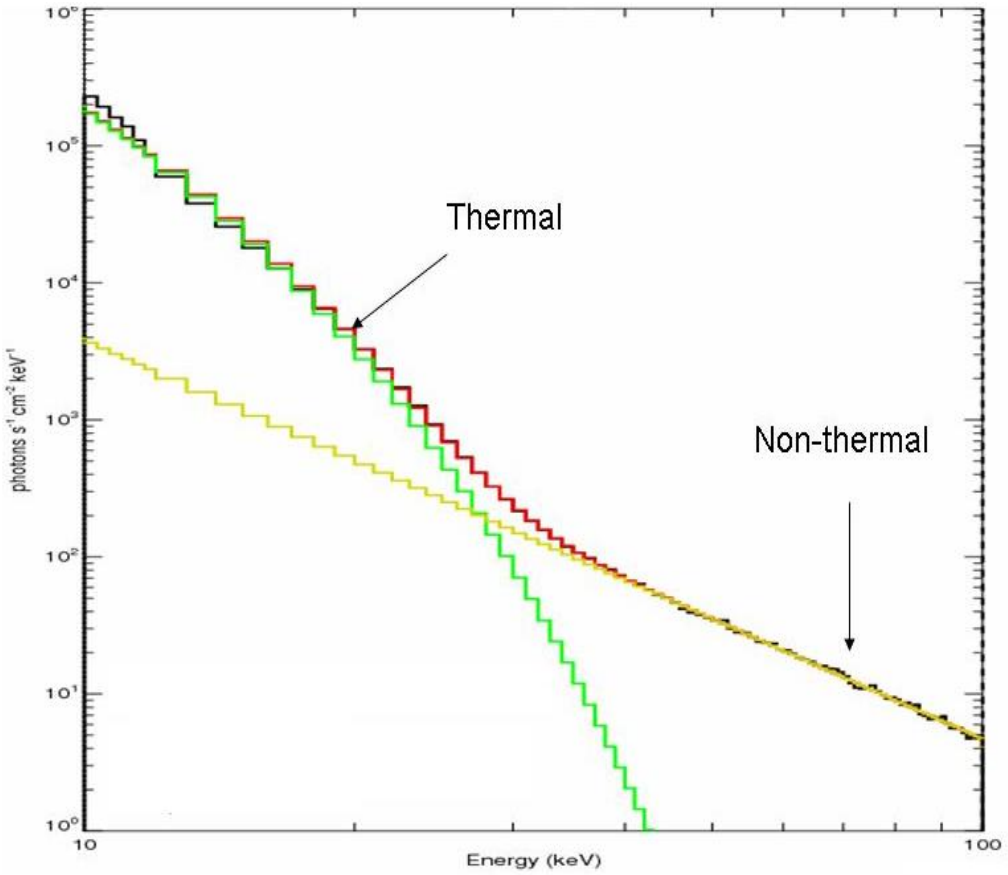

Figure 4.3: X-ray spectrum of a solar flare observed by RHESSI characterizing thermal and non-thermal component. Thermal (low energy) portion is fitted with the variable thermal component while the non-thermal (high energy) portion is fitted with a single power law.

Sometimes there were two peaks with equal emission. In that case, the time of the earliest peak has been taken. The end time is the time when the intensity of the flare returned to the pre-flare background or where it leveled off, whichever occurred earlier.

Out of ten selected flares observed by RHESSI, the data from the detector 5F was employed for analysis of 14 July 2004 and 5 April 2004 flares, and for 27 July 05 data from the detector 9F was used, while for the rest of the seven flares, the data from detector 4F was used, which has relatively good spectral resolution (FWHM ~ 0.98 keV).

Table 4.1: Physical Properties of Flares observed by SOXS and RHESSI

(a)	(b)	(c)	(d)	(e)	(f)	(g)	(h)	(i)
S. No.	Date	Start time	Peak time	End time	Peak flux (Counts s^{-1} cm^{-2} keV^{-1})	GOES Class	Location	NOAA Active Region
1	13-NOVEMBER-2003	04:59:16	05:02:16	05:11:54	3550	M1.6	N01E90	10501
2	19-NOVEMBER-2003	03:57:48	04:01:44	04:13:55	3653	M1.7	N01E06	10501
3	6 –JANUARY-2004	06:18:00	06:26:55	06:52:30	5170	M5.8	N05E90	10537
4	5-APRIL-2004	05:35:30	05:50:41	06:35:36	2737	M1.7	S18E35	10588
5	14 –JULY-2004	05:12:41	05:22:55	05:39:01	14775	M6.2	N12W62	10646
6	31-OCTOBER-2004	05:24:36	05:31:00	05:51:27	6884	M2.3	N13W34	10691
7	27-JULY-2005	04:36:20	04:58:52	05:30:00	8102	M3.7	N11E90	10792
8	3-AUGUST-2005	04:56:15	05:05:41	05:25:14	7356	M3.4	S13E45	10794
9	25-AUGUST-2005	04:35:06	04:39:21	05:01:24	15842	M6.4	N09E80	10803
10	17-SEPTEMBER-2005	06:00:33	06:05:21	06:19:58	17649	M9.8	S10W39	10808
11	7-FEBRUARY-2010	04:44:42	04:51:52	05:13:11	1443	C9.9	N20E07	1045
12	8-FEBRUARY-2010	B04:06:20	04:14:17	04:32:05	8410	C7.7	N21W01	1045
13	8-FEBRUARY-2010	04:58:26	05:21:35	05:53:27	1053	C8.6	N21W01	1045

4.3 Spectral Analysis and Results:

4.3.1 Spectral Analysis of 6 January 2004 Flare (SOXS):

The spectral analysis techniques are described in chapter 3. Figure 4.4 shows the temporal mode observations *i.e.* light curve of 6 January 2004 solar flare in two energy bands, 4.1-12 and 12-24.7 keV. The time resolution for temporal and spectral mode observations during quiet periods is one second and three seconds respectively, but during the flare mode, it is 100 ms for both temporal and spectral modes. However, it is restricted to 287.5 s only in view of telemetry constraints. The count flux (counts s^{-1} cm^{-2} keV^{-1}) shown in Figure 4.4 is a 3 second moving average of the 100 ms observed data. The flare was simultaneously observed by RHESSI (discussed in next section).

I formed the count spectrum by integrating the high cadence spectra over different intervals. I analyze the energy spectra observed by the Si detector to derive the plasma parameters of the flares such as temperature, emission measure and spectral indices using the OSPEX spectral fitting program.

The temperature in the flare plasma varies during its evolution in general and during the rise time in particular (Jain *et al.* 2006b). Therefore, the flare plasma cannot be considered isothermal for the period of integration of the spectra of about 30 s or more. Thus, I consider the multi-thermal power-law function for thermal plasma and single power-law function for non-thermal continuum using the CHIANTI codes for fitting the observed spectrum of the flare.

In the multi-thermal power-law, the minimum coronal plasma temperature (T_0) is considered to be constant = 0.5 keV in context to Jain *et al*. (2005) who showed that corona is very hot up to 5 keV without flares (cf. Figure 4.1(top). The maximum plasma temperature T and spectral index α (multi-thermal power-law index for calculating the DEM at T) are free parameters, determined by the best fit. The multi-thermal power-law function also enables to measure the relative abundance (a4) for Fe/Ni, Calcium, Sulfur and Si relative to coronal abundance. However, in the current investigation, the relative abundance (a4) is kept fixed =1.

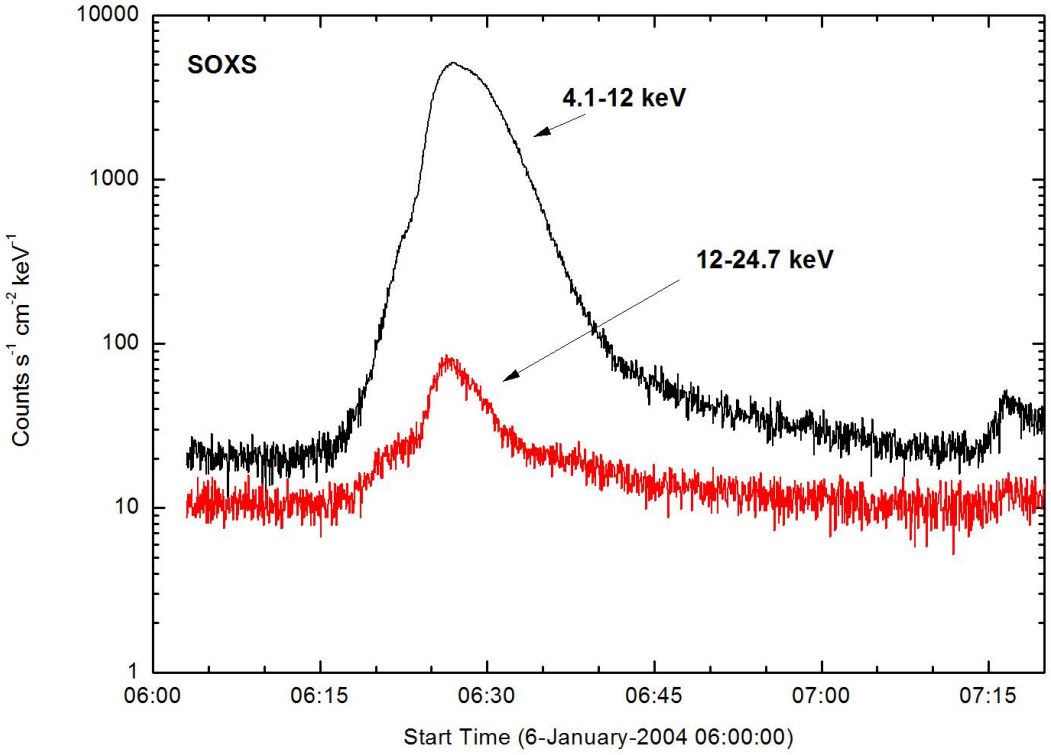

Figure 4.4: Light curve of the 6 January 2004 solar flare in energy range 4.1-12 (black) and 12-24.7 (red) keV energy bands of the Si detector of the SLD/SOXS mission.

The non-thermal part of the spectrum is fitted with a single power-law function. The epivot is kept constant =12 keV in view of the fact that the low-energy cut-off of non-thermal continuum emission is not precisely known, and varies between 10-20 keV during the early evolution of the flare. The fit with single power-law yields the parameters such as normalization at epivot F_{12} (photon flux of first power-law at epivot) and spectral index γ (negative power-law index). During the rise time of the flare, there is a significant contribution of thermal continuum in many flares. A forward fit is done for a particular time interval by a best fit to the spectrum features based on the minimum reduced chi-squared (difference counts) technique (Jain *et al.* 2006b). The fit is considered to be acceptable based on the following considerations: (i) The value of reduced chi-squared (χ^2) ≤ 3. (ii) The temperature and emission measure should have a consistent time history *i. e.* their variation should not be too large. The fitted count spectrum is de-convolved over the instrumental response of the instrument to obtain the photon spectrum. Figure 4.5 shows

the observed count spectrum integrated over a time interval from 06:26:30 to 06:27:00 UT during the rise period. The photon spectrum derived from the forward fit of the count spectrum and the residual plot after fitting is shown in Figure 4.6. The multi_therm_pow function (green), 1pow (yellow), pileup_mod (pink) and their total (red) fit to the observed spectrum (black) are shown.

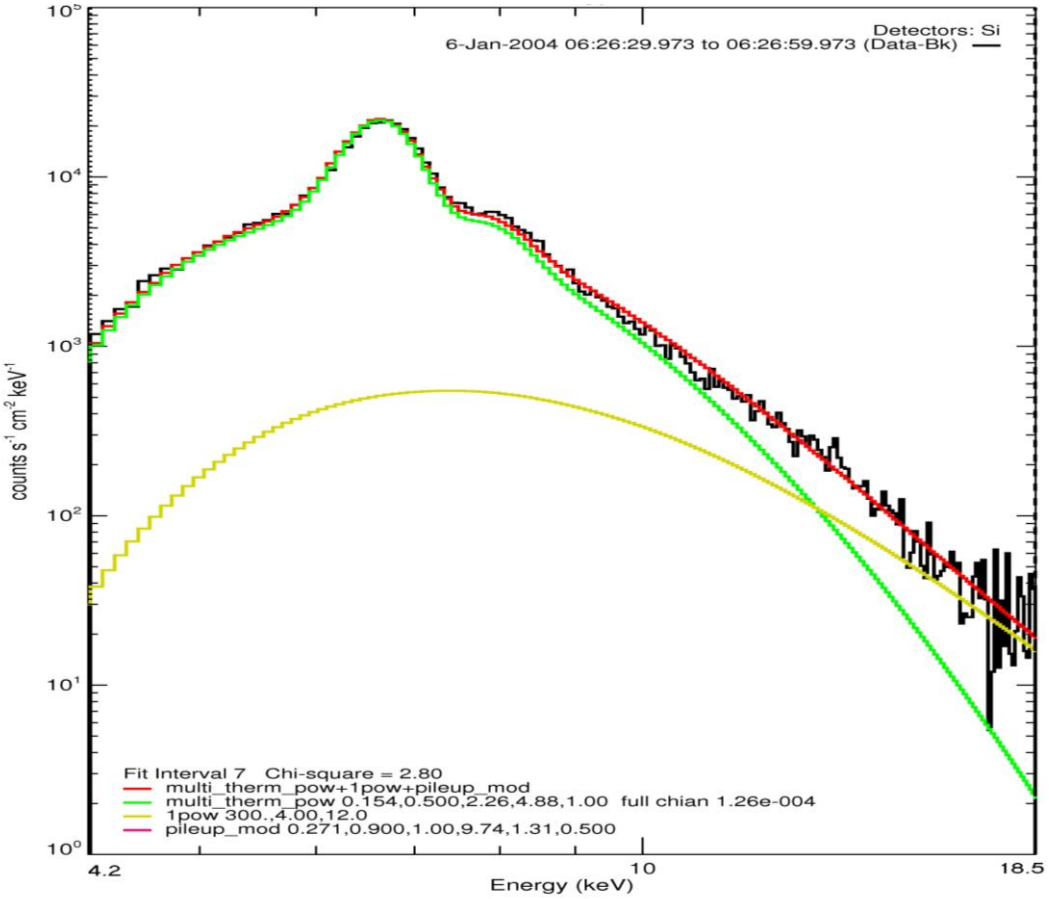

Figure 4.5: The count spectra of 6 January 2004 flare during 06:26:30-06:27:00 UT. The count flux (counts s^{-1} cm^{-2} keV^{-1}) is shown as a function of energy.

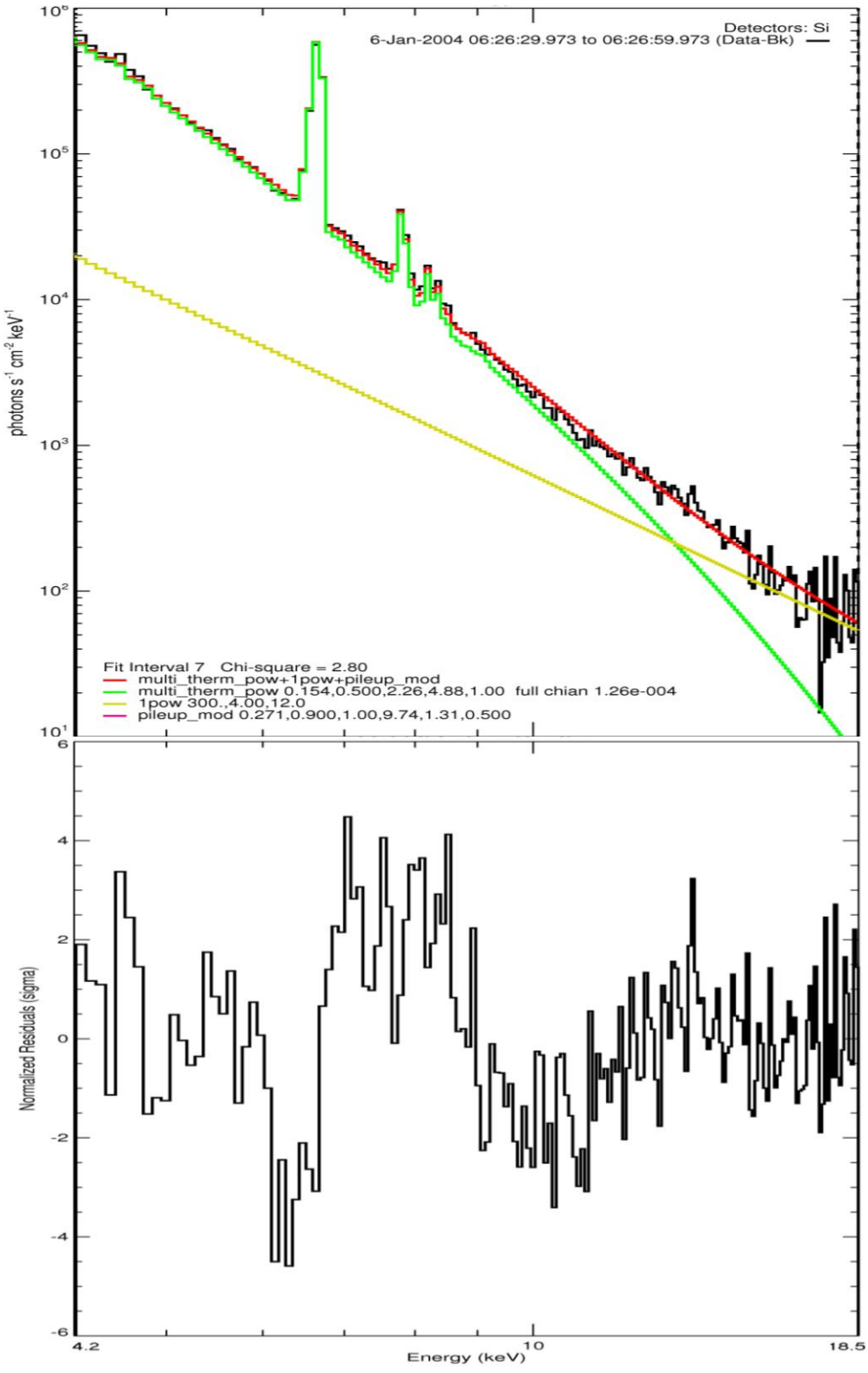

Figure 4.6: Photon spectrum (top) for 6-January-2004 flare with model fits performed in 4.2-18.5 keV. The multi_therm_pow function (green), single power (yellow), and their total (red) fit to the observed spectrum (black) are shown. Normalized residuals (bottom) for each energy bin.

In this manner, the spectral fit is performed for the different intervals during the rise, peak and the decay phase of the flare. The emission measure is then calculated using the following equation.

$$EM = \frac{2^{\alpha} \times DEM(T^{(1-\alpha)} - T_0^{(1-\alpha)})}{(1-\alpha)} \quad (\text{cm}^{-3}) \qquad (4.1)$$

The temporal evolution of the above mentioned spectral parameters is shown in Figure 4.7. The evolution of emission measure is plotted in first panel in Figure 4.7. The emission measure peaks with a value of 20.0 ± 1.14 (10^{49} cm^{-3}) at 06:27:15 UT. The time history of the multi-thermal temperature is shown in second panel of Figure 4.7.

The temperature rises gradually and peaks with a value of 27.5 ± 0.83 MK at 06:26:15 UT. It is observed that the temperature peaks before the emission measure. The plasma gradually cools after the peak in the flare emission. The third panel in Figure 4.7 shows the evolution of spectral index α and I found that it varies between 3.3 ± 0.8 to 5.3 ± 0.3. The fourth panel in Figure 4.7 shows the non-thermal photon flux F_{12} and the fifth panel shows the variation of the non-thermal power-law spectral index γ, which varies between 4 and 5. I observed that the nature of the photon flux is almost same as the light curve.

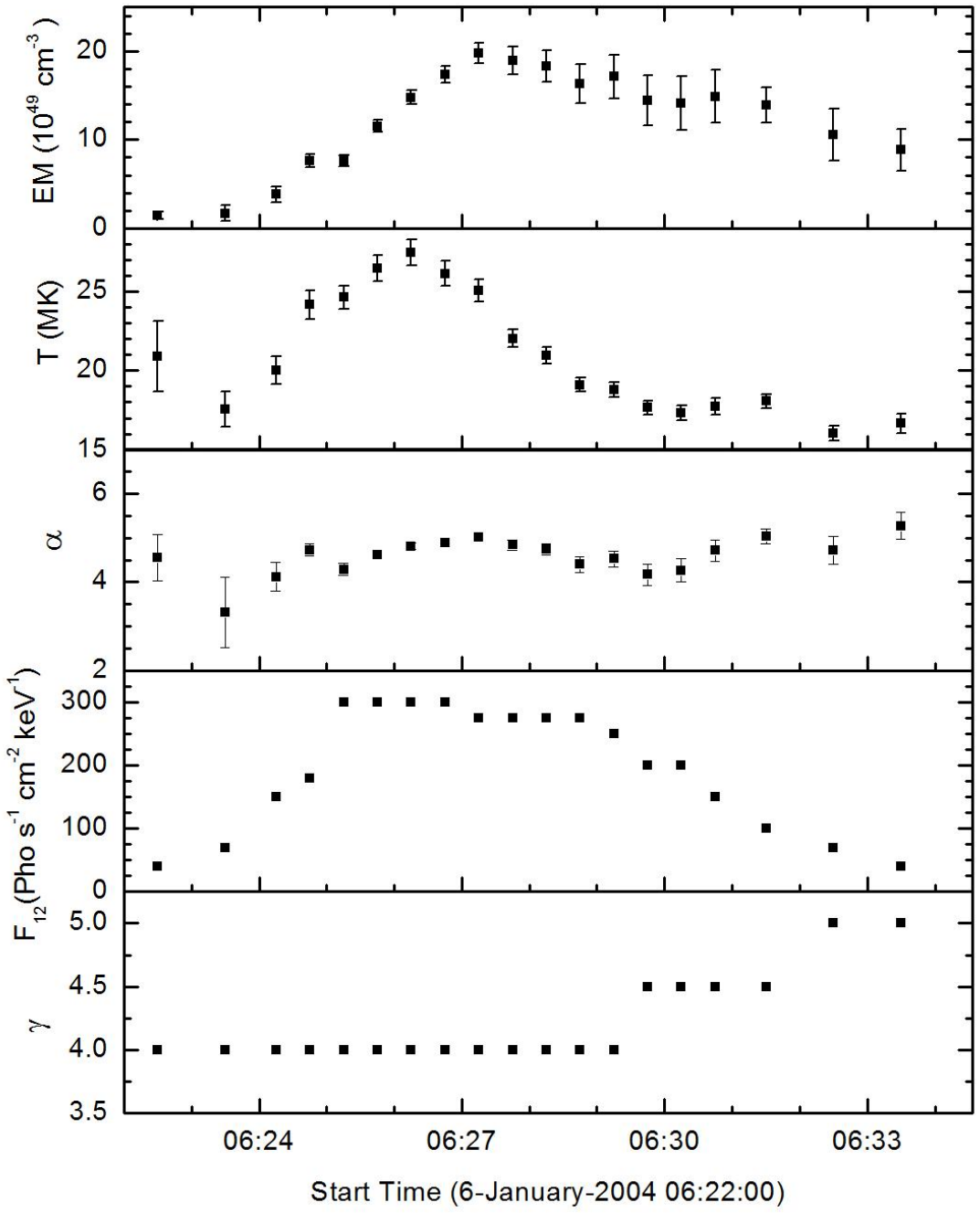

Figure 4.7: Temporal evolution of spectral parameters for 6-January-2004 determined from spectral fitting (SOXS). From top to bottom: (1) Emission measure of multi-thermal plasma (EM); (2) Temperature of multi-thermal plasma (T); (3) Spectral index α (multi-thermal); (4) Photon flux at 12 keV (F_{12}) and (5) spectral index γ (negative power-law). Error bars for emission measure, temperature, and α are as reported by OSPEX showing the limits.

4.3.2 Spectral Analysis of 6 January 2004 Flare (RHESSI):

The 6 January 2004 flare event was simultaneously observed by RHESSI and its temporal evolution in two energy bands (12-25 and 25-100 keV) is shown in Figure 4.8.

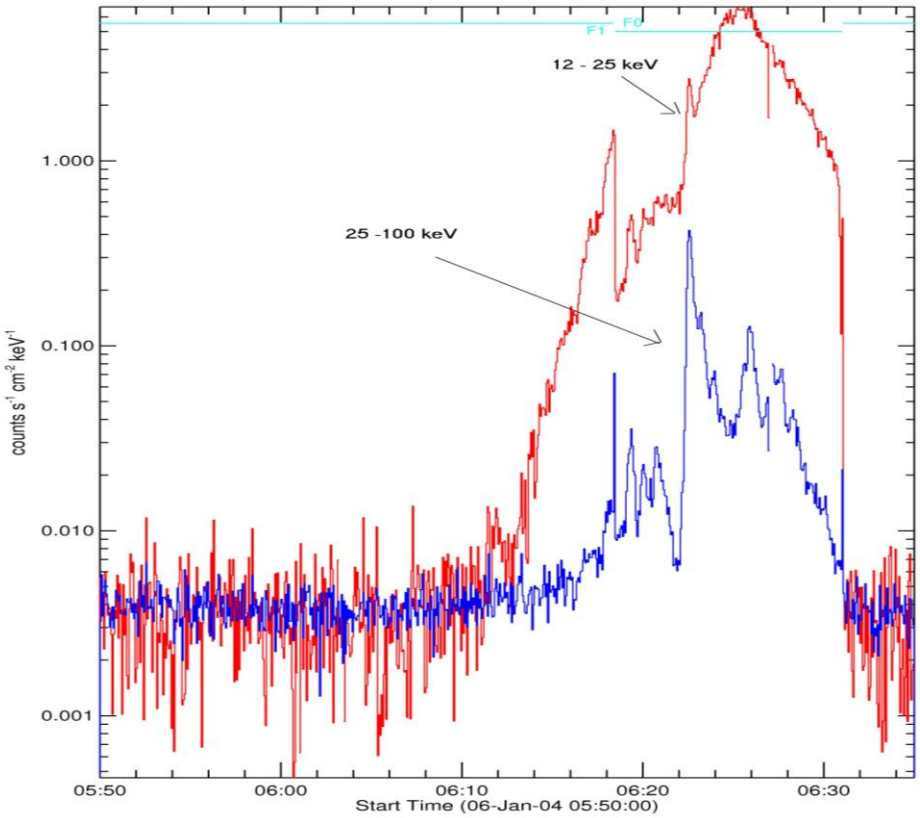

Figure 4.8: RHESSI X-ray light curve of 6 January 2004 solar flare in the energy range 12-25 keV (red) and 25-100 keV (blue) using detector 4F.

To avoid the issues of detectors cross-calibration on one hand and to achieve better energy resolution on the other hand I performed the analysis using a single detector 4F for the 6 January 2004 flare event. This flare was observed in two attenuator states A0 and A1 (shown as a horizontal line (cyan) at the top in Figure 4.8). The spectral analysis techniques for RHESSI data are described in detail in chapter 3. I generated the count spectrum through hessi IDL routine, using 1 keV wide energy bin for the energy range 12-100 keV, and 4s time bins. Spectral fits are obtained using the SolarSoftware (SSW) spectral analysis routine SPEX. Before fitting the data, I corrected the observed counts for pulse pileup and decimation. The spectra were fitted in the energy range 13 to 100 keV unless the background flux merged with the flare flux below this energy. For example, before 06:22:28

UT, the spectral fits could not be obtained above 60 keV. Systematic uncertainty is set to 0.00. The lower limit 13 keV is considered because of the instrumental effect at ~ 11 keV (B. Dennis 2010, private communication). Although, there exists a lower temperature component below ~ 13 keV which is not considered in the present analysis as the observations below 13 keV are obtained from SOXS. The spatially integrated count flux spectra are fitted using the combination of isothermal component (*Variable thermal model vth***)** and a single power law which yields the following four free parameters: Isothermal components: Emission measure EM (10^{49} cm^{-3}) and plasma temperature T (keV) and non-thermal components: normalization at epivot (photon flux of first power-law at epivot F_{20}= 20keV) and spectral index γ (negative power-law index). The isothermal function also enables to measure the relative abundance (a2) for Fe/Ni, Calcium, Sulfur and Si relative to coronal abundance. However, in the current investigation, the relative abundance (a2) is kept fixed =1.

The free parameters are varied until a reasonably good fit is obtained. The fits were considered acceptable if reduced chi-squared ≤ 2. Figure 4.9 shows the observed count spectrum integrated over a time interval from 06:26:28 to 06:27:28 UT during the rise period. The photon spectrum derived from the forward fit of the count spectrum and the residual plot after fitting is shown in Figure 4.10. The vth function (green), 1pow (yellow), and their total (red) fit to the observed spectrum (black) are shown. In this manner, the spectral fit is performed for the different intervals during the rise, peak and the decay phase of the flare. The temporal evolution of the above mentioned spectral parameters is shown in Figure 4.11. The evolution of emission measure is plotted in first panel of Figure 4.11. The emission measure peaks after the peak intensity of the flare with a value of 0.55 ± 0.04 (10^{49} cm^{-3}) at 06:29:00. The time history of the temperature of the isothermal component is shown in the second panel of Figure 4.11. The temperature rises gradually to 25 ± 0.2 MK. The plasma gradually cools after the peak in the flare emission. The time history of the photon flux F_{20} is plotted in third panel. The peak flux at 06:23:00 is 14.7 ± 0.19 photons s^{-1} cm^{-2} keV^{-1}. The temporal variation of the photon flux is almost same as the light curve. The variation of the spectral

index γ is shown in the fourth panel of Figure 4.11 and it varies between 2.6 ± 0.01 and 4.3 ± 0.1.

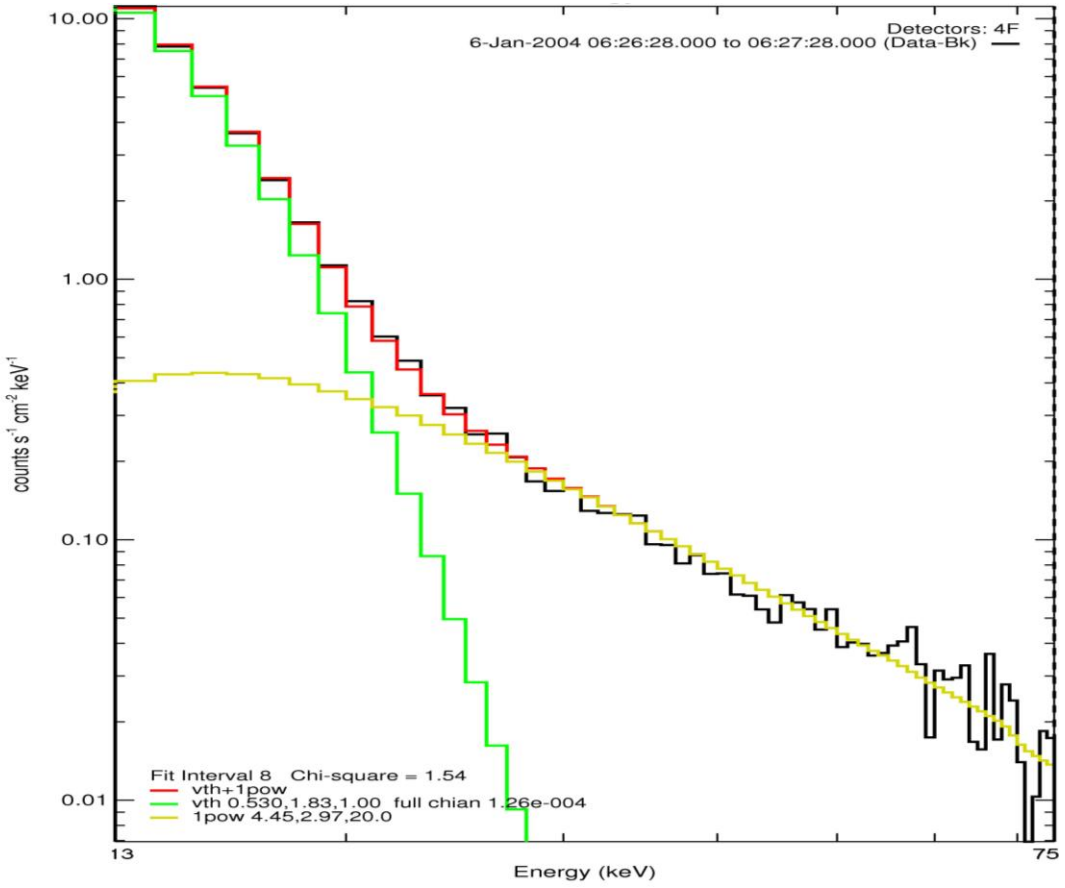

Figure 4.9: RHESSI Count spectrum of 6-January-2004 fitted with vth+1pow function in the energy range 13-75 keV. The vth function (green), 1pow (yellow), and their total (red) fit to the observed spectrum (black) are shown.

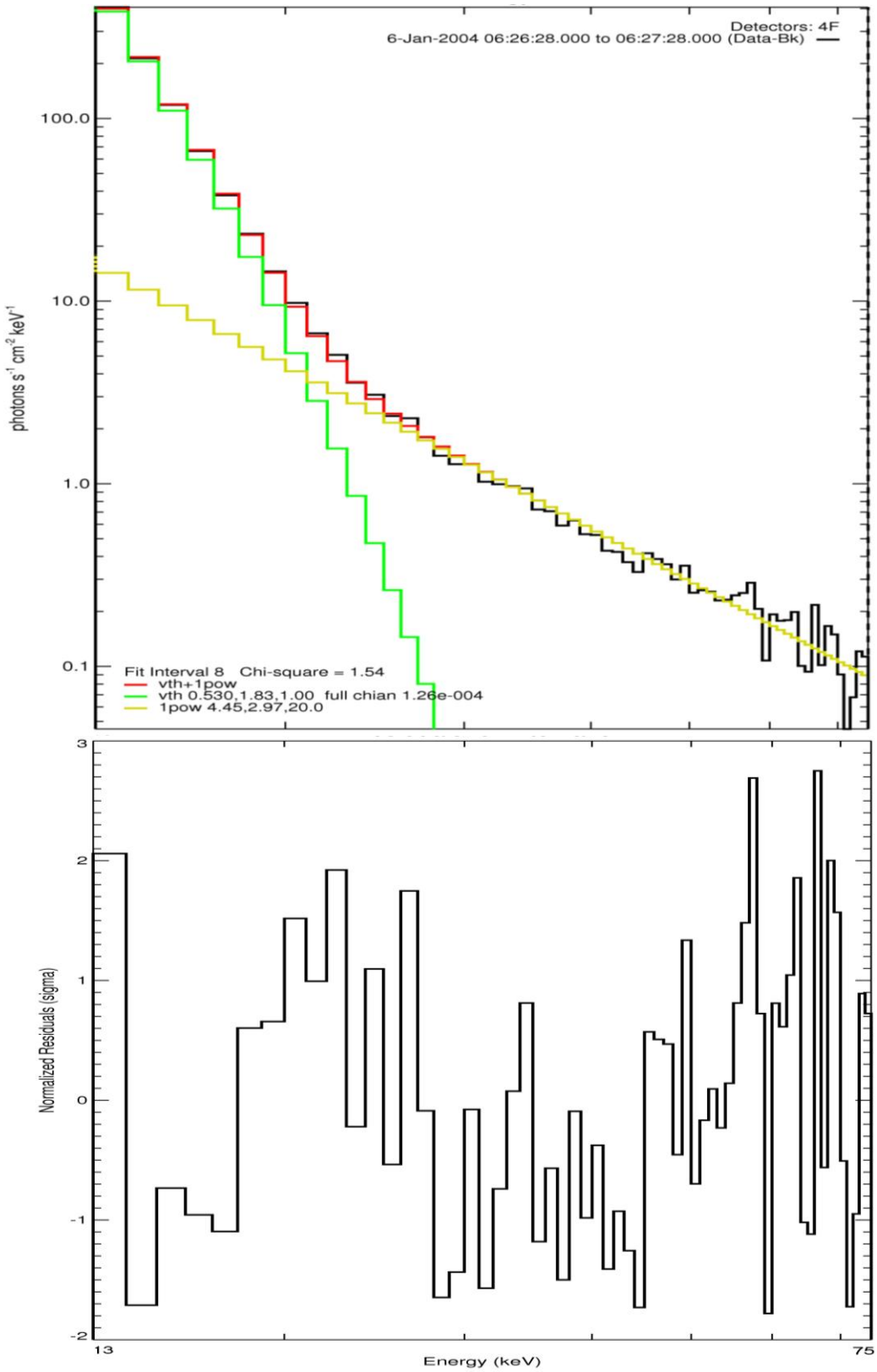

Figure 4.10: Photon spectrum (top) for 6-January-2004 flare event (RHESSI) with model fits. Normalized residuals (bottom) for each energy bin.

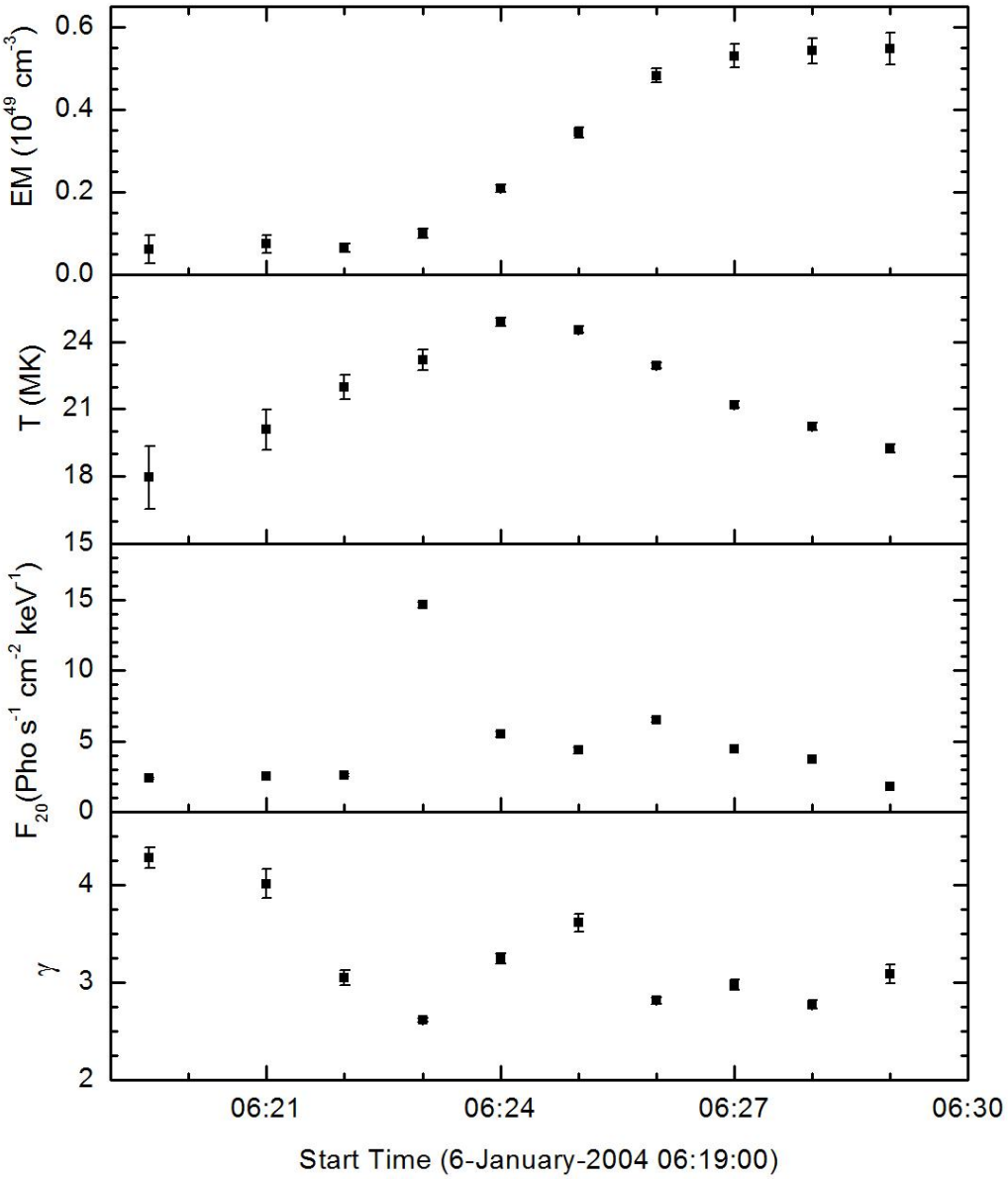

Figure 4.11: Time history of the fit parameters of 6 January 2004 solar flare observed by detector 4F (RHESSI). From top to bottom: (1) isothermal emission measure EM; (2) Temperature T of the isothermal component; (3) Photon flux at 20 keV (F_{20}) and (4) negative power-law index γ. Error bars are as reported by OSPEX showing the limits.

4.4 Spectral Analysis of other flares:

In order to study the spectro-temporal evolution in solar flares, I analyzed the time series spectra of 9 other M class flares observed by SOXS and RHESSI simultaneously as well as 3 C class flares observed by SOXS only (*cf*. Table 4.1). For each selected flare, forward modeling spectral analysis was performed with OSPEX as described earlier in Section 4.3. Spectral fits were performed for all these flares for different time intervals over the flare duration.

The flares observed by SOXS were analyzed in the 4.1-24 keV energy range. As described earlier the epivot is considered to be 12 keV for all the flares observed by SOXS. The spectral fitting of the same flares observed by RHESSI was done in 13-100 keV energy range. During the spectral fitting for all the flares observed by RHESSI in this chapter, epivot is considered to be 20 keV. While performing RHESSI spectral fits, any time interval which was observed in two attenuator states was ignored, to prevent mixed state observations, where the detector response matrix is not well defined. Each of the spectral fit was performed manually to examine the consistency of results.

The light curve as well as temporal evolution of spectral parameters for all the above mentioned flares is shown in Figures 4.12 - 4.32.

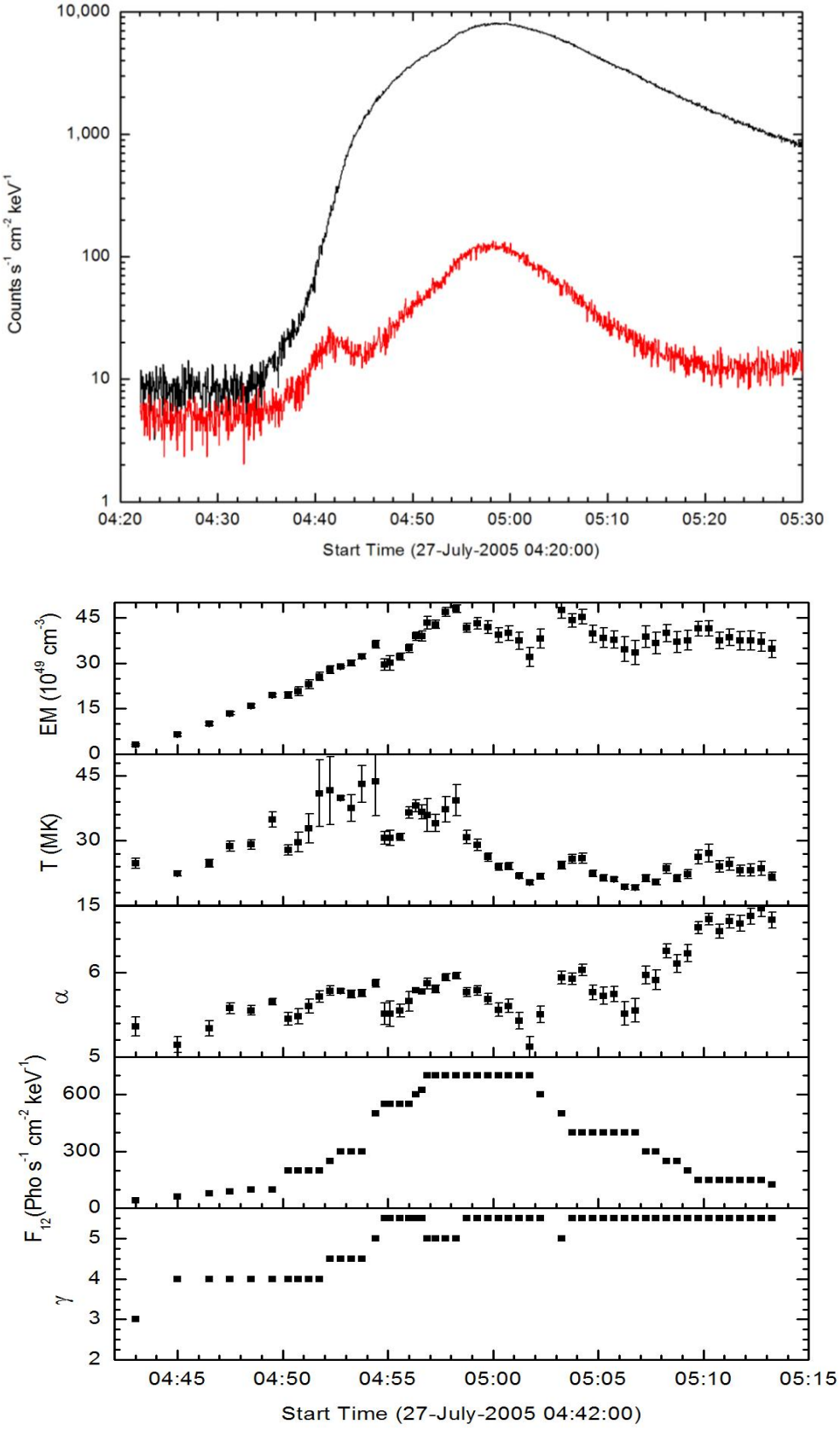

Figure 4.12: Light curve (top) and time history (bottom) of spectral parameters of 27-July-2005 flare (SOXS).

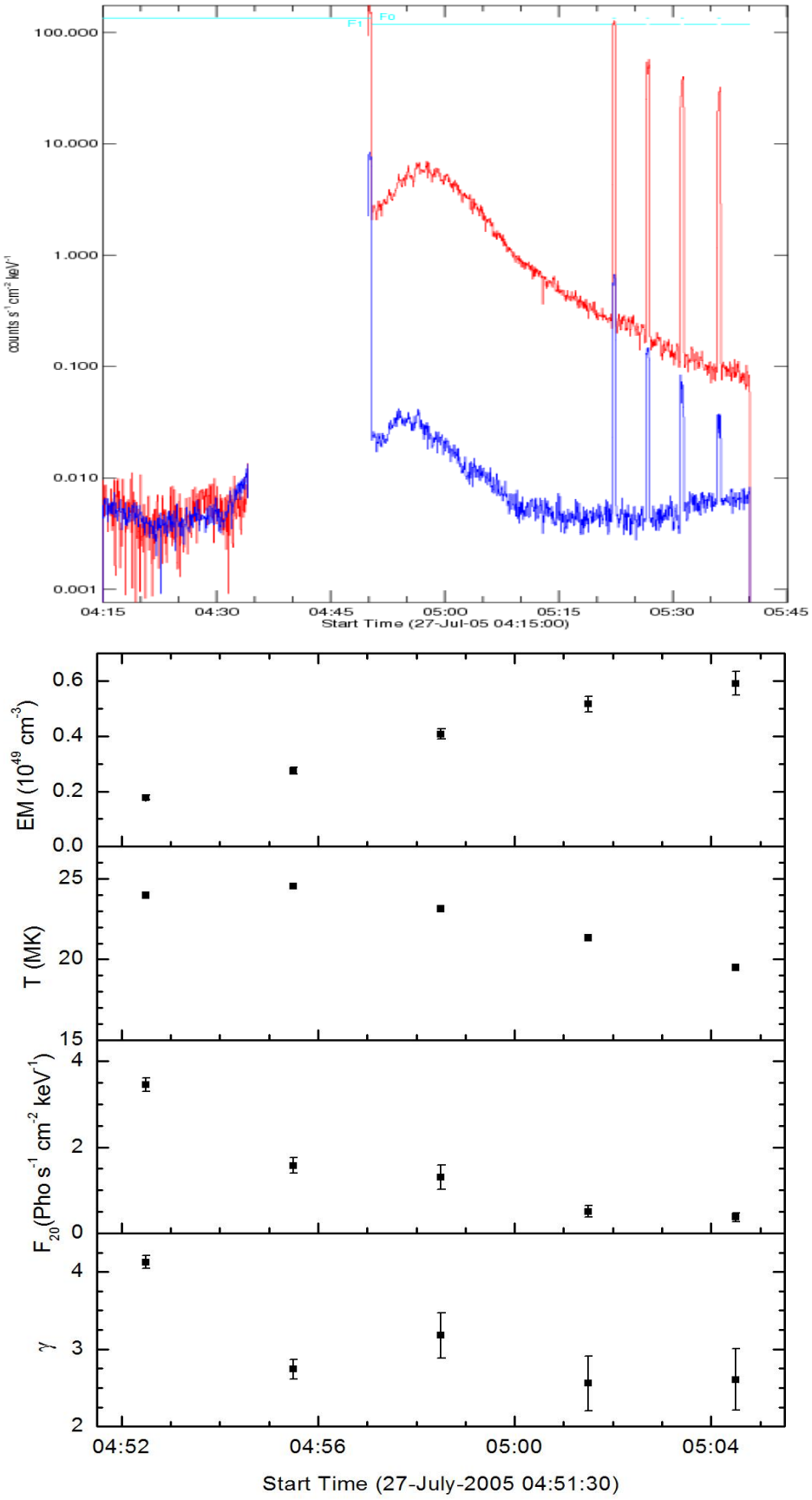

Figure 4.13: Light curve (top) and time history (bottom) of spectral parameters of 27-July-2005 flare (RHESSI).

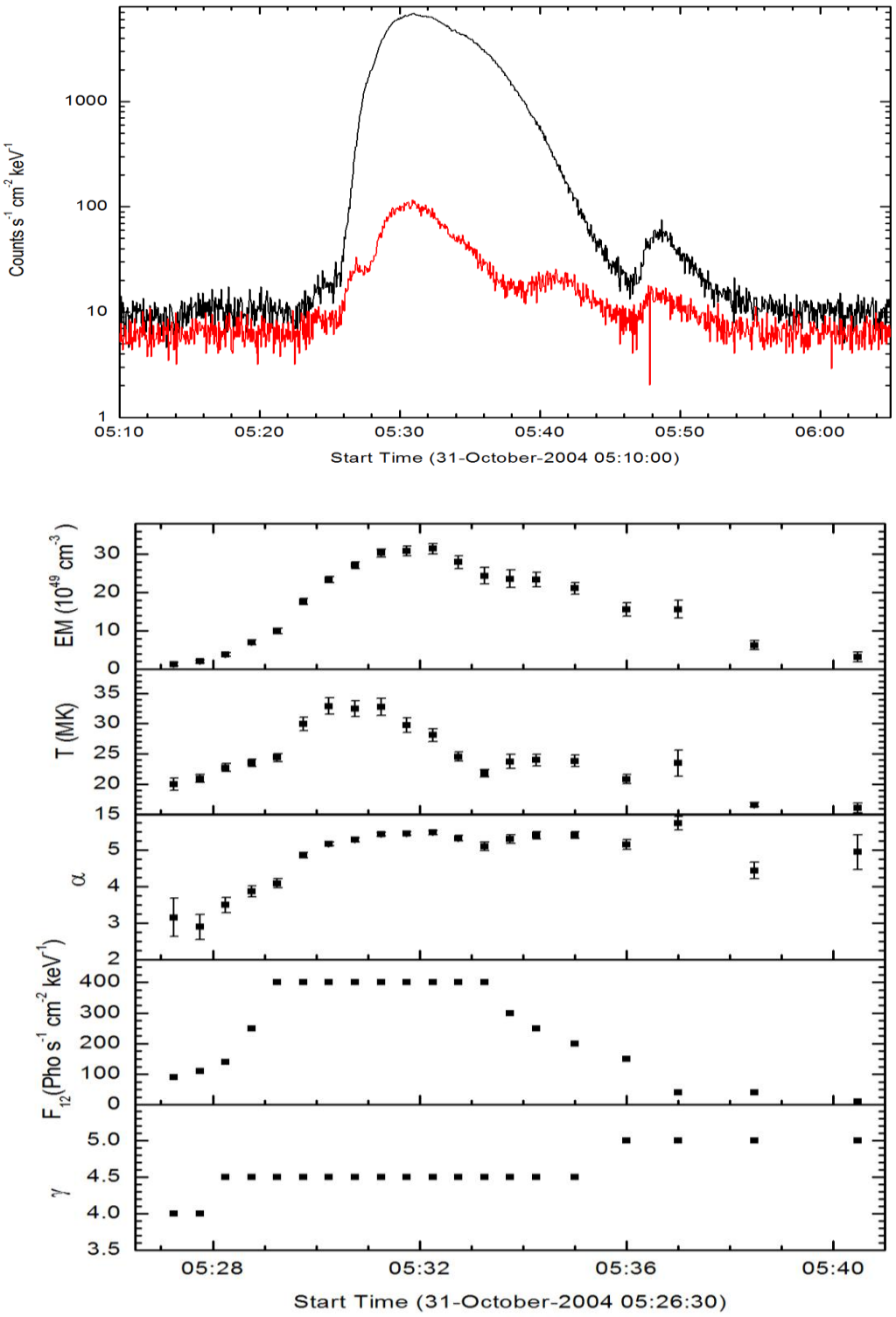

Figure 4.14: Light curve (top) and time history (bottom) of spectral parameters of 31-October-2005 flare (SOXS).

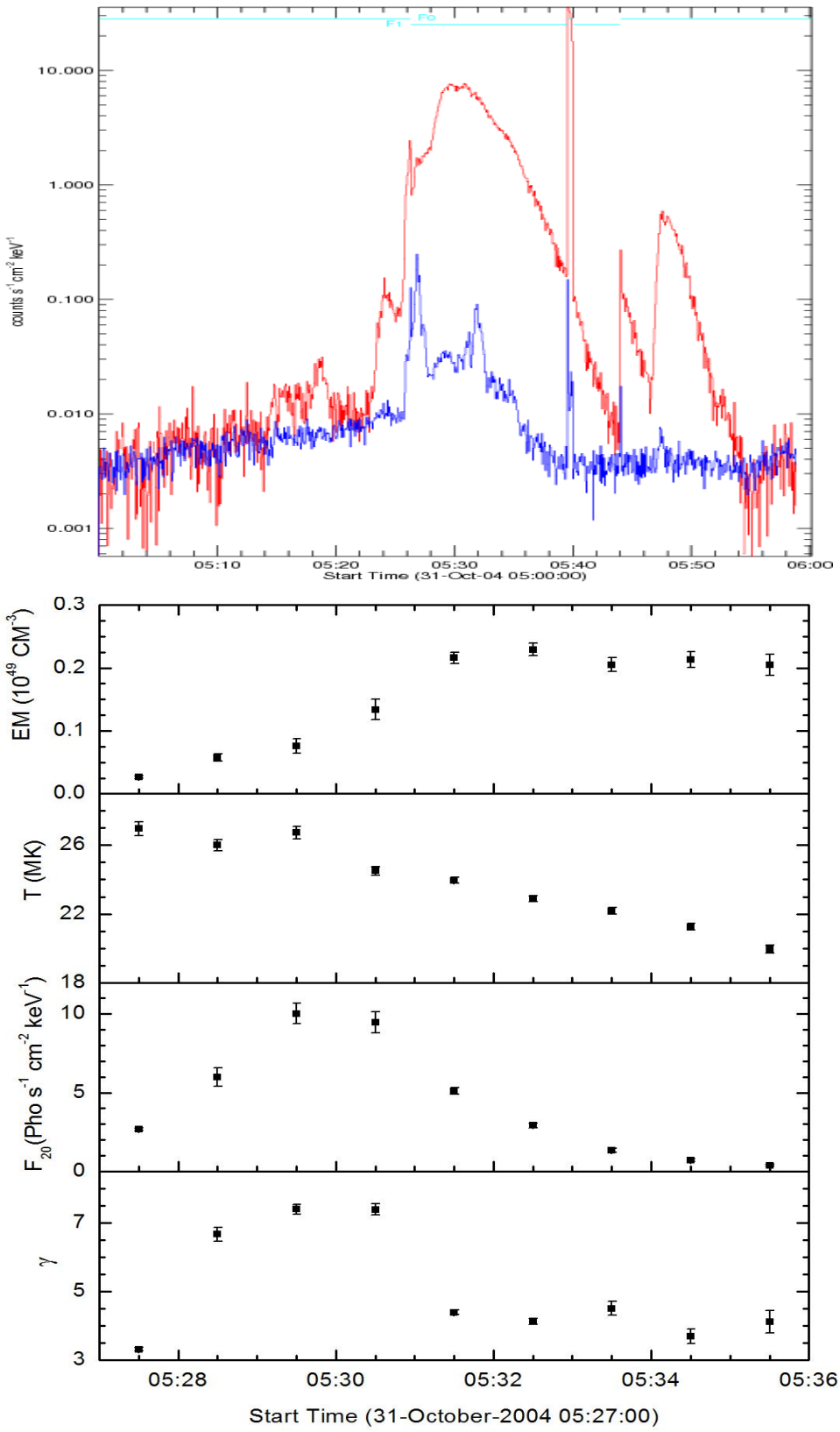

Figure 4.15: Light curve (top) and time history (bottom) of spectral parameters of 31-October-2004 flare (RHESSI).

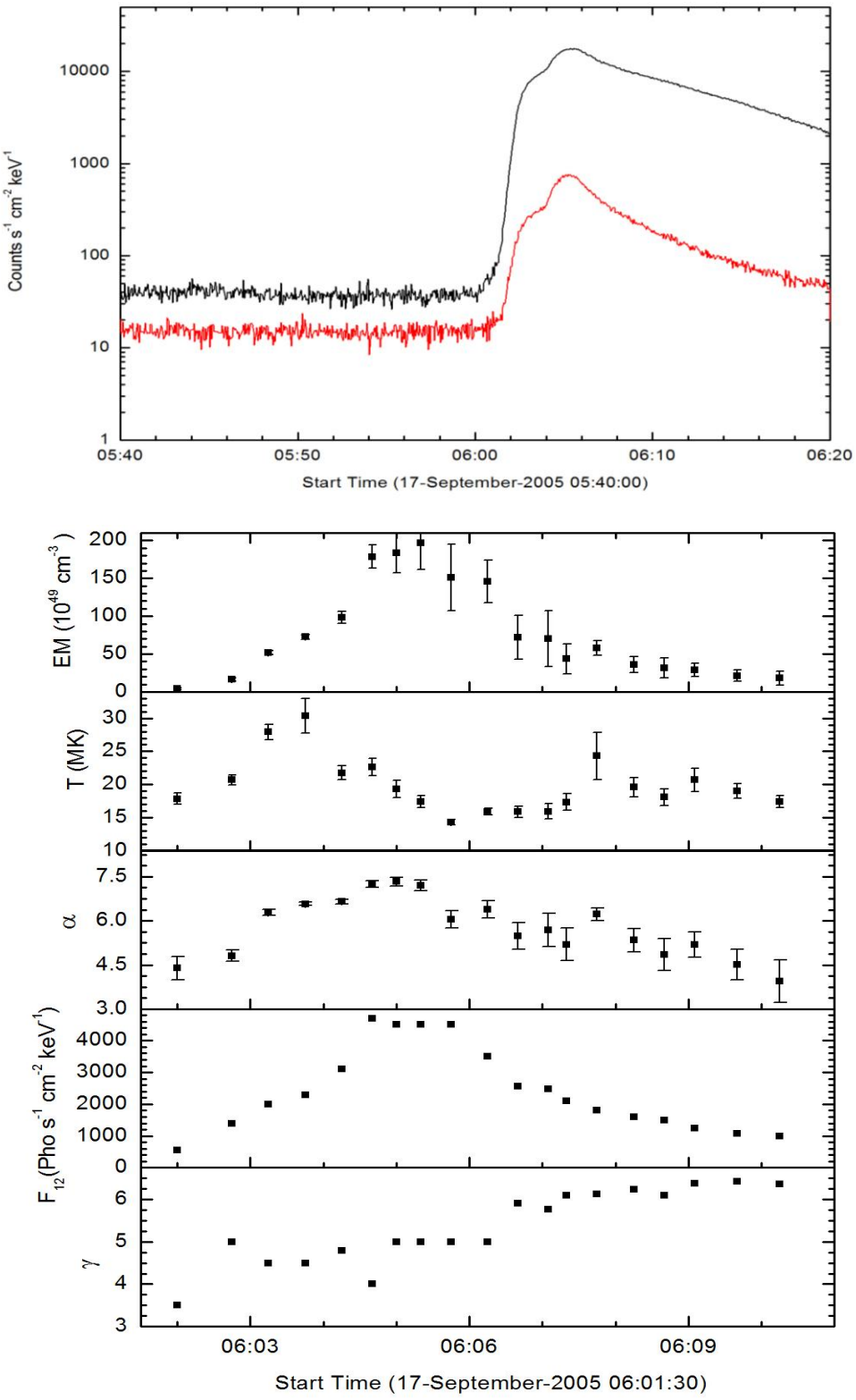

Figure 4.16: Light curve (top) and time history (bottom) of spectral parameters of 17-September-2005 flare (SOXS).

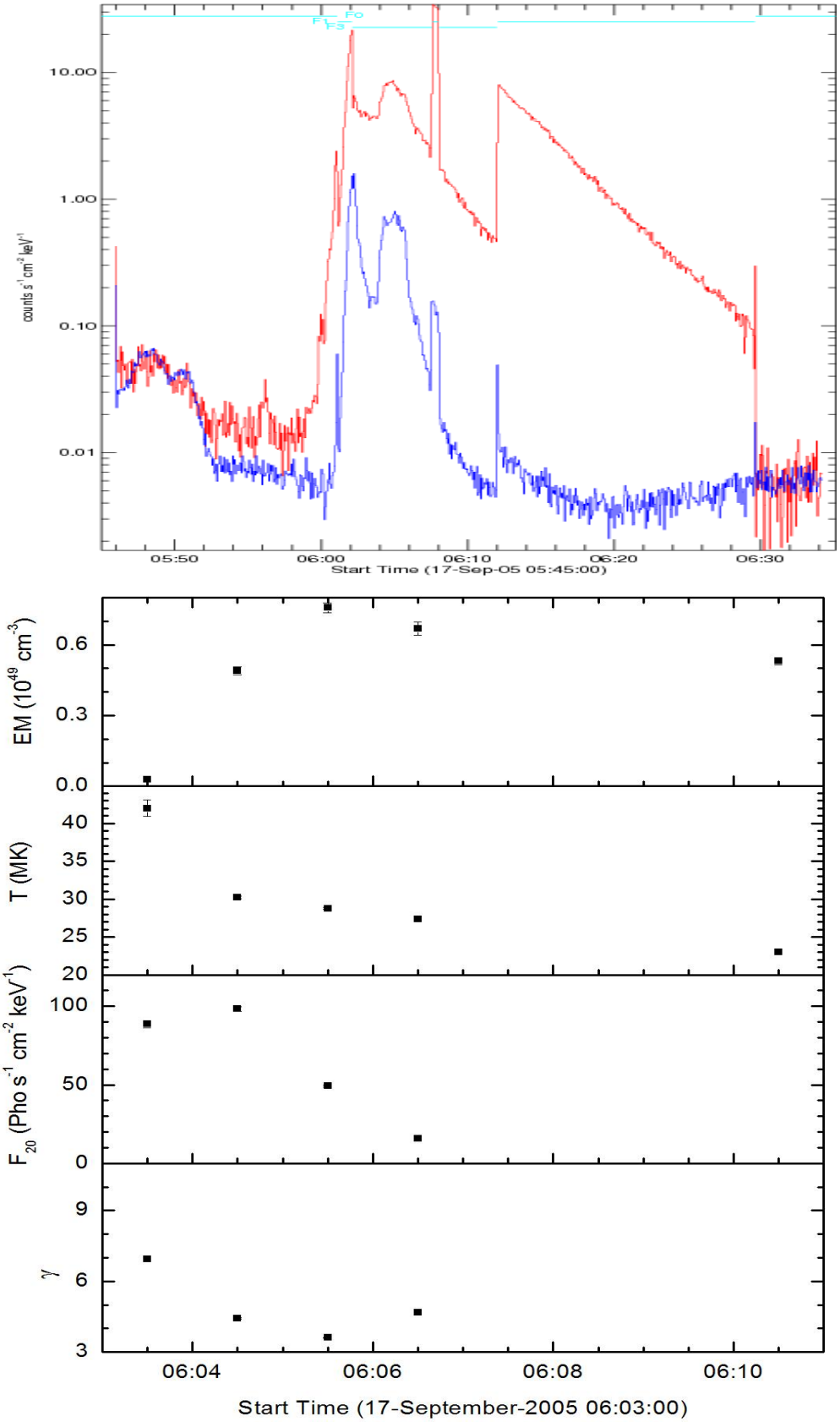

Figure 4.17: Light curve (top) and time history (bottom) of spectral parameters of 17-September-2005 flare (RHESSI).

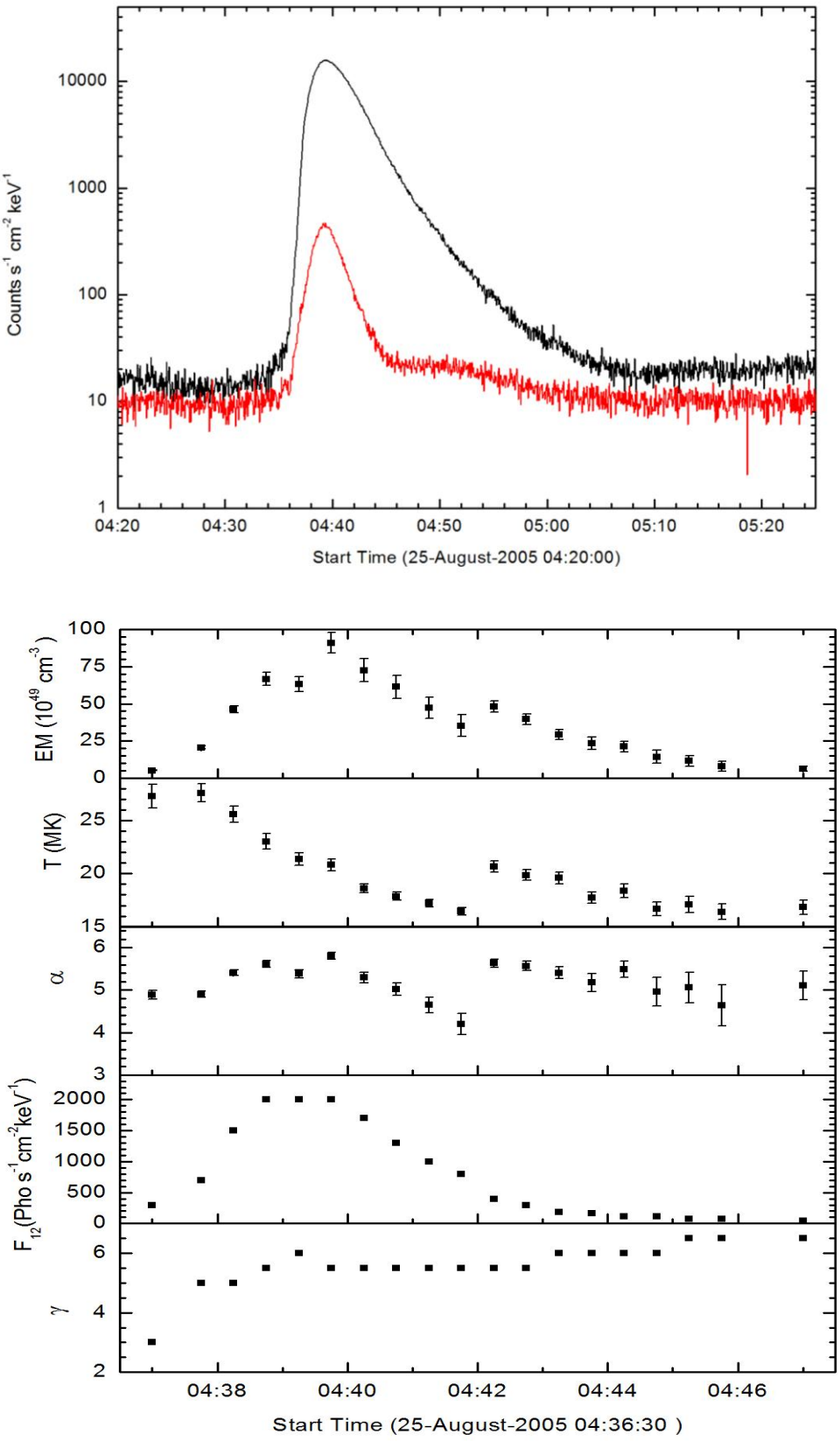

Figure 4.18: Light curve (top) and time history (bottom) of spectral parameters of 25-August-2005 flare (SOXS).

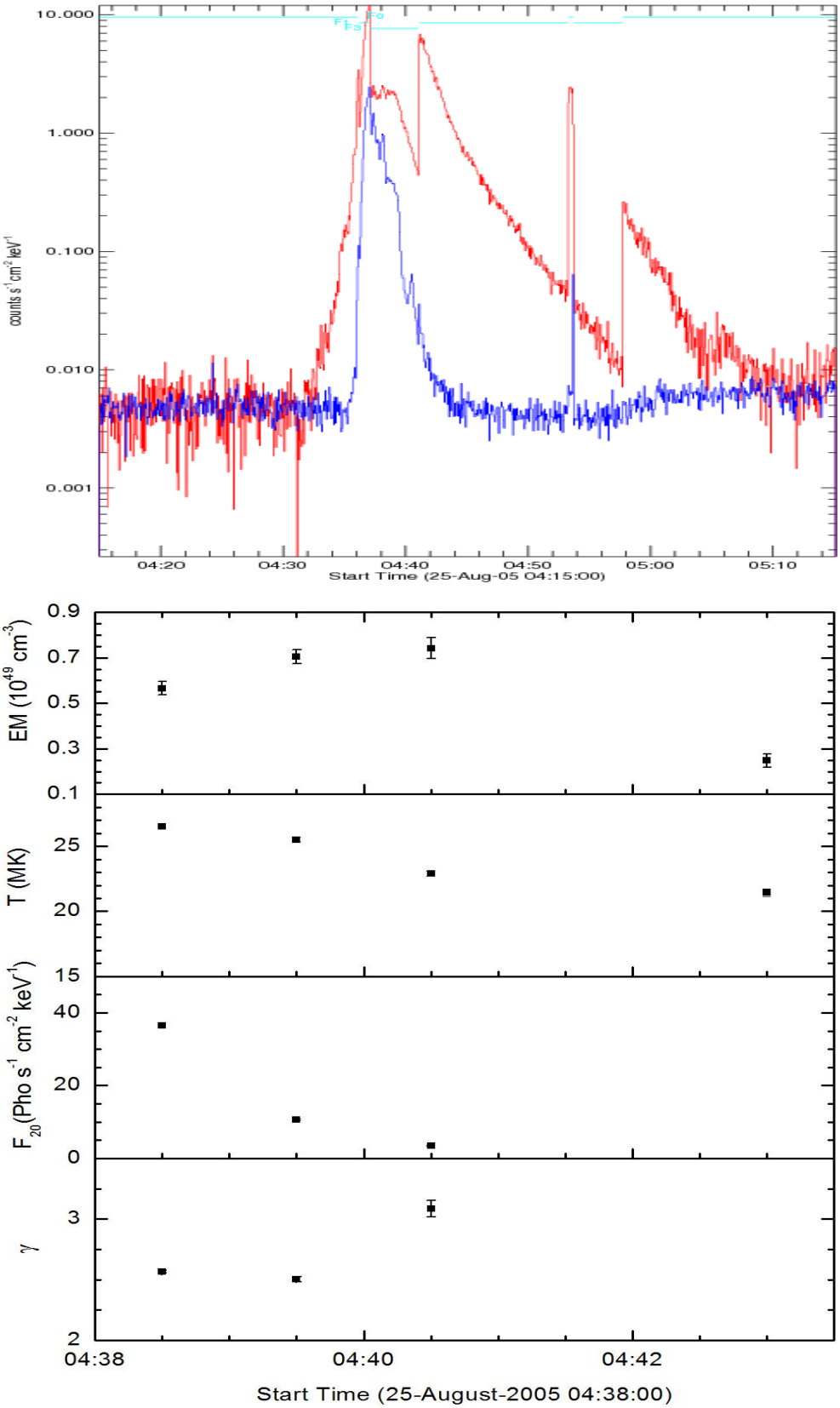

Figure 4.19: Light curve (top) and time history (bottom) of spectral parameters of 25-August-2005 flare (RHESSI).

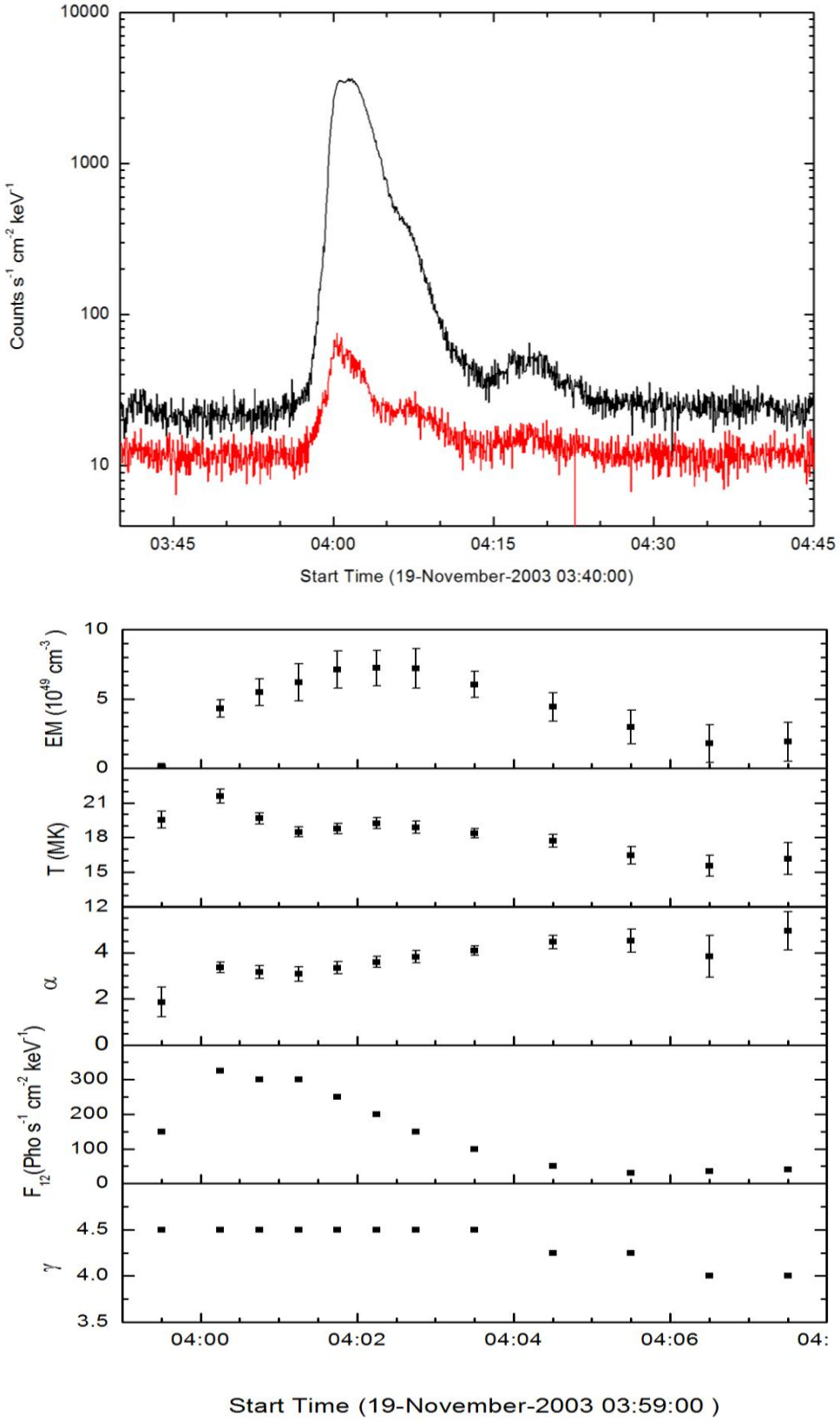

Figure 4.20: Light curve (top) and time history (bottom) of spectral parameters of 19-November-2003 flare (SOXS).

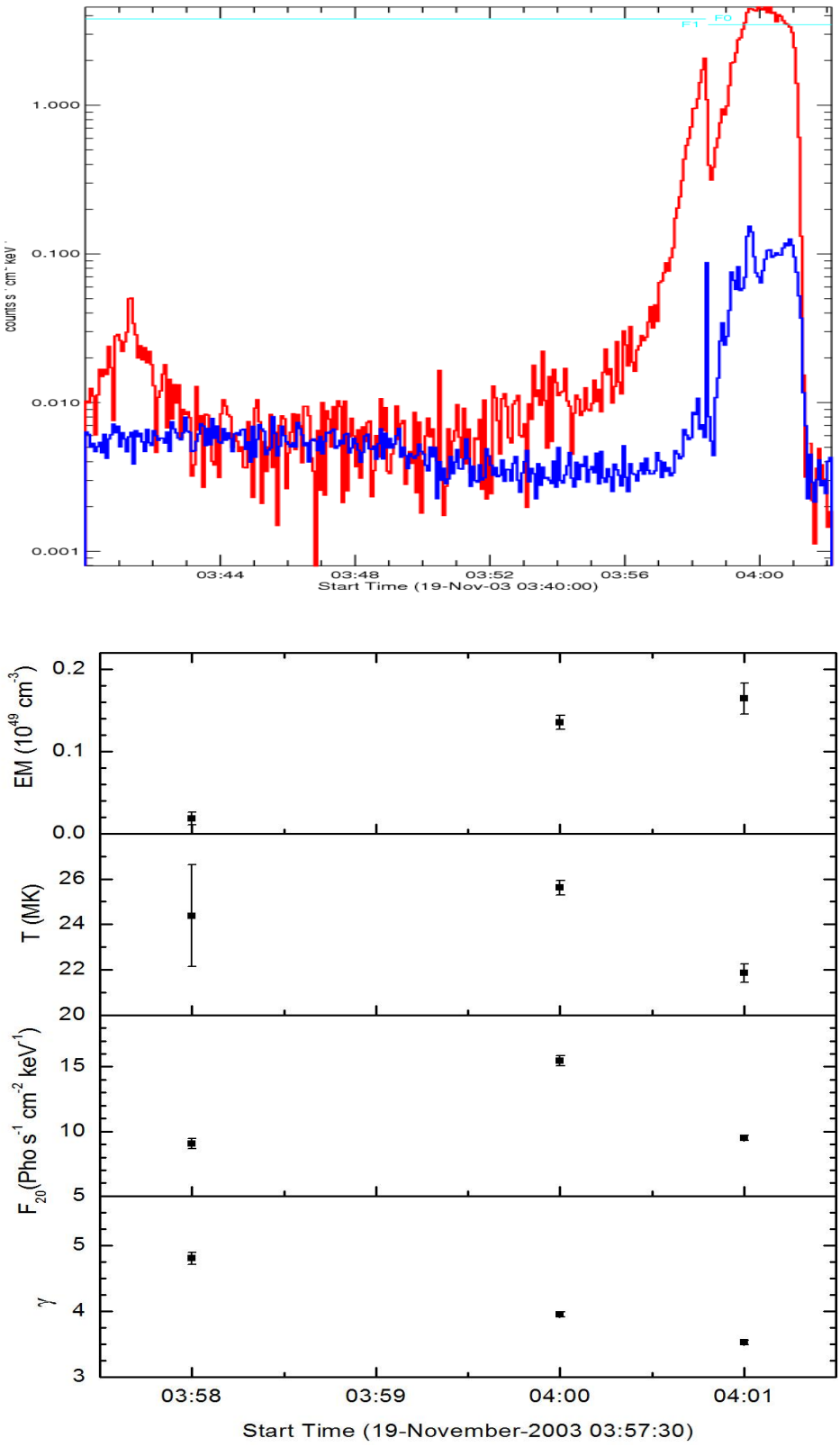

Figure 4.21: Light curve (top) and time history (bottom) of spectral parameters of19-November-2003 flare (RHESSI).

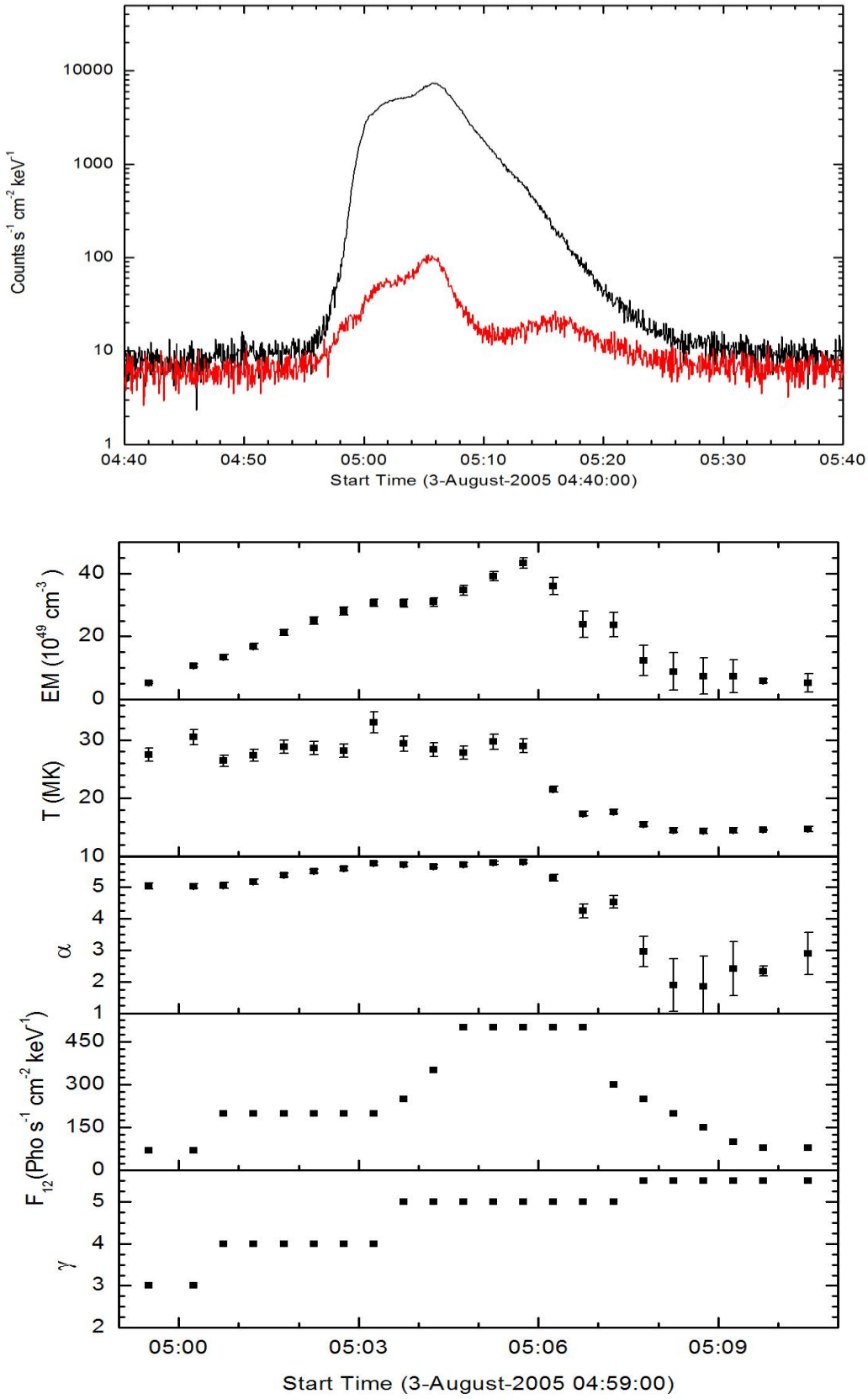

Figure 4.22: Light curve (top) and time history (bottom) of spectral parameters of 3-August-2005 flare (SOXS).

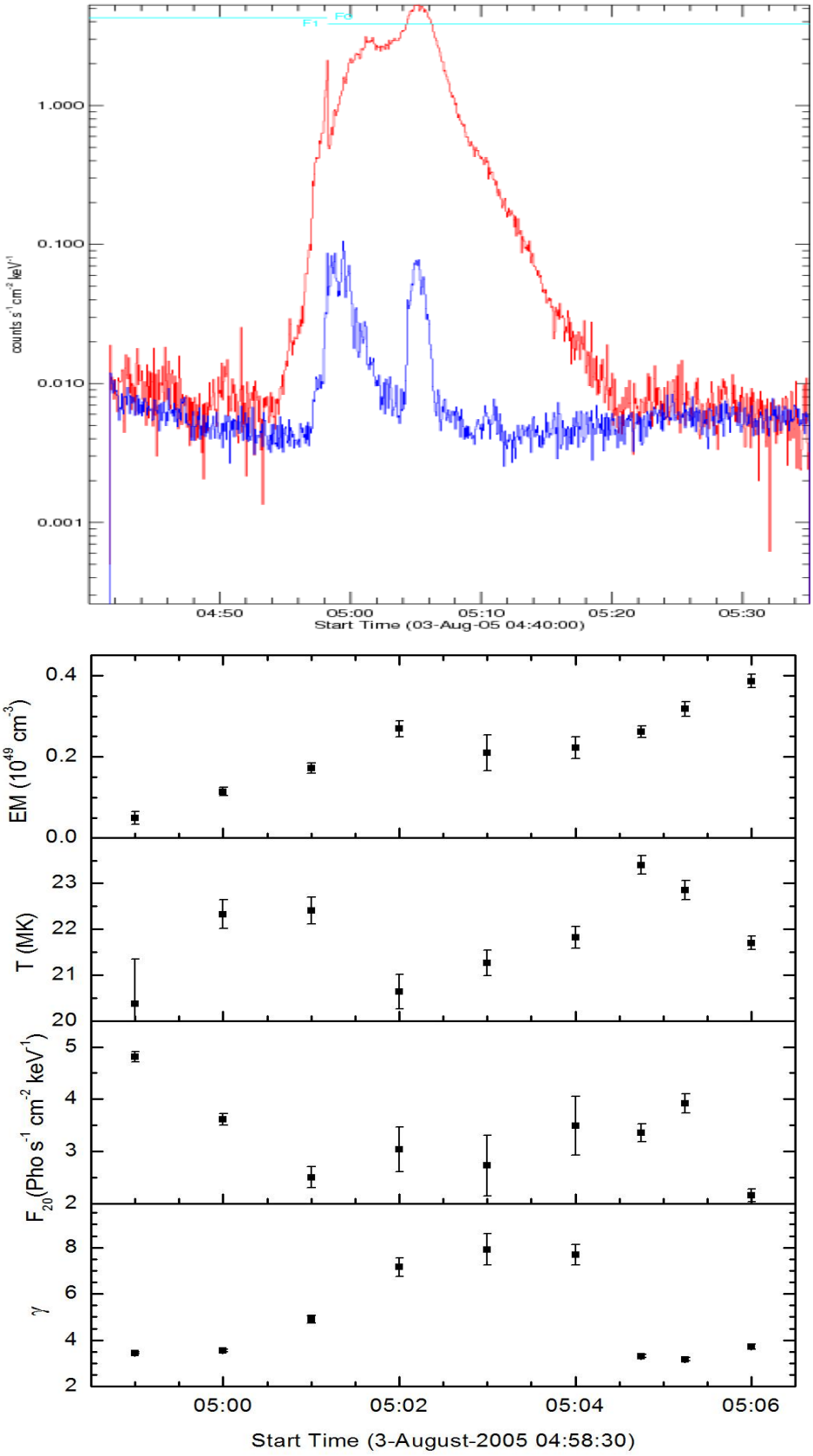

Figure 4.23: Light curve (top) and time history (bottom) of spectral parameters of 3-August-2005 flare (RHESSI).

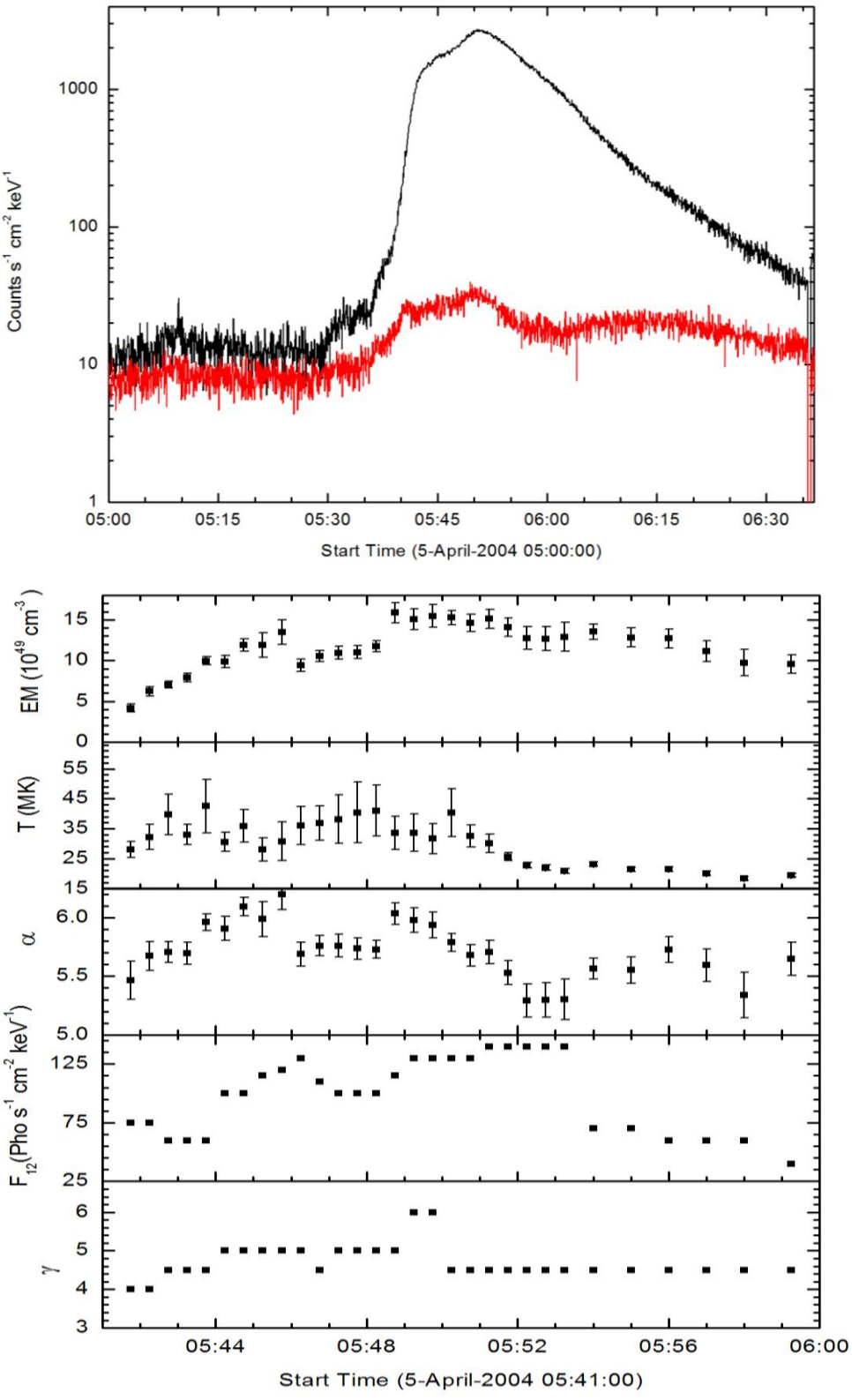

Figure 4.24: Light curve (top) and time history (bottom) of spectral parameters of 5-April-2004 flare (SOXS).

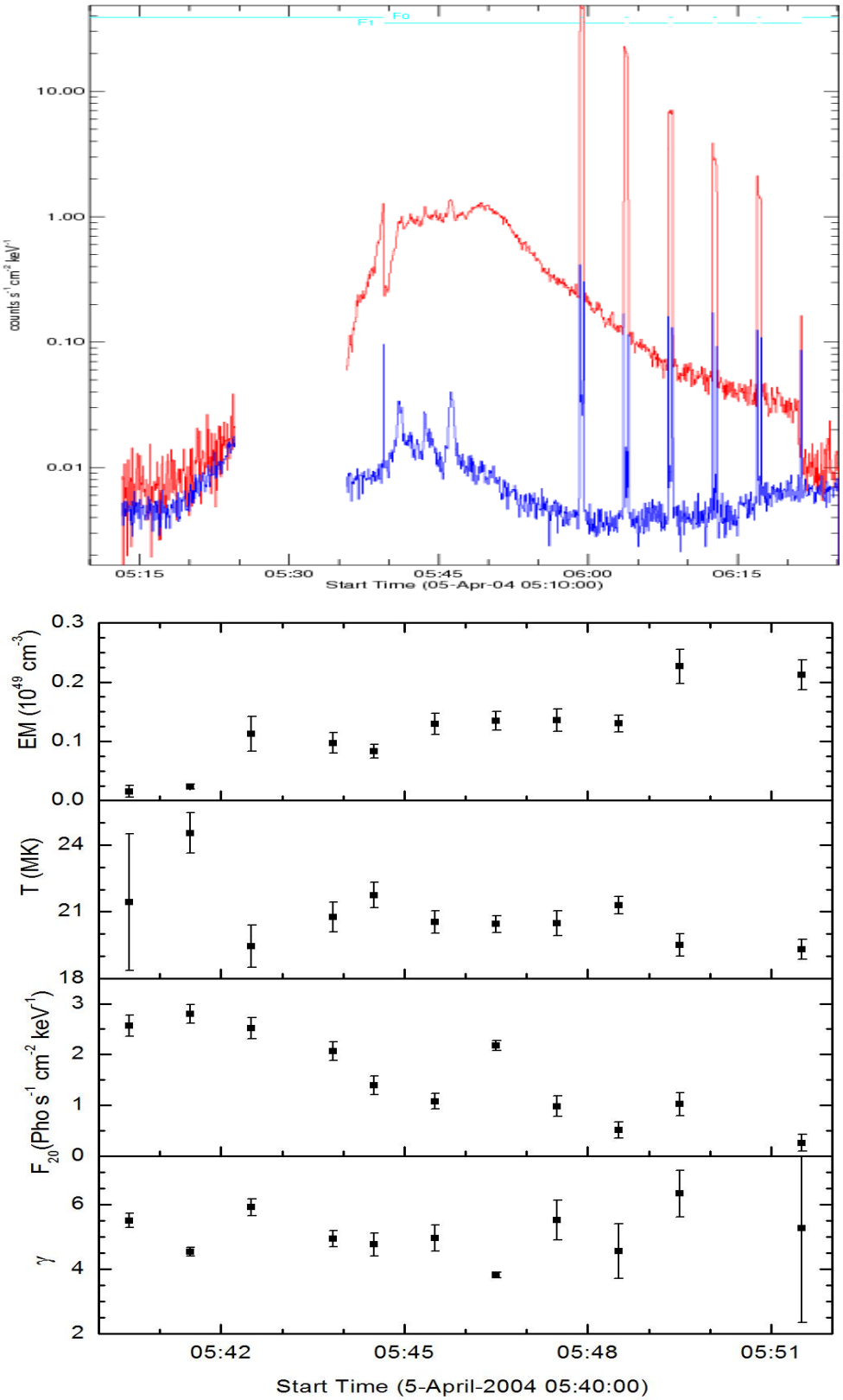

Figure 4.25: Light curve (top) and time history (bottom) of spectral parameters of 5-April-2004 flare (RHESSI).

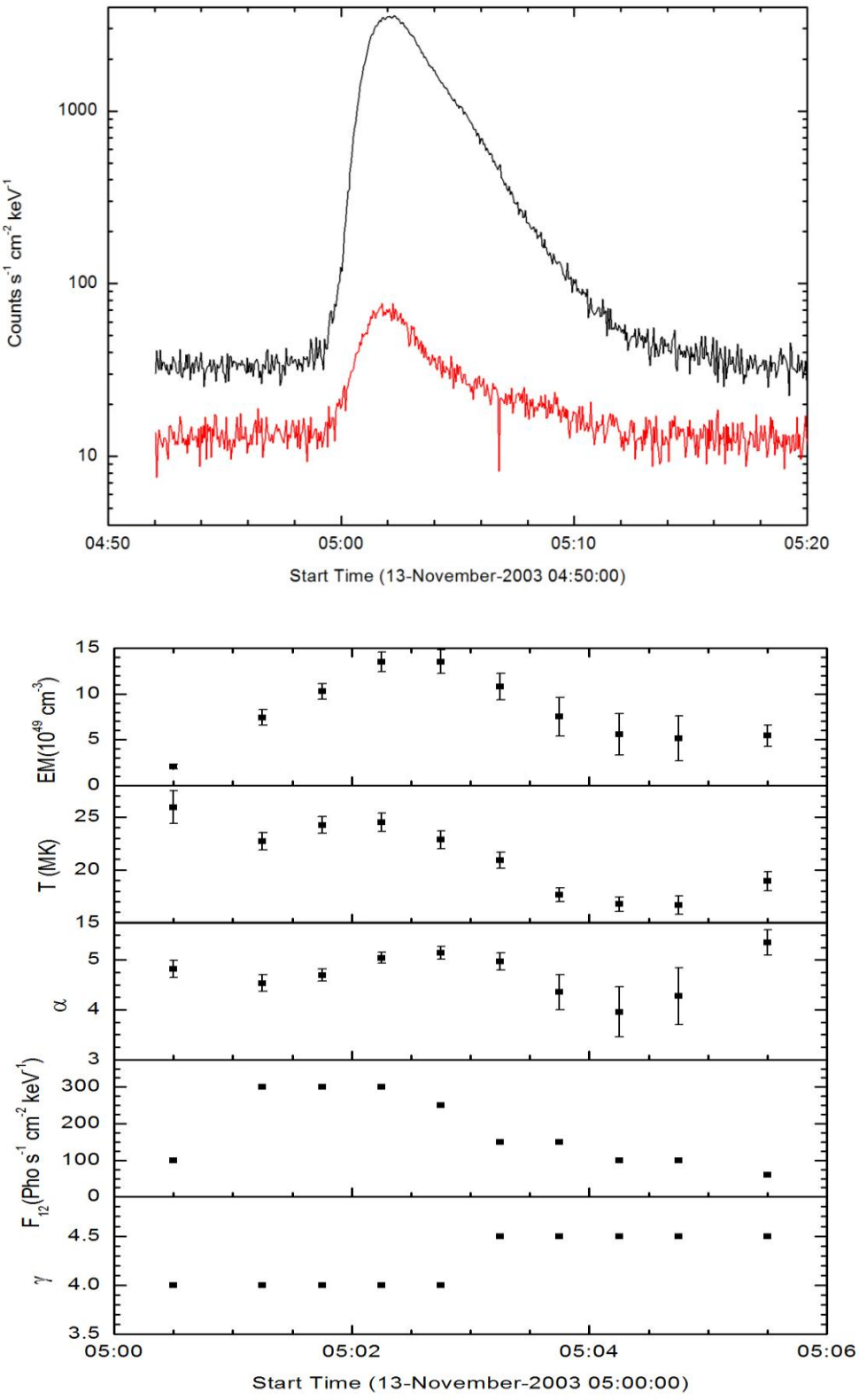

Figure 4.26: Light curve (top) and time history (bottom) of spectral parameters of 13-November-2003 flare (SOXS).

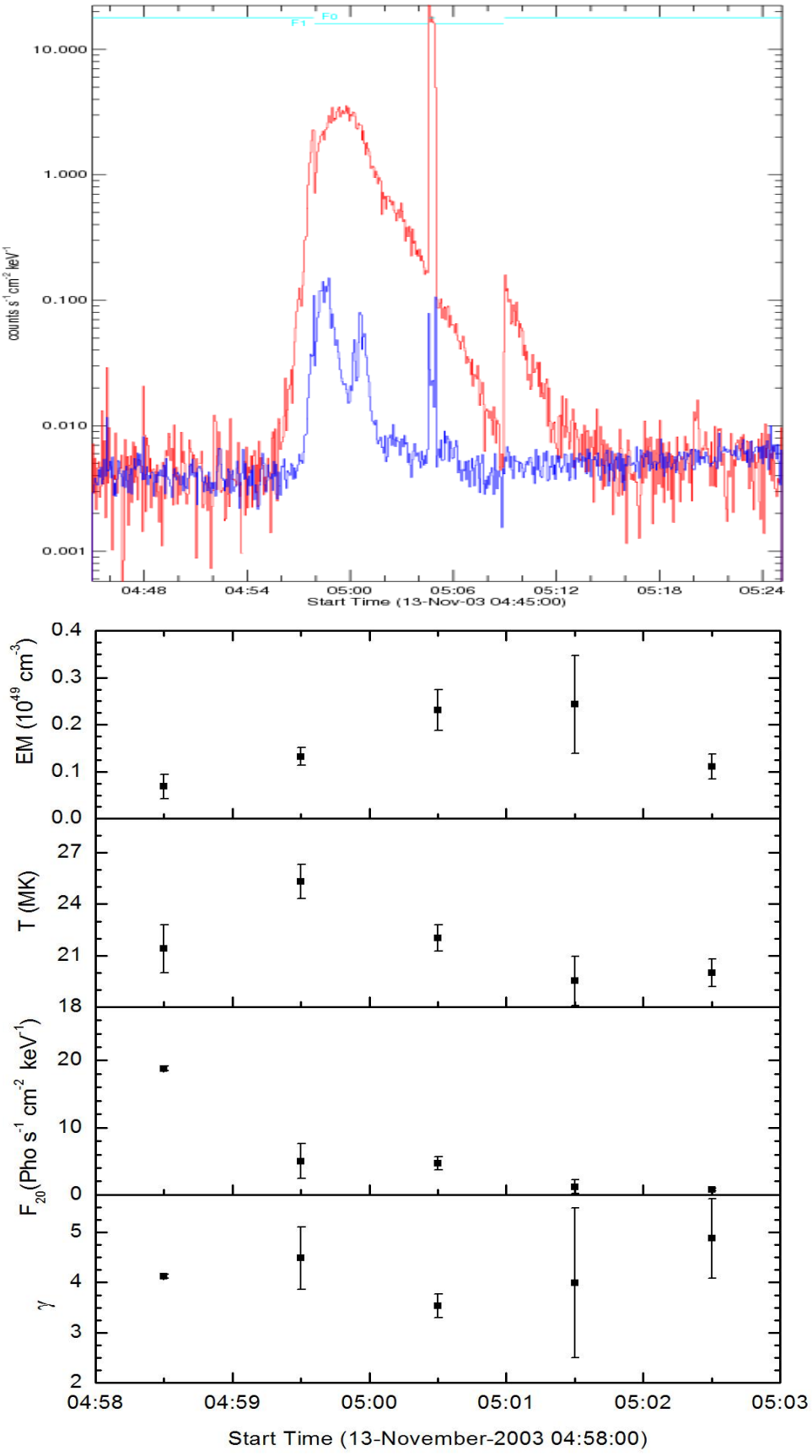

Figure 4.27: Light curve (top) and time history (bottom) of spectral parameters of 13-November-2003 flare (RHESSI).

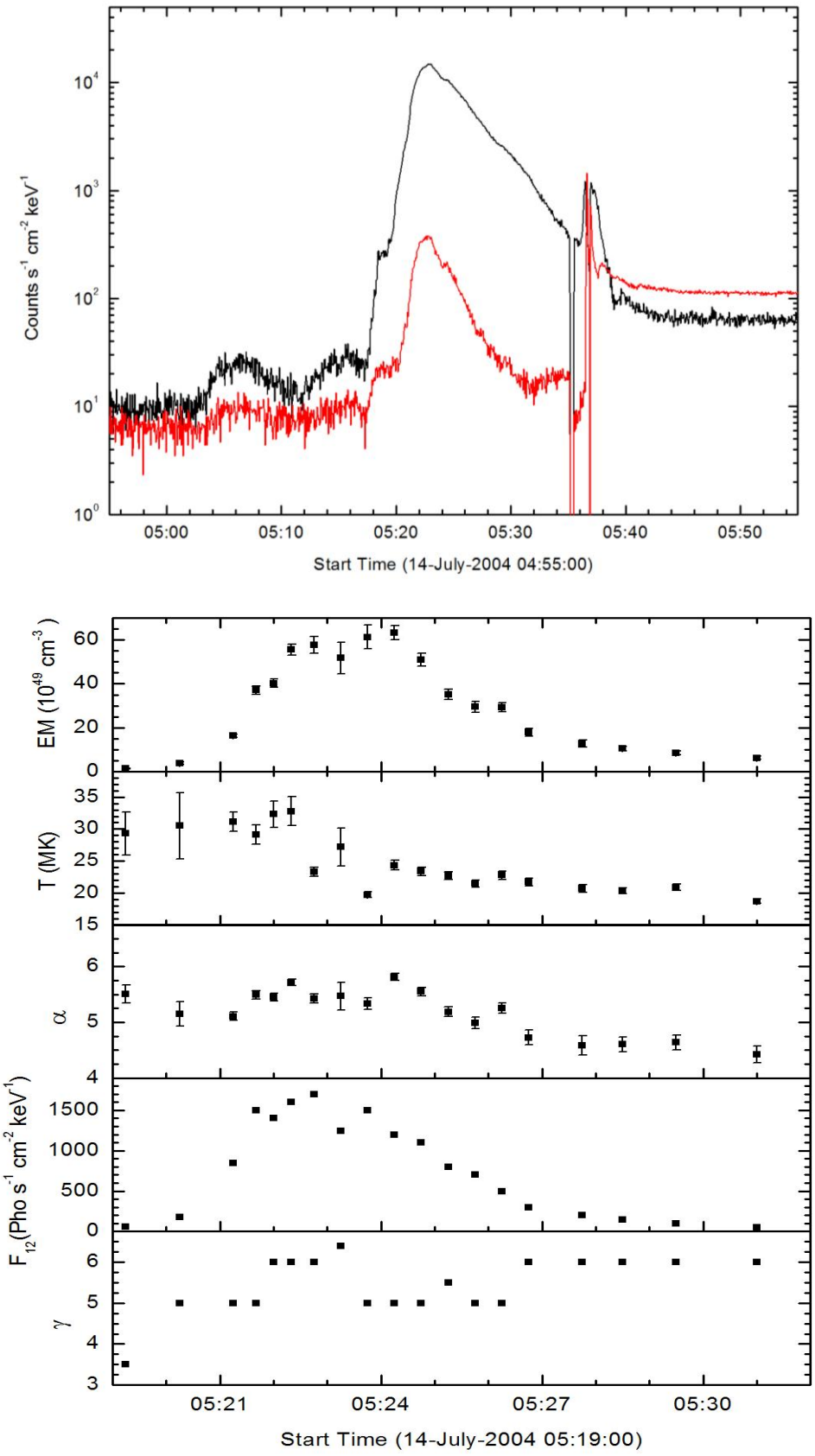

Figure 4.28: Light curve (top) and time history (bottom) of spectral parameters of 14-July-2004 flare (SOXS).

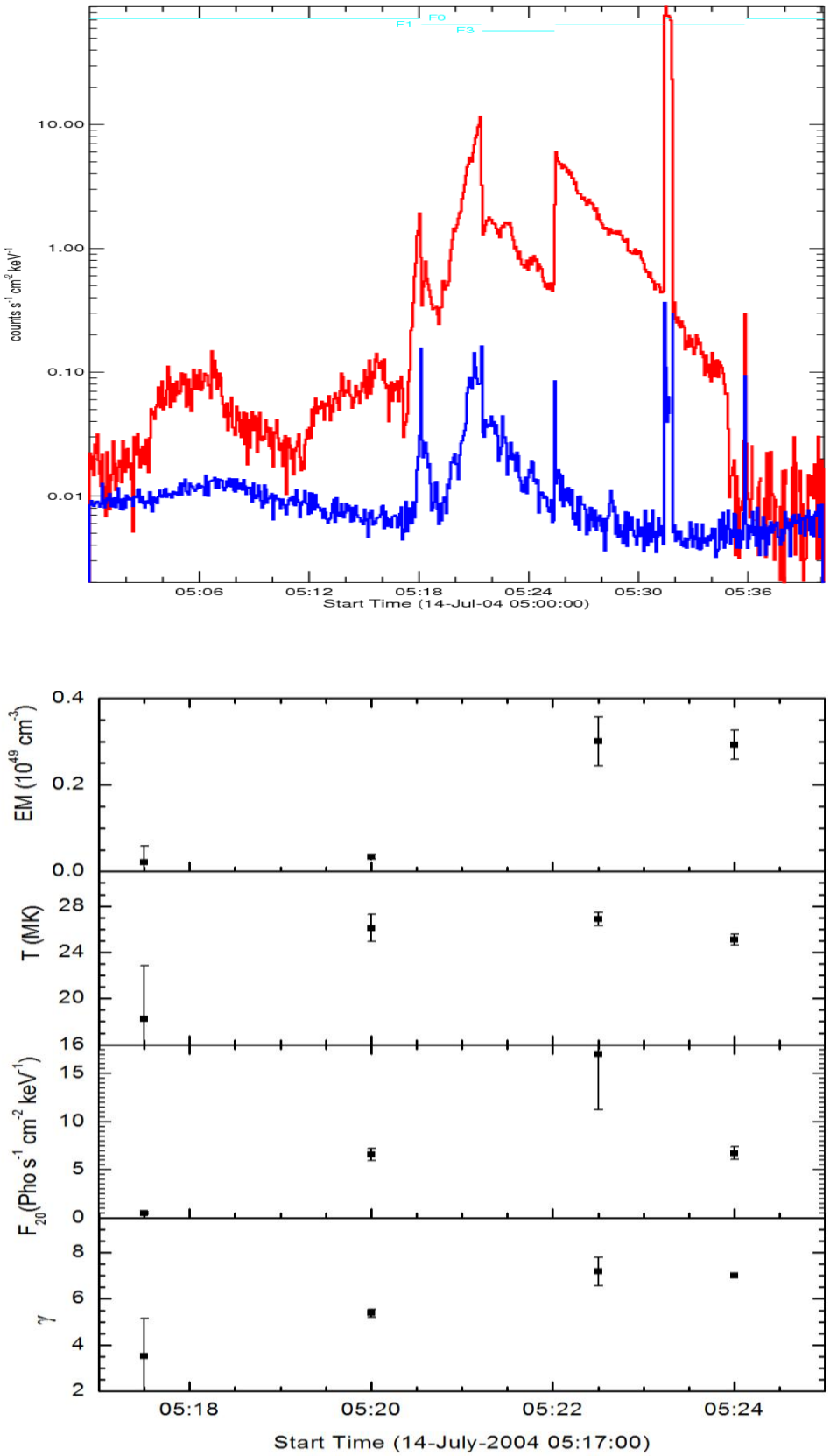

Figure 4.29: Light curve (top) and time history (bottom) of spectral parameters of 14-July-2004 flare (RHESSI).

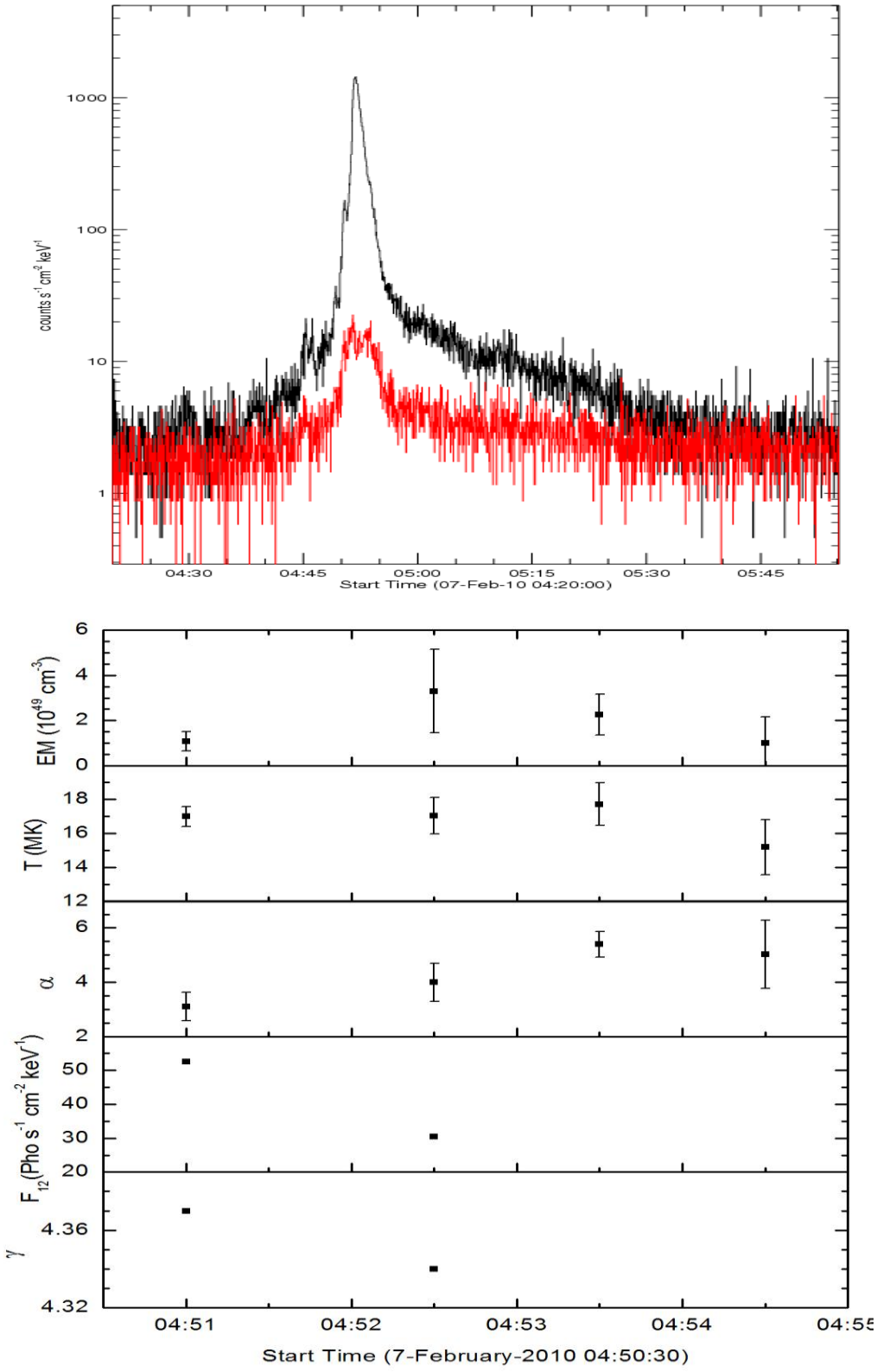

Figure 4.30: Light curve (top) and time history (bottom) of spectral parameters of 7-February-2010 flare (SOXS).

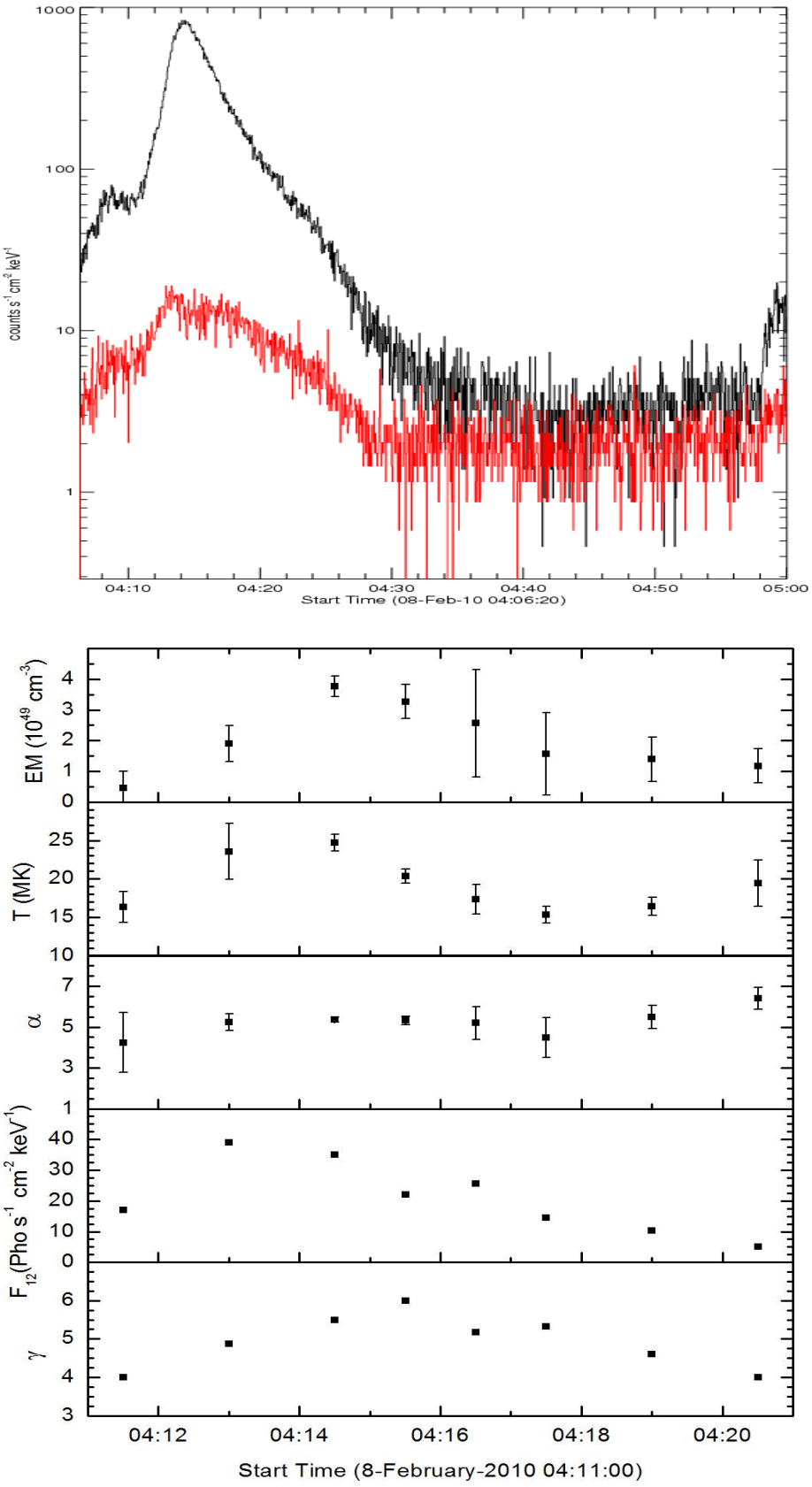

Figure 4.31: Light curve (top) and time history (bottom) of spectral parameters of 8-February-2010 (B04:06:20) flare (SOXS).

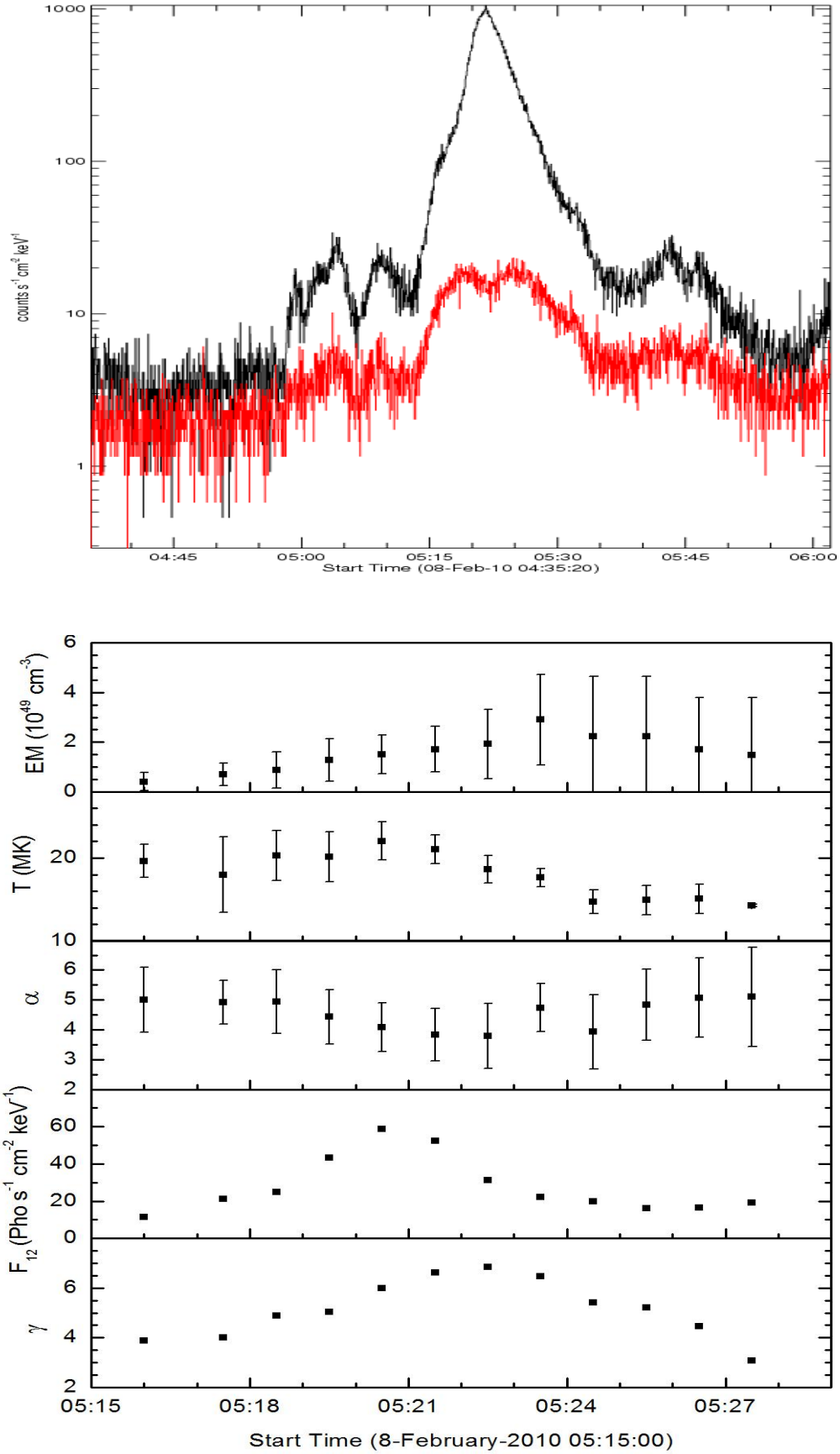

Figure 4.32: Light curve (top) and time history (bottom) of spectral parameters of 8-February-2010 (04:58:26) flare (SOXS).

All the spectral parameters obtained from figure (4.7) and from (4.11) to (4.32) are listed in Table (4.2) irrespective of the timescales. The spectral parameters are mentioned in the first column, the minimum value in the second column and the last column shows their maximum value.

Table 4.2

Range of Spectral parameters obtained from SOXS and RHESSI

Spectral Parameters	Minimum	Maximum
DEM (cm^{-3} keV^{-1}) (SOXS)	$(0.0018 \pm 0.0008) \times 10^{49}$	$(2.05 \pm 1.4) \times 10^{49}$
EM (cm^{-3}) (SOXS)	$(0.15 \pm 0.06) \times 10^{49}$	$(198 \pm 36) \times 10^{49}$
EM (cm^{-3})(RHESSI)	$(0.016 \pm 0.01) \times 10^{49}$	$(0.76 \pm 0.02) \times 10^{49}$
Temperature (MK) (SOXS)	14.3 ± 0.15	43.7 ± 7.9
Temperature (MK)(RHESSI)	18 ± 1.4	42 ± 1.1
α (SOXS)	1.85 ± 0.96	7.4 ± 0.14
F_{12} (photons s^{-1} cm^{-2} keV^{-1})	5	4700
F_{20} (photons s^{-1} cm^{-2} keV^{-1})	0.26 ± 0.17	49.3 ± 0.7
γ (12-24 keV) (SOXS)	3	7
γ (~ 20-100 keV) (RHESSI)	2.5 ± 0.02	7.9 ± 0.7

The range of spectral parameters obtained from the spectral fits from SOXS and RHESSI observations are useful to understand the physics of flare emission. It may be noted from Figures 4.7 and 4.11 to 4.32 that the temperature usually peaks before the emission measure. The emission measure is a measure of electron density (number density) in a flare volume. It is also used to derive the characteristic length scale of the emitting plasma.

DEM gives the emitting power within a given temperature range. The noticeable variation in the values of multi-thermal differential emission measure (*cf*. Table 4.2) clearly suggests that the existence of flare loops of varying size during the whole interval of the flare. This also indicates the multi-temperature existence in flare emission indicating that the flare plasma may be treated as multi-thermal.

I found that the evolution of the temperature in all flares (Figures 4.7 and 4.11 to 4.32) is almost similar to the light curve of the flare, and it peaks around the peak time of the flare. This indicates that flare X-ray photon emission is rather strongly governed by the temperature of the plasma. The SOXS and RHESSI temperatures indicate that the temperatures during the initial phase of M class flares are ~ 14 to 18 MK. The temperature of the hot plasma in the coronal loops sometimes reaches to a super-hot component (~ 40 MK) around the peak time of the flare. The temperature > 40 MK was observed for 27 July 2005 and 5 April 2004 flares from SOXS observations while RHESSI observations show a > 40 MK temperature for 17-September-2005 flare. These high temperatures confirm an existence of super-hot component in M-class solar flares. The multi-thermal temperature derived for 13 flares from SOXS data ranges between 14.3 ± 0.15 MK to 43.7 ± 7.9 MK. On the other hand, isothermal temperature for the selected ten flares observed by RHESSI varies between 18 ± 1.4 MK to 42 ± 1.1 MK, almost close to multi-thermal temperature measured from SOXS data. Based on the spectro-temporal evolution of the flares, I found that the thermal emission in the energy range of about 4.1 – 30 MK is dominated by temperature range of about 14 to 50 MK.

The DEM is a power-law function of temperature with the values of the spectral index α varying approximately between 2 to 7. The lower limit suggests that the thermal component in flare may exceed to traditional energy limit of ~ 20 keV. Evolution of flux follows evolution in temperature in most flares which shows that the flare is dominated by thermal emission mechanism and thus conductive cooling concept during rise phase appears to be valid.

4.5 Estimation of Thermal and Non-thermal Energy:

In the standard model of the solar flares a major part of the energy is first released into energetic non-thermal electrons and ions, which are guided by the magnetic field lines and may get lost into the interplanetary space. However, they also get precipitated into the lower corona and upper chromosphere where they loose their energy by coulomb collisions with the denser medium. This energy is believed to heat up the ambient plasma to tens of MK temperature, which will, therefore, rise and fill the coronal loops. The high temperature plasma will emit soft X-ray emission. Now, an ultimate and interesting question arises: What is the relation between non-thermal and thermal energies? The difference between them can indicate conversion losses and/ or other forms of primary energy release. However, objective of the following section is to address the long enduring question: How does total kinetic energy of electrons that precipitate compare to thermal energy of the plasma?

4.5.1 Estimation of Thermal Energy:

After tracking the evolution of temperature and emission measure for all the selected flares, I am aiming to compute the thermal energy content for these flares. The temporal evolution of thermal energy is computed for all flares under consideration from SOXS and RHESSI observations with the application of following formula.

$$E_{th} = 3 n_e k_B T V \qquad \text{(erg)} \qquad (4.2)$$

Assuming the uniform electron number density n_e over volume V, the volume emission measure

$$Q = n_e^2 V$$

$$E_{th} = 3 n_e k_B T \frac{EM}{n_e^2} = 3 k_B T \frac{EM}{n_e} \qquad \text{(erg)} \qquad (4.3)$$

where k_B = Boltzmann constant = 1.38 x 10^{-16} erg K^{-1}. The electron number density is assumed to be n_e = 10^{11} cm^{-3} for M-class flares. The values of temperature and emission measure are obtained from the spectral fits.

Figures 4.33 to 4.45 show the evolution of thermal energies of all the analyzed flares.

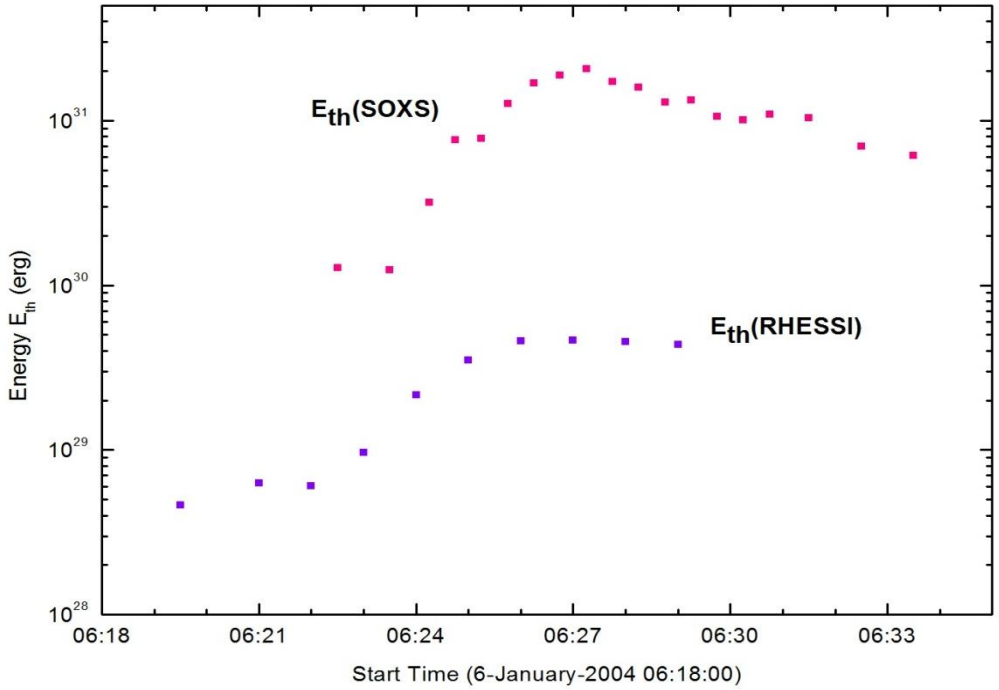

Figure 4.33: Thermal energy release as a function of time in 6-January-2004 flare event observed by SOXS and RHESSI.

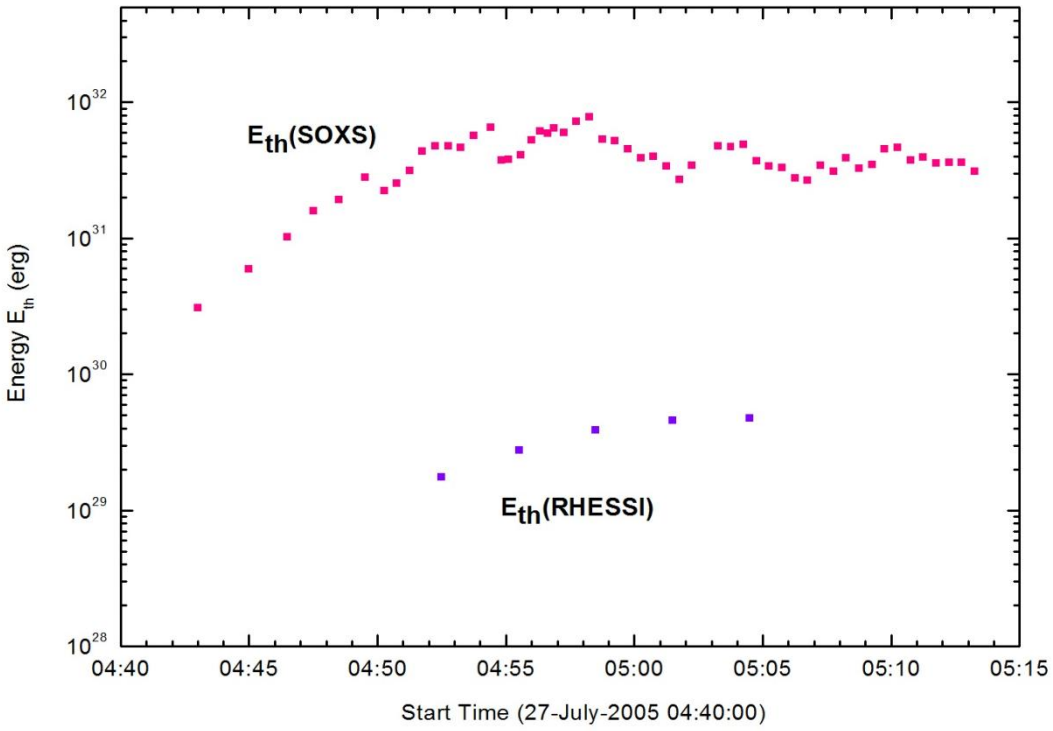

Figure 4.34: Thermal energy release as a function of time in 27-July-2005 flare event observed by SOXS and RHESSI.

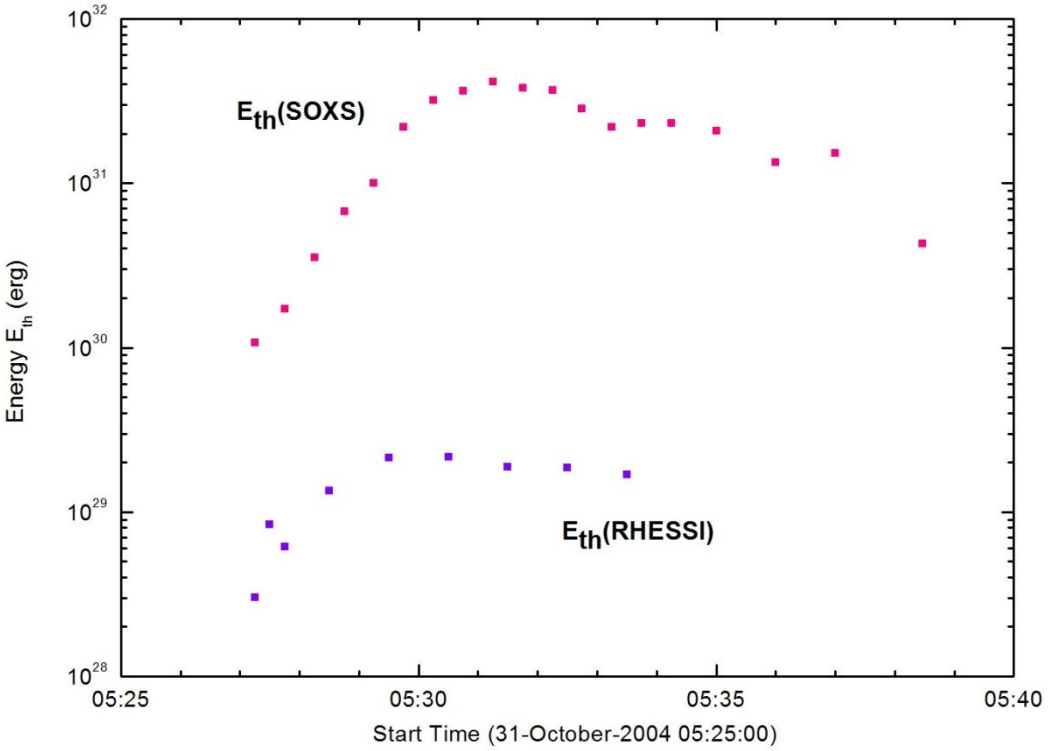

Figure 4.35: Thermal energy release as a function of time in 31-October-2004 flare event observed by SOXS and RHESSI.

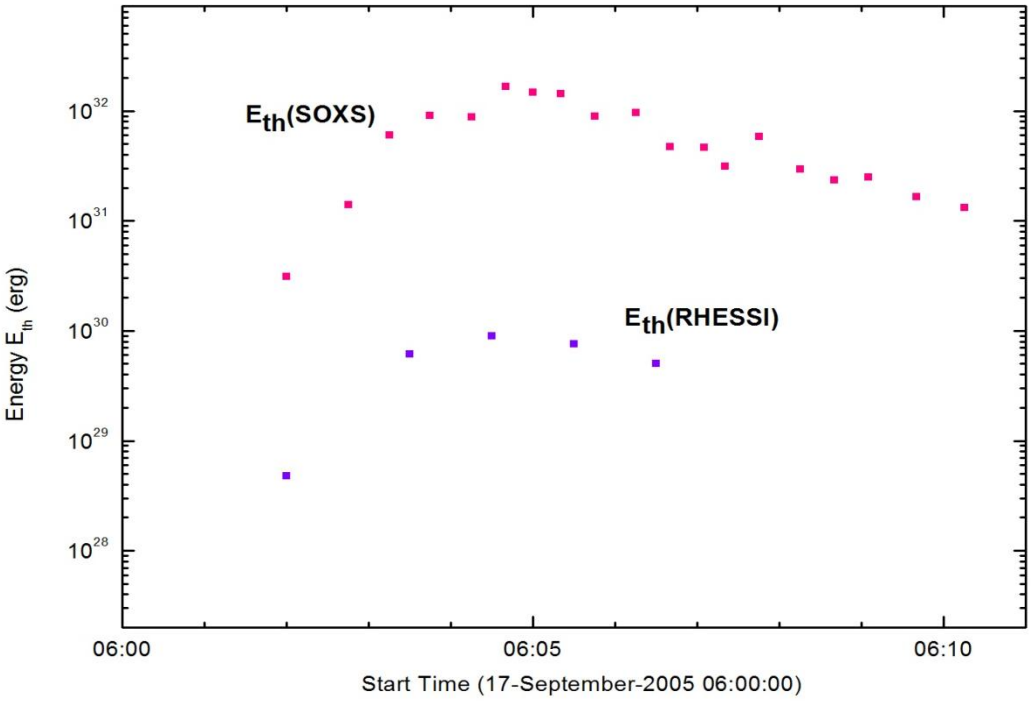

Figure 4.36: Thermal energy release as a function of time in 17-September-2005 flare event observed by SOXS and RHESSI.

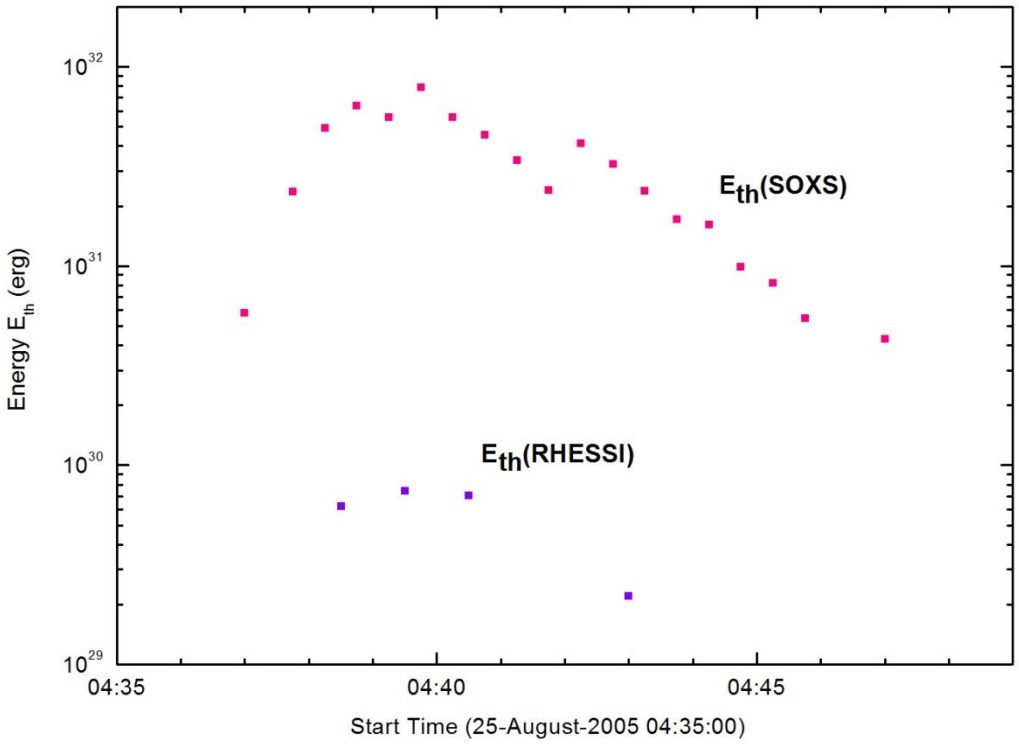

Figure 4.37: Thermal energy release as a function of time in 25-August-2005 flare event observed by SOXS and RHESSI.

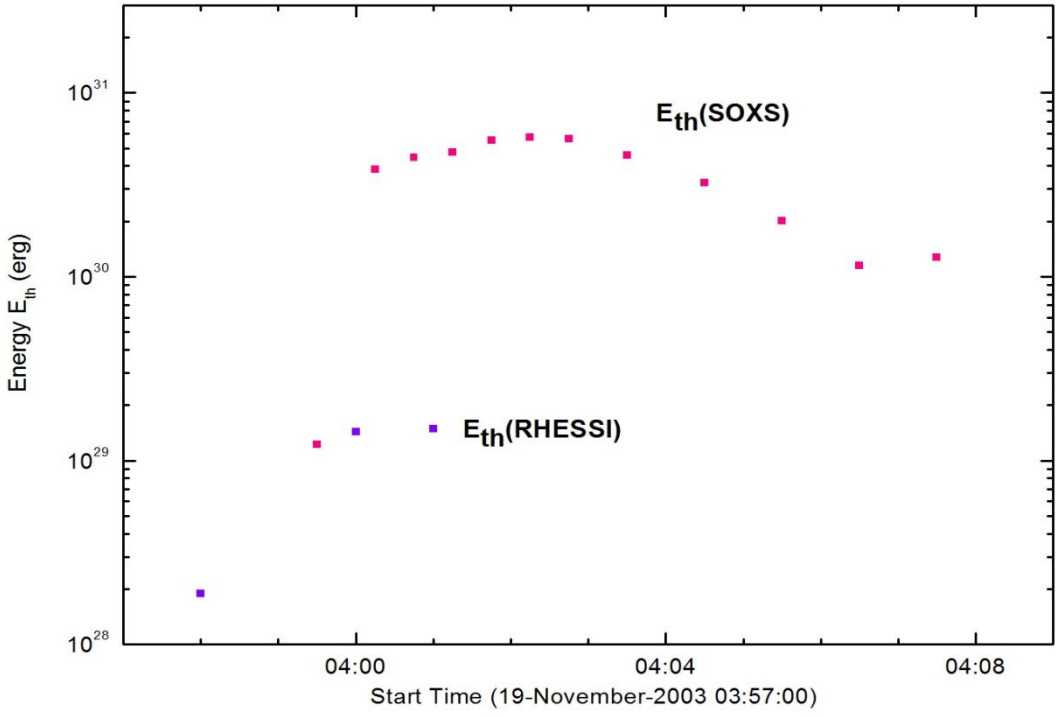

Figure 4.38: Thermal energy release as a function of time in 19-November-2003 flare event observed by SOXS and RHESSI.

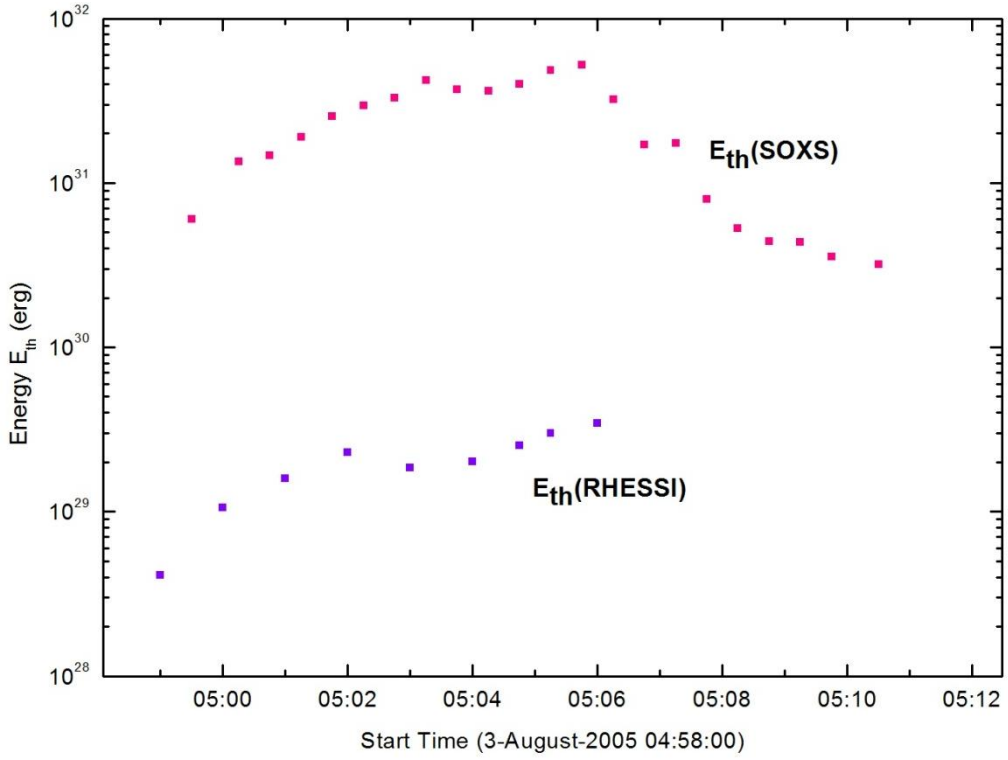

Figure 4.39: Thermal energy release as a function of time in 3-August-2005 flare event observed by SOXS and RHESSI.

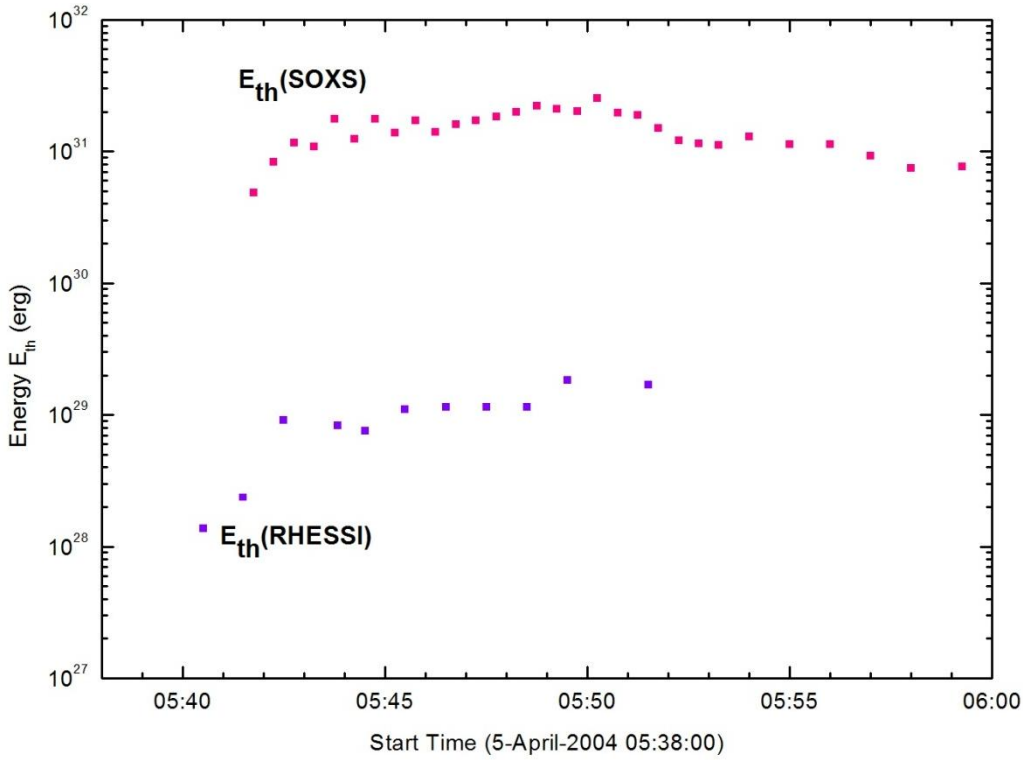

Figure 4.40: Thermal energy release as a function of time in 5-April-2004 flare event observed by SOXS and RHESSI.

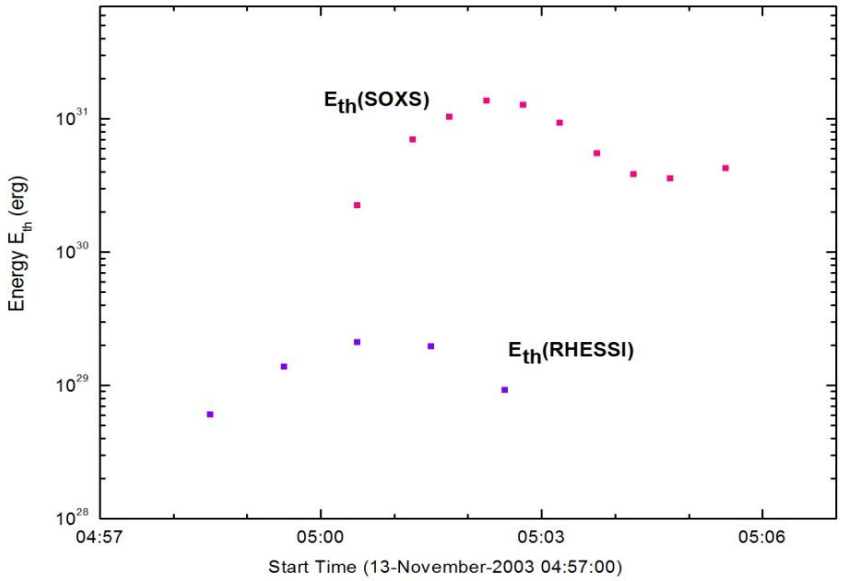

Figure 4.41: Thermal energy release as a function of time in 13-November-2003 flare event observed by SOXS and RHESSI.

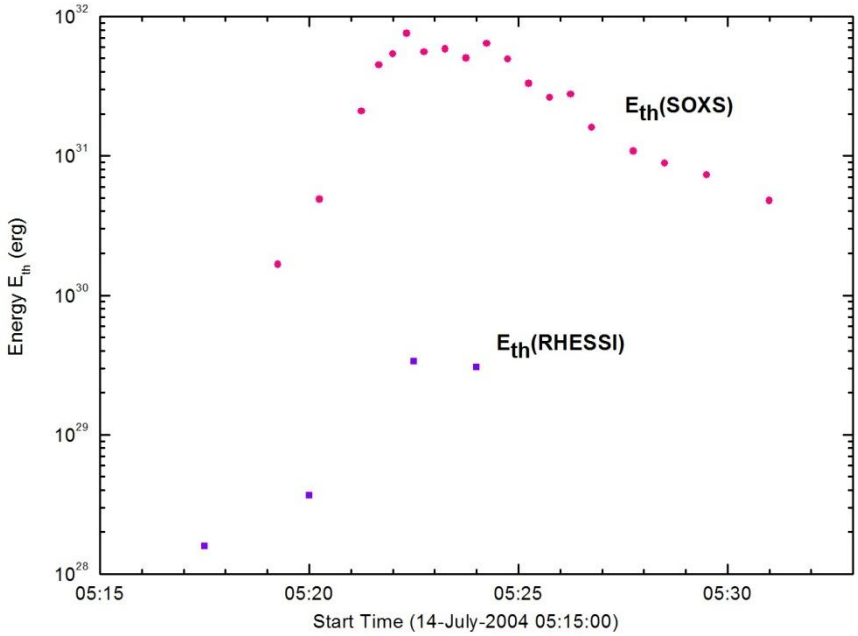

Figure 4.42: Thermal energy release as a function of time in 14-July-2004 flare event observed by SOXS and RHESSI.

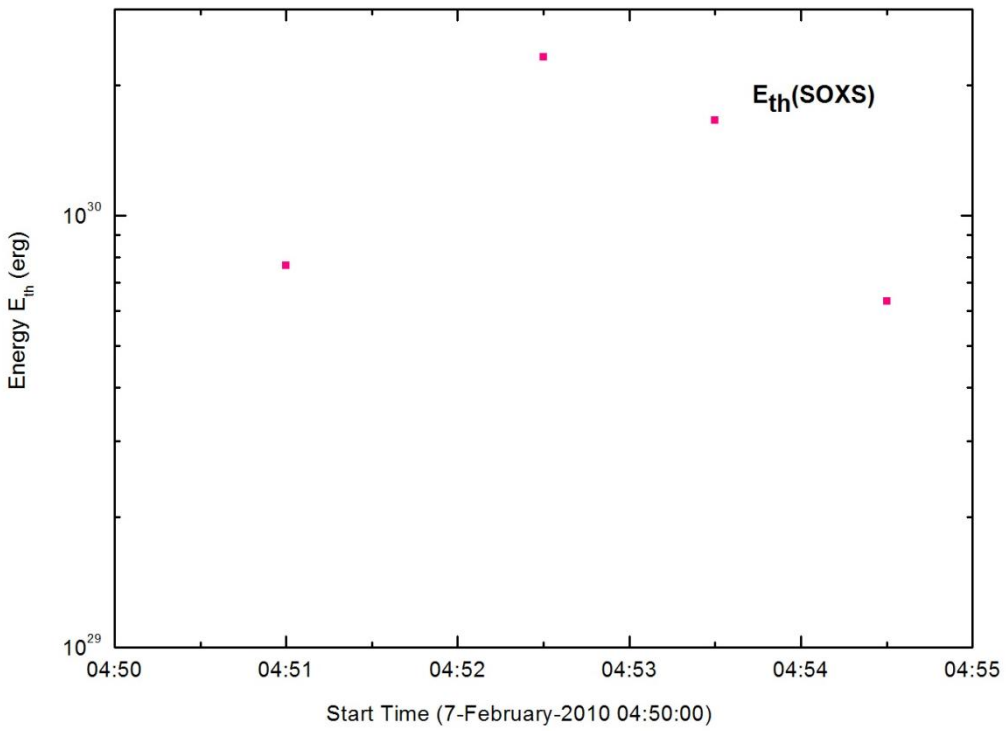

Figure 4.43: Thermal energy release as a function of time in 7-February-2010 flare event observed by SOXS.

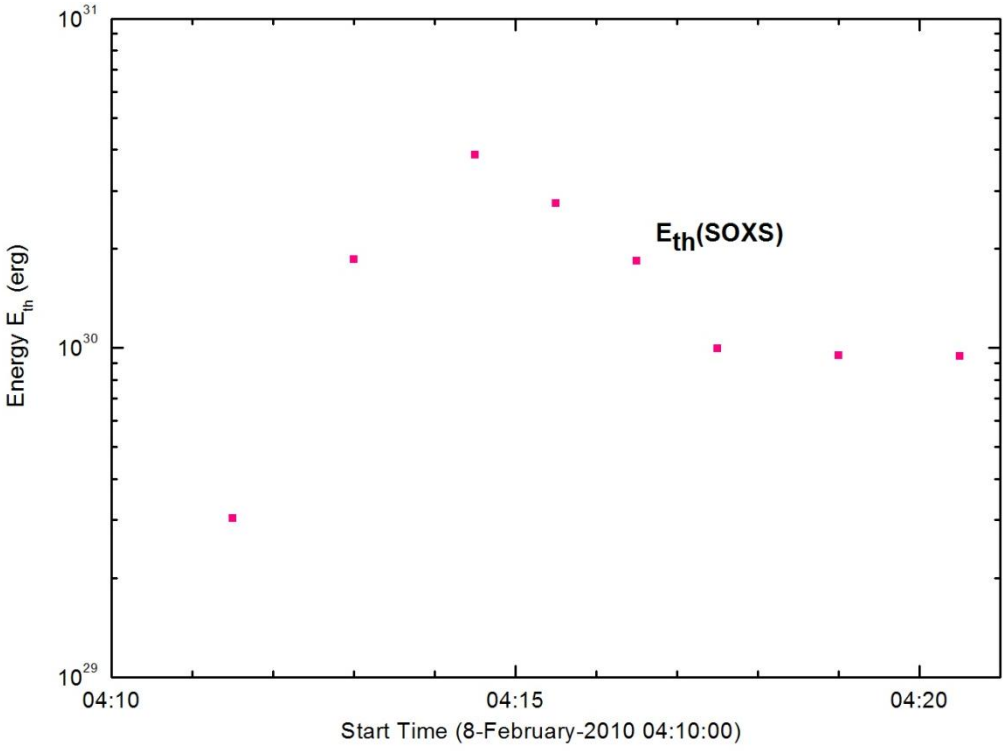

Figure 4.44: Thermal energy release as a function of time in 8-February-2010 flare event observed by SOXS.

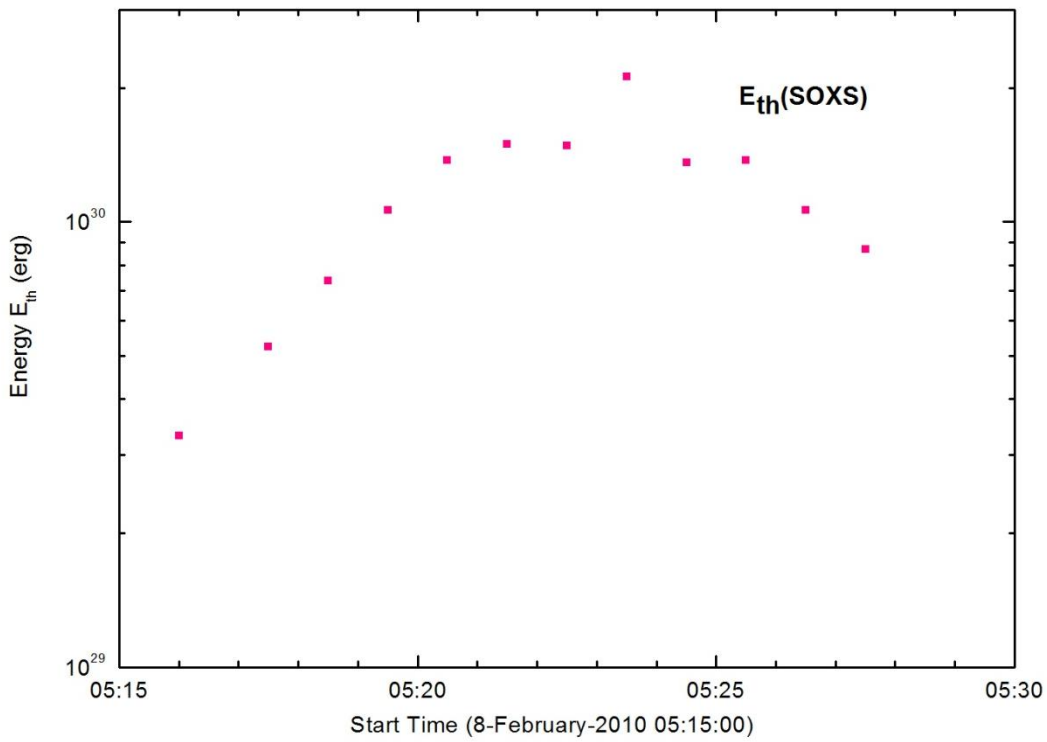

Figure 4.45: Thermal energy release as a function of time in 8-February-2010 flare event observed by SOXS.

I observed from Figures (4.33) to (4.42) that the thermal energy obtained from SOXS observations is 2 to 3 orders higher than that obtained from RHESSI observations. The integrated thermal energy for the whole duration of all the flares under investigation is given in Table 4.3.This may be due to the energy ranges chosen for analysis. In SOXS, the lower energy limit starts from 4.1 keV while in RHESSI, it is 13 keV. However, it may be noted that the temporal evolution of thermal energies from SOXS as well as RHESSI follow a similar pattern. The thermal energy peaks at almost the same time while in some flares (e.g. 13-November-2003 flare) a time difference of about 1-2 minutes in the thermal energy peak is observed.

Table 4.3

Integrated Thermal Energy release Estimates

Date	Integrated Thermal Energy SOXS (erg)	Integrated Thermal Energy RHESSI (erg)
13-NOV-2003	7.26E31	6.99E29
19-NOV-2003	4.2E31	3.11E29
6 –JAN-2004	2.04E32	2.65E30
5-APR-2004	4.37E32	1.09E30
14 –JUL-2004	6.13E32	6.9E29
31-OCT-2004	3.82E32	1.29E+30
27-JUL-2005	2.14E33	1.79E30
3-AUG-2005	4.92E32	1.82E30
25-AUG-2005	5.94E32	2.29E30
17-SEP-2005	1.19E33	2.83E+30
7-FEB-2010	5.38E30	
8-FEB-2010	1.35E31	
8-FEBRUARY-2010	1.38E31	

4.5.2 Estimation of non-thermal energy:

Observations of solar flares over the past several decades have indicated a strong link between magnetic reconnection and particle acceleration. Almost all large flares are accompanied by a burst of hard X-ray emission during the rise phase of the event. The hard X-rays are widely believed to be non-thermal bremsstrahlung emission produced by high-energy electrons precipitating into the chromosphere. The thermalization of precipitating non-thermal electrons leads to the formation of hot dense plasma that evaporates into the corona to form loops that emit strongly at soft X-ray wavelengths. This is the basis of the "thick target" model of hard X-ray emission (e.g., Brown, 1971).

Brown (1971) assumed that the non-thermal hard X-ray emission is thick-target bremsstrahlung. In the thick-target model, the electrons are assumed to lose all their energies due to Coulomb collisions and they heat the confined medium. Using the following formula given by Aschwanden (2006), the power in non-thermal electrons above some cut-off energy ε_C is given by

$$P(E \geq \varepsilon_C) = \int_{\varepsilon_C}^{\infty} F(E)EdE = 4.3 \times 10^{24} b(\gamma) I_1 \left(\frac{\varepsilon_C}{E_1} \right)^{-(\gamma-1)} \text{ (erg s}^{-1}\text{)} \qquad (4.4)$$

In the above equation, $F(E)E =$ thick-target electron injection spectrum (electrons keV^{-1} s^{-1}). $b(\gamma) =$ 0.27 γ^3 (for thick-target case, $\gamma = \delta - 1$ where δ is the index of the electron distribution function). In the above equation $I_1 =$ total number of photons above the lower cut-off energy E_1 (photons cm^{-2} s^{-1}). Using equation (1.13) from chapter 1 in the above equation and multiplying the power by the flare duration, the total energy in non-thermal electrons E_{nth} above some cut-off energy ε_C can be obtained as follows:

$$E_{nth} = 1.6 \times 10^{-9} \frac{\delta - 1}{\delta - 2} N \varepsilon_C \Delta t \qquad \text{(erg)} \qquad (4.5)$$

The spectra were fitted with thick2+vth model in the energy range of 13-100 keV for different intervals during the flare. The spectral fits enabled me to determine the parameters such as total integrated electron flux (10^{35} electrons s^{-1}), index δ of the electron distribution function below break energy and low energy cut-off (keV).

Jain *et al.* (2008) showed that the X-ray bursts associated with solar flares above 25 keV come mostly from the non-thermal bremsstrahlung while the X-ray emission between 10 and 25 keV in principle includes both thermal and non-thermal contributions. Both types of X-ray emission occur during solar flares and the clear demarcation line between the two processes provides quantitative estimation of energy release by each process in solar flares. However, the estimation of the non-thermal energy content in the parent electrons giving rise to flare emission solely depends on the low-energy cutoff and/or the thermal-non-thermal crossover energy (break

energy). However, so far no relation between the low energy cut-off of power-law electrons (E_c) and the break-energy point (E_B) has been established.

The determination of the low energy cut-off ε_C to non-thermal electron distributions is critical in the evaluation of the non-thermal energy in solar flares. The most direct evidence for low energy cut-offs is flattening of the non-thermal X-ray spectra at low energies. In 6-January-2004 flare event, I found that ε_C ranges between 20-29 keV as determined by fitting thick2 function to the HXR spectra, which are the upper limits. It may be noted that ε_C is low in the beginning of the flare, owing to the non-thermal onset of the flare and increases with time as shown in Figure 4.46 as the temperature of the flare also increases. This indicates that ε_C shifts to higher energies due to increasing contribution of thermal bremsstrahlung at higher temperature of the flare plasma.

I computed the non-thermal energy during the flare interval for 6-January-2004 and 5-April-2004 flare events. The temporal evolution of non-thermal energy for 6-January-2004 and 5-April-2004 is shown in Figure 4.47 and 4.48. The thermal energies for both these flares are shown again for the comparison of thermal and non-thermal energies. Time evolution of thermal energy determined by SOXS (pink), thermal energy determined by RHESSI (violet), and non-thermal energy determined by RHESSI (orange). For 6-January-2004 event I observed that the thermal and non-thermal energy obtained from RHESSI lie almost within the same energy range (E_{th} = 4.6 x 10^{28} to 4.6 x 10^{29} erg; E_{nth} = 5 x 10^{28} to 2.3 x 10^{29} erg). For 5-April-2004 flare the thermal and non-thermal energy obtained from RHESSI also lie within the same energy range (E_{th} = 1.4 x 10^{28} to 1.8 x 10^{29} erg; E_{nth} = 2.4 x 10^{28} to 1.6 x 10^{29} erg). Table 4.4 and Table 4.5 show the thermal and non-thermal energies and their ratio (E_{nth} / E_{th}) (%) for 6-January-2004 and 5-April-2004 events respectively.

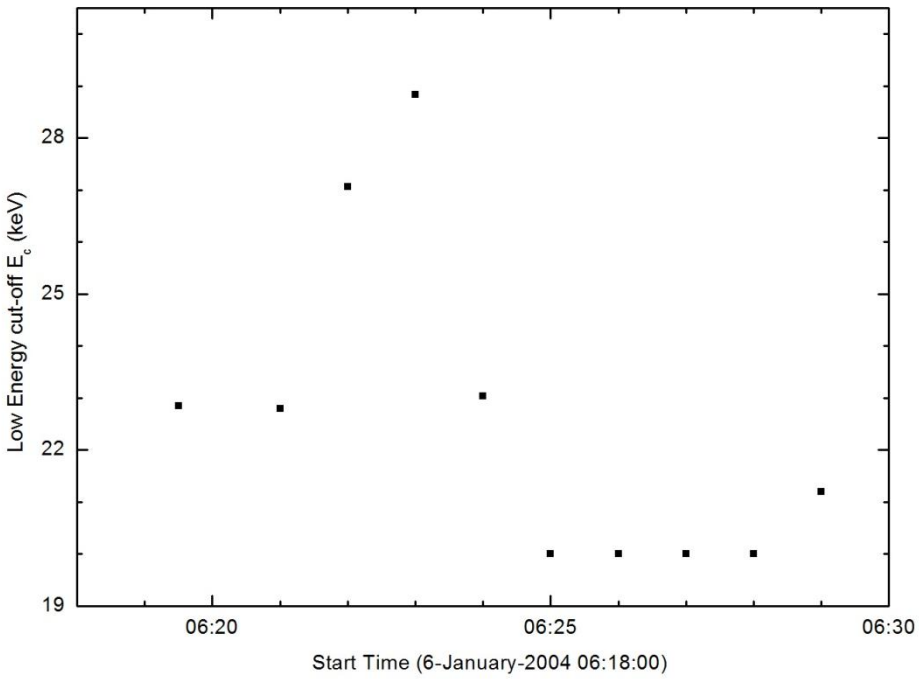

Figure 4.46: Variation of low energy cut-off with time for 6-January-2004 obtained from RHESSI spectral fits using isothermal plus thick2 model.

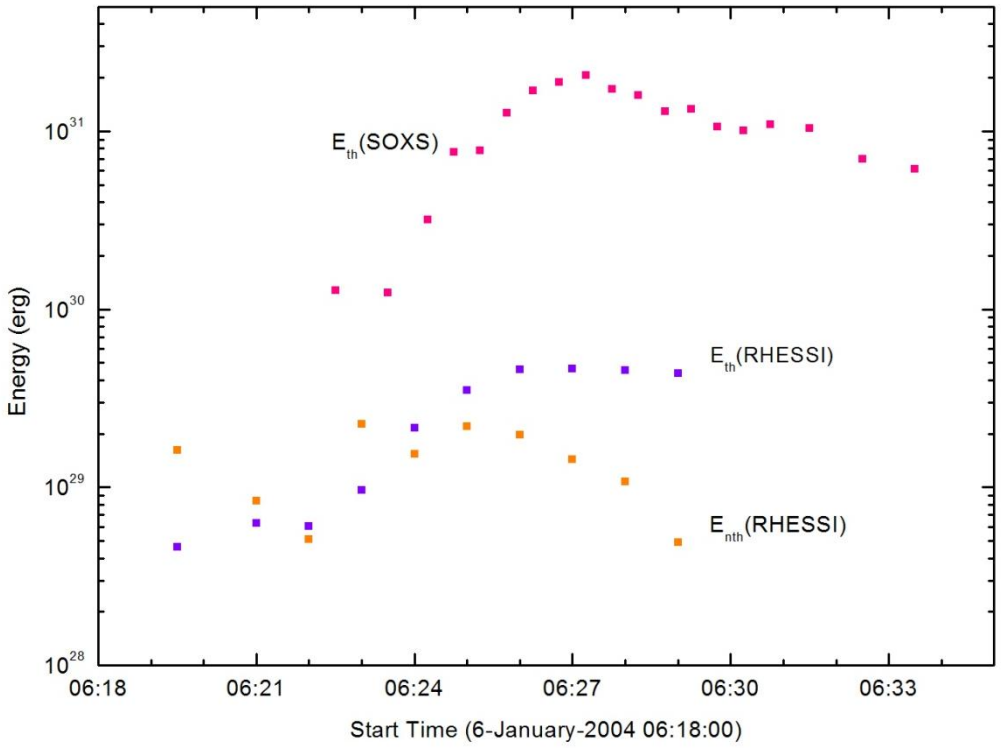

Figure 4.47: Time evolution of thermal energy determined by SOXS (pink) and RHESSI (violet), and non-thermal energy determined by RHESSI (orange) for 6-January-2004 solar flare.

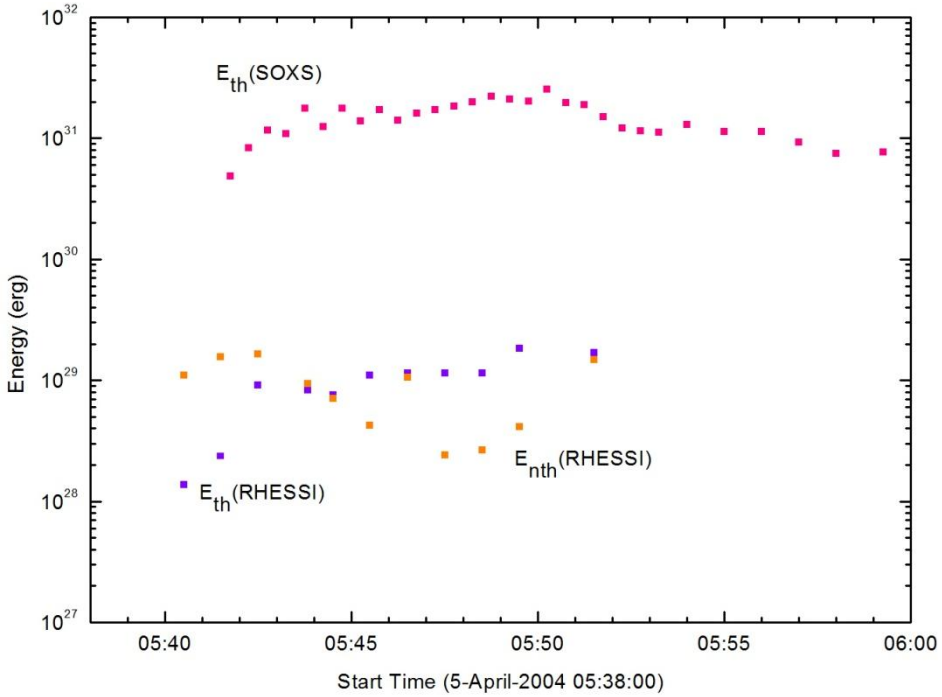

Figure 4.48: Temporal evolution of thermal energy determined by SOXS and RHESSI and non-thermal energy determined for 5-April-2004 solar flare.

Table 4.4

Thermal and non-thermal energies and their ratio for 6 January 2004 flare observed by RHESSI

Time	E_{th} (erg)	E_{nth} (erg)	E_{nth} / E_{th} (%)
06:19:30	4.60E+28	1.61E+29	3.5
06:21:00	6.27E+28	8.36E+28	1.33
06:22:00	6.03E+28	5.09E+28	0.84
06:23:00	9.65E+28	2.27E+29	2.36
06:24:00	2.16E+29	1.53E+29	0.70
06:25:00	3.51E+29	2.19E+29	0.62
06:26:00	4.59E+29	1.96E+29	0.43
06:27:00	4.66E+29	1.43E+29	0.31
06:28:00	4.54E+29	1.08E+29	0.24
06:29:00	4.36E+29	4.89E+28	0.11

Table 4.5

Thermal and non-thermal energies and their ratio for 5 April 2004 flare observed by RHESSI

Time	E_{th} (erg)	E_{nth} (erg)	E_{nth} / E_{th} (%)
05:40:30	1.38E+28	1.10E+29	7.99
05:41:30	2.36E+28	1.55E+29	6.58
05:42:30	9.09E+28	1.64E+29	1.81
05:43:30	8.34E+28	9.33E+28	1.12
05:44:30	7.52E+28	7.04E+28	0.94
05:45:30	1.10E+29	4.25E+28	0.38
05:46:30	1.14E+29	1.06E+29	0.93
05:47:30	1.15E+29	2.41E+28	0.21
05:48:30	1.15E+29	2.65E+28	0.23
05:49:30	1.83E+29	4.15E+28	0.27
05:51:30	1.70E+29	1.47E+29	0.86

Table 4.6 (Integrated thermal and non-thermal energies and their ratio)

Date	Integrated Thermal Energy E_{th} (erg)	Integrated Non-Thermal Energy E_{nth} (erg)	E_{nth} / E_{th} (%)
6-January-2004	2.65E30	1.39E30	0.52
5-April-2004	1.09E30	9.82E29	0.9

The analysis suggests that the thermal and non-thermal energies obtained from RHESSI data for two flares are of the same order of magnitude This result may be interpreted as conversion of non-thermal energy to hot flare plasma. Employing RHESSI observations, Saint & Benz (2005) determined the energy of the thermal flare plasma and the kinetic energy of the non-thermal electrons in 14 hard X-ray peaks from 9 medium-sized solar flares. They suggested that the thermal and non-thermal energies are of the same magnitude which may be interpreted by an efficient conversion of non-thermal energy to hot thermal plasma.

Table 4.6 shows the integrated thermal and non-thermal energies from RHESSI observations for 6-January-2004 and 5-April-2004 flares. The E_{nth} / E_{th} ratio for 6-January-2004 (0.52) and 5-April-2004 (0.9) flare suggests the contribution of non-thermal emission to the thermal plasma. The E_{nth} / E_{th} = 0.9 suggests that the integrated non-thermal energy is 0.9 times the thermal energy which shows clearly that the integrated thermal as well as non-thermal energies are almost of the same magnitude. The SOXS observations reveal the > 40 MK temperatures for this flare. This may be due to the major contribution of the non-thermal electrons to the heating of the thermal plasma.

4.6 Relationship of flare parameters:

In order to characterize thermal and non-thermal properties of the solar flares, I studied the correlation among several thermal (DEM, EM, T, α) and non-thermal parameters (F_{12}, F_{20} and γ) obtained from the spectral fits of 13 (SOXS) and 10 (RHESSI) flares considered for investigation in this chapter. The relations amongst the spectral parameters can give clue regarding plasma heating and acceleration processes in the solar corona.

4.6.1 Spectral index α versus Temperature T (Multi-thermal):

Firstly I explore the relationship between α and multi-thermal peak temperature. For this purpose I plotted all the values of spectral index α as a function of temperature (irrespective of different phases of the flare) for all examined 13 flares observed by SOXS as shown in Figure 4.49(top). The scatter plot includes those points of α for which temperature of the flare derived when thermal plus non-thermal hybrid spectra are fitted. Thus realizing this fact I conduct binning of the data points using 3 MK temperature bin as shown in Figure 4.49 (bottom) and I observed that the multi-thermal spectral index α follows a power-law distribution with the multi-thermal temperature satisfying the following relation:

$$\alpha = (2.17 \pm 0.289) T^{(0.27 \pm 0.03)} \qquad (4.6)$$

The correlation coefficient r = 0.9.

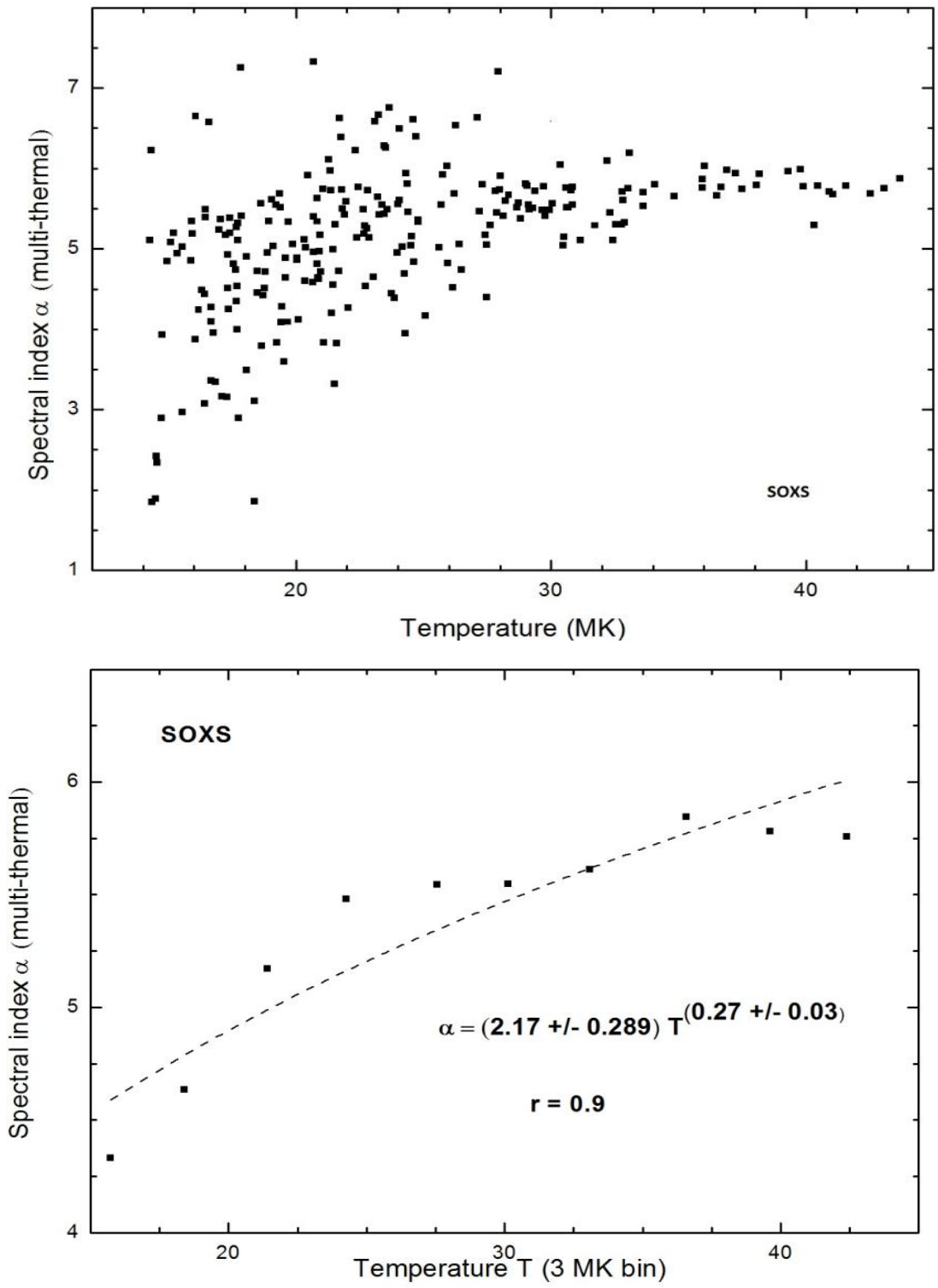

Figure 4.49: Scatter plot (top) of spectral index versus SOXS temperatures in the energy range 4.1-24 keV. The bottom plot (with 3 MK bin) shows the dashed line (power-law) is the best fit with r = 0.9.

Figure (4.49) shows that α increases as a power-law function of multi-thermal temperature.

4.6.2 Photon flux F_{12} versus spectral index α :

To get an idea of the behavior of the photon flux as a function of the multi-thermal spectral index, I plotted F_{12} versus α. Figure 4.50 (top) shows the scatter plot of photon flux F_{12} (photons s^{-1} cm^{-2} keV^{-1}) versus spectral index α. As described the scientific fact in previous section #4.6.1, I did binning of the spectral index α with 0.5 widths and found that the photon flux increases exponentially with the spectral index. The best fit with r = 0.8 is given by the following relation.

$$F_{12} = (41.1 \pm 11.4) e^{(0.42 \pm 0.06)\alpha} \qquad (4.7)$$

Neglecting the lowest binned value of α (i.e. 1.86 ± 0.01) improves the correlation to 0.91.

4.6.3 Emission Measure versus Temperature:

I explore the emission measure and the temperature relationship for all the flares observed by SOXS and RHESSI. However, I did not get any clear relationship between isothermal temperature and emission measure from RHESSI observations. The explanation of DEM vs multi-thermal temperature is as follows:

Differential Emission Measure versus Multi-thermal temperature:

Figure 4.51(top) shows the scatter plot of differential emission measure obtained directly from the multi-thermal model with the multi-thermal temperature. Despite the large scatter of the data in this plot, I got good results after binning as shown in Figure 4.51 (bottom).

I obtained the best fit to the DEM versus temperature (1 MK bin) plot with a correlation coefficient r = 0.68. It is a power-law relationship obeying the following relation:

$$DEM = (9.56 \pm 7.5) T^{(-1.37 \pm 0.2)} \qquad (4.8)$$

This power-law dependence of differential emission measure on temperature is a strong evidence of multi-thermal plasma in flares. It also suggests that the hard X-ray spectrum in the low energy range (4.1 to about 18 keV) should be fitted with multi-thermal model rather than an isothermal model. The low value of α, however, suggests for non-thermal contribution along with thermal emission at least above break energy 12 keV.

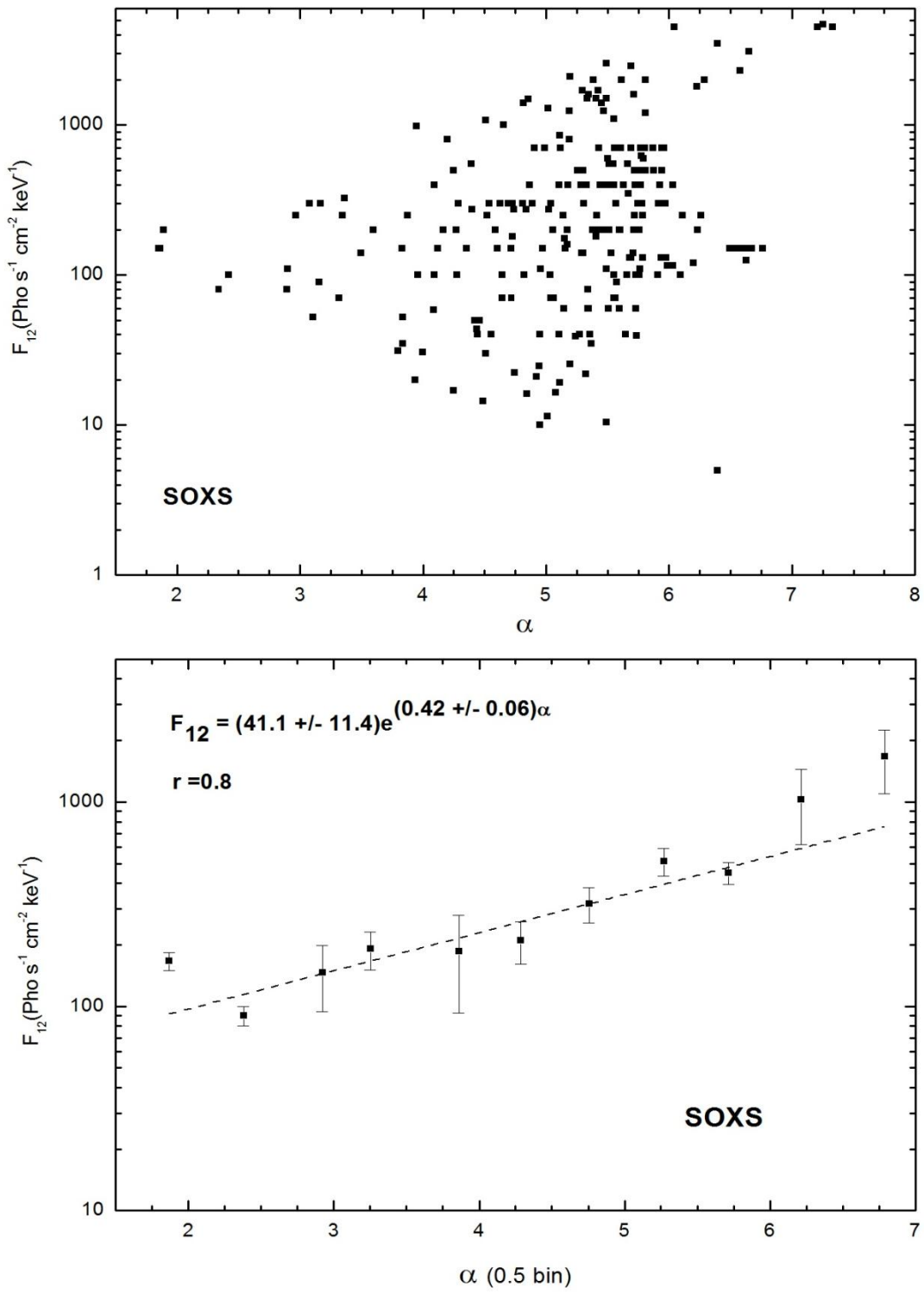

Fig: 4.50: Scatter plot (top) and binned (bottom) plot (0.5 binning for spectral index) of photon flux and spectral index α with exponential correlation of 0.8.

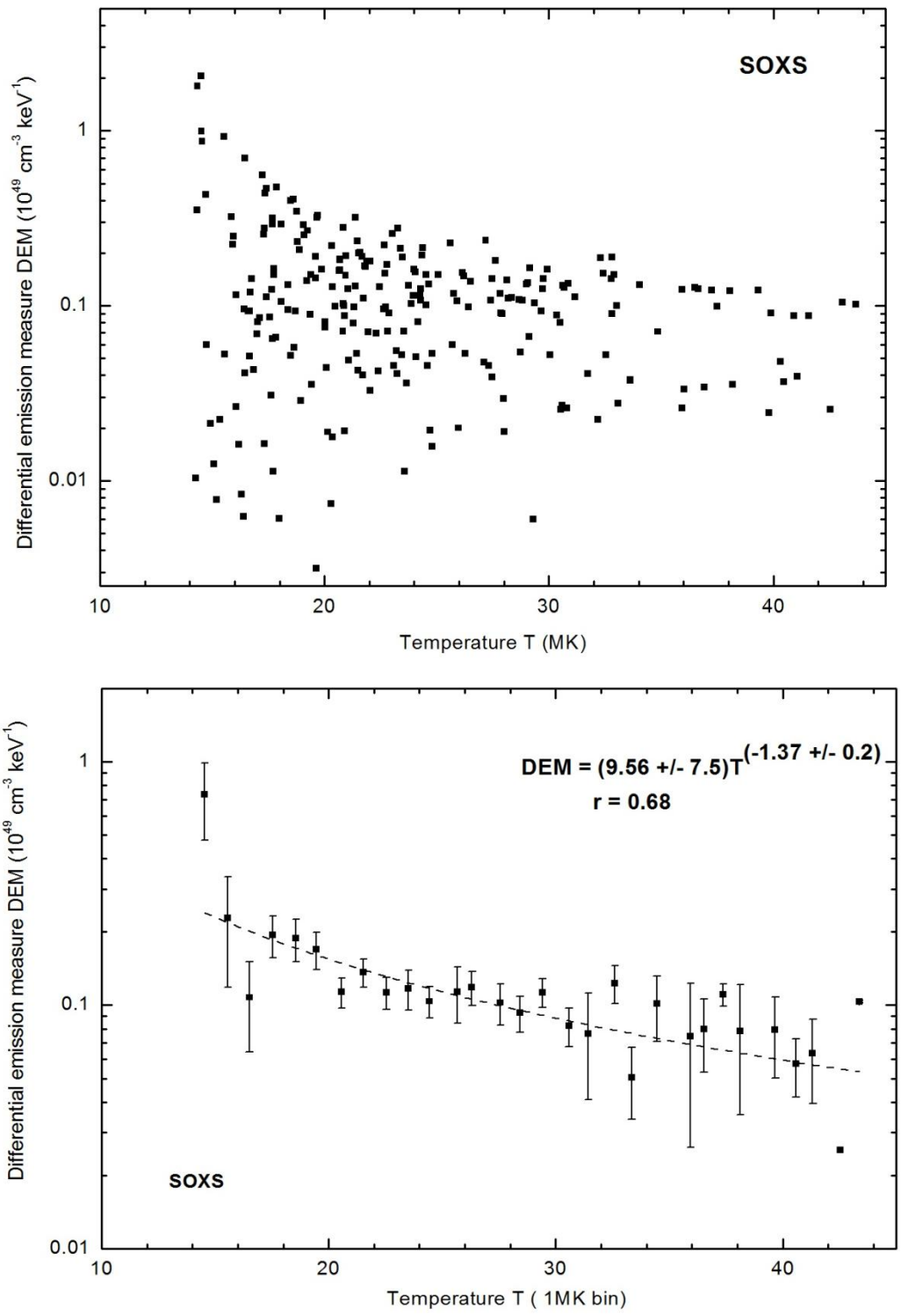

Figure 4.51: Scatter plot (top) of differential emission measure against multi-thermal temperature T and binned plot (1 MK bin) at the bottom

4.6.4 Photon Flux versus Emission Measure:

4.6.4.1 Photon flux F_{12} versus Emission Measure (multi-thermal):

To investigate the relationship between the photon flux and temperature, I plotted F_{12} as a function of multi-thermal emission measure. Figure 4.52 (top) shows the photon flux plotted as a function of emission measure. Figure 4.52(bottom) shows the best fit obtained after binning of emission measure (10 x 10^{49} cm^{-3} bins). The correlation coefficient is 0.96. The power-law relationship is expressed by the following relation:

$$F_{12} = (16.4 \pm 6) EM^{(0.94 \pm 0.07)} \qquad (4.9)$$

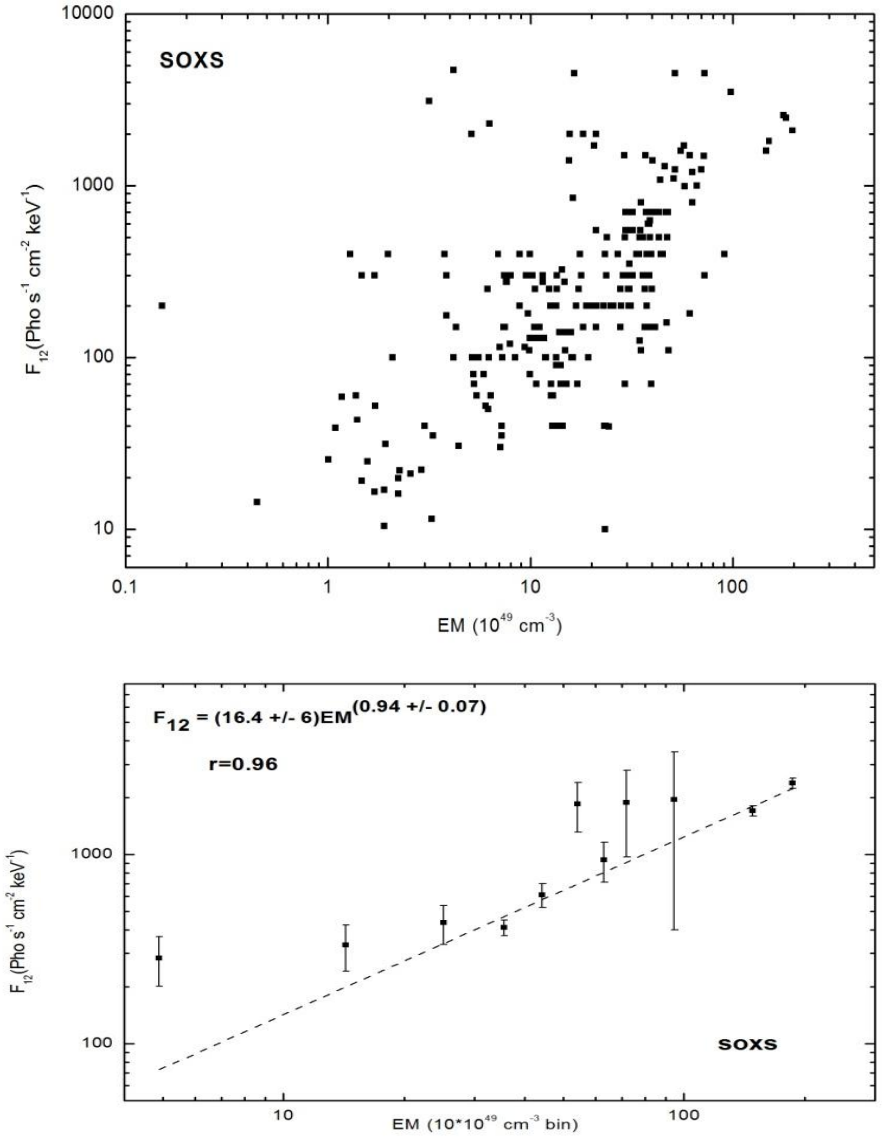

Figure 4.52: The scatter plot (top) of photon flux as a function of multi-thermal emission measure. The power-law fit (for 10*10^{49} cm^{-3} binning of emission measure) with a correlation coefficient of 0.96 (bottom).

4.6.4.2 Photon Flux F_{20} versus Emission Measure (Isothermal):

To explore the relationship between the photon flux and isothermal temperature, I plotted F_{12} as a function of isothermal emission measure as shown in Figure 4.53 (top). The best fit obtained after binning of emission measure (0.1 x 10^{49} cm^{-3} bins) is a power-law relationship as shown in Figure 4.53(bottom) expressed by the following equation with r = 0.94

$$F_{20} = (1.48 \pm 0.46) e^{(3.53 \pm 0.5) EM} \qquad (4.10)$$

The relation is in agreement with the general flare scenario that flares with high flux (high density) produce more emission (heated plasma). The magnificently high correlation in Figures 4.52(bottom) and 4.53(bottom) strongly suggests that during early rise phase as soon as the reconnection sets on, the electrons are accelerated and simultaneously they are heated up to very high temperature, which enhances the electron density and energy state (Jain *et al*., 2006). The flux is proportional to computed total emission measure (and not the DEM) in section 4.6.4.1. However, there has been observed a delay in time between the peak of EM and T ranging between 1 – 4 minutes, which, in fact, may be interpreted as time required for plasma heating after acceleration.

4.6.5 Photon Flux F_{20} versus Temperature (Isothermal):

In order to study the photon flux - temperature relationship using RHESSI observations, the photon flux at 20 keV was plotted as a function of isothermal temperature as shown in Figure 4.54 (top). The plot clearly shows the increase in temperature with corresponding increase in non-thermal flux. I observed that the correlationship became more significant when plotted with 1 MK temperature binning as shown in Figure 4.54 (bottom). The best fit is a power-law fit with correlation coefficient of 0.94. The corresponding relation is given by

$$F_{20} = (4.5 * 10^{-11} \pm 1.1 * 10^{-10}) T^{(8 \pm 0.8)} \qquad (4.11)$$

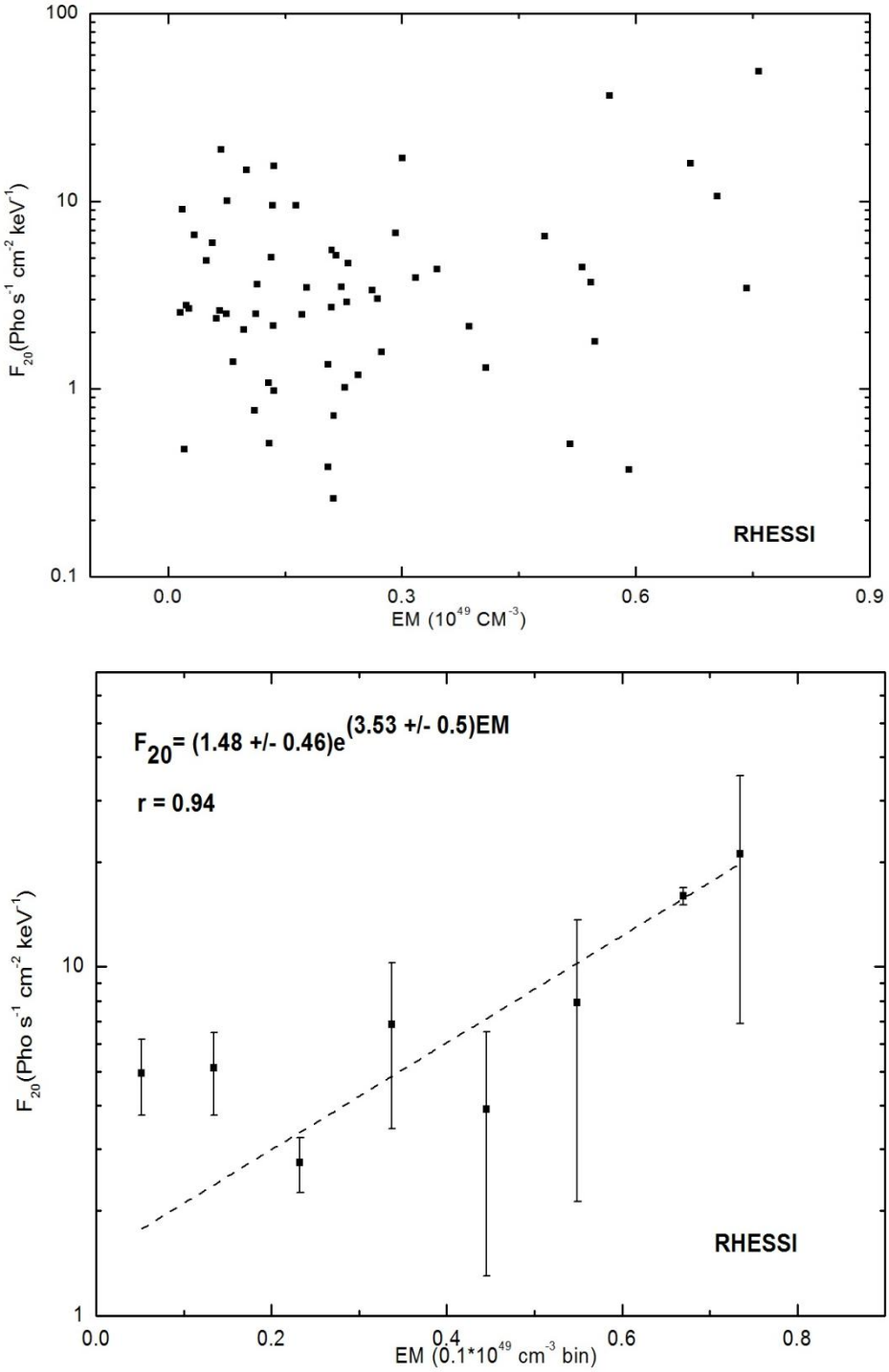

Figure 4.53: The variation of photon flux at 20 keV with emission measure (top). The best fit showing the exponential relationship with r =0.94 after binning of emission measure (0.1×10^{49} cm^{-3}).

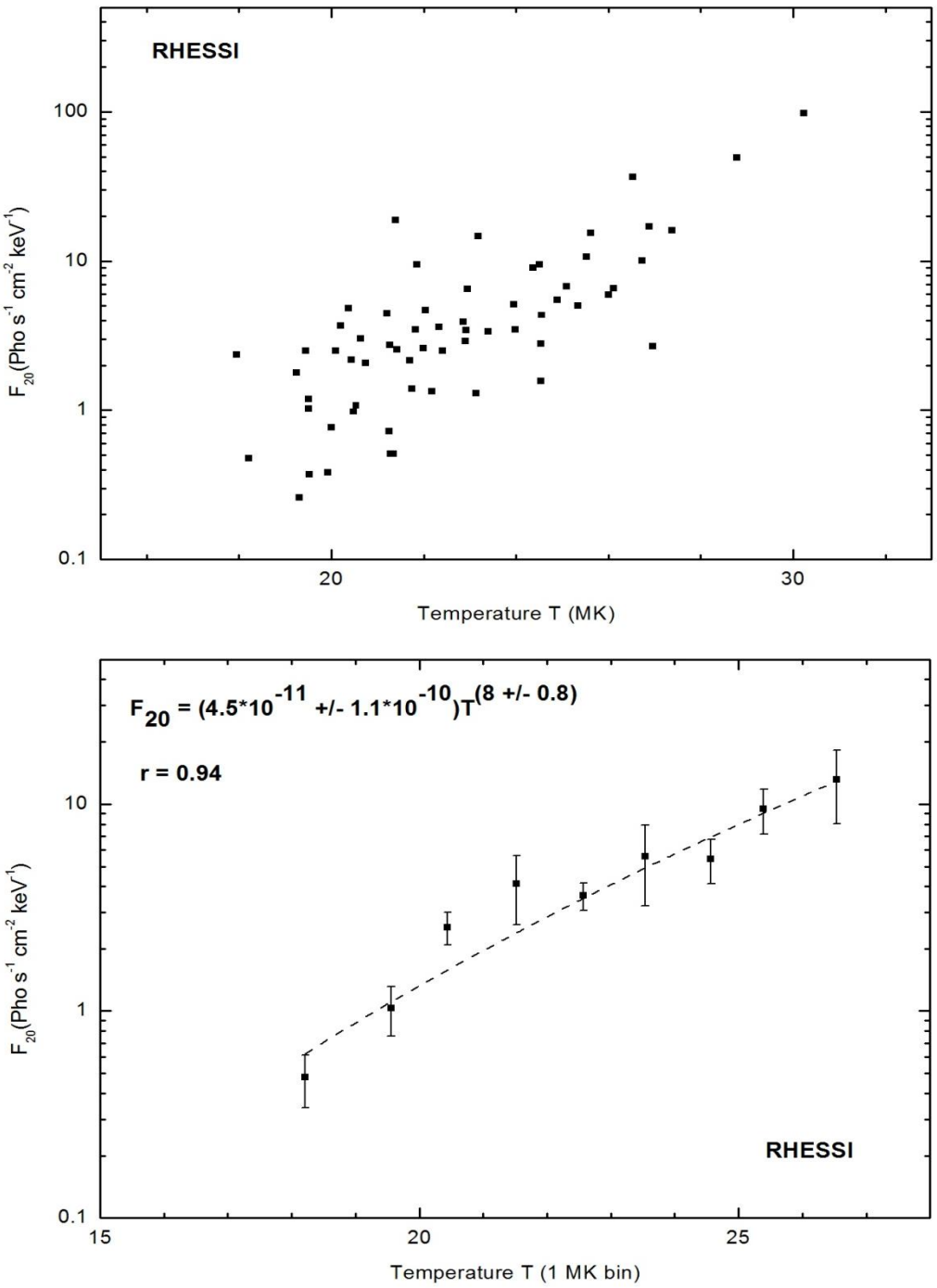

Figure 4.54: The non-thermal photon flux at 20 keV is plotted as a function of isothermal temperature (top). The results after binning of temperature (1 MK bin) are shown in bottom plot.

This confirms the general flare scenario that the non-thermal electrons contribute to the heating of the plasma. This contribution is in agreement with the result obtained in Table 4.6.

4.6.6 Spectral Index γ versus multi-thermal Emission Measure:

Jain *et al.* (2008) showed that the X-ray bursts associated with solar flares above 25 keV come mostly from the non-thermal Bremsstrahlung while the X-ray emission between 10 and 25 keV in principle includes both thermal and non-thermal contributions. Both types of X-ray emission occur during solar flares and the clear demarcation line between the two processes provides quantitative estimation of energy release by each process in solar flares. In this context, I further explored the relationship between thermal parameter (emission measure) and non-thermal parameter (spectral index γ **)**.

The non-thermal spectral index γ is plotted against multi-thermal emission measure for all spectra in Figure 4.55(top) which shows a scatter plot with unclear behavior. However, the correlationship improved significantly when this behavior was studied with 10×10^{-49} cm^{-3} bin of emission measure as shown in Figure 4.55 (bottom). The power-law relationship with an excellent correlationship (r = 0.94) is obtained. The relationship is given by

$$\gamma = (3.75 \pm 0.19) EM^{(0.09 \pm 0.01)} \qquad (4.12)$$

This relationship strongly confirms the contribution of non-thermal plasma to the thermal emission by chromospheric evaporation. This result confirms a strong relationship between the thermal and non-thermal behavior observed in solar flares. The spectral index in equation (4.12) corresponds to the energy range 20 – 100 keV which is supposed to be more of non-thermal behavior. It indicates that as the spectrum becomes harder, the emission measure increases. This confirms the contribution of non-thermal electrons to the thermal plasma via Bremsstrahlung process.

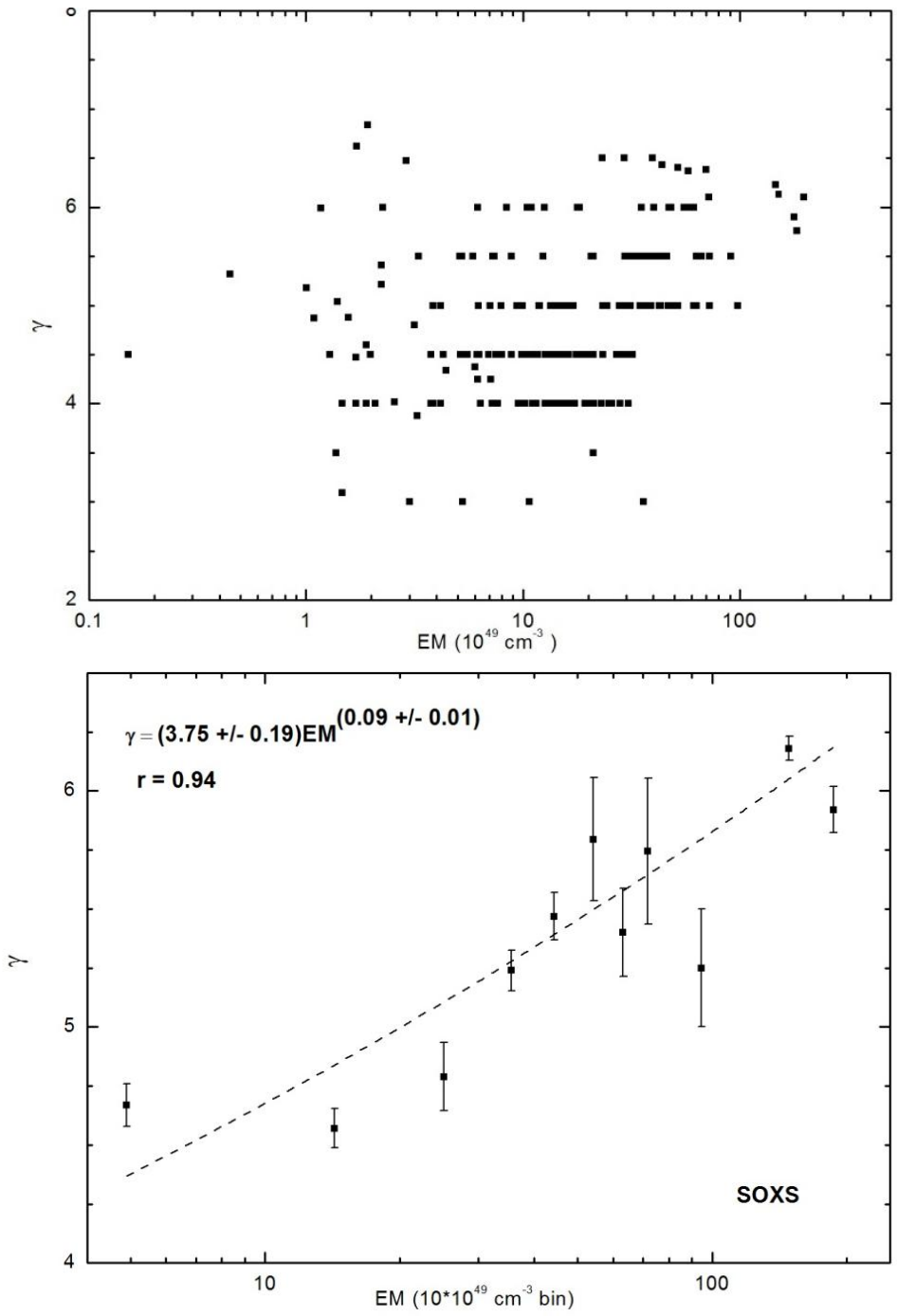

Figure 4.55: Scatter plot (top) of spectral index γ and multi-thermal emission measure. The correlationship improves drastically with the binning of emission measure (bottom).

4.7 Conduction and radiation power:

Conductive power:

The conductive power (conductive flux integrated over A and L) is given by

$$P_{con} = \frac{\kappa T^{7/2} A}{L} \qquad \text{erg s}^{-1}$$

where κ = Spitzer conduction coefficient= 9.2 x 10^{-7} erg s^{-1} cm^{-1} $K^{-7/2}$

T = temperature in K

A= area of cross-section of the loops in cm^2

L= half length of the loops in cm

For RHESSI flares, the typical foot-point area A= 10^{16} cm^2 and the loop half length is about L = 10^9 cm (Aschwanden, private communication, 2011). Considering these values, the conductive power will be

$$\therefore P_{con} = 9.2T^{7/2} \qquad \text{erg s}^{-1} \qquad (4.13)$$

Radiative power:

The radiative power is given by

$$P_{rad} = EM(\Lambda(T)) \qquad \textbf{(}\text{erg s}^{-1}\text{)}$$

where $\Lambda(T)$ is the radiative loss function (erg cm^3 s^{-1}) which is a temperature dependent function. Rosner *et al*. (1978) generated an analytical fit to the radiative loss function which may be approximated by a sequence of power-laws joined continuously. Using these expressions for the power law expression for temperature > $10^{7.3}$K (Aschwanden, 2008), which is

$$\Lambda(T) = 10^{-24.66} T^{1/4} \qquad (\text{erg cm}^3\,\text{s}^{-1})$$

The radiative power is then given by

$$P_{rad} = EM \times 10^{-24.66} (T)^{1/4} \qquad \textbf{(}\text{erg s}^{-1}\textbf{)} \qquad \textbf{(4.14)}$$

Employing equations (4.13) and (4.14), I computed the conductive as well as the radiative power for the 27-July-2005 and 5-April-2004 flares. The temporal variation of the radiation as well as the conduction power for these two flares is shown in Figures 4.56 and 4.57 respectively.

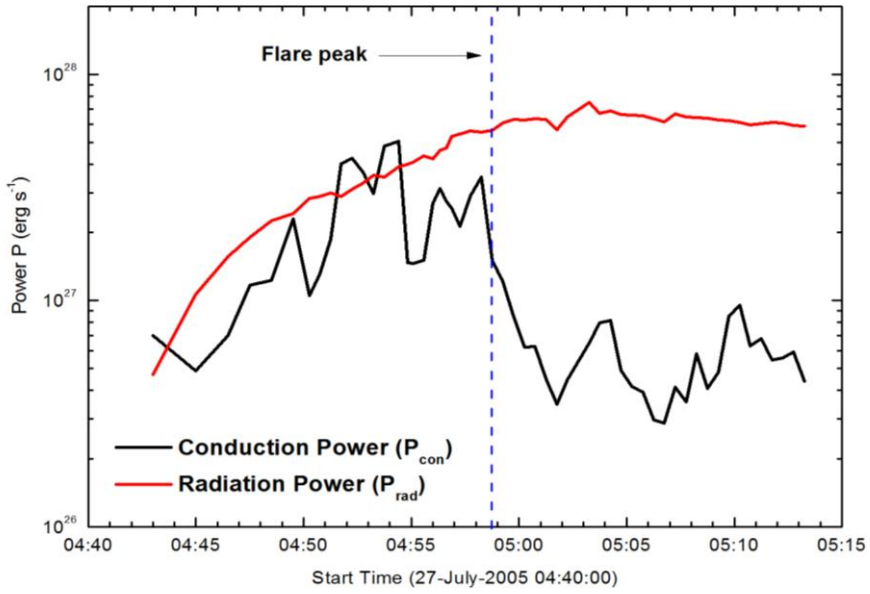

Figure 4.56: Temporal variation of radiative and conductive power for 27-July-2005 flare.

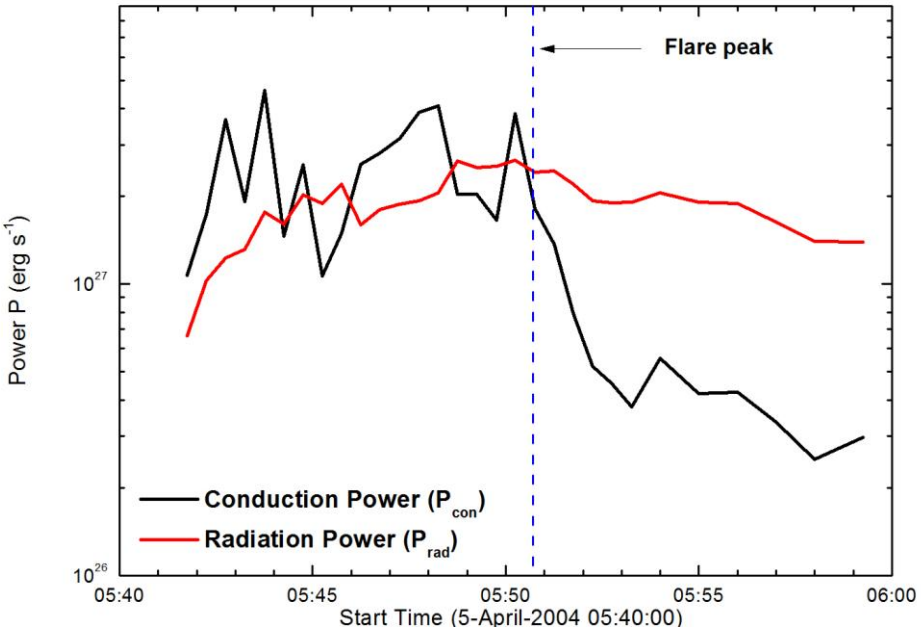

Figure 4.57: Temporal variation of radiative and conductive power for 5-April-2004 flare.

For both the flares, the temperature reached 40-45 MK (super-hot component) during the rise phase. Figure 4.57 suggests that thermal conduction is a dominant during the rise phase. This clearly indicates that in flare loops at higher temperatures, thermal conduction is a dominant mechanism during the rise phase. Both figures also indicates that in post-flare

loops (or decay phase), radiative cooling is the dominant mechanism in thermal energy range.

4.8 Discussion and Conclusions:

The study of solar flares X-ray emission allows me to conclude that the solar corona is inhomogeneous plasma, composed of regions differing in terms of their temperature, density, and dynamic behavior, threaded by magnetic field lines. There are open regions, where the magnetic field lines may extend far into interplanetary space ($\beta < 1$), and closed regions, where the magnetic fields are anchored (or line-tied) at both ends in the solar photosphere (where $\beta > 1$). However, in this chapter I focused only on closed regions and especially distinct structures called coronal loops, where charged particles clearly follow the arcing magnetic field lines and emit strongly at EUV and X-ray wavelengths.

In the current analysis of solar flares observed by SOXS and RHESSI simultaneously, the spectra in the dynamic range of about 4.1-24 keV (SOXS) and 13-100 keV RHESSI) were analyzed using multi-thermal plus single power-law (SOXS) and isothermal plus single power-law (RHESSI). The emission measure (EM) computed employing multi-thermal function given by equation (4.1) for the solar flares observed by SOXS mission is found to vary between $(0.15 \pm 0.06) \times 10^{49}$ cm^{-3} to $(198 \pm 36) \times 10^{49}$ cm^{-3}. On the other hand, the isothermal emission measure obtained with RHESSI observations varies between $(0.016 \pm 0.01) \times 10^{49}$ cm^{-3} and $(0.76 \pm 0.02) \times 10^{49}$ cm^{-3}. It may be noted that EM for SOXS flares varies by 3 orders while for RHESSI flares it varies by one order. The reason behind this appears to be the energy range considered for fitting the spectra. In the first case of SOXS flares, I consider spectral fit from 4.1-24 keV, while in the later case of RHESSI the energy range for fitting the spectra is higher from 13-100 keV. The Figures of temporal evolution of the spectral fits show that the isothermal temperature and hence emission measure, by and large remains uniform over thermal energy range perhaps from 13-30 keV , while contribution from non-thermal in the energy range 30-100 keV significantly varies over temporal evolution. On the other hand, on lower energy range 4.1-24 keV, in the SOXS flares, multi-

thermal emission measure plays significant role relative to non-thermal contribution in this dynamic energy range.

I found that the evolution of the temperature in all flares is almost similar to the light curve of the flare, and it peaks around the peak time of the flare indicating that flare X-ray photon emission is rather strongly governed by the temperature of the flare plasma. Thus increasing temperature enhances ionization and thereby thermal bremsstrahlung also increases. On the other hand during explosive phase of the flare due to non-thermal bremsstrahlung chromospheric evaporation takes place and that also contributes in enhancing the temperature of the flare plasma. The multi-thermal temperature ranges between 14.3 ± 0.15 to 43.7 ± 7.9 MK for the flares observed by the SOXS, while for the flares observed by RHESSI the isothermal temperature ranges between 18 ± 1.4 to 42 ± 1.1 MK. The lower limit of the temperature range in the case of RHESSI data analysis is found to be ~3.5 MK higher than multi-thermal lower limit derived from the SOXS data. This is simply because energy range considered in RHESSI for spectra-fit is higher (13-100 keV).

In this chapter I estimated thermal and non-thermal energies released in solar flares under investigation. However, the close observational relationship between hard X-ray emission and the evolution of high-temperature thermal flare plasma is often referred to as the "Neupert effect." Neupert (1968) found that the soft X-ray flux observed during the rise phase of a flare was generally proportional to the time-integrated microwave intensity, which is gyro-synchrotron emission is also believed to be produced by non-thermal particles. Systematic studies have shown that the Neupert effect is exhibited during the rise phase of many flares (e.g., Dennis & Zarro 1993; McTiernan *et al*. 1999; Veronig *et al*. 2002a, Aschwanden, 2007, Jain *et al*., 2011). Using a sample of 1114 events, Veronig *et al*. (2002b) obtained a linear correlation coefficient of 0.71 between the time-integrated hard X-ray emission and the peak soft X-ray emission. For modest flares there is considerable scatter and the correlation is poor. For the largest flares (M and X class), however, the relationship between the integrated hard X-ray emission and the peak soft X-ray flux is linear (see Veronig *et al*. 2002a).

The X-ray emission from solar flares has been traditionally treated as well as shown to be isothermal in nature (Landi *et al.,*2003, 2005, 2006;

Phillips *et al.,*2003; Caspi and Lin, 2010), particularly while simulating spectral line and continuum intensities using CHIANTI atomic database (Landi and Klimchuk, 2010). However, Craig and Brown (1976) formulated the concept of multi-temperature plasma in the flare considering differential emission measure (DEM). Aschwanden (2007) has for the first time investigated the nature of X-ray emission in solar flares with the help of modeling the spectral-temporal hard X-ray flux in terms of multi-temperature plasma governed by thermal conduction cooling. He suggested three physical processes that lead to measurable time delays as a function of energy in solar flares: 1) time-of-flight dispersion of free-streaming electrons, 2) collisional trapping of electrons, 3) and the Neupert effect (Hudson 1991; Dennis and Zarro 1993), *i.e*., the thermal delays can be caused by the temperature dependence of the cooling process, such as thermal conduction, $\tau_c(T) \propto T^{-5/2}$ (*e.g*., Antiochos and Sturrock 1978; Culhane *et al.,*1994) or radiative cooling $\tau_r(T) \propto T^{5/3}$. In his quantitative model, he has characterized the multi-temperature differential emission measure distribution (DEM) and non-thermal spectra with power-law functions. By fitting this model to the spectra and energy-dependent time delays on the RHESSI flare observations from 10 keV and above he suggested the flare X-ray emission to be multi-thermal in nature. However, the nature of the flare emission below 10 keV is still not addressed in the context of isothermal versus multi-thermal whose cause is mostly thermal Bremsstrahlung. Thus it is extremely important to characterize the soft X-ray emission below 10 keV. Further, the X-ray emission between 10 and 25 keV should in principle include both thermal and non-thermal contributions (Aschwanden, 2007; Jain *et al.,* 2008). Therefore, the characterization of flare plasma up to 25 keV with high spectral resolution observations becomes further important.

In 6-January-2004 flare event, I found that ε_C ranges between 20-29 keV as determined by fitting thick2 function to the HXR spectra, which are the upper limits. The shift of ε_C to higher energies is due to increasing contribution of thermal Bremsstrahlung at higher temperature of the flare plasma. Aschwanden (2007), ignoring possible low-energy cutoff, has found the thermal-non-thermal crossover energy 18±3.4 keV using the power law

approximation of X-ray emission. On the other hand, Gan *et al.* (2002) estimated the low energy cut-off (E_c) of the non-thermal emission by fitting the hard X-ray spectra obtained from BATSE/CGRO. They found value of E_c varies between 45 and 97 keV with an average of 60 keV for 44% of the events considered for investigation. For another 44% events they suggested that E_c could be lower than 45 keV due to non-availability of data below 45 keV. On the other hand, for 11% of events the hard X-ray spectra could not be explained by a beam of power-law electrons with low-energy cutoff, which supports the break-energy concept and that could be on the lower side (Jain *et al.*, 2000a; Aschwanden, 2007). However, Sui *et al.* (2005) found 24±2 keV as the low-energy cutoff (E_c) to ensure that always thermal emission dominates over non-thermal emission in low energy. They estimated the non-thermal energy content in the electrons of the order of 1.6×10^{30} ergs. On the other hand, Saint and Benz (2005) considering 20 keV as the turnover energy, which is perhaps the same as the break energy (E_b), estimated the non-thermal energy to be $\approx 2 * 10^{30}$ ergs, almost the same value as Sui *et al.* (2005) found for an M1.2 class flare. However, the low-energy cutoff seems physically not realistic as such a configuration leads to plasma instability. Such instabilities have a growth rate typically of the order of local plasma frequency, *i.e.*, orders of magnitude shorter than the propagation time of the beam within the acceleration region. Therefore, the turnover of break energy appears to be more physically realistic and needs to be measured as precisely as possible.

In the context of the above issues of isothermal versus multi-thermal and crucial need of measurement of break energy point I undertook study of M-class flares observed by the Si detector of Solar X-ray Spectrometer (SOXS) experiment onboard the Indian GSAT-2 spacecraft, and could successfully prove that flare plasma in the explosive phase is multi-thermal in nature, primarily in the energy range below 12 keV (break energy). Jain *et al*. (2011) showed break energy varies between 17 and 24 keV depending upon magnitude of the flare and degree of involvement of non-thermal energy process over thermal process.

I have estimated thermal and non-thermal energy release for two flares in greater detail and the same can be related through conductive and radiative cooling of flare plasma as stated above. The analysis suggests that radiative cooling is the dominant mechanism in thermal energy range during the decay phase of the flare.

CHAPTER 5
INVESTIGATING SOLAR VARIABLES AFFECTING TERRESTRIAL ENVIRONMENT

I present the results of an investigation of non-thermal X-ray spectral characteristics of 30 major solar flares (GOES M and X class) of solar cycle 23 observed by RHESSI during the 2002-2006 solar storm events. The relationship between the speed of CMEs and the spectral index (non-thermal) of the associated X-ray solar flares is explored. About 63% of these flare events were followed by SEP enhancement at Earth. I investigate the non-thermal spectral relationship of these flares with SEP spectra observed near earth.

5.1 Solar Activity and its Impact on Earth's Environment: A Brief Overview of Previous Studies:

In 1859, Mr. R. C. Carrington observed the solar flare for the first time while performing the sunspot observations. A strong geomagnetic storm occurred 17 hours and 40 hours later. In his report to the Royal Society, mentioned the potential connection of this solar event with the geomagnetic storm. This discovery can be considered as the beginning of space weather research. Extensive studies have been carried out by many researchers regarding the active phenomena occurring on the sun and their impact on earth's environment.

It has been described in Chapter 1 that the solar flares affect all layers of the solar atmosphere (photosphere, chromosphere, and corona), where the medium plasma is heated to tens of MK and electrons, protons, and heavier ions are accelerated to near the speed of light. They produce radiation across the electromagnetic spectrum at all wavelengths, from radio waves to gamma rays, although most of the energy goes to frequencies outside the visual range and for this reason the majority of the flares are not

visible to the naked eye and must be observed with special instruments. Flares occur in active regions around sunspots, where intense magnetic fields penetrate the photosphere to link the corona to the solar interior. Flares are powered by the sudden (timescales of minutes to tens of minutes) release of magnetic energy stored in the corona. The same energy releases may produce coronal mass ejections (CME), although the relation between CMEs and flares is still not well established (Jain, 2010). Solar flares strongly influence the local space weather in the vicinity of the Earth. They can produce streams of highly energetic particles in the solar wind, known as a solar proton event. These particles can impact the Earth's magnetosphere (cf. Chapter 1), and present radiation hazards to spacecraft, astronauts and cosmonauts. On the other hand, the soft X-ray flux of X class flares increases the ionization of the upper atmosphere, which can interfere with short-wave radio communication and can heat the outer atmosphere and thus increase the drag on low orbiting satellites, leading to orbital decay. Energetic particles in the magnetosphere contribute to the aurora borealis and aurora australis. Energy in the form of hard X-rays, which are generally the result of large plasma ejection in the upper chromosphere, can damage to spacecraft electronics.

The radiation risks posed by coronal mass ejections are major concern in manned mission to Mars, the moon, or other planets. Energetic protons can pass through the human body, causing biochemical damage, and hence present a hazard to astronauts during interplanetary travel. Some kind of physical or magnetic shielding would be required to protect the astronauts. Most proton storms take two or more hours from the time of visual detection to reach Earth's orbit. A solar flare on January 20, 2005 released the highest concentration of protons ever directly measured, taking only 15 minutes after observation to reach Earth, indicating a velocity of approximately one-third light speed, giving astronauts as little as 15 minutes to reach shelter.

Recently, Hanuise *et al*. (2006) studied the impact of 27–28 May 2003 solar events on the magnetosphere, ionosphere and thermosphere and found that the most notable consequences on geospace, including space weather

effects, were (1) the expansion of the auroral oval, and aurorae seen at mid latitudes, (2) the significant modification of the total electron content in the sunlight high-latitude ionosphere, (3) the perturbation of radio-wave propagation manifested by HF blackouts and increased GPS signal scintillation, and (4) the heating of the thermosphere, causing increased satellite drag. Solar activity in AR 10696 (on 4, 6, 7 & 10^{th} November-2004) resulted in two super-intense storms (-373 nT on 8 – November-2004 and -289 nT on 10 – November - 2004) with the SEP intensity later remaining above 10 pfu for about a week. During the intense solar activity in late October 2003 and early November 2003, the highly energetic protons associated with SEP events penetrated into mesosphere and stratosphere where they produced ozone depletion (Jackman *et al*. 2005). These flares associated with CMEs caused geomagnetic storms. Information available from Earth and space science missions indicate that about 59% of the spacecraft and about 18% of the instrument groups experienced some effect from the solar activity between mid-October and early November 2003 (Barbieri & Mahmot, 2004). Saldanha *et al*. (2008) studied the progressive spectral hardening in January 2005 solar flare events and confirmed that the progressive spectral hardening in these flares are related to solar energetic particle (SEP) events. The January 2005 solar activity originated in AR 10720 was followed by geomagnetic storm (~ -100 nT) on 18, 19, 21 and 22 January 2005. All these studies confirm the sun-earth connection suggesting a strong need to explore this connection further to understand the solar variables responsible for the near-earth disturbance.

5.1.1 Flare-CME relationship:

The flare-CME relationship is a big issue in solar physics (Gosling 1993; Hudson *et al*. 1995). Both of these phenomena often occur in conjunction but the exact nature of the flare-CME triggers and the relationship between the cause and consequence is still open and quite puzzling. A temporal relationship between CMEs and Flares has been studied by Zhang *et al*. (2001) suggesting that the impulsive acceleration of the CMEs coincides with the rise phase of the flare. Statistical studies show that CME parameters, like

the speed or kinetic energy, are correlated with characteristics of the associated flare, e.g., the soft X-ray (SXR) peak flux or the integrated flux (Moon *et al*. 2002, 2003; Burkepile *et al*. 2004; Vrˇsnak *et al*. 2005; Chen & Zong 2009; Kay *et al*. 2003). Comparing the X-ray flare fluxes with CME masses of 826 CME/flare paired events, Aarnio *et al*. (2011) found that CME mass increases with flare flux, following an approximately log-linear, broken relationship. Temmer *et al*. (2010) studied three fast coronal mass ejections observed by Solar Terrestrial Relations Observatory (STEREO) and their associated high-energy flare emissions in terms of RHESSI hard X-ray (HXR) spectra and flux evolution. They found that the CME acceleration profile and the flare energy release as evidenced in the RHESSI HXR flux evolve in a synchronized manner. However, the ultimate question still remains open, how and in what form the flare HXR emission (count rate, spectral parameters) is associated with the CME acceleration magnitude, and from where the energy is withdrawn for these two simultaneous events? More recently Jain *et al*. (2010) found that the speed of CMEs increases with plasma temperature (R=0.82) of X-ray flare. They suggested the heating of the coronal plasma appears significant to release CME from the reconnection region where the flare also occurs. They proposed that initiation and speed of CMEs perhaps depend upon the dominant process of conversion of the magnetic field energy of the active region to heating/ accelerating the coronal plasma in the reconnected loops. They addressed very important question related to relationship of flares and CMEs and showed that a flare and associated CME are two components of one-energy release system, perhaps, magnetic field free energy. The above results imply that there exist close physical connections between CME kinematics and flaring processes, at least for a certain class of CME-flare pairs. However, no study has been made on the relationship between the dynamics of CMEs and the high-energy X-ray flare plasma characteristics to address the important question of whether solar flares and associated CMEs are related with impulsive acceleration taking place during reconnection of the magnetized loops? In this context, and in contrast to Jain *et al*., (2010) who employed SOXS data for 4-50 keV, I study the X-ray emission characteristics of solar flares observed by the RHESSI

mission in the energy band 13–100 keV and compare them with dynamics of the associated CMEs.

5.1.2 Flare-SEP relationship:

Solar X-ray flares exhibit mainly two types of spectral behavior: soft-hard-soft (SHS) and soft-hard-hard (SHH). Parks & Winckler (1969) discovered the SHS behavior, in which the spectrum becomes harder in the course of increased emission and is followed by a spectral softening after the peak emission. On the contrary, soft-hard-hard (SHH) behavior is a phenomenon observed in solar flares characterized by the absence of softening as the flux declines. A low spectral index (obtained from the non-thermal power law fit) corresponds to a harder spectrum. Frost & Dennis (1971) observed the progressive hardening exhibited in the hard X-ray spectrum of a solar flare.

Following to pioneering work namely “A new approach for predicting proton events” by Jain (1986) suggesting a special class of flares only produce proton events, Kiplinger (1995) studied the hard X-ray spectral evolution in solar flares and their associations with energetic interplanetary proton events. He employed data from the Hard X-ray Burst Spectrometer (HXRBS) instrument onboard the Solar Maximum Mission (SMM). He found a strong association of hard X-ray progressive spectral hardening with interplanetary proton events. Grigis and Benz (2008) studied the spectral hardening in large solar flares and proposed that the hardening during the decay phase is caused by continuing particle acceleration with longer trapping in the accelerator before escape. Grayson *et al*. (2009) studied 37 magnetically well-connected flares (W30-W90) observed by RHESSI and found that 12 flares of 18 with SHH behavior produced SEP events and none of 19 flares without SHH behaviors produced SEPs.

However, all these studies are based on temporal evolution of spectra, while no study has been carried out in detail to estimating the evolution of the spectral index (hardness parameter) over time and its relation with spectral index of the associated SEP event. Therefore I studied hard X-ray spectra of the flares in greater detail in context to their relationship with the SEPs. I

employed the RHESSI observations for this investigation in the current chapter.

5.2 The Data:

5.2.1 Flare Selection Procedure:

I employed RHESSI X-ray flares for the period of 2002-2006. However, selection of flares is carried out based on their 'Geoeffectiveness' in terms of variation in the disturbance storm time (Dst) index. On the other hand, I used the CME Catalogue of LASCO/ SOHO for firm identification of Flare-CME-Dst association in the current investigation. For the period 2002-2006, I looked for the days on which Dst index ≤ - 50 nT. Then I searched for GOES (M and X class) flares which occurred one to four days prior to the Dst event from the flare-CME-Dst plots from the CME catalog available at http://cdaw.gsfc.nasa.gov/CME_list/.

To illustrate, as an example, I represent the Dst-CME-Flare occurrence during 27-30 May-2003 in Figure 5.1. The Dst plot (top) shows that Dst value reached -144 nT on 29-May-2003 at 24:00 UT. The middle plot shows the height-time plot of CMEs and the bottom panel (in circle) shows three flares: (i) 27-May-2003 at 22:56 UT (X1.3) (ii) 28-May-2003 at 00:17 UT (X3.6) and (iii) 29-May-2003 at 00:51 UT (X1.2) which occurred prior to the Dst event. On the other hand, to establish the flare-CME correlation, following to Jain *et al*. (2010), I considered those events in which the CME onset time was within ±30 minutes (LASCO time cadence constraint) of the flare onset as observed by GOES. Further, on viewing the movies of the GOES soft X-ray plots in 1 - 8 Å band along with the CME time lapse images made available at c2eit_gxray and c2rdif_gxray helped in identifying flare association with CMEs.

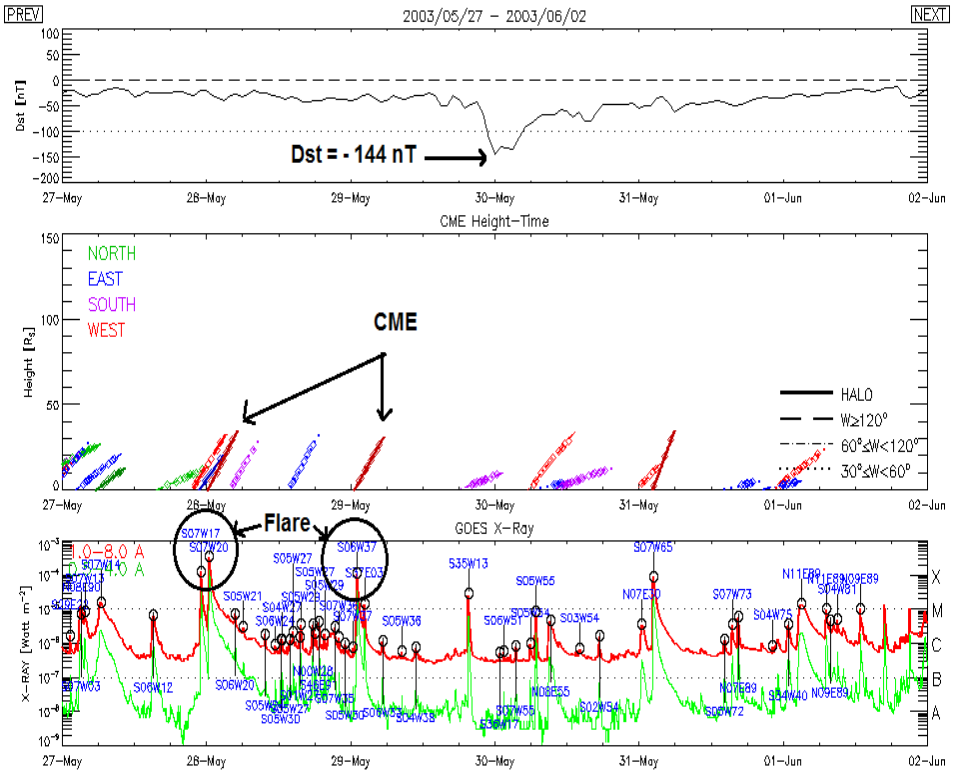

Figure 5.1: Image showing the Dst-CME-flare occurrences during 27-30 May-2003. The Dst plot (top) shows that the Dst value reached -144 nT on 29-May-2003 at 24:00 UT. The middle plot shows the CME height-time and the bottom panel shows GOES soft X-ray light curves. The following three flares are marked in circles: (i) 27-May-2003 at 22:56 UT (X1.3) (ii) 28-May-2003 at 00:17 UT (X3.6) and (iii) 29-May-2003 at 00:51 UT (X1.2) which occurred prior to the Dst event (Image: SOHO LASCO CME Catalog).

In case of non-halo CMEs, the identification was done using the central position angle (CPA) and angular width of the CME. They should be coinciding with the quadrant in which the flare is located. Figure 5.2 shows such an example of 18-March-2003 flare-CME event. The 18-March-2003 flare was located in the south-west quadrant which coincides with the CPA=263° of the CME. The CME onset time (ONSET1) obtained from the catalogue is 12:11:30 which coincides with the flare duration as seen in Figure 5.2 (right).

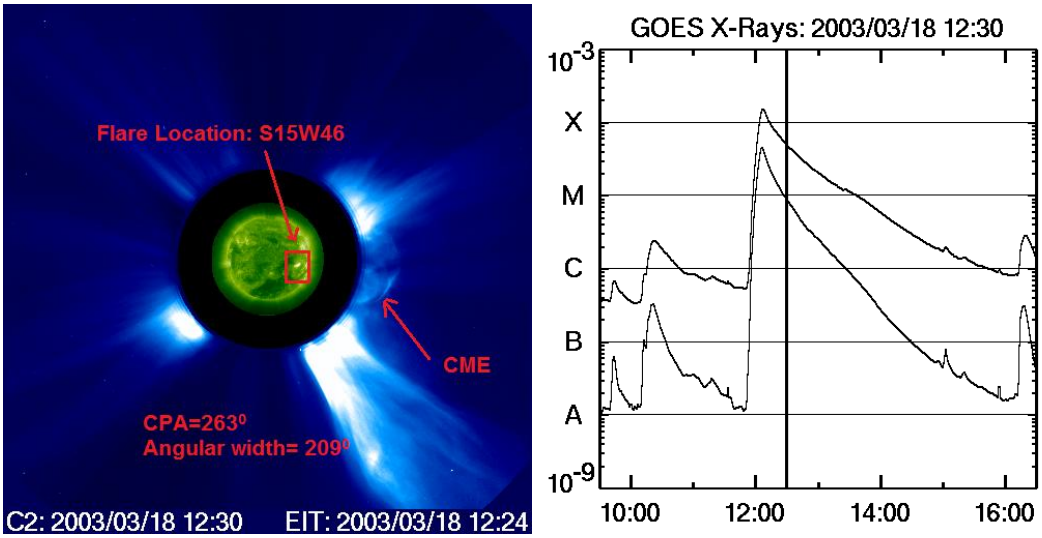

Figure 5.2: A frame of a JavaScript movie of the c2eit_gxray image (left) showing the flare location in the south-west quadrant (S15W46).The GOES soft X-ray light curve (right) with the time of LASCO C2 image at 12:30 UT on 18-March-2003 is shown as a vertical line(Image: SOHO LASCO CME Catalog).

Figure 5.3 shows the 29-May-2003 flare-CME event. The top left of the figure shows a frame of a JavaScript movie of the LASCO C2 image (c2rdif_gxray). It clearly shows a Halo CME prominent in the South-West quadrant. Figure 5.3 (top right) shows the c2eit_gxray image at the same time showing the flare location in the south-west quadrant (S06W37). Figure 5.3 (bottom) shows GOES soft X-ray light curves with the time of the LASCO C2 image at 01:27 UT as a vertical line. Only those flares were short listed which were associated with a CME temporally as well as spatially irrespective of the flare/CME location (east-west) on the sun.

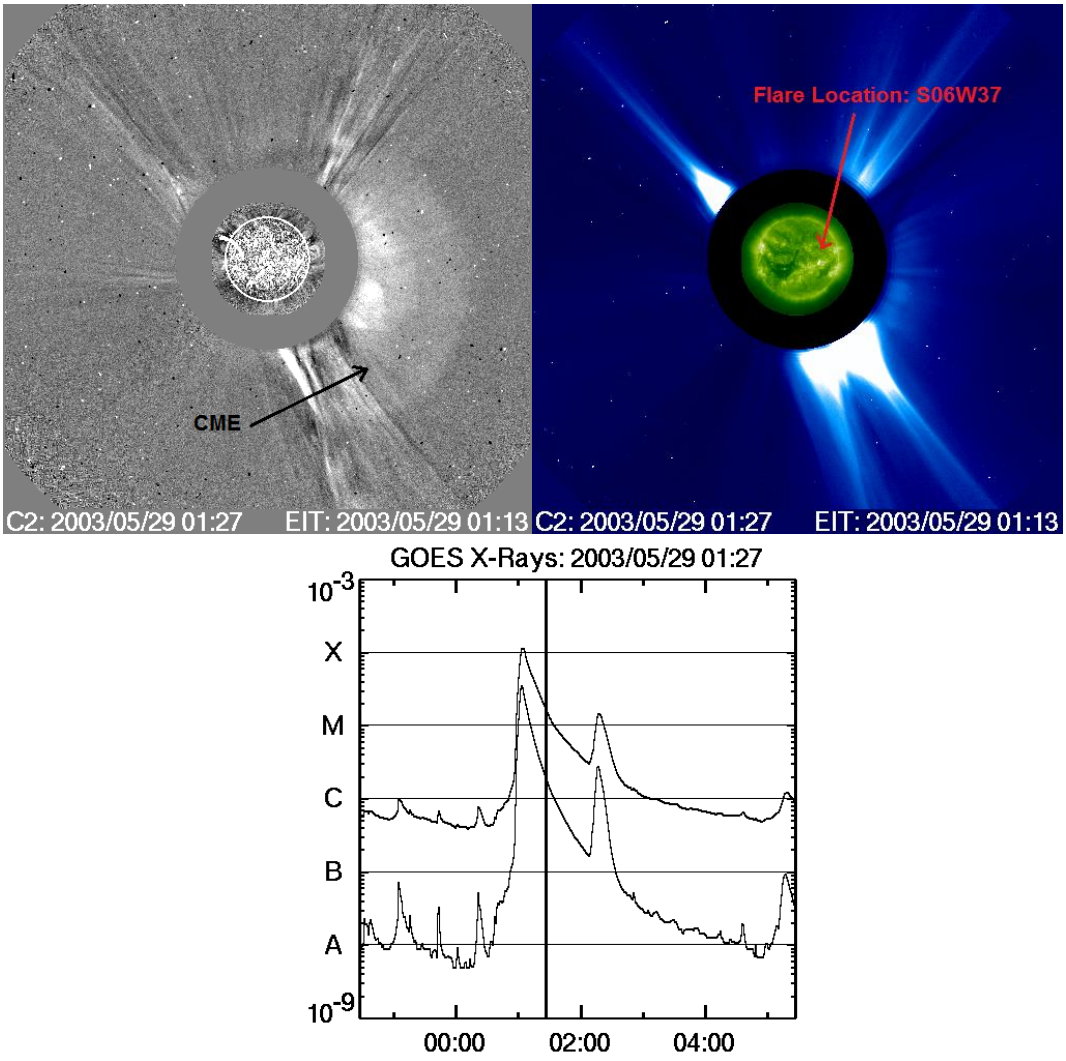

Figure 5.3: A frame of a JavaScript movie of the LASCO C2 c2rdif_gxray image (top left) of 29-May-2003 event. It clearly shows a Halo CME prominent in the South-West quadrant. The c2eit_gxray image (top right) at the same time showing the flare location in the south-west quadrant (S06W37).The GOES soft X-ray light curve (bottom) with the time of LASCO C2 image at 01:27 UT shown as a vertical line (Image: SOHO LASCO CME Catalogue).

About 70 flares were found to be associated with a CME and satisfying the above selection criteria. Now, in order to get hard X-ray data, simultaneously, I looked for the flares that were observed by RHESSI during the GOES flare interval. However, I could succeed in getting reasonably good observations for 40 flares only due to several constraints of RHESSI such as period to be spent in the eclipse and SAA (South Atlantic Anomaly), and thereby either missing the flares completely or rise and/ or peak of many flares.

Using RHESSI IDL routine, I generated the count spectra for all these flares employing the techniques described in chapter 3. In some flares, the generated count spectrum was not of good quality due to poor photon statistics and therefore I did not consider them for analysis. On the other hand, in some flares, the spectral analysis could be done in 13-40 keV only as the background supersedes above 50 keV. Such flares were not well-observed in 50-100 keV energy range. Considering all such difficulties of observations finally I was then left with a sample of 27 flares. However, over and above this set of flares, three flares were added with an exemption from the above mentioned selection criteria. (i) 23 July 2002 (Dst = -31 nT) flare was an X class flare associated with a CME and hence a valuable data set. (ii) 22 and 23 October 2003 flares (corresponding Dst = -44 nT on 24-October-2003 and -49 nT on 25-October-2003) were considered owing to the space weather impacts of late October 2003 events. Finally, I had 30 flares, 15 flares with partial coverage and 15 flares with full RHESSI coverage.

5.2.2 Dataset:

Table 5.1 lists the physical parameters of 30 X-ray flares observed by RHESSI and associated CMEs. For the spectral analysis, I used the data from detector 4 (reason mentioned earlier in chapter 3) for almost all flares except for 19-December-2002 (5F), 22-October-2003 (5F) and 27-July-2005 (9F). Columns c, d and e show the start, peak and end times of the flare under investigation. The start and end times were taken from the RHESSL flare list. The peak time (column d) and peak flux in column f in counts $(4s)^{-1}$ were determined in 12-25 keV energy band. The peak time is the time of maximum flux in 12-25 keV energy band. Sometimes there were two peaks with equal emission. In that case, the time of the earliest peak has been considered. Column g, h and i show the GOES class, flare location and NOAA active region (AR) respectively. The details of the flare associated CME are given in columns j to m (onset time in j, central position angle CPA (degree) in k, angular width (degree) in l and linear speed (km s^{-1}) in m). Column n shows the Dst index 1-4 days after the flare-CME event.

Table 5.1 (Details of Flares, CMEs and geomagnetic activity)

a	b	c	d	e	f	g	h	i	j	K	l	m	n
S.No.	Date	Start	Peak (12-25keV)	End	Peak flux (12-25 keV) Counts /(4s)	GOES class	Location	NOAA AR	LASCO CME onset time (ONSET1)	LASCO CME CPA (degree)	LASCO Angular width (degree)	LASCO CME Velocity (km/s)	Dst index nT
1	23/Jul/2002	00:18:44	0:35:50	1:16:08	55297	X4.8	S13E72	10039	00:27:06	HALO	360	2285	-31
2	19/Dec/2002	21:32:48	21:45:54	22:32:44	900	M2.7	N15W09	10229	21:27:05	HALO	360	1092	-75
3	18/Mar/2003	11:55:44	12:06:30	12:21:48	12038	X1.5	S15W46	10314	12:11:30	263	209	601	-64
4	27/May/2003	23:02:52	23:05:46	00:00:32	3738	X1.3	S07W17	10365	22:56:37	HALO	360	964	-144
5	29/May/2003	00:42:16	1:06:06	1:45:12	8174	X1.2	S06W37	10365	00:46:03	HALO	360	1237	-150 to -50
6	15/Jun/2003	23:43:32	23:50:50	00:23:36	6365	X1.3	S07E80	10386	23:39:40	HALO	360	2053	-141
7	17/Jun/2003	22:23:48	22:50:22	23:07:16	19609	M6.8	S07E57	10386	22:38:53	HALO	360	1813	-50
8	19/Oct/2003	16:38:20	16:40:30	17:38:44	7012	X1.1	N08E58	10484	16:27:13	34	150	472	-61
9	22/Oct/2003	19:55:04	19:59:38	20:37:44	9412	M9.9	S18E78	10486	19:43:42	93	134	1085	-44
10	23/Oct/2003	19:56:44	19:57:54	20:32:28	1179	X1.1	S21E88	10486	19:42:43	103	95	1136	-49
11	24/Oct/2003	02:47:12	02:49:57	03:22:04	2664	M7.6	S9E72	10486	02:34:26	113	123	1055	-52
12	28/Oct/2003	10:37:00	11:13:33	11:30:12	73012	X17.2	S16E08	10486	11:06:20	HALO	360	2459	-353
13	29/Oct/2003	20:35:56	20:44:38	21:08:24	58421	X10.0	S15W02	10486	20:41:22	HALO	360	2029	-383
14	2/Nov/2003	17:08:48	17:18:42	17:29:24	56664	X8.3	S14W56	10486	17:19:52	HALO	360	2598	-69
15	3/Nov/2003	9:43:44	9:51:13	10:01:40	61388	X3.9	N08W77	10488	9:53:17	293	103	1420	-69

Table continued on next page……...

a	b	c	d	e	f	g	h	i	j	k	l	m	n
S.No.	Date	Start	Peak (12-25keV)	End	Peak flux (12-25 keV) Counts /(4s)	GOES class	Location	NOAA AR	LASCO CME onset time (ONSET1)	LASCO CME CPA (degree)	LASCO Angular width (degree)	LASCO CME Velocity (km/s)	Dst index nT
16	6/Jan/2004	6:10:28	6:26:01	6:31:28	10040	M5.8	N05E90	10537	5:58:00	88	166	1469	-69
17	15/Jul/2004	1:12:44	1:39:50	2:25:48	5266	X1.8	S10E54	10649	1:34:47	101	113	584	-80
18	21/Jul/2004	23:52:56	0:30:02	0:55:28	6872	M9.1	N03E17	10652	0:44:19	184	83	492	-101
19	4/Nov/2004	22:29:48	23:01:41	23:30:24	6574	M5.4	N08E18	10696	23:01:01	338	>293	1055	-373
20	6/Nov/2004	0:11:48	0:31:14	1:06:04	1562	M9.3	N09E05	10696	0:52:37	HALO	360	818	-373
21	7/Nov/2004	16:22:48	16:29:02	16:32:20	363	X2.0	N09W17	10696	16:22:12	HALO	360	1759	-289
22	10/Nov/2004	2:01:24	2:10:09	2:40:24	13531	X2.5	N09W49	10696	2:08:28	HALO	360	3387	-109
23	15/Jan/2005	22:22:20	22:48:58	23:17:40	3907	X2.6	N15W05	10720	22:40:25	HALO	360	2861	-74
24	17/Jan/2005	9:35:36	9:47:17	10:38:28	3605	X3.8	N15W25	10720	9:43:00	HALO	360	2547	-121
25	19/Jan/2005	7:57:20	8:15:02	9:03:24	18384	X1.3	N15W51	10720	8:08:30	HALO	360	2020	-99
26	20/Jan/2005	6:33:00	6:48:17	7:27:12	63914	X7.1	N14W61	10720	6:08:58	HALO	360	882	-105
27	13/May/2005	16:36:28	16:52:48	17:14:20	1189	M8.0	N12E11	10759	16:47:00	HALO	360	1689	-263
28	17/May/2005	2:32:20	2:37:34	3:08:28	1179	M1.8	S15W00	10763	2:13:17	252	89	1689	-103
29	27/Jul/2005	4:49:56	4:57:38	5:42:12	9337	M3.7	N11E90	10792	4:41:21	HALO	360	1787	-50
30	13/Dec/2006	2:28:12	2:32:30	3:30:56	43926	X3.4	S06W23	10930	2:25:03	HALO	360	1774	-139

5.3 Exploring the Flare-CME relationship: Observations, Analysis and Results:

In order to study the non-thermal characteristics of the selected flares mentioned in Table 5.1, I performed the spectral analysis of these flares 1-2 minutes before the flare peak determined in 12-25 keV energy band. Figure 5.4 shows the light curve of 29- October-2003 solar flare in two energy bands (12-25 and 25-100 keV). In Figure (5.4), the energy range 12-25 keV (red) corresponds to the thermal emission while the non-thermal component is characterized by higher energy range of 25-100 keV.

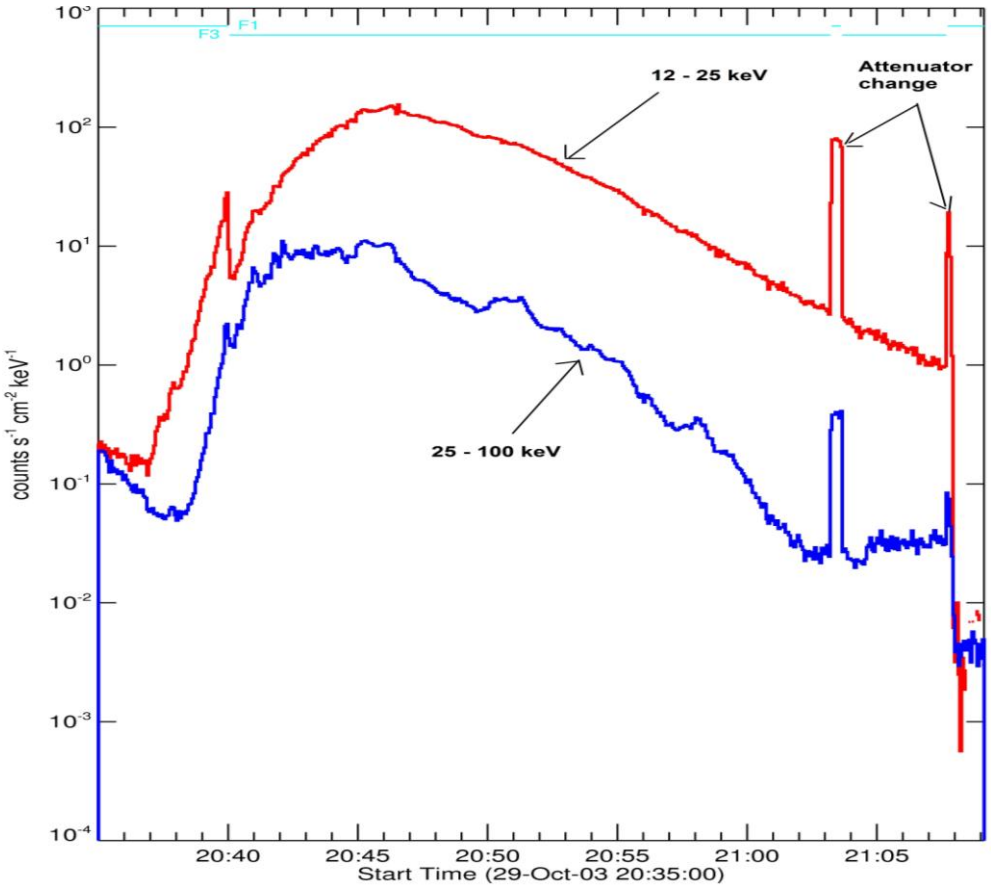

Figure 5.4: RHESSI X-ray light curve of 29-October-2003 in the energy range 12-25 keV (red) and 25-100 keV (blue) using detector 4F.

To simplify the analysis by avoiding the issues of detector cross-calibration, I performed the analysis using a single detector. In the 29-October-2003 flare event, I used the detector 4F, which had the best nominal front-segment resolution (~0.98 keV). This flare was observed in two

attenuator states A1 and A3 states. The spectral analysis techniques for RHESSI data are described in detail in chapter 3. I generated the count spectrum through hessi IDL routine, using 1 keV wide energy bin for the energy range 12-100 keV, and 4s time bins. Before fitting the data, I corrected the observed counts for pulse pileup and decimation. The spectra were fitted in the energy range 13 to 100 keV (reason mentioned in chapter 4 (4.3.2)) to the energy where S/N>1. Systematic uncertainty is set to 0.00 but in some cases where the model fitted excellently but the chi-squared value was > 3, setting the uncertainty to 0.01 or 0.02 minimized the value of chi-squared. The spatially integrated count flux spectra are fitted between 13-100 keV using the combination of isothermal component (Variable thermal model vth**)** and a single power law which yields the following four free parameters: Isothermal components: Emission measure EM (10^{49} cm^{-3}) and plasma temperature T (keV) and non-thermal components: normalization at epivot (photon flux of first power-law at epivot F_{50}= 50 keV) and spectral index γ (slope of the power-law).

The free parameters are varied until a reasonably good fit is obtained. The fits were considered acceptable if reduced chi-squared ≤ 3. The peak time in 12-25 keV energy range of 29-October-2003 flare was 20:44:38 UT with a peak flux of 58421 counts $(4s)^{-1}$. Figure 5.5(top) shows the observed count spectrum before the peak for 29-October-2003 flare event integrated over a time interval from 20:44:04 to 20:44:36 UT. The spectrum is fitted with isothermal plus single power-law model. The vth function (green), 1pow (yellow), and their total (red) fit to the observed spectrum (black) are shown. The middle panel of Figure 5.5 shows the photon spectrum derived from the forward fit of the count spectrum and the residual plot after fitting is shown in the bottom panel of Figure 5.5.

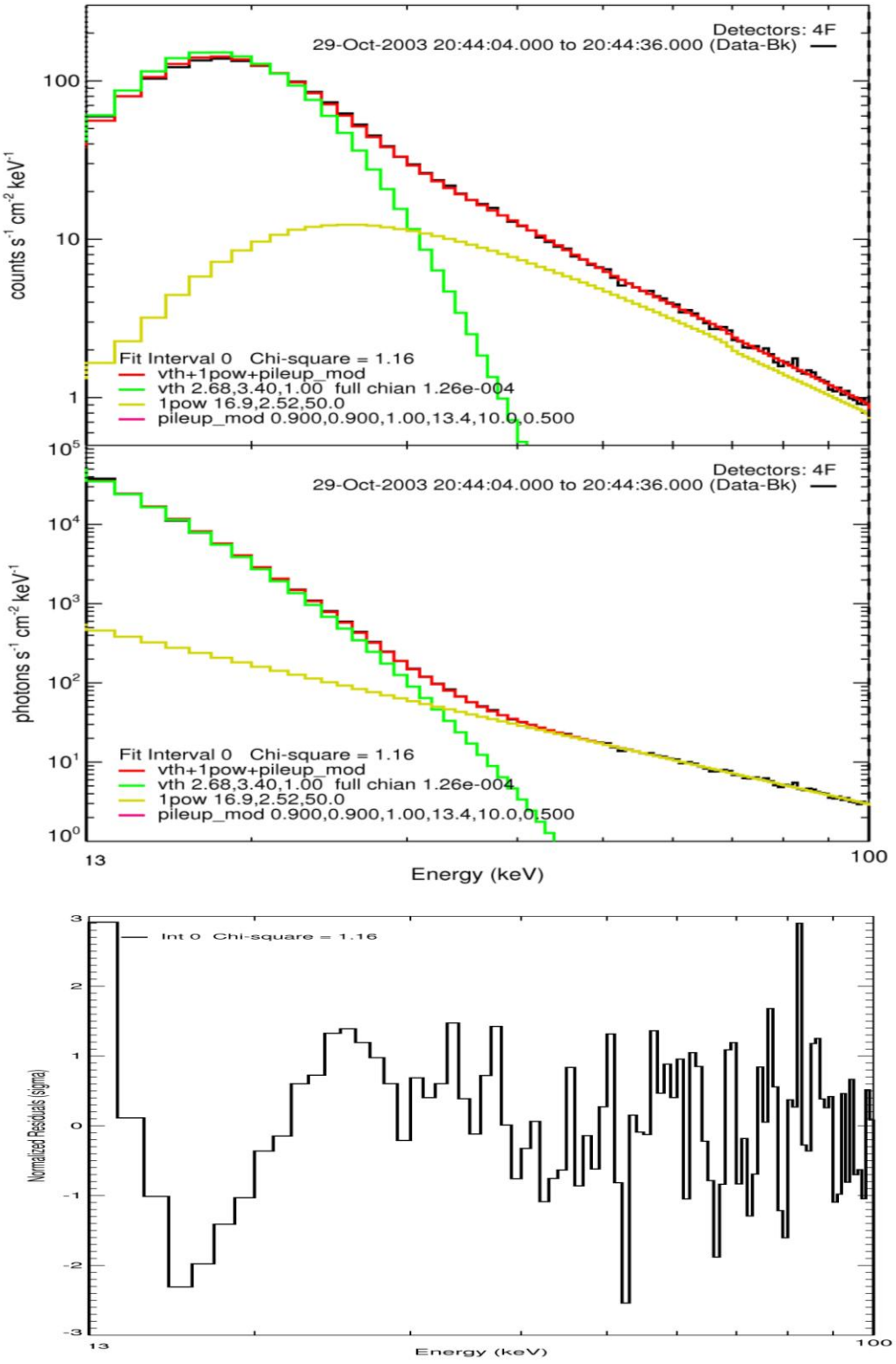

Figure 5.5: RHESSI Count spectrum (top) of 29-October-2003 for the time interval just before the peak is fitted with vth+1pow function in the energy range 13-100 keV. The vth function (green), 1pow (yellow), and their total (red) fit to the observed spectrum (black) are shown. The middle plot shows the photon spectrum with model fits. The fitted parameters are given in the legend (left corner). Normalized residuals for each energy bin are shown in the bottom plot.

In this way, I obtained the non-thermal spectral index γ for all 30 flares analyzed before the peak time of the flare. While majority of the flares were fitted with isothermal plus single power-law model, I observed that there was a break in energy at about 50 keV in the 28-October-2003 in the spectrum accumulated before the peak (11:13:33 UT) and therefore I fitted the spectrum with isothermal plus a broken power-law model. In that case, the spectral index above the break energy was considered for investigation.

Though the fits were performed with an isothermal plus a single power-law (or broken power-law), I have explored only the non-thermal spectral index γ (hardness parameter) for the current investigation in contrast to investigation of CME dynamics with flare plasma temperature which has already been carried out earlier by Jain *et al*. (2010).

Figure 5.6 shows the relationship between the spectral index γ obtained from the fitted spectra for 30 flares and the associated CME linear speed. I obtained the best fit to the plot which is a power-law fit with a correlation coefficient of 0.77. This statistically significant relationship can be expressed in the following form:

$$\gamma = (134.9 \pm 65.3)v^{(-0.5\pm0.07)} \qquad (5.1)$$

I observed that the peak flux for the selected 30 flares varied between 363 and 73012 c $(4s)^{-1}$ in the energy range of 12-25 keV. I observed that the correlation improved to 0.84 when the events were classified in terms of peak flux in 12-25 keV energy range < 11000 c $(4s)^{-1}$. Figure 5.7 shows a strong correlationship between γ and v for the flares whose flux is <11000 c $(4s)^{-1}$.

$$\gamma = (276.2 \pm 160.2)v^{(-0.6\pm0.1)} \qquad (5.2)$$

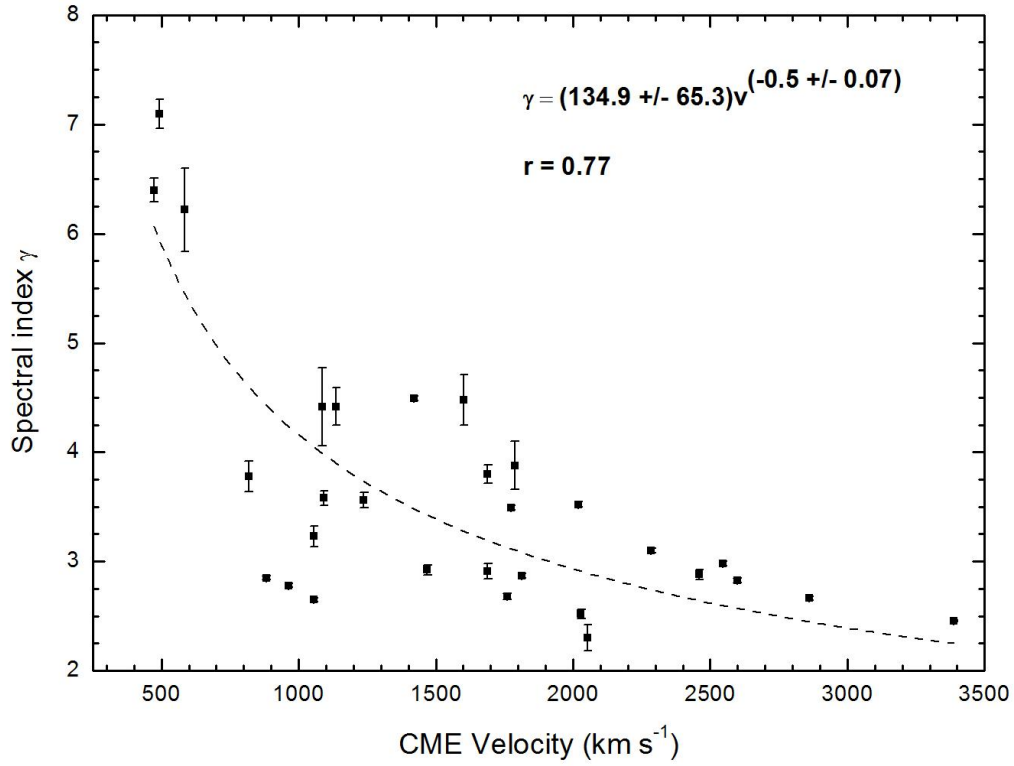

Figure 5.6: The spectral index obtained from the fitted spectra for 30 flares is plotted as a function of the associated CME linear speed. The best fit is a power-law relationship with r = 0.77.

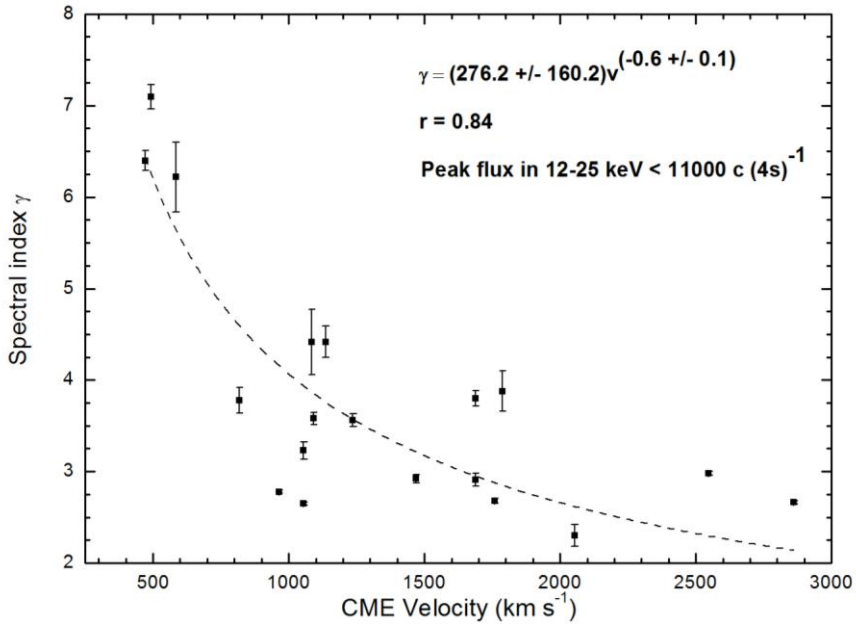

Figure 5.7: The spectral index plotted as a function of CME speed for 19 flare-CME pairs. The peak photon flux in 12-25 keV for these 19 flares is <11000 c $(4s)^{-1}$. The best fit is a power-law relationship with r = 0.84.

This analysis with new perspectives of relationship of high energy processes with coronal mass ejections, which affect the terrestrial environment, suggests that the flare and CME seed population are closely associated and they may be considered as a composite event. The association of non-thermal flare plasma to kinematics of a CME in addition to the temperature of the flare plasma suggests that high energy processes of the solar explosion leading to X-ray emission may be a better tool to predict the geomagnetic storm.

5.4 Investigation of Flare-SEP relationship: Observations, Analysis and Results:

Recent investigations show that flare X-ray emission may be a good tool to predict SEPs (*cf*. section 5.1.2). This motivated me to explore the physical relationship of the flare events listed in Table 5.1 with the proton enhancement observed near the earth. I found that 19 flares were followed by a SEP event. Following to the definition of Grayson, Krucker and Lin (2009) for the selection of SEP events I also considered those SEP events in which the proton flux enhancement at energies > 10 MeV exceeded the background flux (0.1 particles cm^{-2} s^{-1} sr-1) as observed by GOES. GOES temporal mode observations reveals proton flux (particles cm^{-2} s^{-1} sr^{-1} MeV^{-1}) as a function of time for fixed energy bands (0.8 – 4, 4 – 9, 9 – 15, 15 – 40, 40 – 80, 80 – 165 and 165 - 500 MeV). I have considered the typical background flux level to be ~ 0.1 (particles.cm^{-2} s^{-1} sr^{-1}) for all energy bands in the energy range 2.4-332 MeV above which the particle enhancement is observed.

SEP events were determined from in situ proton observations by GOES. Figure 5.8 (top) shows the GOES11 proton flux plot for 13-December-2006 SEP event. The proton enhancement in >10, >50 as well as >100 Mev is seen at about 3:00 UT. This enhancement occurred following the 13-December-2006 flare (X3.4) event that also observed by GOES X-ray detector in Figure 5.8 (bottom).

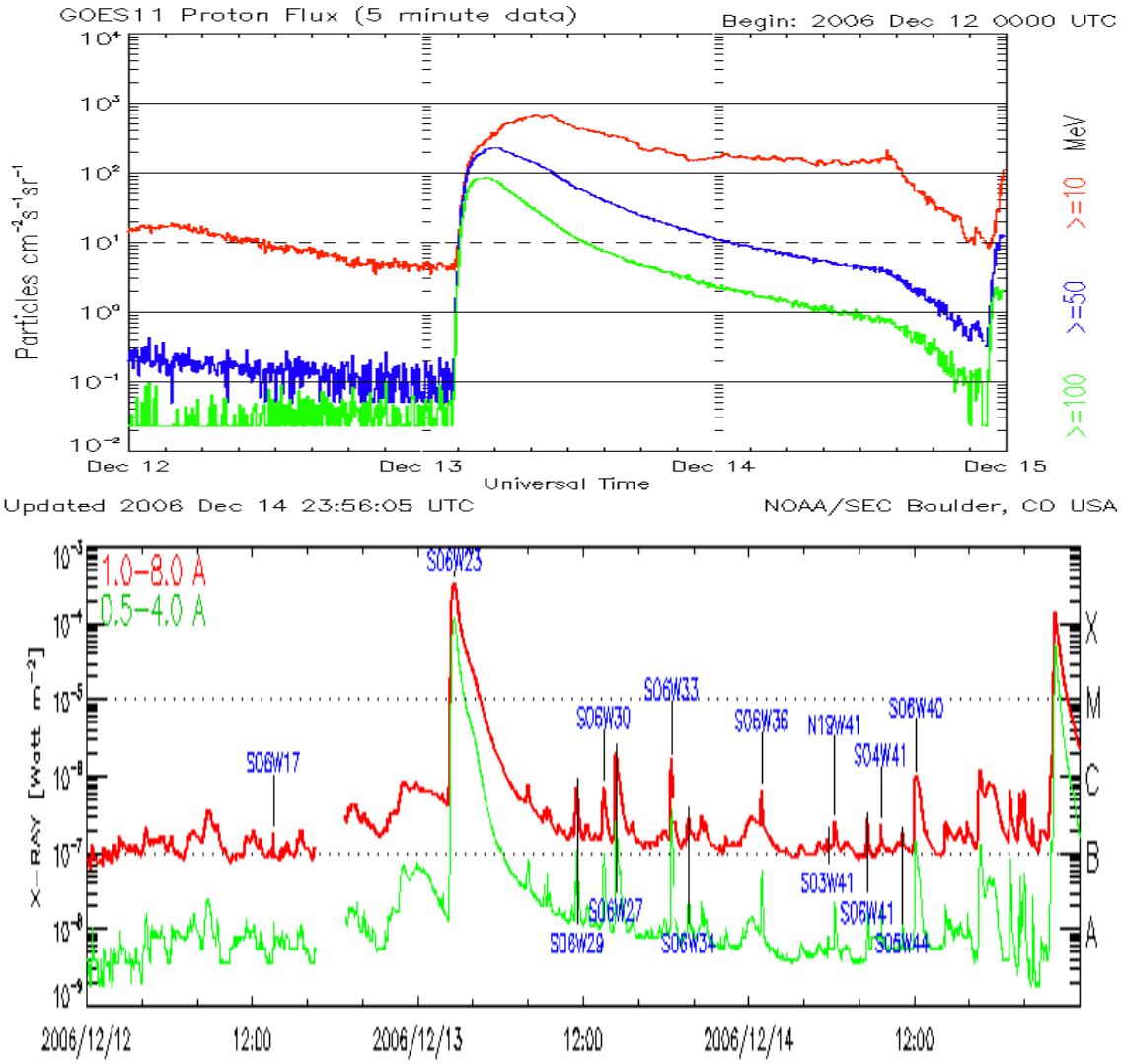

Figure 5.8: GOES Proton flux (top) enhancement at energies >10, >50 and >100 Mev as seen at about 3:00 UT on 13-December-2006. The bottom panel shows the 13-December-2006 flare (X3.4) event as observed by GOES. (Image: SWPC/NOAA (top) and SOHO/ LASCO-CME-CATALOGUE (bottom)).

The short listed flare events out of the 30 flare events in Table 5.1 which were followed by SEP arrival at earth are shown in Table 5.2. Table 5.2 gives the details of the flare and related SEP events. The flare event date and its start time are given in column b and c. Peak Flux of the flare at 50 keV in counts/ (4s) is given in column d, flare location in e, SEP event start time (approximate) in f, and the energy range in which the proton flux was observed is given in column g. Column h shows the remarks (selected or rejected).

During the analysis, I found that in 19 December 2002, 17 June 2003, 22-24 October 2003 and 21 July 2004 flare/SEP events, the proton enhancement was observed only upto 12 MeV. This would give a poor spectrum with only 3 energy channels in the low energy range 0.8-15 MeV. Hence these events were not used in the spectral analysis. The 27-July-2005 event was also dropped owing to the extremely low flux (F_{50} ~ 9.8 c $(4s)^{-1}$). I would like to mention here that after the above mentioned criteria being satisfied, I observed that all the neglected flare events followed by SEP event at earth were located in the E17°-E90° solar longitude and the remaining 12 flares were located in E11°-W61° solar longitude. This is in agreement to the general scenario according to which the west side active phenomenon producing SEPs are likely to reach the earth. Jain (1986) proposed that when the CME is launched in the western hemisphere of the Sun, the CME accelerated energetic particles propagate along the curved Parker spiral interplanetary magnetic field and they are likely to reach the Earth. Finally, I was left with a sample of 12 flare-SEP pairs for investigation. The flare flux at 50 keV for these 12 events ranged from ~ 37 c $(4s)^{-1}$ in 13-May-2005 flare event to as high as ~ 739 c $(4s)^{-1}$ for the 20-January-2005 flare which is found to be associated with the hardest proton event observed at earth.

Table 5.2 (Details of Flares and SEP events)

a	b	c	d	e	f	g	h
S.No.	Flare Date	Start	Peak Flux at 50 keV in counts/ (4s)	Location	SEP Event (start)* (Day/UT)	Energy range in which proton flux was observed	Remarks
1	19/Dec/2002	21:32:48	15	N15W09	19Dec/2300	>10	rejected
2	27/May/2003	23:02:52	83	S07W17	28May/600	>10, >50	selected
3	29/May/2003	00:42:16	93	S06W37	29May/1600	>10, >50	selected
4	17/Jun/2003	22:23:48	172	S07E57	18Jun/0900	>10	rejected
5	22/Oct/2003	19:55:04	26	S18E78	22Oct/2100	>10	rejected
6	23/Oct/2003	19:56:44	13	S21E88	24Oct/0300	>10	rejected
7	24/Oct/2003	2:47:12	78	S9E72	24Oct/0300	>10	rejected
8	28/Oct/2003	10:37:00	174	S16E08	28Oct /1215	>10, >50, >100	selected
9	29/Oct/2003	20:35:56	581	S15W02	29oct/2100	>10, >50, >100	selected
10	2/Nov/2003	17:08:48	621	S14W56	2nov/1800	>10, >50, >100	selected
11	21/Jul/2004	23:52:56	20	N03E17	22Jul/1800	>10	rejected
12	7/Nov/2004	16:22:48	339	N09W17	7Nov/1910	>10, >50, >100	selected
13	10/Nov/2004	2:01:24	244	N09W49	10nov/0300	>10, >50, >100	selected
14	15/Jan/2005	22:22:20	249	N15W05	Jan16/0210	>10, >50, >100	selected
15	17/Jan/2005	9:35:36	520	N15W25	17jan/1200	>10, >50, >100	selected
16	20/Jan/2005	6:33:00	739	N14W61	20jan/0700	>10, >50, >100	selected
17	13/May/2005	16:36:28	37	N12E11	May13/1800	>10, >50	selected
18	27/Jul/2005	04:49:56	9.8	N11E90	27Jul/2200	>10, >50	rejected
19	13/Dec/2006	2:28:12	255	S06W23	13Dec/0310	>10, >50, >100	selected

* indicates the approximate SEP event onset time

5.4.1 Flare Spectral Analysis:

In this section, the events were studied with prime importance given to the hardness parameter γ in the non-thermal energy range of 50-100 keV. The non-thermal emission is considered to be significant above the 50 keV energy range. I carried out the spectral analysis of all the 12 flares for the flare duration in order to obtain the temporal evolution of the spectral index. The flare time interval was divided into appropriate subintervals and I studied their respective spectra in the energy range 13-100 keV. I took extreme care that an attenuator does not change during the selected time interval for forming the spectra. The non-thermal hard X-ray energy range was determined individually for each flare interval before fitting by S/N ratio to ensure that the signal did not mix with the background. Now considering forward fitting method I carried out spectra fitting in the energy range 13 to 100 keV (*cf*. chapter 4 (4.3.2)), however, depending upon the goodness of the S/N ratio. I considered the spectra-fit to be good if $\chi^2 \leq 3$ by setting systematic uncertainty to 0.00, and if $\chi^2 > 3$, then setting the uncertainty to 0.01 or 0.02 to minimize the χ^2 to <3. The spatially integrated count flux spectra are fitted between 13-100 keV using the combination of isothermal component (*Variable thermal model vth***)** and a single power law which yields the following four free parameters. Isothermal component: Emission measure EM (10^{49} cm^{-3}) and plasma temperature T (keV), and non-thermal component: normalization at epivot (photon flux of first power-law at epivot F_{50}= 50 keV), and spectral index γ (slope of the power-law). The free parameters were varied until a reasonably good fit was obtained. The fits were considered acceptable if reduced chi-squared ≤ 3. Majority of the flares were best fitted with isothermal plus single power-law model. However, in some flares, a break in the non-thermal part of the spectrum was observed during some temporal interval of the flare duration (e.g. 17-January-2005, 20-January-2005). In that case, I fitted the spectrum for that particular time interval with isothermal plus a broken power-law model. In the case of broken power-law fit, the spectral index above the break energy was considered for investigation. Even though the fits were performed with an isothermal plus a single power-law (or broken power-law), I have explored the temporal evolution of non-thermal spectral

index γ in 50-100 keV energy range for the current investigation. Figure 5.9 shows the light curve (top) of 13-December-2006 flare and the temporal evolution (bottom) of spectral index γ in the energy range 50-100 keV.

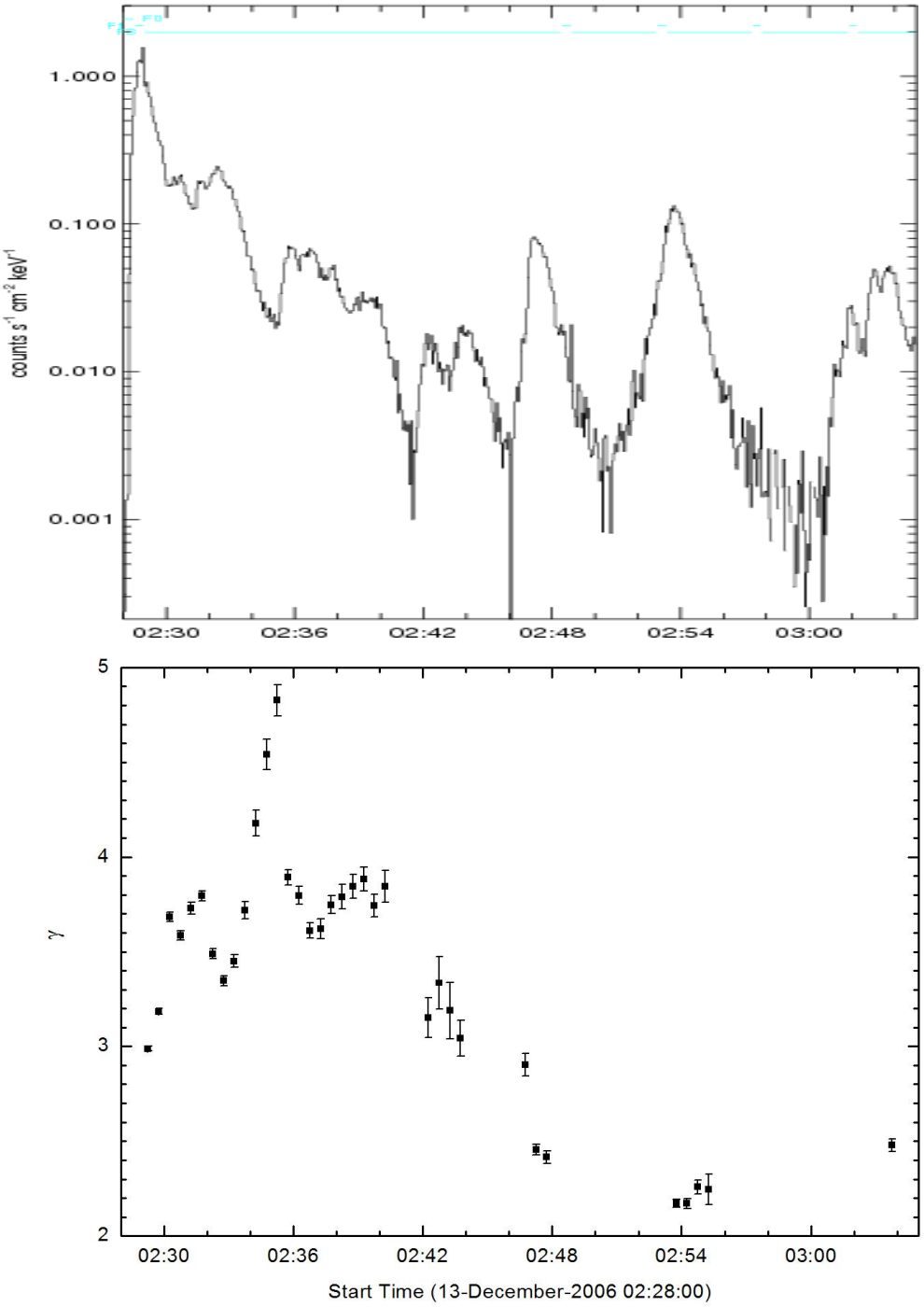

Figure 5.9: The light curve (top) and temporal evolution of the spectral index γ (bottom) 13-December-2006 flare in 50-100 keV energy range.

Out of all the fitted spectra for a particular flare, I considered the hardest spectra (the one in which the spectral index was minimum) in the 50-100 keV energy range. In the case of 13-December-2006 flare, the spectrum was hardest during the decay phase of the flare from 02:54:00 -02:54:28 UT with the value of spectral parameter γ equal to 2.16 ± 0.027. Similarly, I carried out the spectral analysis for the remaining 11 flares. Figure 5.10 to Figure 5.20 show the light curve as well as the temporal evolution of the spectral index γ in 50-100 keV energy range. The fitted spectra which gave the hardest value of spectral index γ for all flares are given in Appendix A.

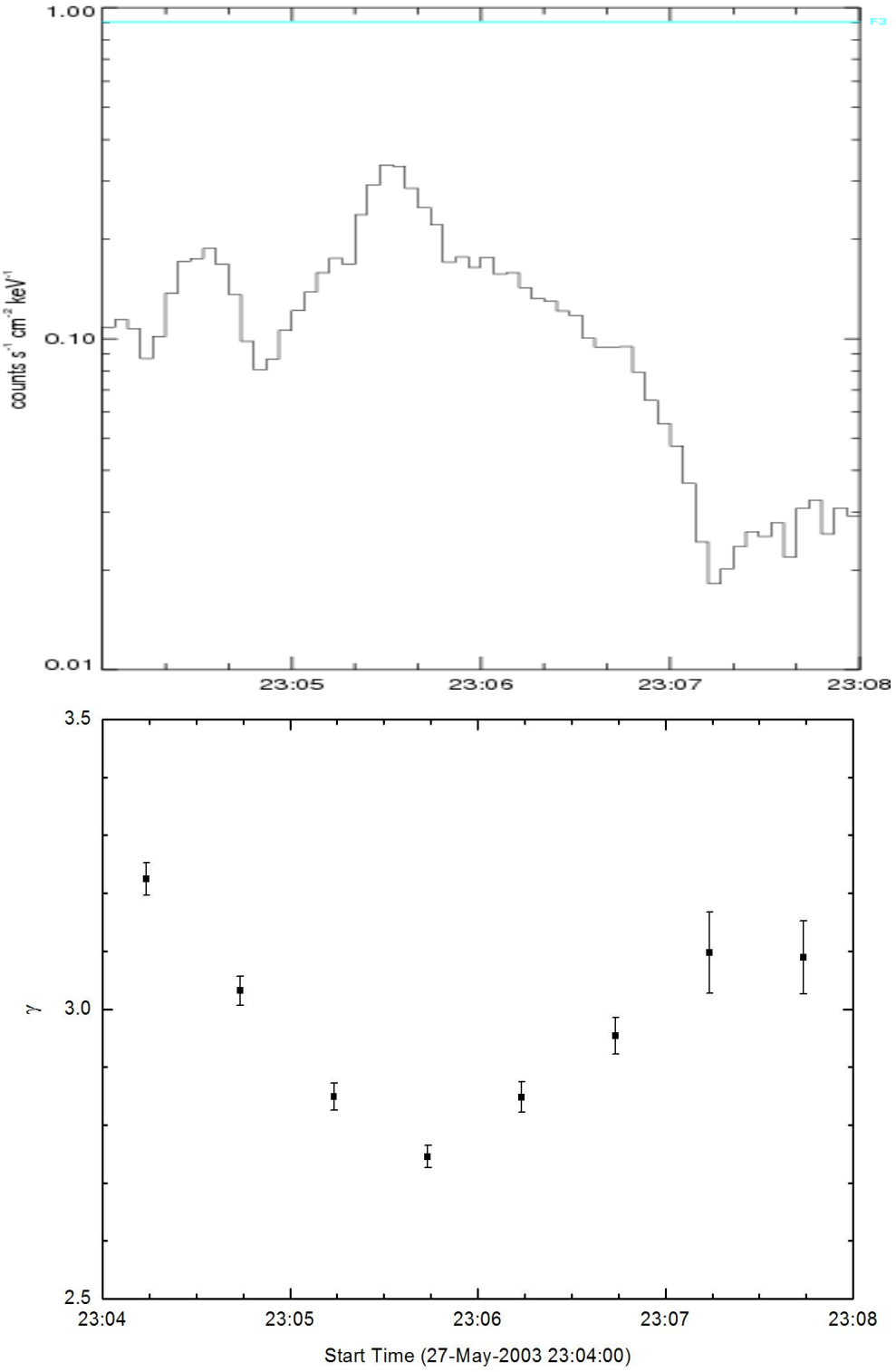

Figure 5.10: The light curve (top) of 27-May-2003 and temporal evolution of the spectral index γ (bottom) in 50-100 keV energy range.

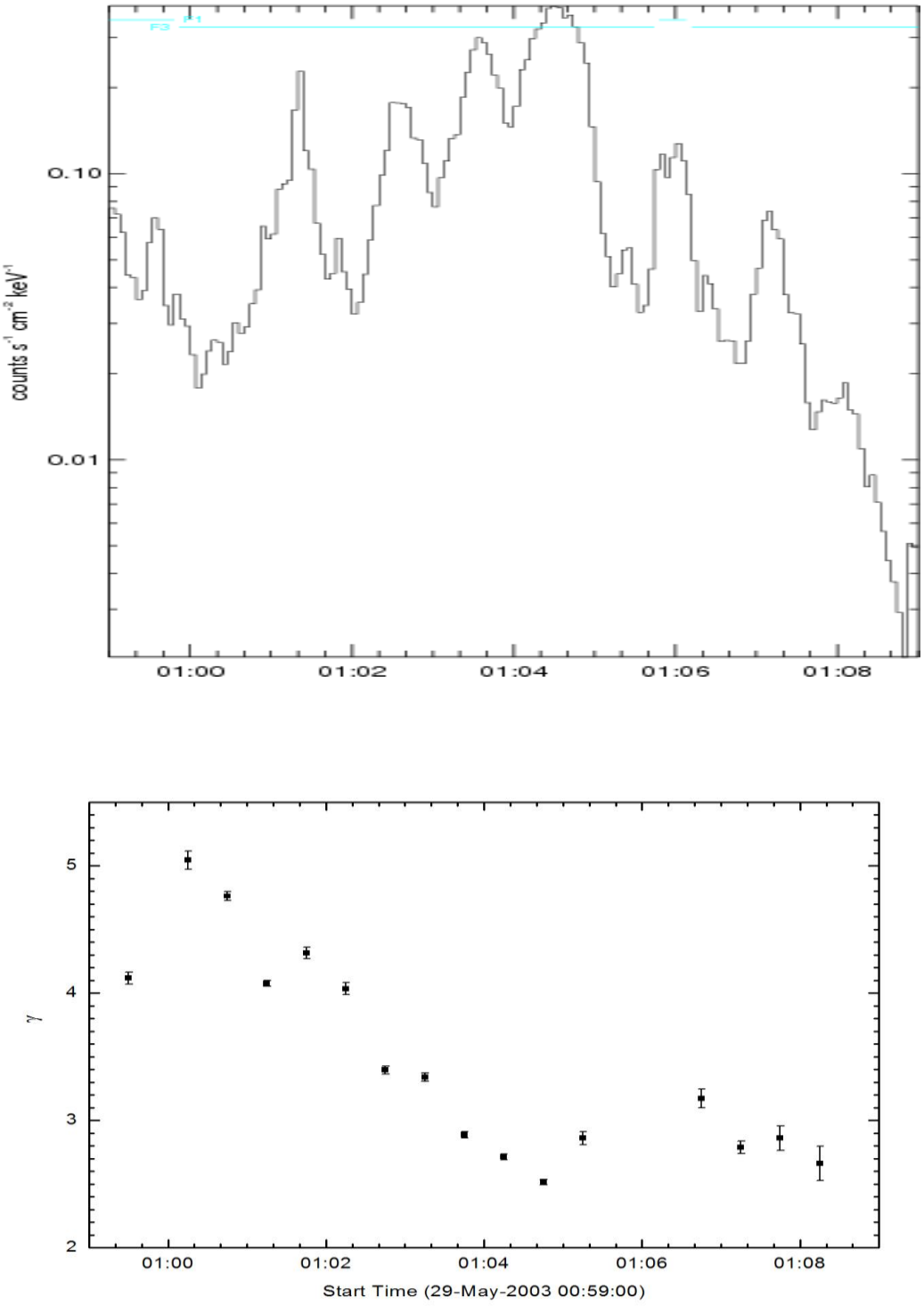

Figure 5.11: The light curve (top) and temporal evolution of the spectral index γ (bottom) of 29-May-2003 in 50-100 keV energy range.

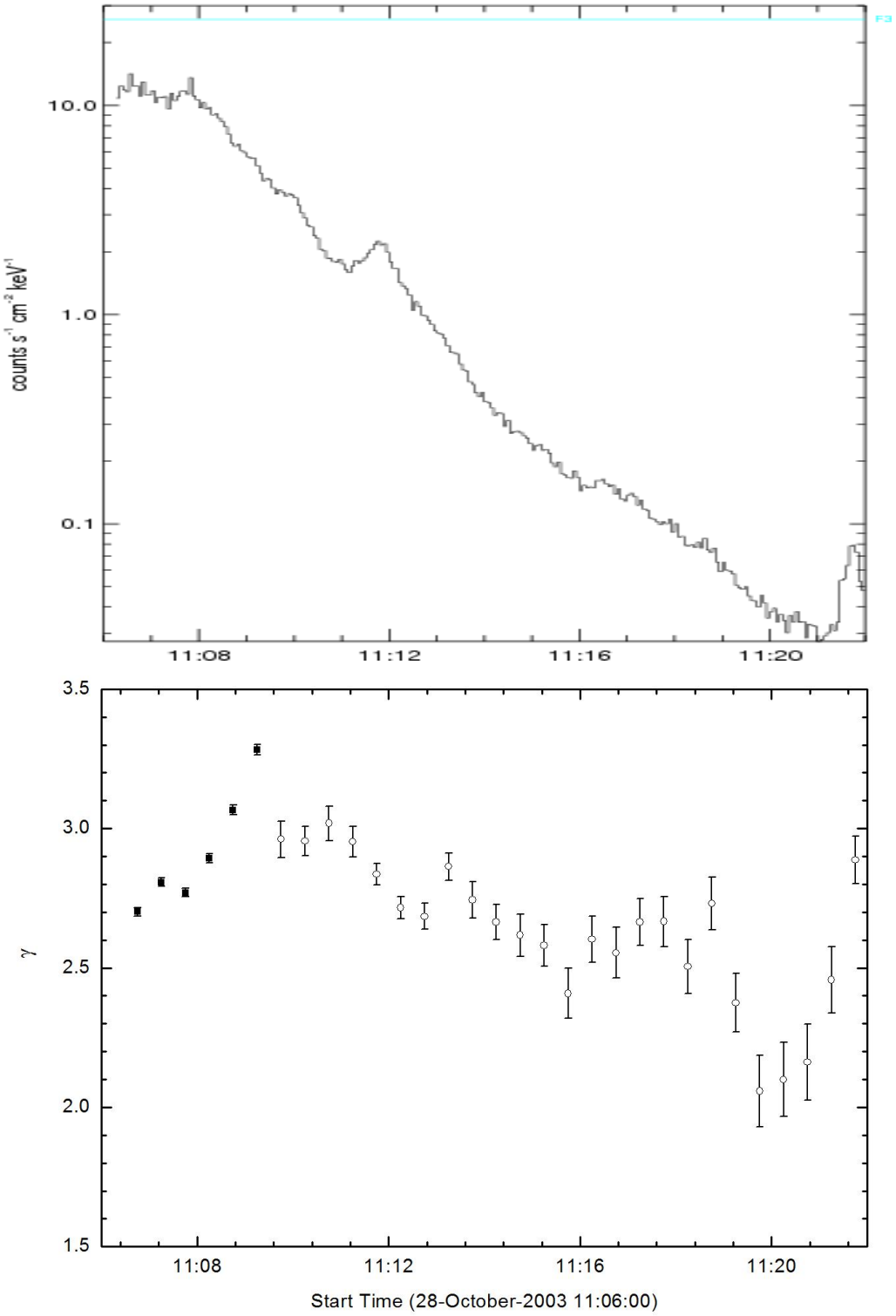

Figure 5.12: The light curve (top) and temporal evolution of the spectral index γ (bottom) of 28-October-2003 in 50-100 keV energy range. The dark circles denote the spectral index obtained from single power law. The open circles denote the values of the spectral index (above the break energy) obtained from the broken power-law fit.

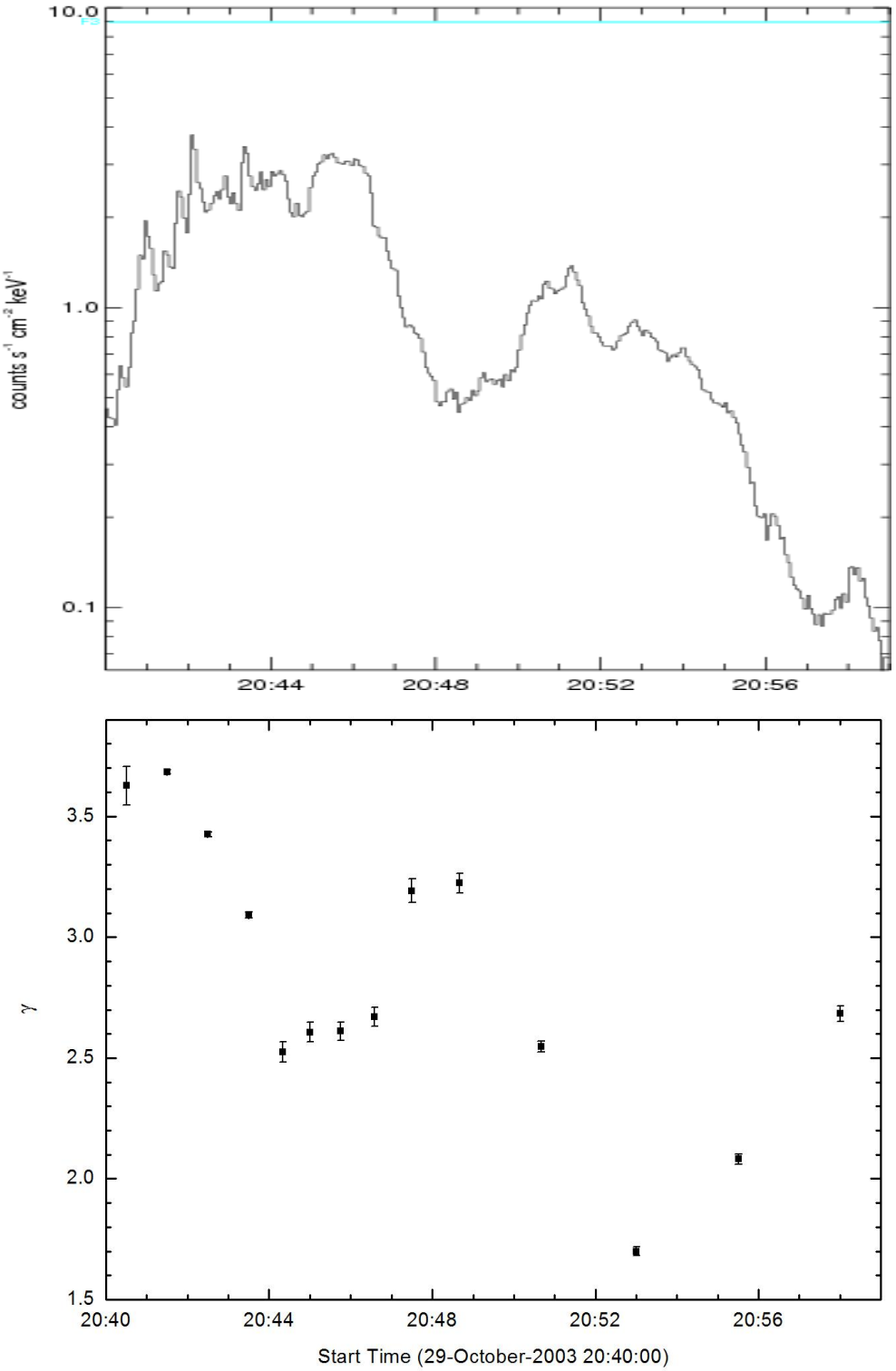

Figure 5.13: The light curve (top) and temporal evolution of the spectral index γ (bottom) of 29-October-2003 in 50-100 keV energy range.

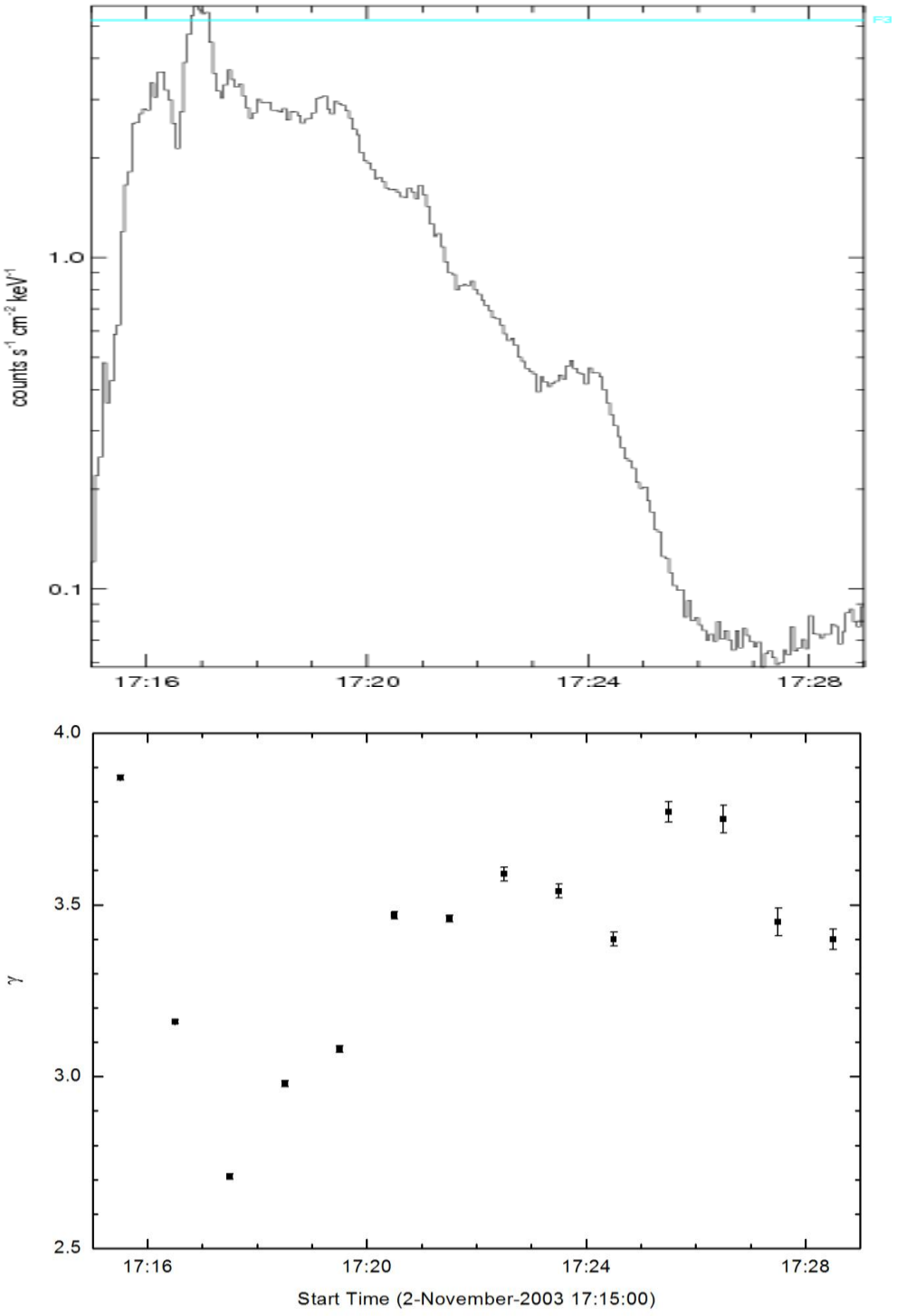

Figure 5.14: The light curve (top) and temporal evolution of the spectral index γ (bottom) of 2-November-2003 in and 50-100 keV energy range.

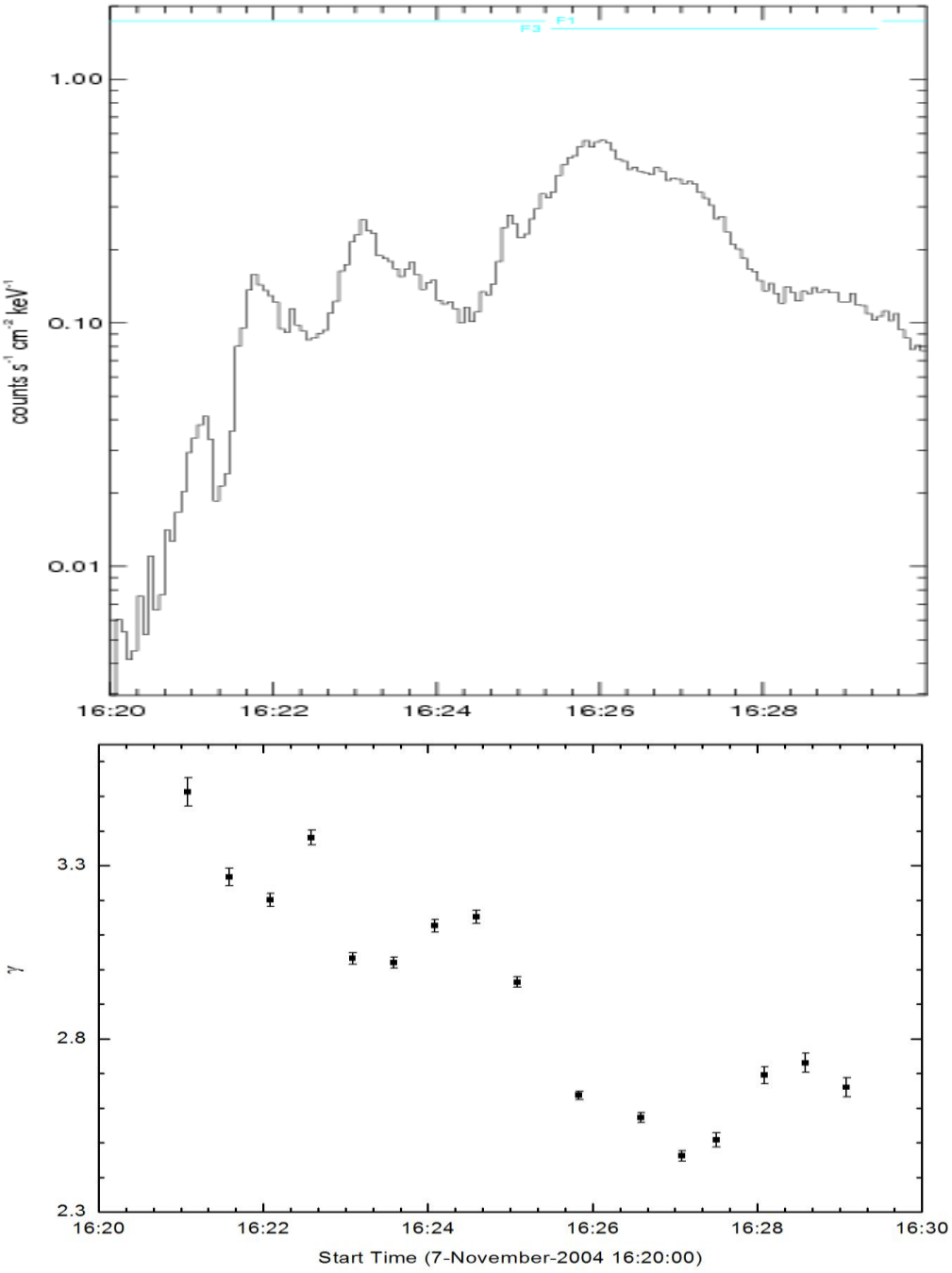

Figure 5.15: The light curve (top) and temporal evolution of the spectral index γ (bottom) of 07-November-2004 in 50-100 keV energy range.

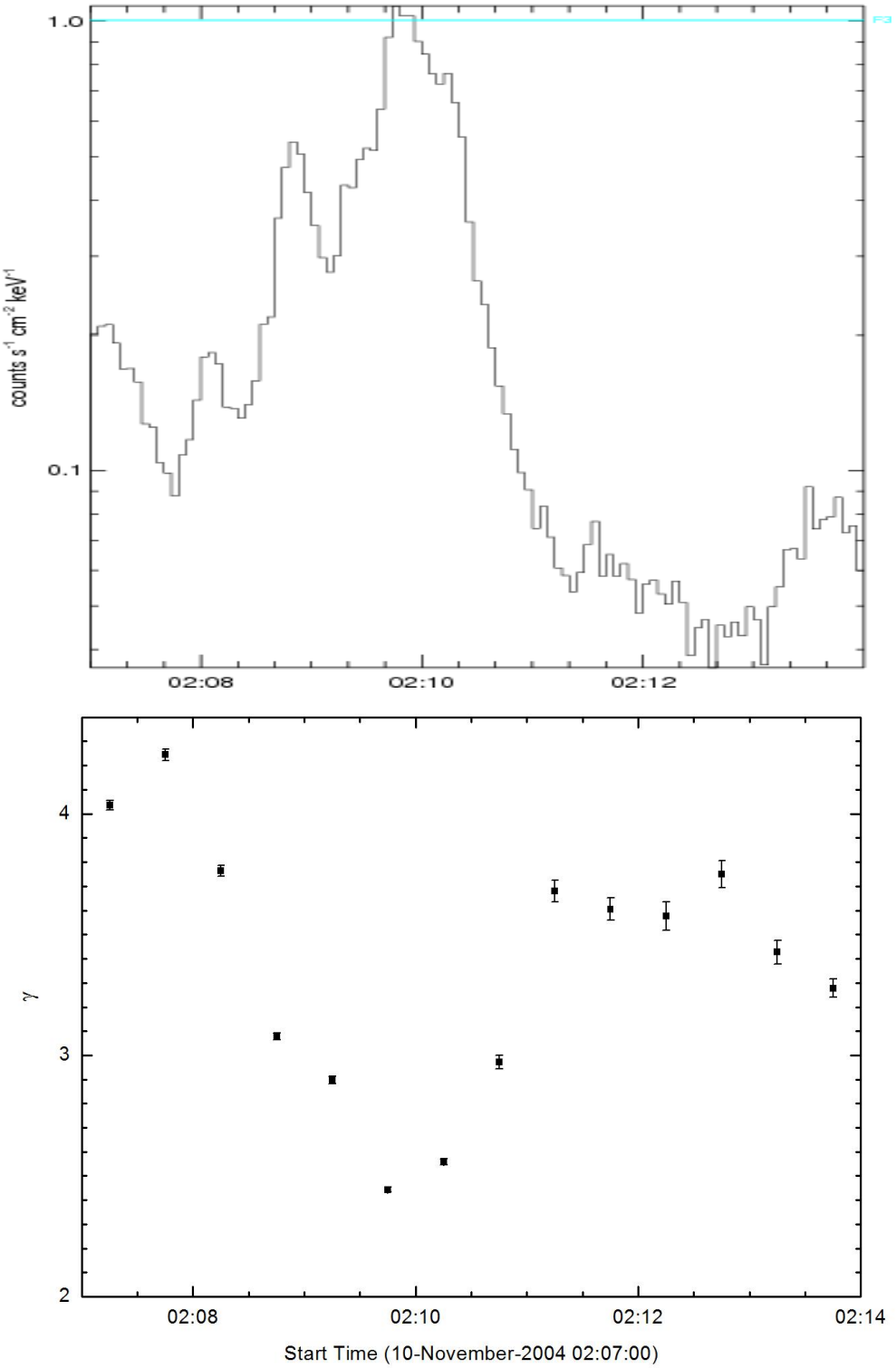

Figure 5.16: The light curve (top) temporal evolution of the spectral index γ (bottom) of 10-November-2004 in 50-100 keV energy range.

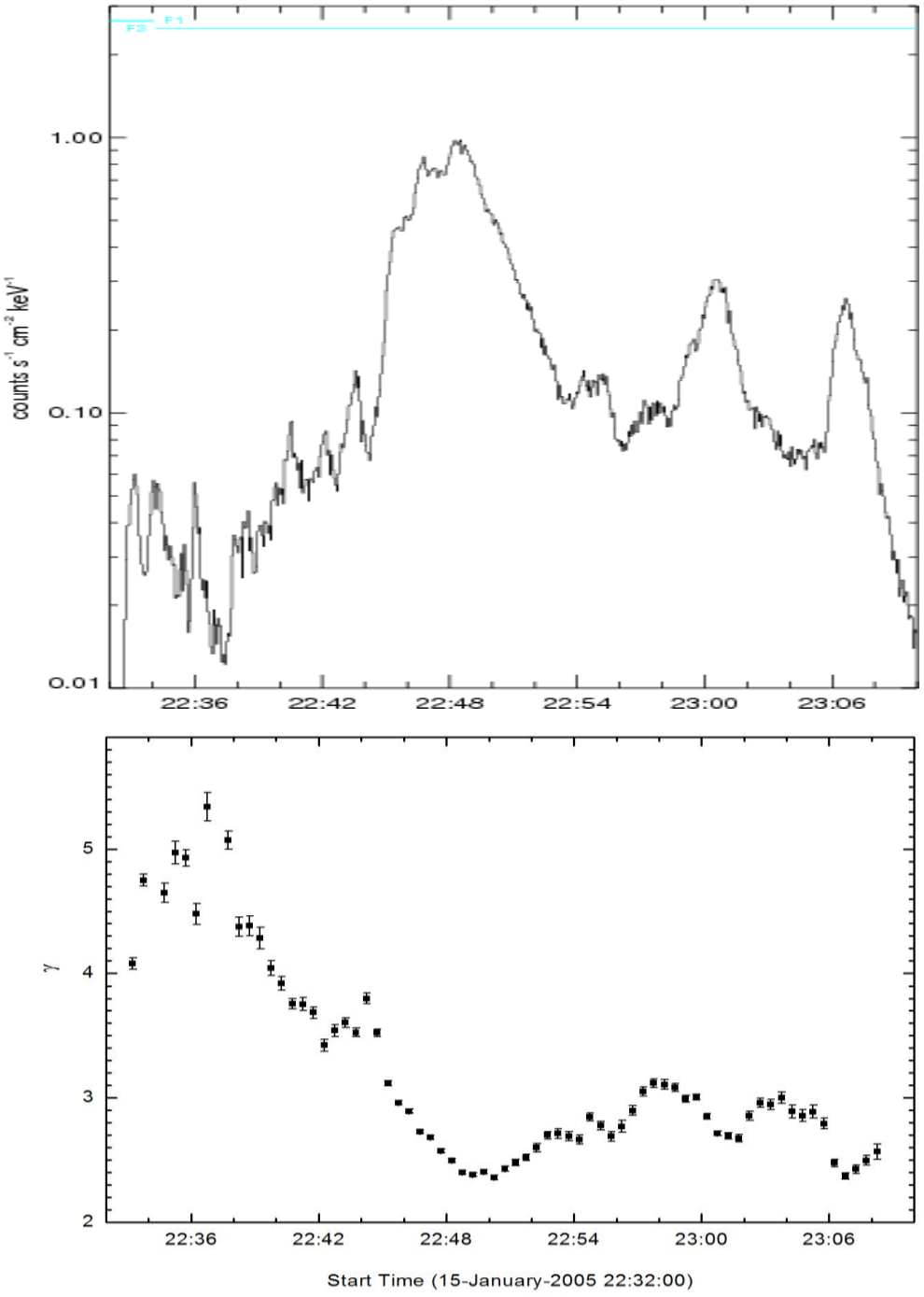

Figure 5.17: The light curve (top) and temporal evolution of the spectral index γ (bottom) of 15-January-2005 in 50-100 keV energy range.

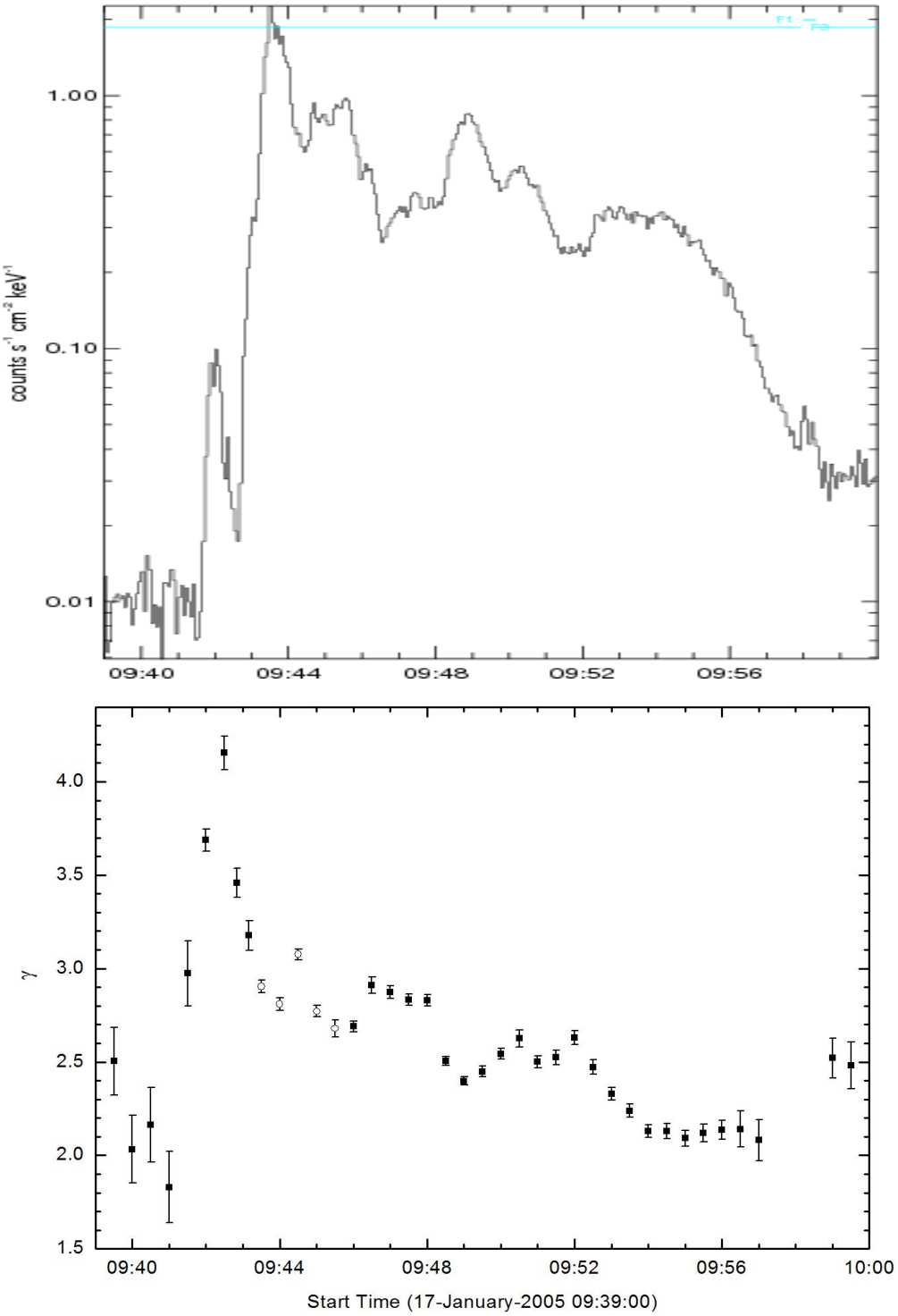

Figure 5.18: The light curve (top) and temporal evolution of the spectral index γ (bottom) of 17-January-2005 and 50-100 keV energy range. The dark circles denote the spectral index obtained from single power law. The open circles denote the values of the spectral index (above the break energy) obtained from the broken power-law fit.

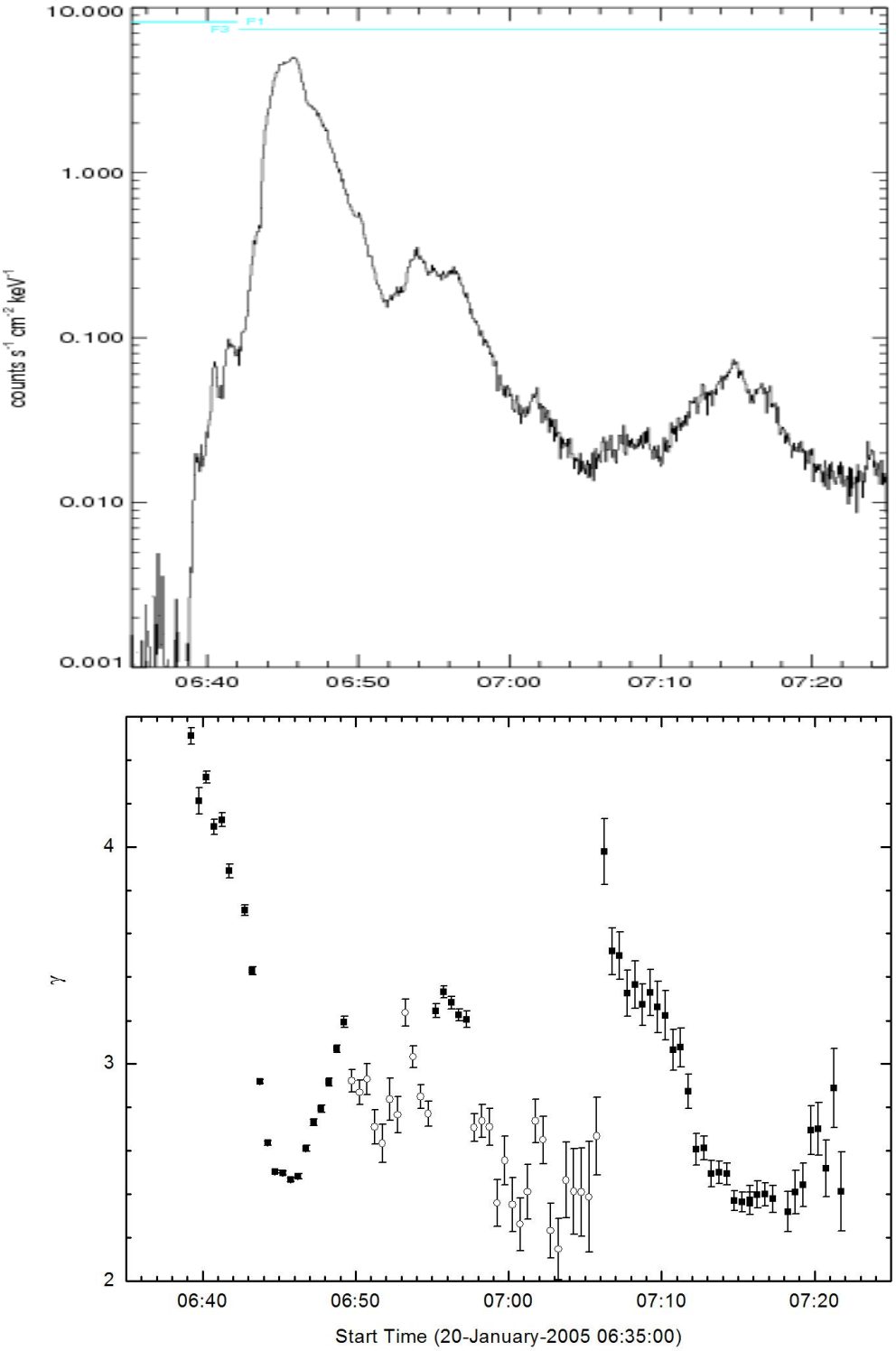

Figure 5.19: The light curve (top) and temporal evolution of the spectral index γ (bottom) of 20-January-2005 in 50-100 keV energy range. The dark circles denote the spectral index obtained from single power law. The open circles denote the values of the spectral index (above the break energy) obtained from the broken power-law fit.

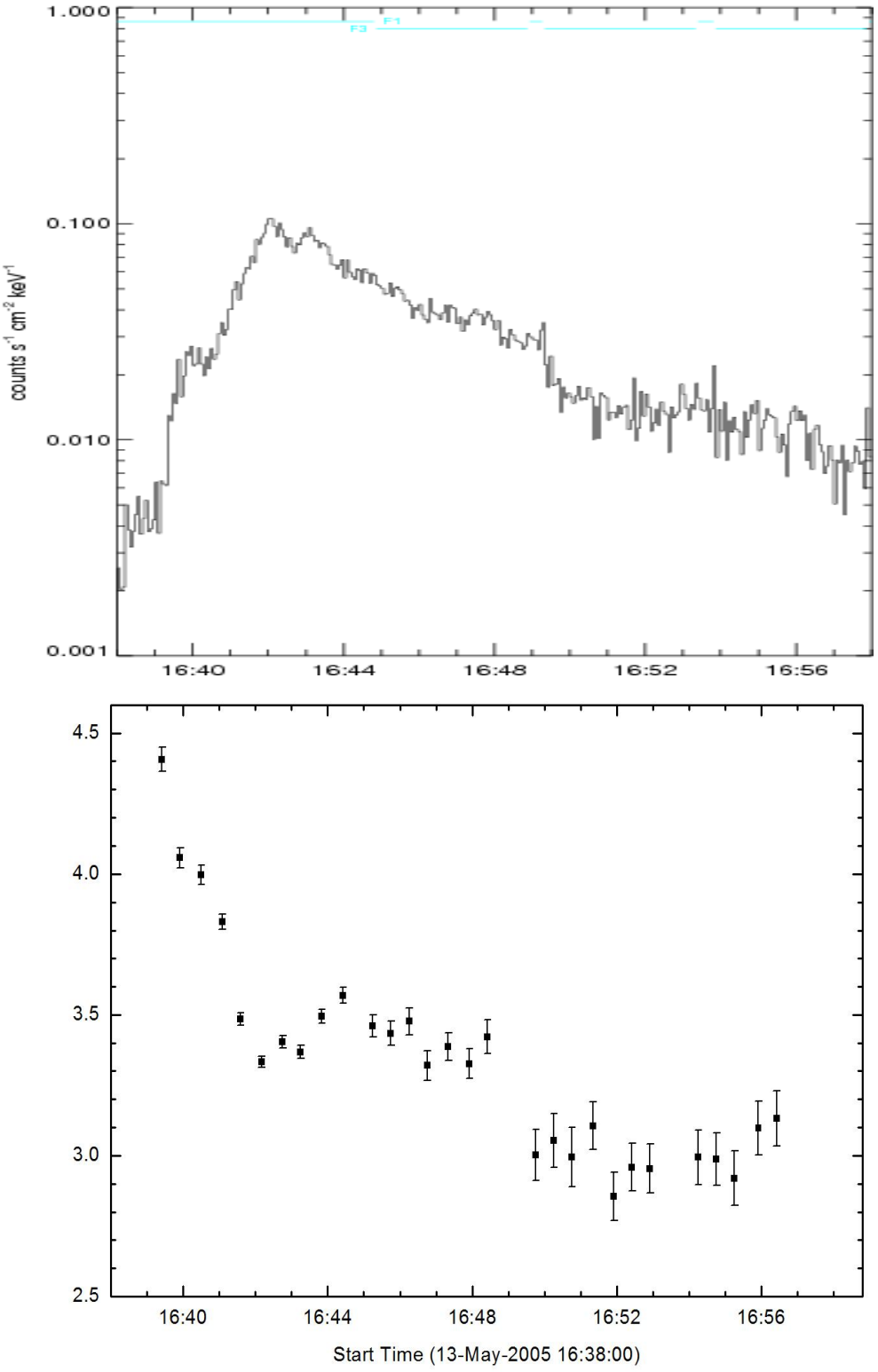

Figure 5.20: The light curve (top) temporal evolution of the spectral index γ (bottom) of 13-May-2005 in 50-100 keV energy range.

I observed that the hardest spectrum (observed upto 100 keV) needs not necessarily to be in the decay phase of the flare. Progressive hardening refers to X-ray spectra that harden as fluxes decline, regardless of timescales (Kiplinger, 1995). I observed that the hardest spectrum (observed upto 100 keV) may be in the rise phase or the decay phase of the flare.

In some flares, the hardest behavior in 50-100 keV energy range was observed before the flare peak. In some flares, the hardest spectrum was observed during the decay. In 27-May-2003 flare shown in Figure 5.10, the spectrum was hardest (γ = 2.75 ± 0.019) in the rise phase just before the peak at 23:05:46 UT. Figure 5.11 shows that the spectrum of 29-May-2003 was hardest (γ = 2.51 ± 0.019) in the rise phase (flare peak 01:06:06 UT). On the other hand, in the flare event of 28-October-2003 (Figure 5.12) there was a break in energy at about 50 keV in the spectrum. Therefore I fitted the spectrum with isothermal plus a broken power-law model. Further, on the contrary, in 17-January-2005 flare event, the spectrum (observed from 13-100 keV) was hardest in the decay phase 2.09 ± 0.04 (*cf*. Figure 5.18). The values of the spectral index of the hardest spectrum and the corresponding photon flux at 50 kV are given in Table (5.3). However, in the events in which the the fits were performed using the broken power-law, the flux in table 5.3 corresponds to the break energy (e.g. in 28-October-2003 event, the flux corresponds to a break energy= 50.1 keV). The value of γ reached 1.83 in the rise phase but was not considered as the corresponding spectrum was observed only upto 13-78 keV. I observed that in 28-October-2003 (figure 5.12), 20-January-2005 (figure 5.19, around 07:03 UT) and 13-May-2005 (figure 5.20) flares, the spectrum was hardest when the count flux in 50-100 keV was low (~ 0.1 to 0.3 Photons s^{-1} cm^{-2} keV^{-1}) as mentioned in table (5.3).

Table 5.3

Spectral index and photon flux at 50 keV for the hardest spectrum

S. No.	Date	Spectral index (γ)	Photon Flux (F_{50}) at 50 keV (Photons s^{-1} cm^{-2} keV^{-1})
1	27-05-2003	2.75 ± 0.019	2.24 ± 0.01
2	29-05-2003	2.51 ± 0.019	2.53 ± 0.02
3	28-10-2003	2.06 ± 0.13	0.31 ± 0.01
4	29-10-2003	1.7 ± 0.018	3.85 ± 0.05
5	02-11-2003	2.7 ± 0.008	38.3 ± 0.1
6	07-11-2004	2.4 ± 0.015	2.93 ± 0.02
7	10-11-2004	2.44 ± 0.01	7.35 ± 0.03
8	15-01-2005	2.36 ± 0.019	3.73 ± 0.02
9	17-01-2005	2.09 ± 0.04	2.18 ± 0.023
10	20-01-2005	2.14 ± 0.14	0.13 ± 0.01
11	13-05-2005	2.85 ± 0.08	0.13 ± 0.003
12	13-12-2006	2.16 ± 0.027	0.5 ± 0.005

I observed that out of the 12 SEP related flare events, the 29-October-2003 event gave the hardest flare spectrum with the spectral index equal to 1.7 ± 0.018 and a corresponding photon flux at 50 keV = 3.85 ± 0.05. As mentioned earlier, all these flares were followed by a geomagnetic storm whose intensity varied between – 69 nT and -383 nT. It is interesting to note that out of these 12 events, the largest geomagnetic storm was related to the 29-October-2003 event (Dst = - 383 nT). This indicates that the hardness of the flare spectrum is related to the storm magnitude.

5.4.2 SEP Spectral Analysis:

In this section, I present the analysis of the spectral fits of the proton spectra in the energy range 0.8-500 MeV for the SEP events observed after the flare onset. The associated proton spectra were prepared from the proton flux data taken from the GOES-8 and GOES-11 satellites. I accumulated the proton data (integrated over 3 hour /6 hour), starting from the SEP onset time to 24 h after the onset time. The temporal mode observations reveals proton flux (particles cm^{-2} s^{-1} sr^{-1} MeV^{-1}) as a function of time for fixed energy bands (0.8 – 4, 4 – 9, 9 – 15, 15 – 40, 40 – 80, 80 – 165 and 165 - 500 MeV). Similarly, the spectral mode observations reveal the particle flux as a function of energy at a given time. There are only seven energy channels in which the flux can be plotted. I then generated the proton spectra for a 13-December-2006 event within the energy range of 0.8-500 MeV. I fitted all the spectra (between 2.4 MeV to 332 Mev) with power-law given by

$$F(P) = AE^{-\beta} \qquad \text{(particles } cm^{-2}\ s^{-1}\ sr^{-1}\ MeV^{-1}\text{)} \qquad (5.3)$$

where $F(P)$ = the proton flux in particles cm^{-2} s^{-1} sr^{-1} MeV^{-1}, A = Normalization at epivot (proton flux at epivot in particles cm^{-2} s^{-1} sr^{-1} MeV^{-1}), E = energy in MeV and β is the proton spectral index.

In 13-December-2006 SEP event, the spectrum (for the duration 06:00 to 09:00) was observed from 2.4 to 332.5 MeV with a break in the spectrum at 12 MeV. So I considered the energy range to fit = 15 to 500 MeV. The background-subtracted proton spectrum of 13-December-2006 in the energy

range 15-500 MeV for the interval 6:00 to 9:00 UT is shown in Figure 5.21. The proton spectral index denoted by β was determined for each interval. The temporal evolution of proton flux (top) and spectral index β (bottom) of 13-December-2006 proton event in the energy range 0.8 - 500 MeV is shown in Figure 5.22.

For a particular proton event I considered the hardest (most flat) spectra in the highest energy range. For example in figure 5.22, the lowest value of β is 1.43 ± 0.52 at 15:00 UT but it is in the energy range 0.8-60 MeV (also observed in figure 5.22(top)) while at 6:00 UT, β=1.76 ± 0.03 (*cf*. Figure 5.21) and the corresponding spectrum is observed in upto 500 MeV energy range. Therefore, β =1.76 ± 0.03 is considered the lowest/hardest value in the highest energy range.

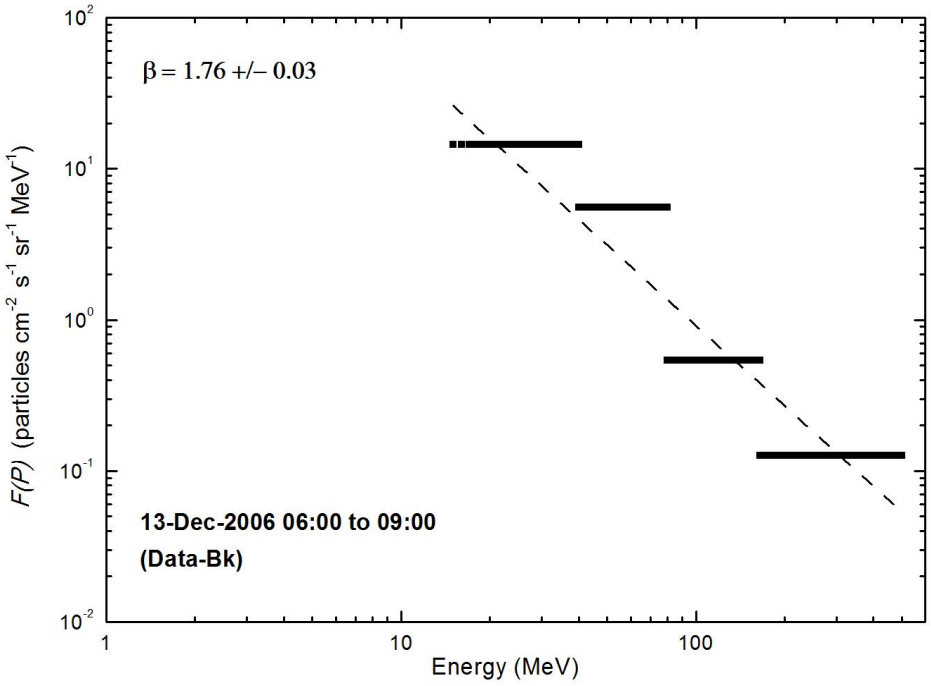

Figure 5.21: The background-subtracted proton spectrum of 13-December-2006 in the energy range of 15-500 MeV for the interval 6:00 to 9:00 UT.

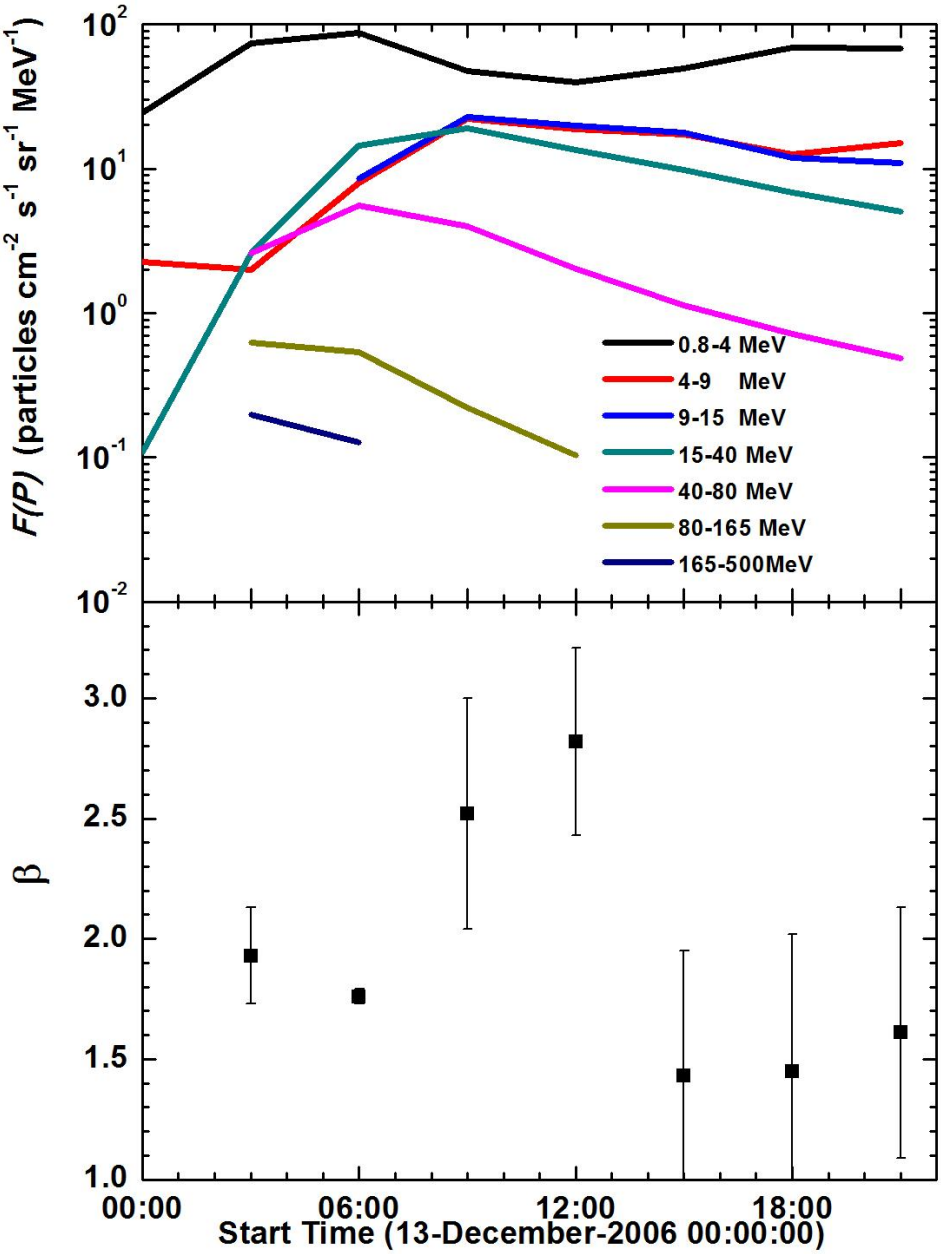

Figure 5.22: The temporal evolution of proton flux (top) and spectral index β (bottom) of 13-December-2006 proton event in the energy range 0.8 - 500 MeV.

The spectral analysis for the remaining 11 proton events was carried out in the similar fashion. The temporal evolution of the proton flux and the spectral parameter β of these events are shown in Figures 5.23 to 5.33.

The fitted spectra (fitted according to the above mentioned criteria) which gave the hardest value of spectral index β for all SEP events are given

in Appendix A. In some spectra, the spectral index below the break in the spectrum could not be obtained because of the spectrum was too flat with a spectral index ≤ 1. In some events, only two energy channels were left after fitting the spectrum above the break energy. In some events, the spectrum was observed upto 332.5 MeV with a break in the spectrum, in that case the spectrum was fitted with two power-laws and the average spectral index was considered.

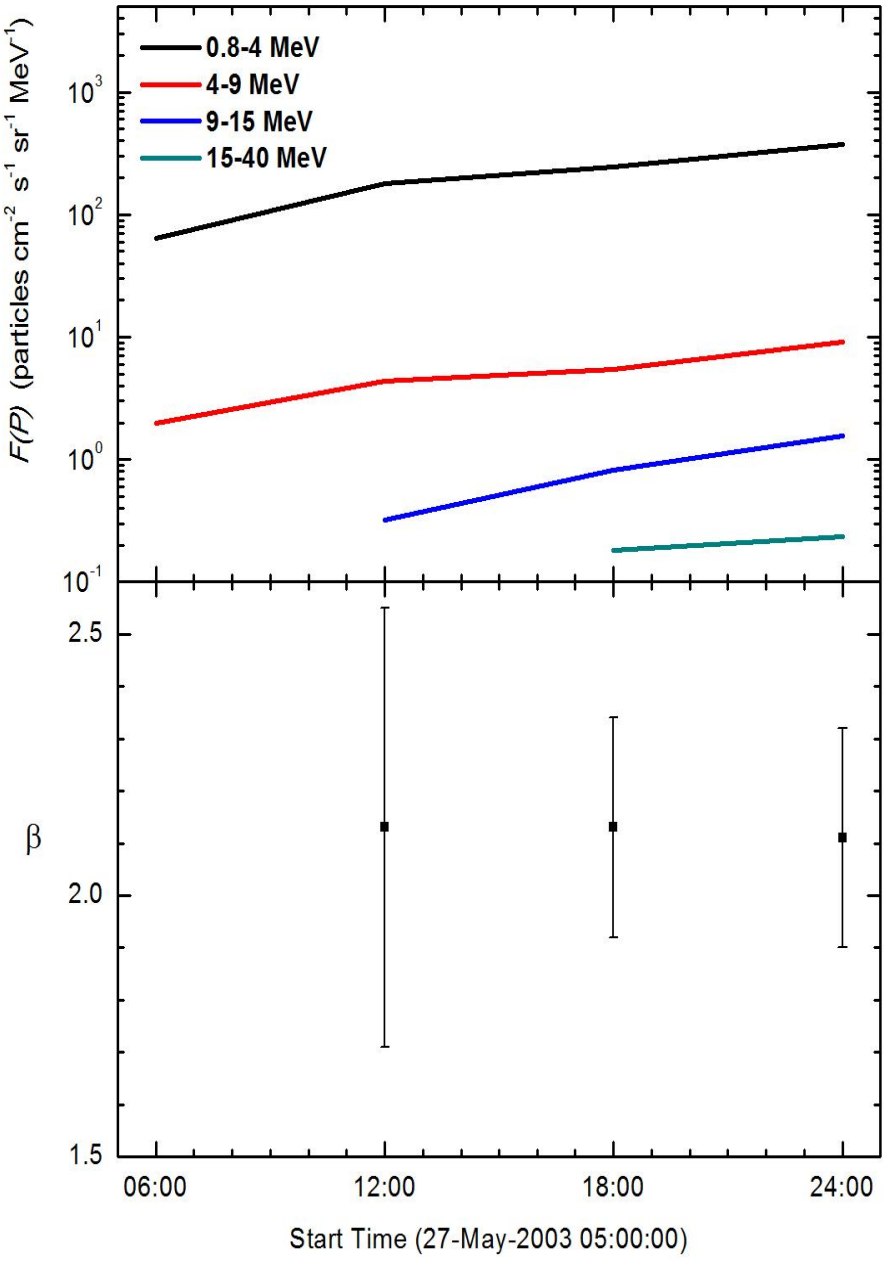

Figure 5.23: The temporal evolution of proton flux (top) and spectral index β (bottom) of 27-May-2003 proton event in the energy range 0.8 - 40 MeV.

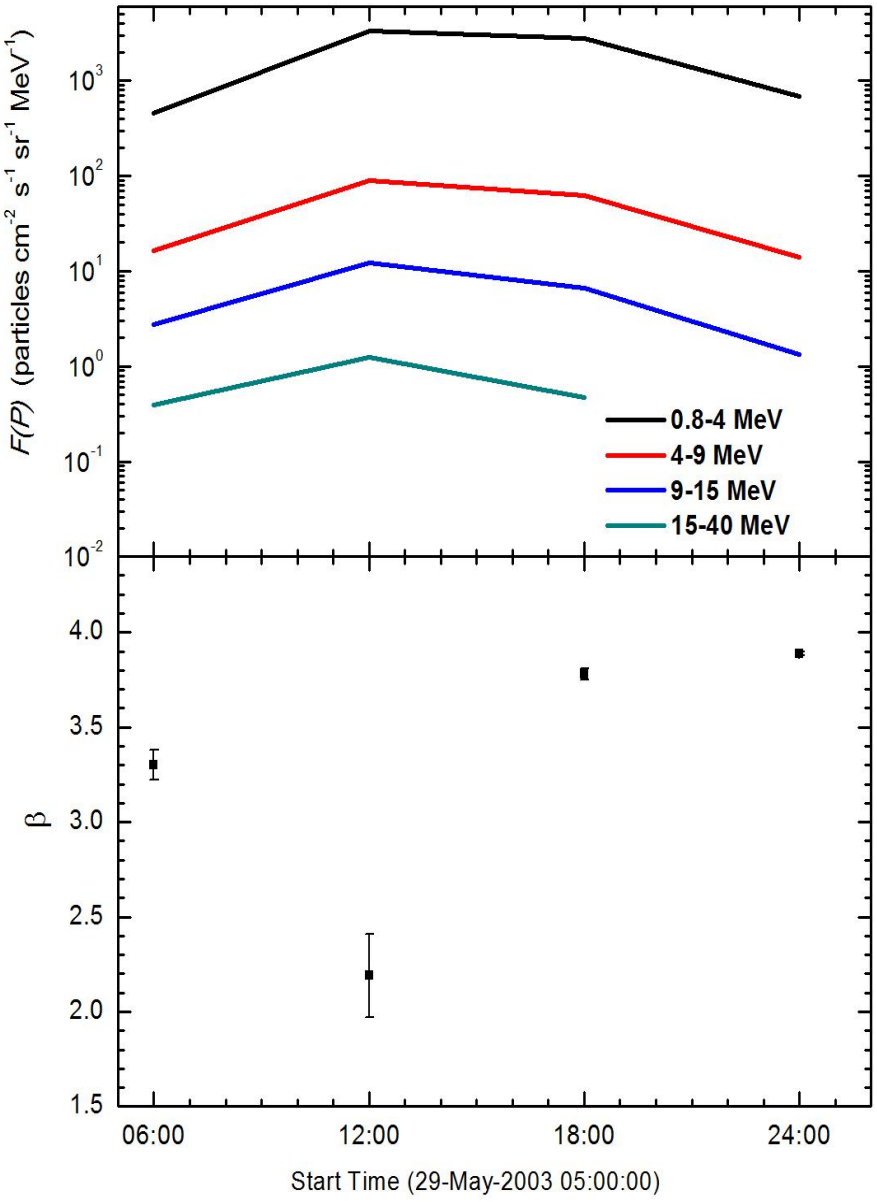

Figure 5.24: The temporal evolution of proton flux (top) and spectral index β (bottom) of 29-May-2003 proton event in the energy range 0.8 - 40 MeV.

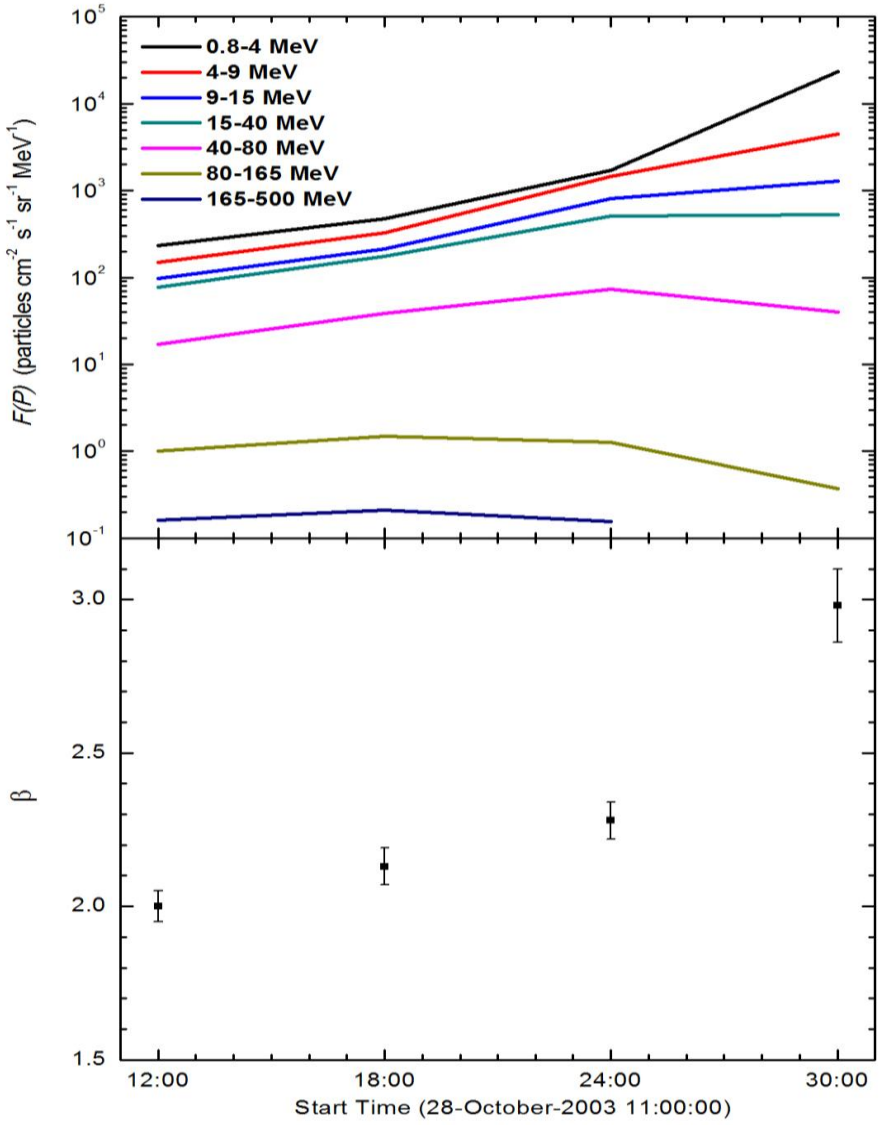

Figure 5.25: The temporal evolution of proton flux (top) and spectral index β (bottom) of 28-October-2003 proton event in the energy range 0.8 - 500 MeV.

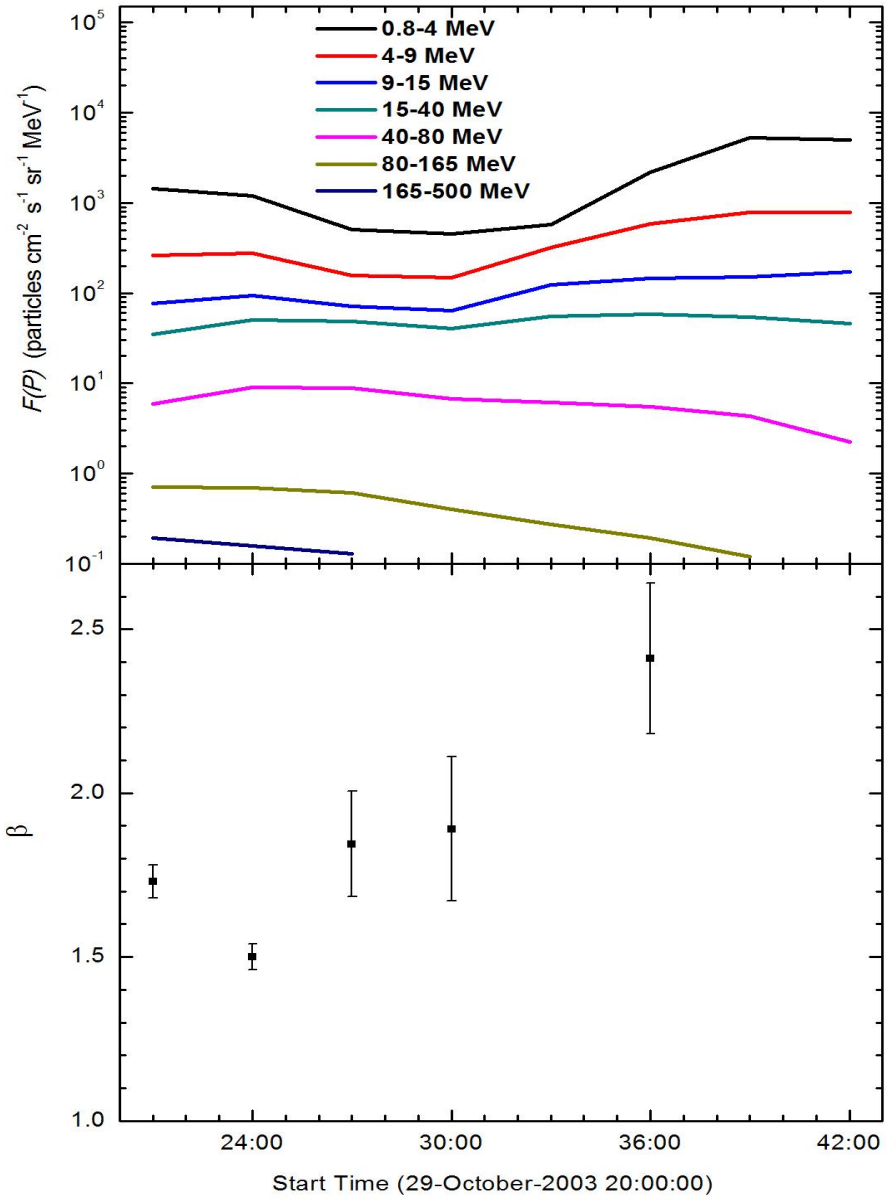

Figure 5.26: The temporal evolution of proton flux (top) and spectral index β (bottom) of 29-October-2003 proton event in the energy range 0.8 - 500 MeV.

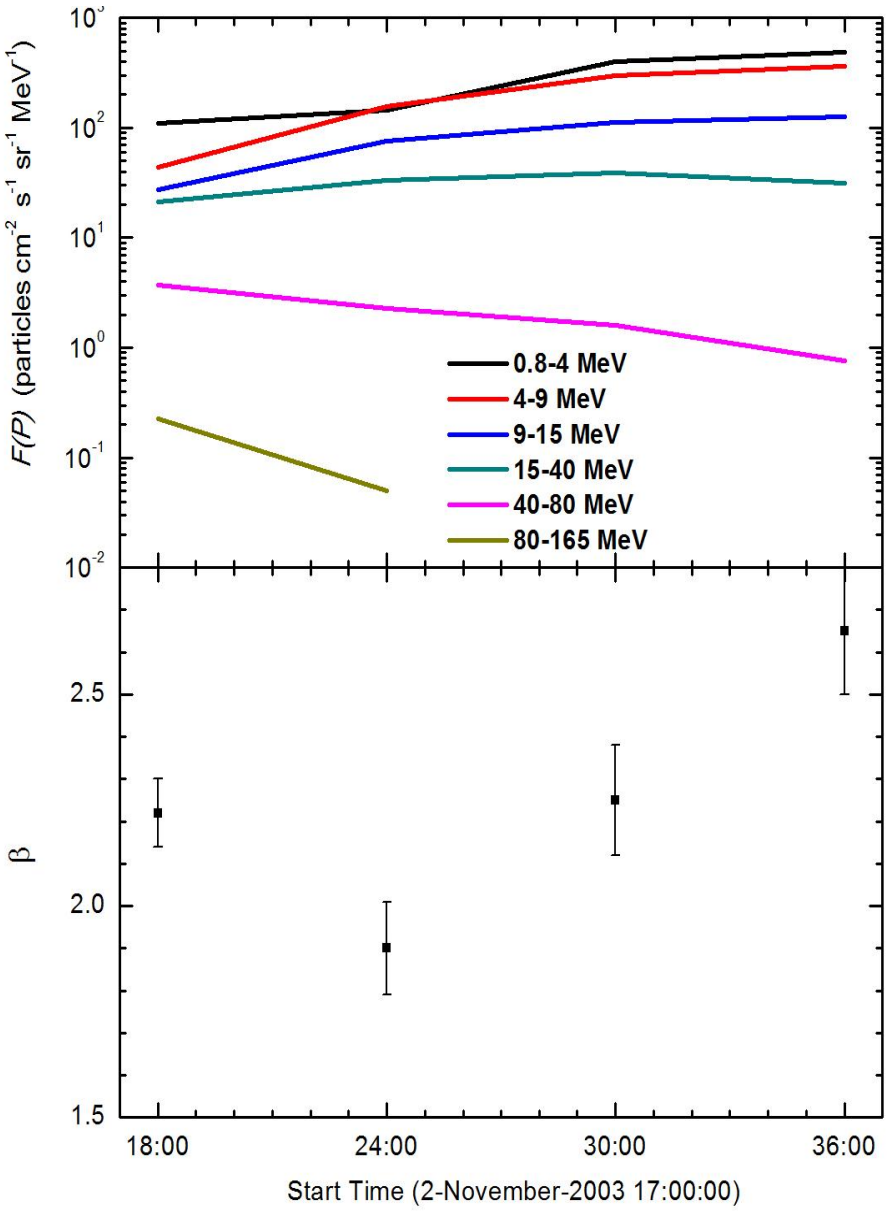

Figure 5.27: The temporal evolution of proton flux (top) and spectral index β (bottom) of 2-November-2003 proton event in the energy range 0.8 - 165 MeV.

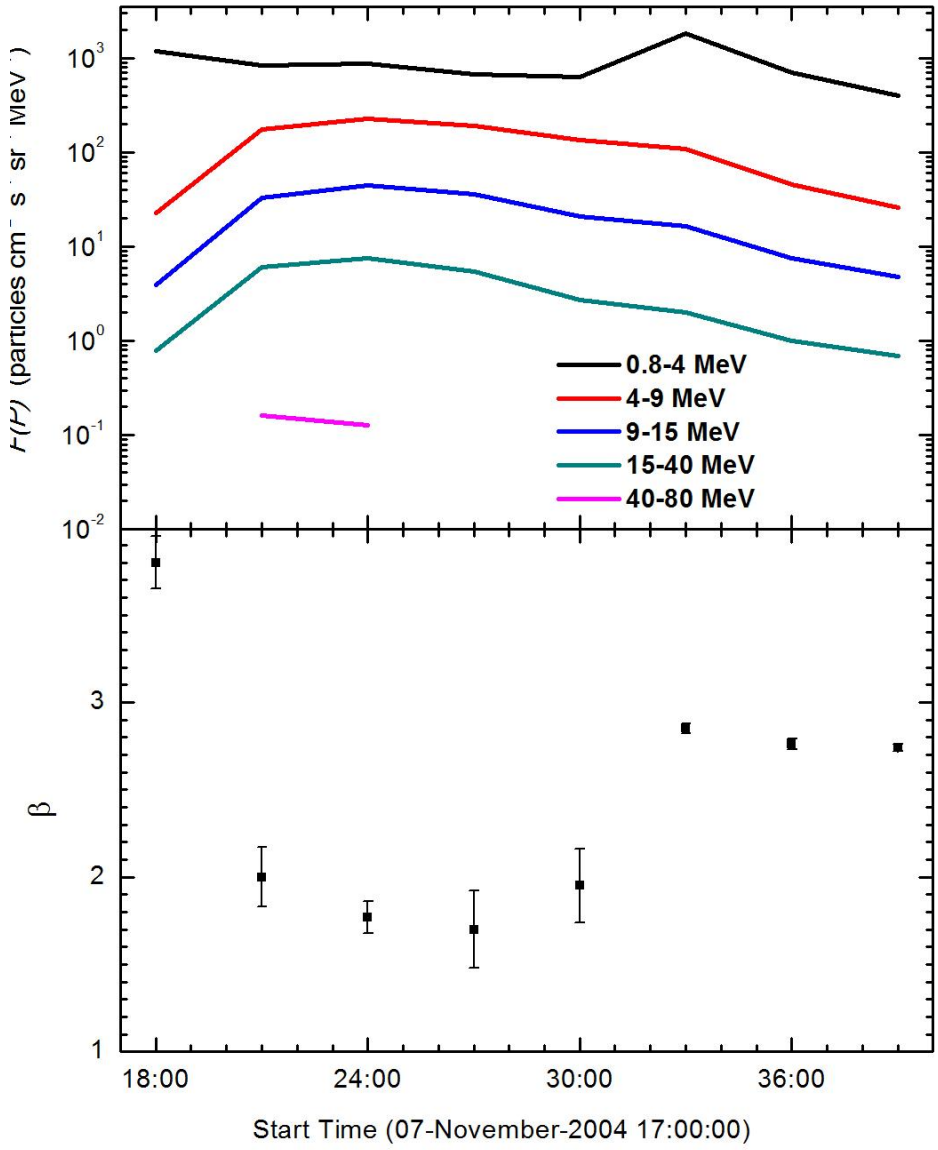

Figure 5.28: The temporal evolution of proton flux (top) and spectral index β (bottom) of 7-November-2004 proton event in the energy range 0.8 - 80 MeV.

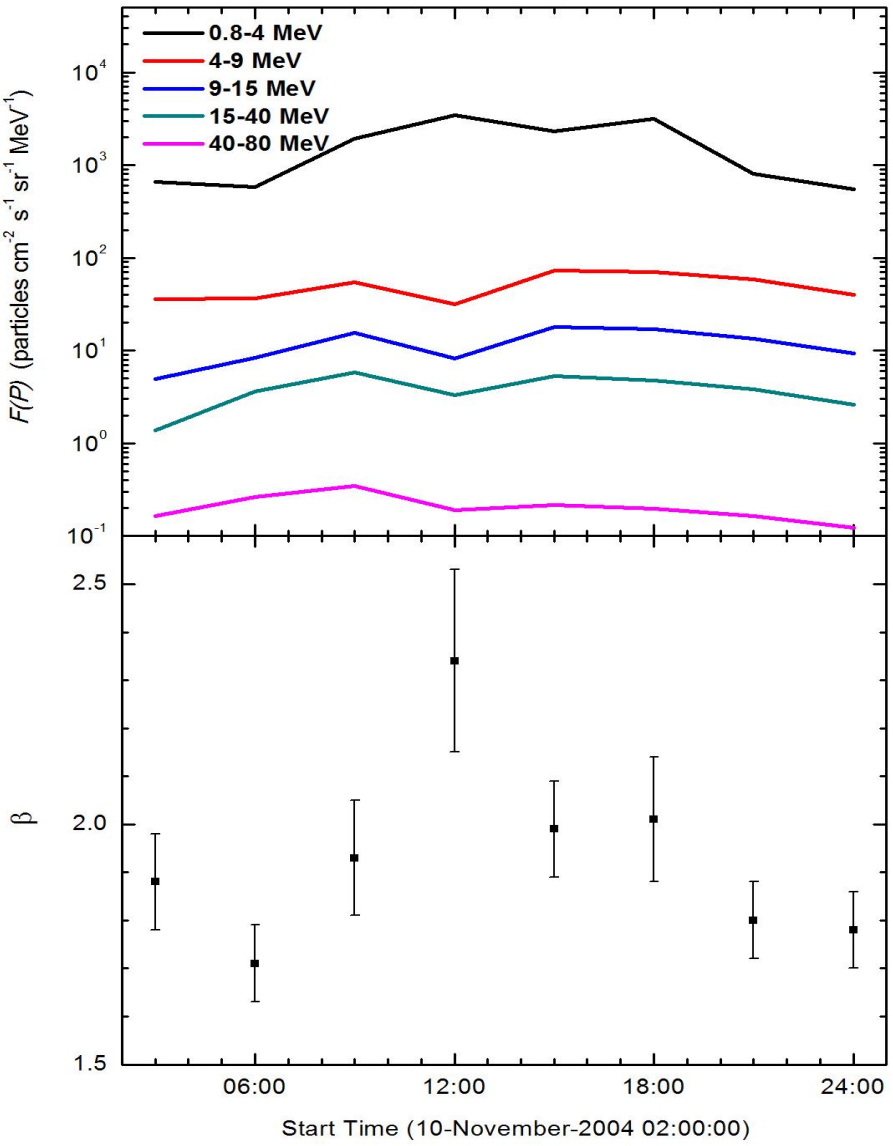

Figure 5.29: The temporal evolution of proton flux (top) and spectral index β (bottom) of 10-November-2004 proton event in the energy range 0.8 - 80 MeV.

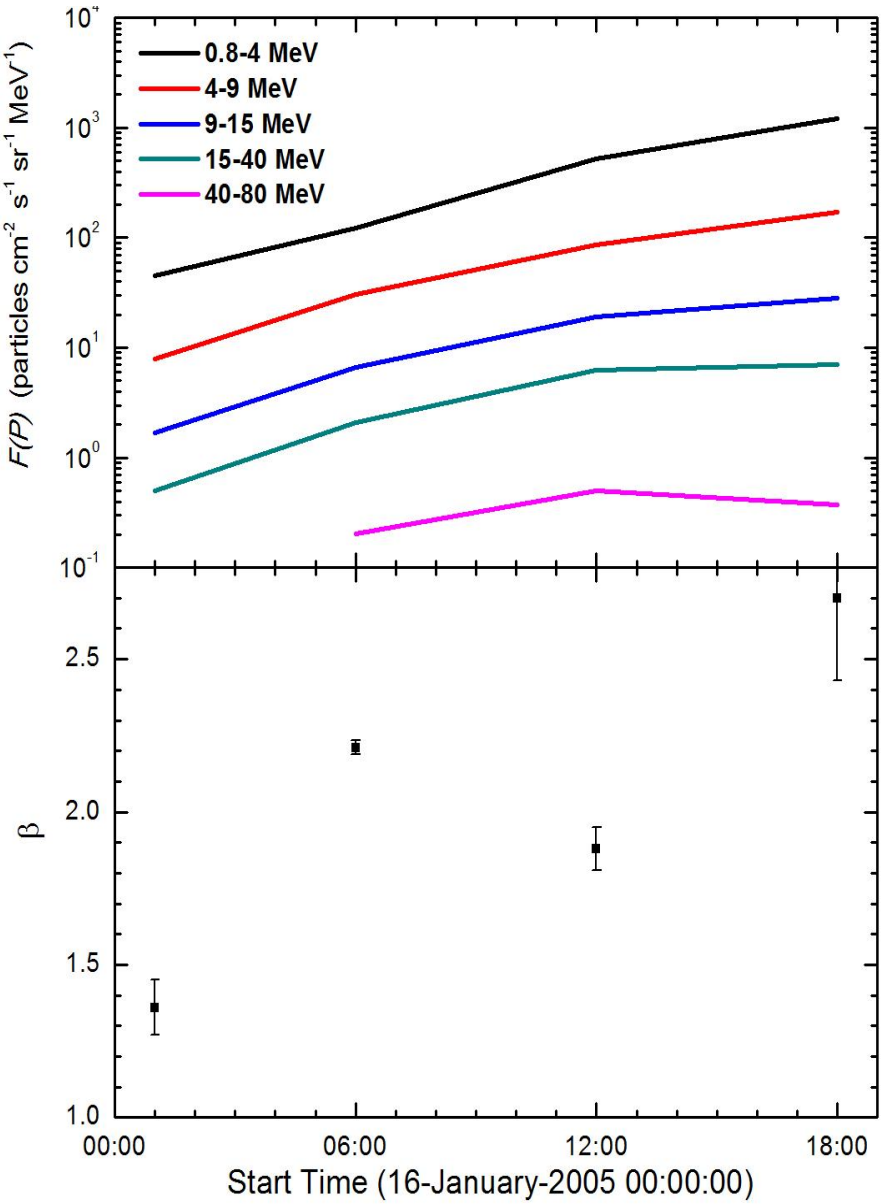

Figure 5.30: The temporal evolution of proton flux (top) and spectral index β (bottom) of 15-January-2005 proton event in the energy range 0.8 - 80 MeV.

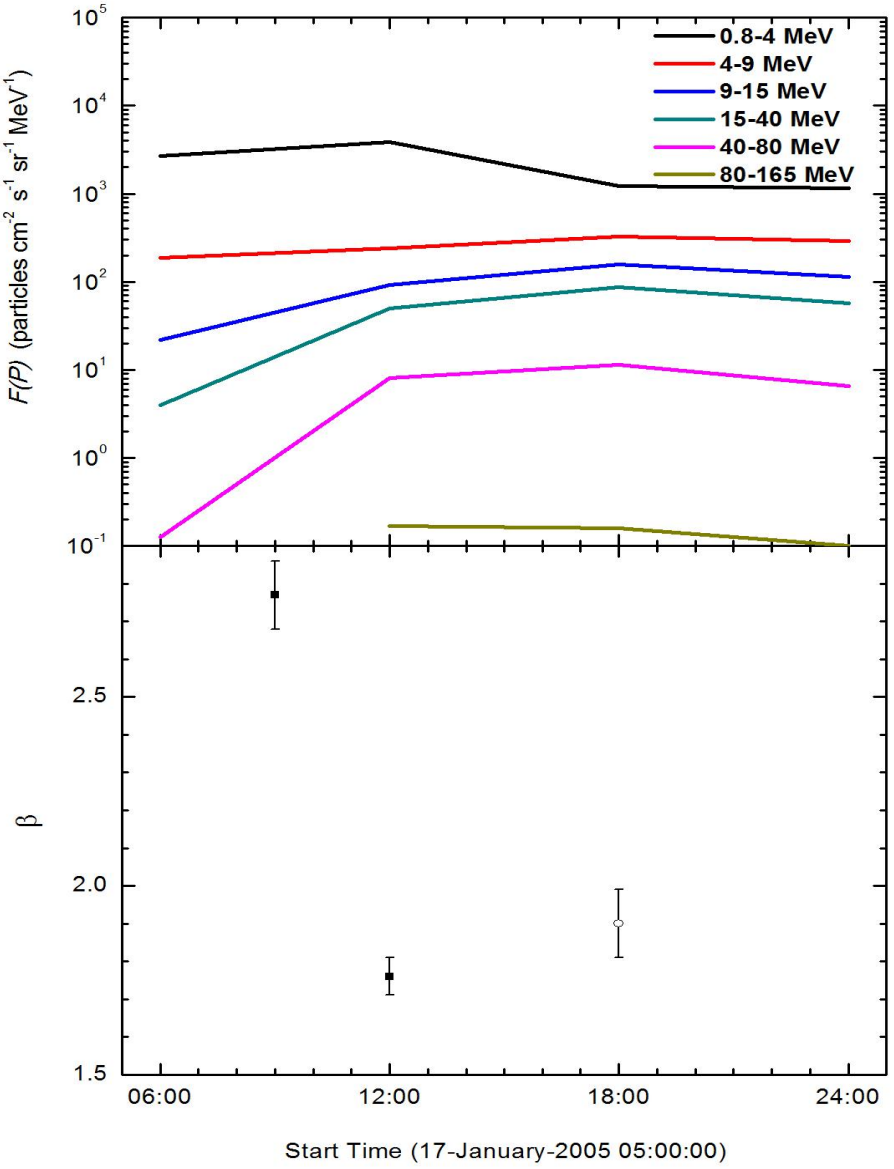

Figure 5.31: The temporal evolution of proton flux (top) and spectral index β (bottom) of 17-January-2005 proton event in the energy range 0.8 - 165 MeV.

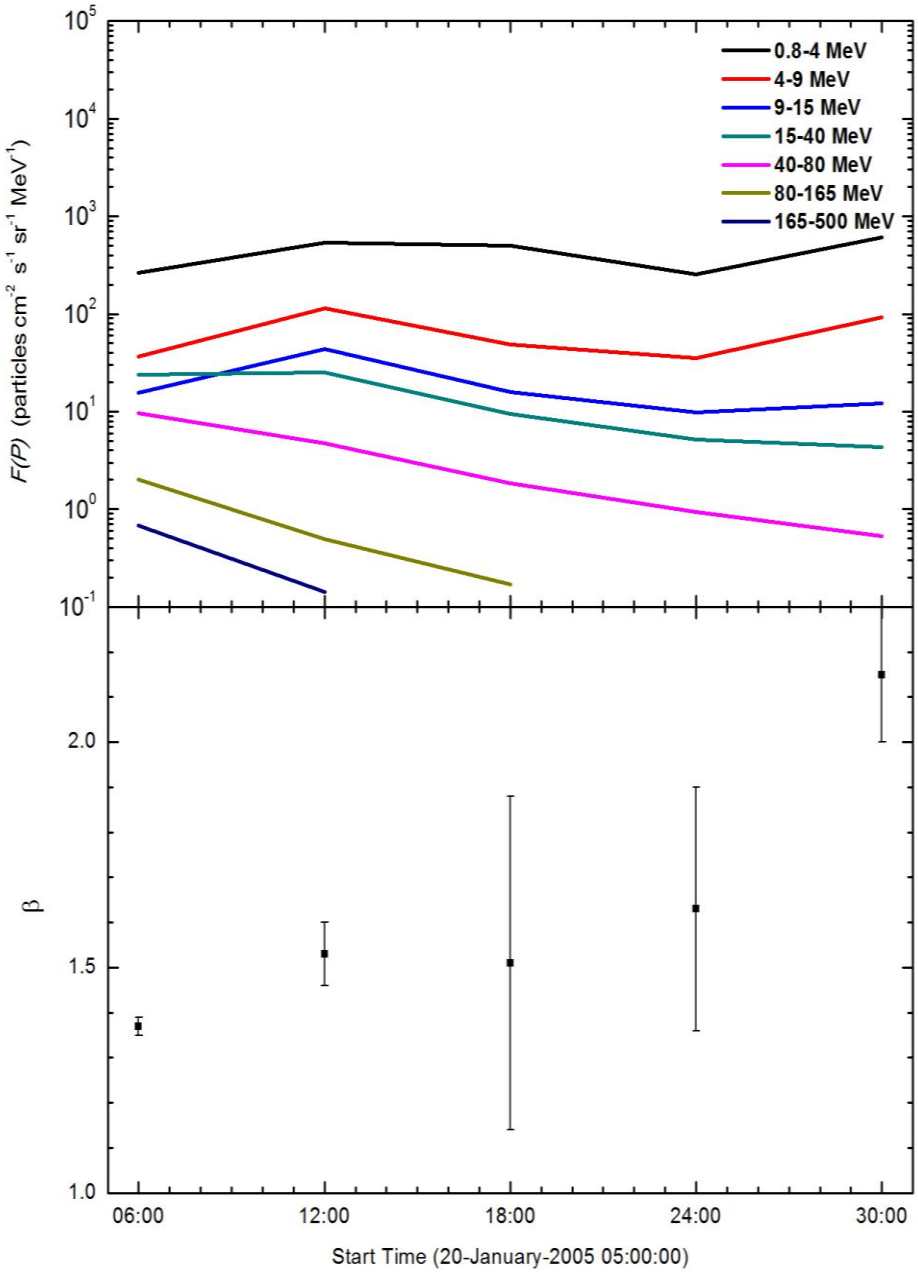

Figure 5.32: The temporal evolution of proton flux (top) and spectral index β (bottom) of 20-January-2005 proton event in the energy range 0.8 - 500 MeV.

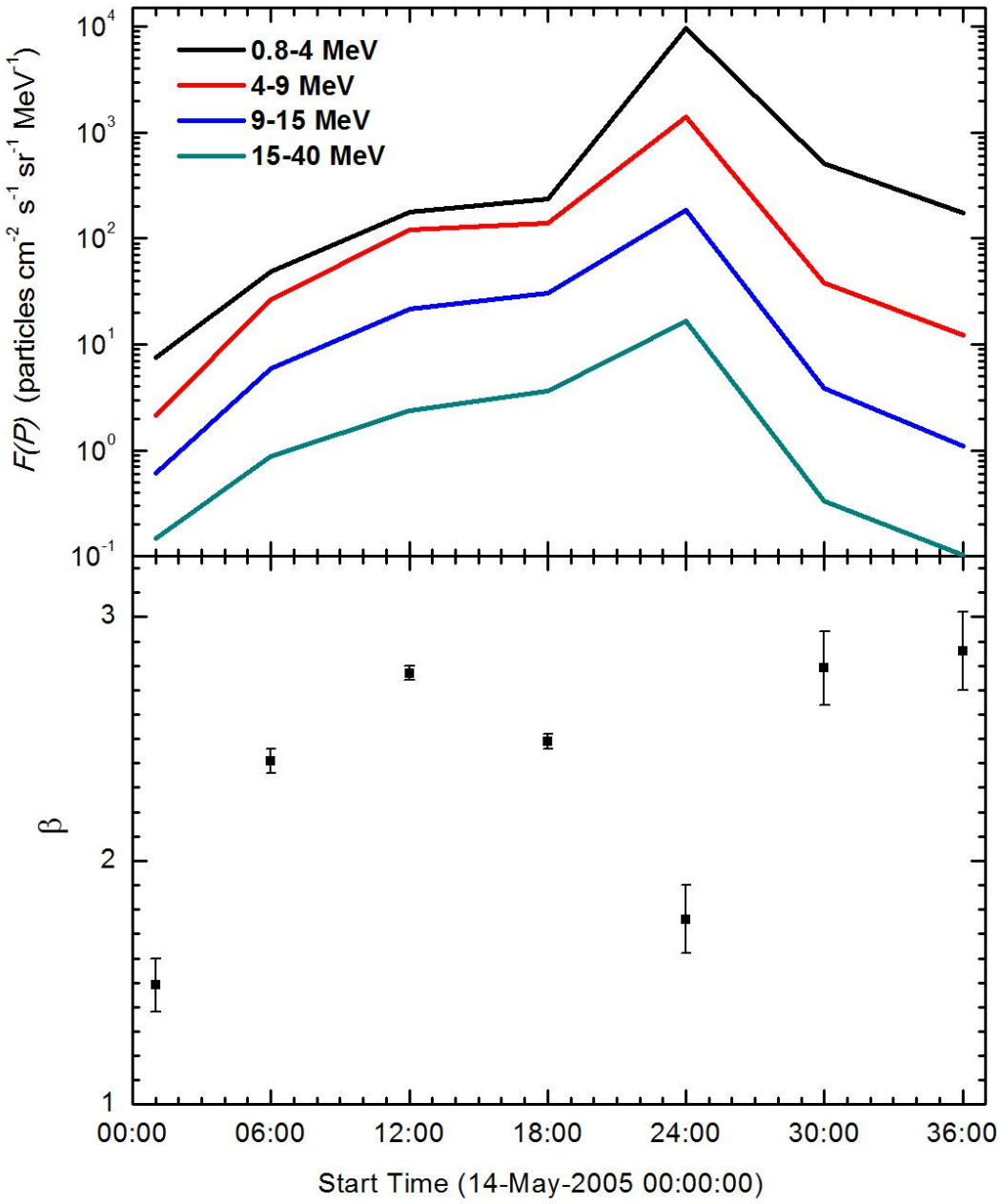

Figure 5.33: The temporal evolution of proton flux (top) and spectral index β (bottom) of 13-May-2005 proton event in the energy range 0.8 - 40 MeV.

I plotted the SEP spectral index β (obtained from the hardest spectrum in the highest energy range) as a function of hardest X-ray spectral index γ of the flare derived from the RHESSI observations as described above for all the 12 flare-SEP events as shown in Figure 5.34.

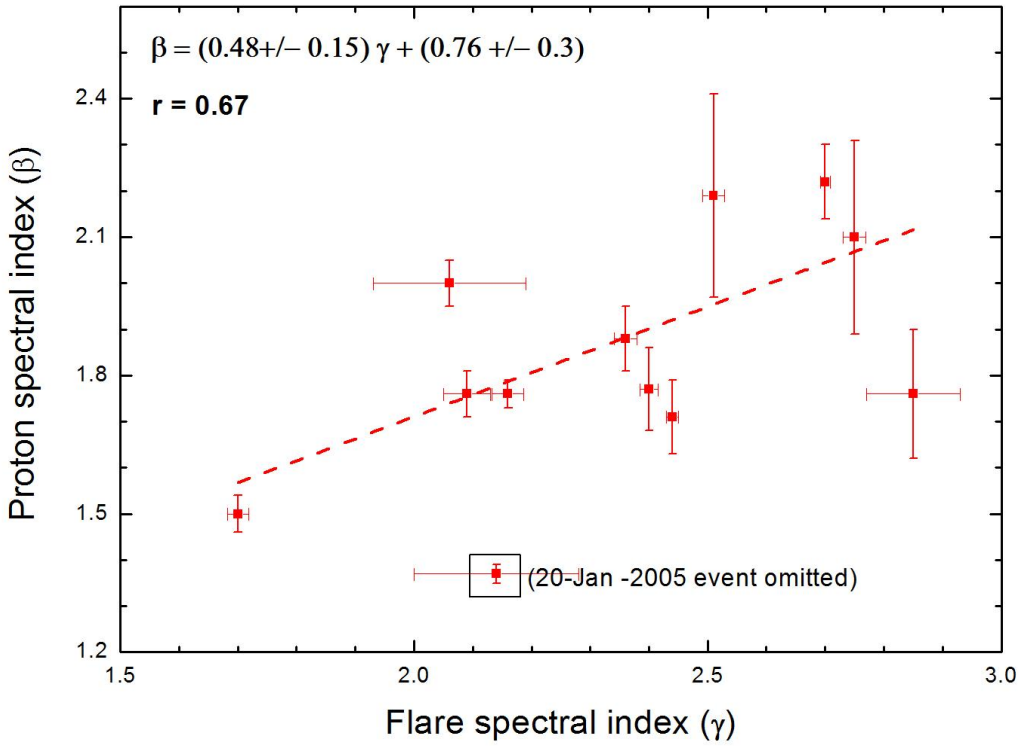

Figure 5.34: The proton spectral index β as a function of flare spectral index γ. The best fit with a correlation coefficient of 0.67 is obtained. Note that the 20-January-2005 event is not considered in the fit.

The 20-Januay-2005 event seemed to be an outlier (maybe because of highest flare flux ~ 739 c/4s) while performing the linear fit. Hence, if this event is not considered in the fit process, a good correlation is seen with flatter HXR flare spectra corresponding to flatter proton spectra. The best fit is a linear fit given by the following relation:

$$\gamma = (0.48 \pm 0.15)\beta + (0.76 \pm 0.3) \qquad (5.4)$$

The correlation coefficient r = 0.67.

This correlation coefficient r=0.67 between the hardest flare photon spectral index with hardest proton spectral index suggests a connection between the hard X-ray producing electrons in the flare and the escaping energetic protons in the interplanetary space. Though events are very limited but this important relation implies that both electrons and protons are accelerated together via same reconnection, and the source of the SEPs is of solar origin.

5.5 Discussion and Conclusions:

In this chapter, I analyzed the HXR emission of the flare and CME dynamics for 30 flare-CME pairs. I conclude that the initial linear speed of the CME right at the solar surface is strongly related (power-law relationship with r=0.77 for all 30 flares and r=0.84 for 19 flares for which the peak photon flux in 12-25 keV is <11000 c $(4s)^{-1}$) to the non-thermal spectral characteristics, however, before-the-peak interval of the associated flare event. My results indicate that the flare and the associated CME are the two components of one energy release system and perhaps occur together at the time of impulsive acceleration.

Temmer *et al*. (2010) studied three fast coronal mass ejections observed by Solar Terrestrial Relations Observatory (STEREO) and their associated high-energy flare emissions in terms of RHESSI hard X-ray (HXR) spectra and flux evolution. They indicated a correlation between the CME acceleration peak and the flare hard X-ray peak flux and suggested that a large sample of events may be studied to arrive to a better conclusion. They further suggested a possible relationship between the spectral slope of the HXR spectra and the CME acceleration. However, I studied in greater detail the 30 solar flare events associated with CMEs in contrast to 3 events investigated by Temmer *et al*., (2010) and achieved a new significant result that showing a good correlation between non-thermal hard X-ray spectral index and CME linear velocity. This new result rather strongly suggests that flare and CME are the two phenomena that occur together as a consequence of reconnection in the corona. In fact each flare should accompany smaller or large mass ejection, and similarly each mass ejection should lead to smaller or bigger flare, however, their visibility is restricted to the observations made in the line-of-sight. Thus current investigation should not be considered to selection criteria. My aim was to show that these two phenomena are two components of one energy release system. The thermal and non-thermal energy release observed in flares is down-flow from the point of reconnection, while outflow of plasma material from that point is CME, which is in agreement to the standard model of solar flare and CME production, also widely known as CSHKP model (*cf*. Chapter 1)

As mentioned in section 5.1.2, the flare-SEP relationship has been studied by many researchers. Previous investigations revealed that spectral hardening in solar flares has relationship with energetic proton events observed at earth. These investigations proposed the link between soft-hard-hard (SHH) behavior of the X-ray spectra and the SEPs observed at Earth. Krucker *et al*. (2007) compared the hard X-ray (HXR) photon spectra observed by the *RHESSI* with the spectra of the electrons in the associated solar impulsive particle events observed near 1 AU by the *WIND* 3D Plasma and Energetic Particle (3DP) instrument. They found that the HXR photon power-law spectral index and the in situ observed electron spectral index measured above 50 keV show a good linear fit (r= 0.83) for prompt events and a weak correlation (r=0.43) for delayed events.

The 12 major solar flares selected to probe the relationship between HXR photon power-law spectral index and the proton spectral index, revealed a good linear correlation of r = 0.67 (neglecting 20-January-2005 event). The 20 January 2005 solar flare is the hardest flare ever detected in space near solar minimum. Out of all the 12 SEP events analyzed in this chapter, the lowest (hardest) value of proton spectral index obtained from the proton spectral fits is 1.37 ± 0.02 for 20-January-2005 SEP event. I observed that in 28-October-2003 (Figure 5.12), 20-January-2005 (figure 5.19, around 7:03 UT) and 13-May-2005 (Figure 5.20) flares, the spectrum was hardest when the count flux in 50-100 keV was low (~ 0.1 to 0.3 Photons s^{-1} cm^{-2} keV^{-1}). My current result is new in contrast to previously known for electrons, as well as soft-hard-hard nature of X-ray spectra because it suggests that proton (ions) acceleration is in simultaneous to electrons at the same site, and the source for SEP is in the solar corona.

I conclude that the primary acceleration of the protons is at the flare site where the electrons also get accelerated, and the flare, CME and SEP events are connected with one another and should be regarded within the framework of a solar eruption, which may affect the Earth's environment.

CHAPTER 6
PREDICTION OF SUNSPOT CYCLE 24

Precursor techniques, in particular those using geomagnetic indices, often are used in the prediction of the maximum amplitude for a sunspot cycle. In this chapter, I predict the maximum amplitude and timing of the current sunspot cycle 24 using precursor techniques. I also predict the annual mean geomagnetic activity for the solar maximum year for the current cycle 24.

6.1 Sunspot cycle Prediction: A brief overview:

Solar outbursts cause inclement space weather that sometimes wrecks havoc on technological systems on which our society is progressively more dependent. These outbursts involve the sudden release of energy that is stored in stressed coronal magnetic fields. They occur on a wide variety of scales depending upon the available free magnetic energy, which, however, is drawn from sunspot magnetic fields. Predictions of solar and geomagnetic activities are important for various purposes, including the operation of low-earth orbiting satellites, operation of power grids on Earth, and satellite communication systems. Various techniques, namely, even/odd behavior, precursor, spectral, climatology and neural networks and flux transport dynamo model have been used in the past for the prediction of the solar activity. Many researchers (Ohl, 1966; Kane 1978, 2007; Thompson, 1993; Jain, 1997; Hathaway and Wilson, 2006) have used the 'precursor' technique to predict the solar activity. Also the report entitled "*Solar Cycle 23 Project: Summary and Panel Findings*" (Joselyn *et al.*, 1997) has mentioned precursor techniques as being the most successful. Jain (1997) used a 'precursor' technique to predict the amplitude of the solar cycle 23 using the geomagnetic activity *aa* index and predicted the maximum annual mean sunspot number for cycle 23 to be 166.2, which, however, was found to be higher than the observed values of 120. Had he used an error estimate, perhaps his forecast would have been within the error limits. The high level of geomagnetic activity occurs not only at sunspot maximum but also in the following two to four years, thereby supporting the idea of the 'extended solar cycle' where a solar

cycle really begins some years before solar minimum and where two solar cycles co-exist on the Sun for a number of years. Wilson and Hathaway (2008a, 2008b) observed that the variation of the *aa* index usually peaks after a sunspot maximum, which appears to be directly related to increased solar wind speed, which probably is the result of high-speed streams from coronal holes. The prediction of maximum amplitude of a sunspot cycle using various aspects of the *aa* index has been pursued for many years (since the 1960s) by many authors. For example, Ohl (1966, 1971) and Wilson (1990) showed that the *aa* index values in the few years prior to a sunspot cycle minimum can be used to gauge the size of the next unfolding sunspot cycle. The level of geomagnetic activity near the time of solar activity minimum has been found to be a reliable indication of the amplitude of the following solar activity maximum (Hathaway and Wilson, 2006). In this view, I was motivated to predict the amplitude of the maximum annual mean sunspot number of solar cycle 24 using the technique employed by Jain (1997). I also attempt to predict the annual mean geomagnetic activity for the solar maximum year for the current cycle 24.

6.2 Data:

To predict the amplitude of a solar cycle, a few precursor techniques employ geomagnetic activity indices *viz.* Ap and *aa*. I have employed the *aa* geomagnetic index in the current investigation. The details of the observatories and instruments are given in section 2.6 and the data acquisition has been described in section 3.7. Further, the details of the data acquisition related to yearly sunspot number are described in section 3.8. For our current investigation, I have used the data for the period January 1868 – November 2008.

6.3. Analysis and Results:

6.3.1 Defining the Sunspot Minimum Year of Cycle 24:

The trend of observed annual mean sunspot number and annual mean *aa* index for the period 1868-1992 is shown in Figure 6.1 while for the period 1992-2008 is shown in Figure 6.2.

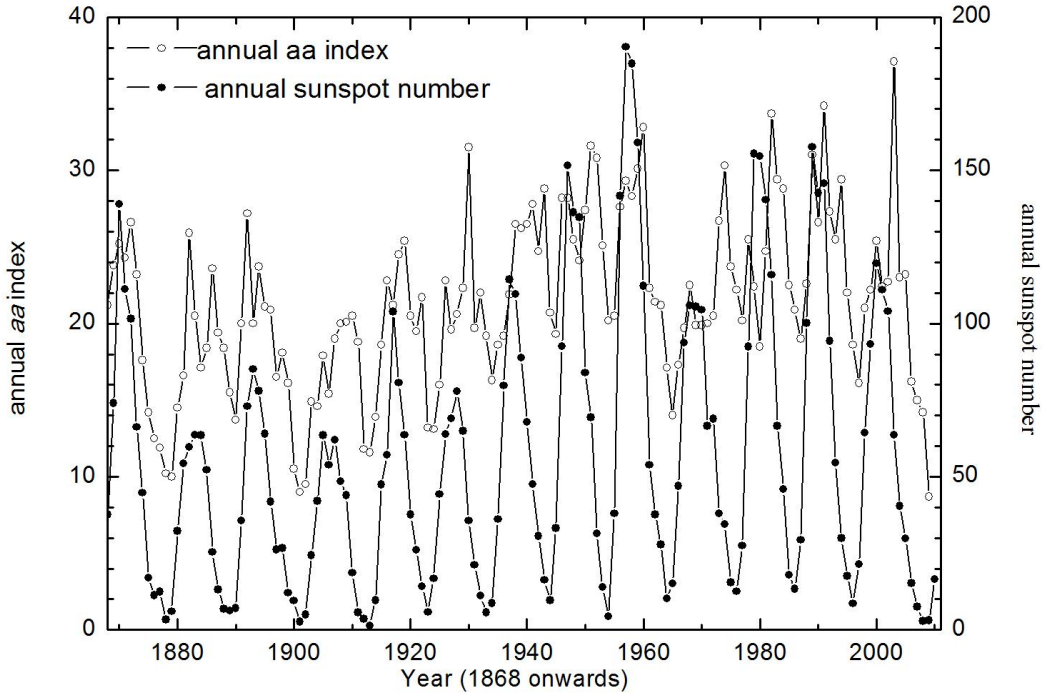

Figure 6.1: The observed annual mean *aa* index (1868 to 2009) and annual mean sunspot number (1868 to 2010).

I observed from Figure 6.1 and 6.2 that the annual mean *aa* index ranges from 9 nT in 1901 to 37.1 in 2003 which is an indicator of minimum and maximum geomagnetic activity respectively, during the period of 1868–2008. Whereas, the annual mean sunspot number varies between 1.4 in 1913 and 190.2 in 1957. Sunspot numbers rise steadily to maximum and then fall steadily to a low level during each sunspot cycle, whereas geomagnetic indices (Ap or aa) show two or more maxima per cycle, one near or before the sunspot maximum and others in the declining phase, and the gap between the two primary maxima (the Gnevyshev gap) results in the quasi-biennial and quasi-triennial periodicities observed in the geomagnetic indices (Kane 1997). In this investigation the year of the sunspot minimum of solar cycle 24 is of greatest importance and thus at least its precise determination is explicitly necessary. According to “The Weekly” report by NOAA/Space Weather Prediction Center (available at http://www.swpc.noaa.gov/weekly/pdf2008/prf1688.pdf the first sunspot of solar cycle 24 was observed on 4 January 2008 and it was numbered NOAA AR 10981. Later, NOAA AR 10990 and 10993 were observed in April and

May 2008 respectively, and these have also been classified as sunspots of cycle 24.

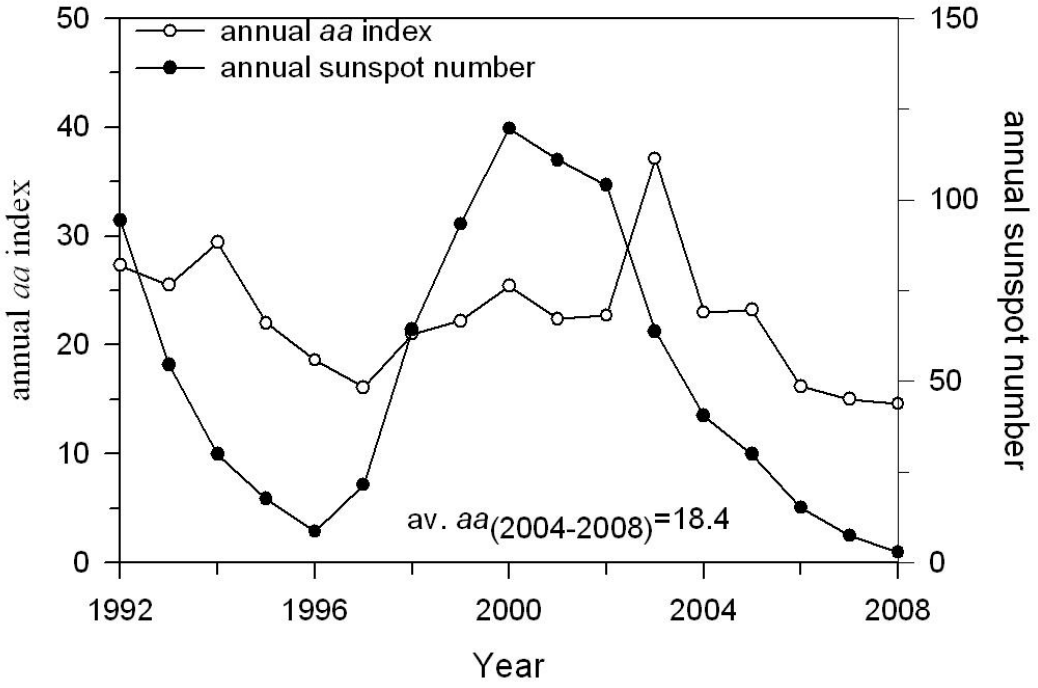

Figure 6.2: The observed annual mean *aa* index and annual sunspot number for the period of 1992 – 2008. Note that the annual mean *aa* index for the period of 2004 – 2008 is 18.4.

However, in parallel and simultaneously, sunspots of solar cycle 23 were also been appearing near the equator until and even after mid 2008. Thus, the year 2008 is considered as the transition period from one cycle to the next. Monthly *aa* values for 2008 are identified at the website only for January–November. The *aa* value for December 2008 is estimated to be about 14.4 +/− 4.3, which is found close to the observed value 10.1. In this investigation, however, I employ the 2008 *aa* to be about 14.6, and the average *aa* value for the sunspot minimum year together with the preceding four years (2004 – 2008) is estimated to be about 18.4. The annual mean sunspot number for the year 2008 is found to be 2.9 (lower than 7.5 in 2007), which is well within the range of a typical sunspot minimum value (Dabas *et al.*, 2008). Therefore in the current study I considered 2008 as the year of the sunspot minimum and August 2008 as the month of the year of the sunspot minimum of solar cycle 24.

6.3.2 Prediction of the Maximum Annual Mean Sunspot Number:

Following to the method described by Jain (1997), I examined the level of geomagnetic activity to predict the amplitude of solar cycle 24. The annual mean sunspot number for the period 1868 – 2008 and the annual mean of geomagnetic activity *aa* index for the period 1868 - 2008, are considered in the present investigation. I have determined $(aa_n^*)_{dsc}$, an average of the geomagnetic *aa* index for the year of sunspot minimum and preceding four years of the descending phase of the n^{th} cycle (*i.e.* in total 5 years) and compared with the observed maximum annual mean sunspot number $(R_{n+1})^{max}$ of the next, $(n+1)^{th}$, cycle. The variation of observed amplitude $(R_{n+1})^{max}$ for the $(n+1)^{th}$ cycle is plotted as a function of $(aa_n^*)_{dsc}$ as shown in Figure 6.3. I obtained the best linear fit to the data with the correlation coefficient (r) of 0.89. Figure 6.3 demonstrates the validation of Ohl's precursor method for deducing the size of maximum amplitude for a sunspot cycle. Ohl (1966) observed that the geomagnetic activity level during the declining phase of a solar cycle was related to the maximum level of solar activity of the next cycle.

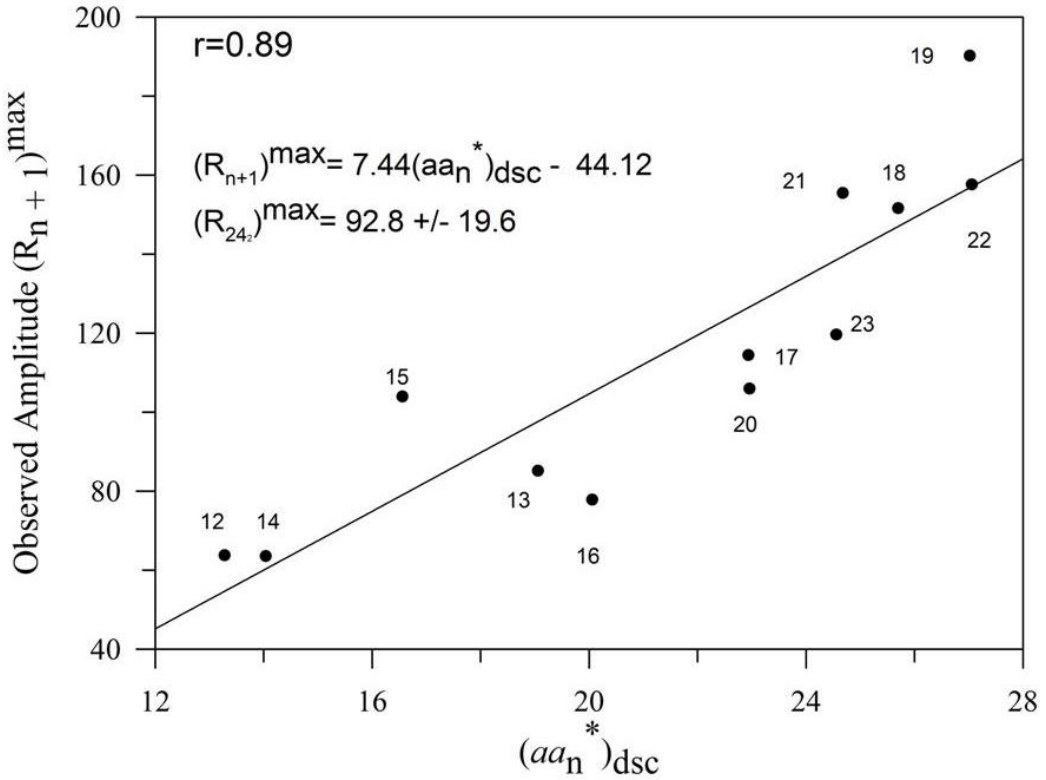

Figure 6.3: Plot of $(R_{n+1})^{max}$ of the $(n+1)^{th}$ cycle as a function of $(aa_n^*)_{dsc,}$ The solid line is the best fit with a correlation coefficient of r=0.89.

The linear equation derived from the fit of the data ranging for cycle 11 to 23 is of the following form:

$$(R_{n+1})^{max} = 7.44\ (aa_n^*)_{dsc} - 44.12 \qquad (6.1)$$

Using equation (6.1), I predicted the maximum annual mean sunspot number $(R_{n+1})^{max}$ for cycles 12 to 24 using $(aa_n^*)_{dsc}$ of the previous cycle. The predicted (open circle) and observed (triangle) maximum annual mean sunspot number, $(R_n)^{max}$ for cycle 12 to 23 as well as predicted value for cycle 24 are shown in Figure 6.4. I found the amplitude of the predicted annual mean sunspot number of cycle 24 to be 92.8 ± 19.6 (1-sigma accuracy). The maximum amplitude of cycle 24 is estimated to be about 92.8 ± 35.5 (the 90% prediction interval). This suggests that there is only a 5% chance that $(R_{24})^{max}$ is expected to exceed 128.3 or be below 57.3, unless cycle 24 proves to be a statistical outlier. My predicted amplitude of 92.8 ± 19.6 for cycle 24 is in agreement with the predictions made by a few other investigators (Kane, 1999; Wang *et al.,* 2002; de Meyer, 2003; Sello, 2003; Duhau, 2003, Schatten, 2005; Svalgaard, Cliver, & Kamide, 2005; Xu *et al, 2008*).

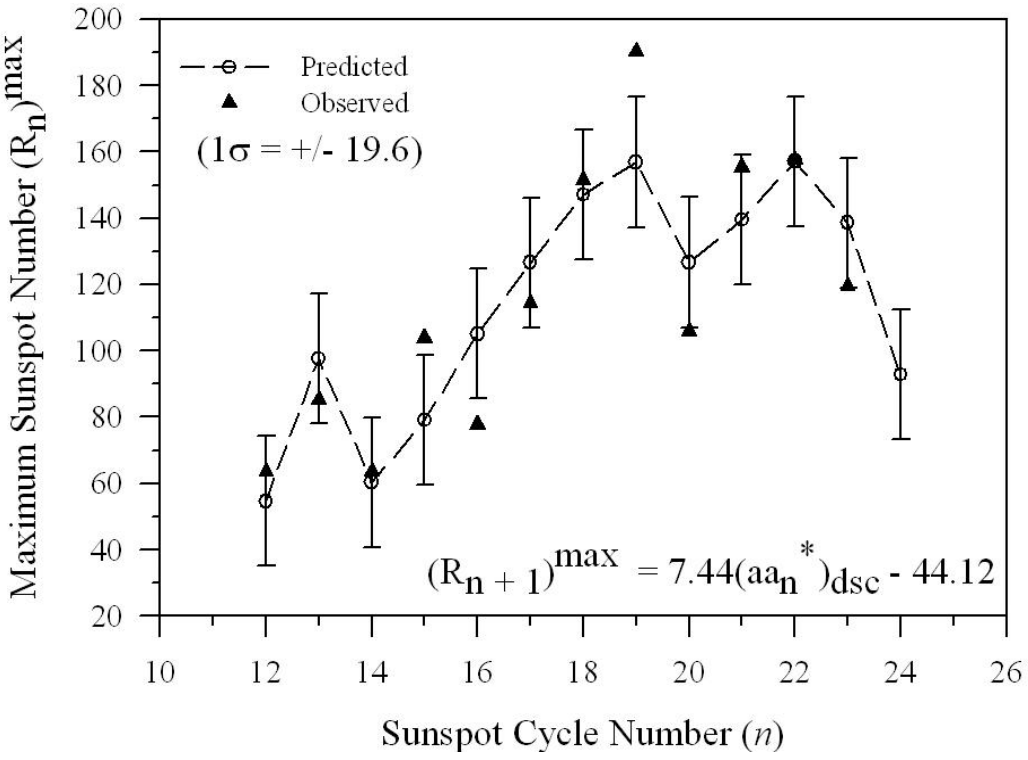

Figure 6.4: Variation of predicted (open circle) and observed (triangle) maximum annual mean sunspot number $(R_n)^{max}$ as a function of sunspot cycle number (*n*). The predicted $(R_n)^{max}$ are connected with dashed line.

6.3.3 Prediction of the Ascending Period of Cycle 24:

The ascent duration of a solar cycle is observed to be inversely correlated with the maximum amplitude of a solar cycle. Waldmeier (1935) showed that there is an inverse correlation between the length of the ascending duration of a solar cycle, and the peak sunspot number of that cycle. This phenomenon is often called the "Waldmeier effect". To predict the ascending period for solar cycle 24, I studied the relationship between the ascending period in months, $(P_n)_{asc}$ (often simply defined as the elapsed time in months from sunspot minimum amplitude to sunspot maximum amplitude) and (R_n^{max}).

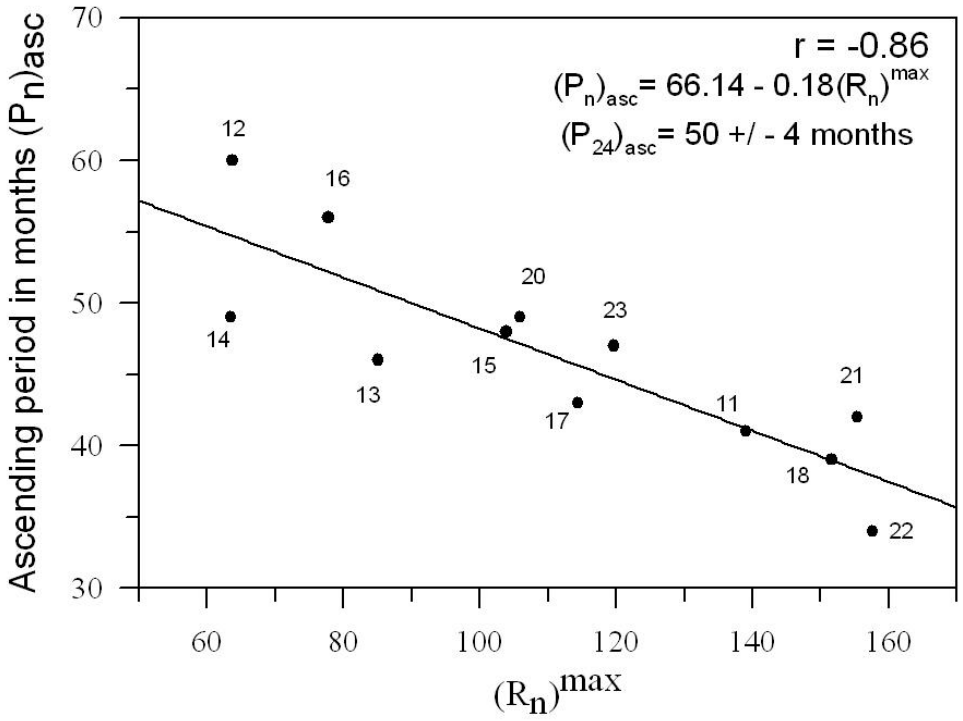

Figure 6.5: The ascending period (in months), $(P_n)_{asc}$ is plotted as a function of $(R_n)^{max}$ for cycles 11 to 23 (Cycle 19 is omitted). The solid line is the best fit with r = - 0.86.

In this investigation, I have considered the ascending period in months for cycles 11 to 23, however, excluding cycle 19 to improve the correlation. The statistical relation between maximum annual mean sunspot number, (R_n^{max}) and the corresponding $(P_n)_{asc}$ for the cycle 11 to 23 is shown in Figure 6.5. This figure unambiguously shows that the $(P_n)_{asc}$ of a solar cycle decreases with the increase in maximum annual mean sunspot number, which is the manifestation of "Waldmeier effect". Figure 6.5 is the best linear fit with a

negative correlation coefficient of ~ 0.86 and a standard error of estimate of 4 months. Figure 6.5 gives a linear relationship which can be expressed in the form of following relation:

$$(P_n)_{asc} = 66.14 - 0.18\,(R_n)^{max} \qquad (6.2)$$

From equation (6.2) the $(P_n)_{asc}$ for cycle 11 to 23 is calculated. Considering $(R_{24})^{max} = 92.8 \pm 19.6$ (Section 6.3.2) in relation (6.2) suggests $(P_n)_{asc} = 50 \pm 4$ months with 1-sigma accuracy or 50 ± 8 months being the 90% prediction interval. Provided that minimum amplitude indeed occurred in August 2008, the maximum amplitude would be expected about October 2012 ± 8 months, inferring only a 5% chance that maximum amplitude for cycle 24 will occur after June 2013 or before February 2012.

6.3.4 Prediction of the annual mean geomagnetic activity for the solar maximum year:

Next, in order to predict the level of geomagnetic activity for the sunspot maximum year in cycle 24, I obtained aa^*, which is the annual mean of *aa* during the year when sunspot is maximum for each cycle 11-23. And then the relation between the observed $(R_n)^{max}$, and aa^* is studied. Figure 6.6 represents the relationship between $(R_n)^{max}$ and aa^* for a given cycle. A linear fit is obtained between the two with a correlation coefficient of ~ 0.85 which can be expressed as

$$aa^* = 0.09(R_n)^{max} + 13.4 \qquad (6.3)$$

Using the above relation, I predicted aa^* for each cycle 11-23, which is in good agreement (standard deviation between the observed and calculated (predicted value is 2.03) with the observations. Considering the predicted amplitude of cycle 24 to be 92.8 ± 19.6 (*cf*. section 6.3.2) enabled me to estimate the aa^* during the sunspot maximum year for cycle 24 to be 21.5 ± 3.8. This predicted value of *aa** is lower relative to the observed 31 (in 1989) and 25.4 (in 2000) for cycle 22 and 23 respectively. This depicts the decreasing trend of geomagnetic activity during the sunspot maximum year of the upcoming cycle 24 as compared to previous two cycles.

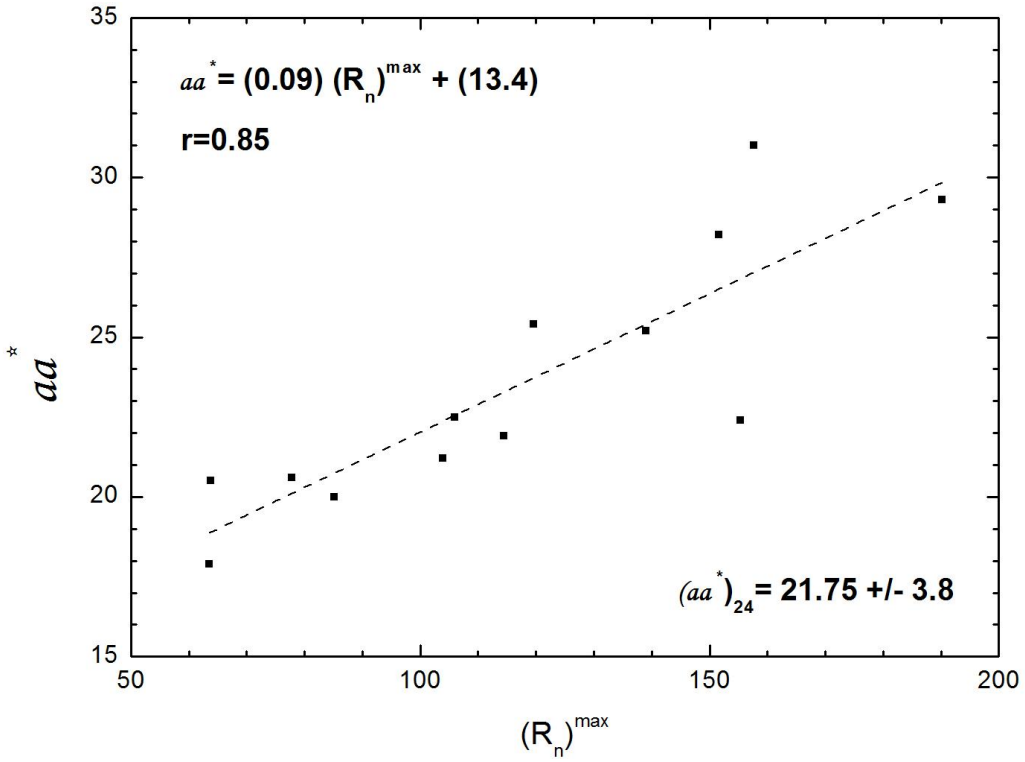

Figure 6.6: Representation of observed values of aa^* as a function of $(R_n)^{max}$ of the same cycle. Correlation coefficient is 0.85.

6.4 Discussion and Conclusion:

In the current investigation, I have used the long term data of sunspot numbers and *aa* indices from year 1868 to 2008 to predict the amplitude of sunspot cycle 24 employing the 'precursor technique' of Jain (1997). However, the prediction by Jain (1997) for cycle 23 was not accompanied by error estimates. Further, the linear relation derived by him (Equation (1) in his paper) to predict the sunspot amplitude for cycle 23 requires modification. For example, if relation (6.1) is used to predict the amplitude of cycle 23, then $(R_{23})^{max}$ = 138.6 with error estimates ±19.6 (Figure 6.4), which is closer to the observed 120. This suggests that the precursor technique employed by Jain (1997) is successful if the current linear relation with error estimates is considered.

In the present investigation, I have predicted the maximum amplitude of cycle 24 considering the error estimates. I predict the maximum amplitude for cycle 24 to be 92.8±19.6 (1-sigma accuracy), which is expected to peak in

October 2012 ± 4 months (1-sigma accuracy). My results suggest that cycle 24 will be about 40%, 41% and 22% weaker than cycle 21, 22 and 23, respectively. Further, my prediction is found to be in agreement with the predictions made by some investigators (Kane, 1999; Wang *et al.*, 2002; de Meyer, 2003; Sello, 2003; Duhau, 2003; Schatten, 2005; Svalgaard, Cliver, and Kamide, 2005; Xu *et al.*, 2008) but in disagreement with many others who have predicted either an acute minimum or an extraordinarily high amplitude of cycle 24. Recently, Wilson and Hathaway (2009) have published a technical report (NASA/TP-2009-215687, February 2009), which appears on the website http://solarscience.msfc.nasa.gov/papers.shtml. They have identified 11 statistically important single-variate fits, and 22 statistically important bi-variate fits for estimating the size of the sunspot maximum amplitude, applying the fits to cycle 24. The weighted mean prediction of 11 statistically important single-variate fits is 116 ± 34 and that of 22 statistically important bi-variate fits is 112 ± 32. Both predictions appear to be on higher side than our prediction. Many investigators have used different “precursor techniques”, and their predictions for the maximum amplitude for solar cycle 24 appear to be varying between 75 (Svalgaard, Cliver, and Kamide, 2005) and 190 (Li, Gao, and Su, 2005). Further, using the solar polar magnetic field strength, Svalgaard, Cliver, and Kamide (2005) have predicted that the approaching cycle (~ 2011 maximum) will have a peak smoothed monthly sunspot number of 75 ± 8, making it potentially the smallest cycle in the last 100 years. According to Dikpati *et al*. (2006), the upcoming cycle 24 will be about 30-50% stronger (R_z = 155-180) using modified flux transport solar dynamo model and the data of sunspot area. Choudhuri *et al.* (2007) modelled the last few solar cycles by ‘feeding’ observational data of the Sun’s polar magnetic field into their solar dynamo model. They predict that cycle 24 will be about 35% weaker than cycle 23. On the other hand, Nandy, Andrés & Petrus, 2011) reported results from kinematic dynamo simulations which demonstrate that a fast meridional flow in the first half of a cycle, followed by a slower flow in the second half, reproduces both characteristics of the minimum of sunspot cycle 23. Their model predicts that, in general, very deep minimum of a solar cycle is associated with weak polar magnetic field, which perhaps, explains the prolonged sunspot minimum in cycle 24.

However, I propose the following two hypotheses to explain the expected low amplitude of cycle 24. First, a given sunspot cycle is an extended sunspot cycle composed of two sunspot cycles, one main and the second sympathetic. The latter begins two-three years after the main cycle, and it produces a rather stronger geomagnetic activity. While comparing the geomagnetic activity during the descending phase of cycles 21, 22 and 23, I found that the *aa* index $(aa_n^*)_{dsc}$ was 27.06, 24.56 and 18.4 respectively indicating that the magnitude of the sympathetic cycle has been decreasing since cycle 21. The weak geomagnetic activity during the descending phase of solar cycle 23 is an indicator of low amplitude of solar cycle 24. My estimate of aa^* during the sunspot maximum year for cycle 24 is 21.5 ± 3.8. This predicted value of *aa** is an indication of weak geomagnetic activity relative to the observed 31(in 1989) and 25.4(in 2000) for cycle 22 and 23 respectively. I propose that the sympathetic cycle plays an important role in governing the amplitude, length and activity of the next main cycle.

My second hypothesis is based on long term periodicities of sunspots over and above 11-year primary sunspot cycle. The ~200-year periodicity (Nordemann, Rigozo, and de Faria, 2005; Ma and Vaquero, 2009 and many previous studies) is well known and we propose that the low amplitude in cycle 24 may be an epoch of this periodicity, which previously occurred in 1816, approximately 196 years ago. However, there might be other possible mechanisms to switch over the Sun to lower amplitude of the solar activity such as the Wolf – Gleissberg cycle, which has a periodicity of about 80 – 100 years.

Nevertheless, currently, the sunspots are not appearing with faster speed, and, therefore, many US based scientists are predicting the sunspots hibernation. However, on the contrary to this statement, I would like to further emphasize in view of my validation of “Waldmeier effect” (*cf.* Figure 6.5) that slow growth is another indication of cycle 24 to be a low-magnitude cycle.

CHAPTER 7
DISCUSSION AND FUTURE PROSPECTS

In this chapter I discuss the results obtained and present the international scenario with future prospects.

Discussion:

In order to improve our current understanding on the solar activity and the Sun-Earth connection in context to the solar eruptions and their impact on Earth's environment, I carried out the following investigations in this thesis:

- X-ray emission characteristics of solar flares (chapter 4).
- Solar flare plasma characteristics in association to CMEs and SEPs (chapter 5).
- Prediction of solar activity using precursor technique (chapter 6).

X-ray emission characteristics of Solar Flares:

In chapter 4 of this thesis I have investigated X-ray emission characteristics of solar flares in detail employing observations from "Solar X-ray Spectrometer (SOXS)" and "Reuven Ramaty High-Energy Solar Spectroscopic Imager (RHESSI)" missions. In the analysis of solar flares observed by SOXS and RHESSI simultaneously, the spectra in the dynamic range of about 4.1-24 keV (SOXS) and 13-100 keV RHESSI) were analyzed using multi-thermal plus single power-law (SOXS) and isothermal plus single power-law (RHESSI). I found that ε_C ranges between 20-29 keV as determined by fitting thick2 function to the HXR spectra for 6-January-2004 event. The shift of ε_C to higher energies is due to increasing contribution of thermal Bremsstrahlung at higher temperature of the flare plasma. Employing RHESSI observations, I estimated the thermal and non-thermal energies for different flare intervals for two M class flares (6-January-2004 and 5-April-2004). The investigation showed that the thermal and non-thermal energies are of the same order of magnitude (~10^{28} -10^{29} erg). The integrated thermal

and non-thermal energies for these two flares range between (~10^{29} -10^{30} erg). The E_{nth} / E_{th} (%) ratio is observed to be 0.52 and 0.9. This result may be inferred as conversion of non-thermal energy to hot flare plasma. However, the thermal energy obtained from SOXS is about 1-2 orders of magnitude higher than the non-thermal energies obtained from RHESSI. This may be due to the different energy ranges chosen for the two different instruments and high value of the computed emission measure from SOXS observations. My result is in agreement to the following results. Aschwanden (2007), ignoring possible low-energy cutoff, has found the thermal-non-thermal crossover energy 18±3.4 keV using the power law approximation of X-ray emission. However, Sui *et al.* (2005) found 24±2 keV as the low-energy cutoff (E_c) to ensure that always thermal emission dominates over non-thermal emission in low energy. They estimated the non-thermal energy content in the electrons of the order of 1.6 x 10^{30} ergs. Saint and Benz (2005) considering 20 keV as the turnover energy, which is perhaps the same as the break energy (E_b), estimated the non-thermal energy to be $\approx 2 \times 10^{30}$ ergs, almost the same value as Sui *et al.* (2005) found for an M1.2 class flare. However, the low-energy cutoff seems physically not realistic as such a configuration leads to plasma instability. Such instabilities have a growth rate typically of the order of local plasma frequency, *i.e.*, orders of magnitude shorter than the propagation time of the beam within the acceleration region. Therefore, the turnover of break energy appears to be more physically realistic and needs to be measured as precisely as possible.

The correlation among the spectral parameters of the flare confirms the general flare scenario of contribution of non-thermal flux in heating up the plasma. This study strongly supports the thermal and non-thermal relationship which confirms the standard flare model. For both the flares, the temperature reached 40-45 MK (super-hot component) during the rise phase.

I also investigated the temporal evolution of conductive and radiative power for 27-July-2005 and 5-April-2004 events. The study suggests that thermal conduction is a dominant during the rise phase which is more evident from 5-April-2004 event. This clearly indicates that in flare loops at higher temperatures, thermal conduction is a dominant mechanism during the rise

phase. Both events also indicate that in post-flare loops (or decay phase), radiative cooling is the dominant mechanism in thermal energy range.

Flare-CME-SEP association:

The flare-CME phenomena often occur in conjunction but the exact nature of the flare-CME triggers and the relationship between the cause and consequence is still open and quite puzzling (Jain *et al*. 2010).

In chapter 5, I analyzed the HXR emission of the flare and CME dynamics for 30 flare-CME pairs. I conclude that the initial linear speed of the coronal mass ejection right at the solar surface is strongly related (power-law relationship with r=0.77 for all 30 flares and r=0.84 for 19 flares for which the peak photon flux in 12-25 keV is <11000 c $(4s)^{-1}$) to the non-thermal spectral characteristics, however, before-the-peak interval of the associated flare event. My results indicate that the flare and the associated CME are the two components of one energy release system and perhaps occur together at the time of impulsive acceleration. Recent investigations regarding flare-CME relationship have been carried out by Aarnio *et al*. (2011) and Temmer *et al*. (2010). Comparing the X-ray flare fluxes with CME masses of 826 CME/flare paired events, Aarnio *et al*. (2011) found that CME mass increases with flare flux, following an approximately log-linear, broken relationship. Recent investigations by Temmer *et al*. (2010) indicated a correlation between the CME acceleration peak and the flare hard X-ray peak flux and suggested that a large sample of events may be studied to arrive to a better conclusion. They further suggested a possible relationship between the spectral slope of the HXR spectra and the CME acceleration. However, I studied in greater detail the 30 solar flare events associated with CMEs in contrast to 3 events investigated by Temmer *et al*., (2010) and achieved a new significant result that showing a good correlation between non-thermal hard X-ray spectral index and CME linear velocity. This new result rather strongly suggests that flare and CME are the two phenomena that occur together as a consequence of reconnection in the corona.

As mentioned in section 5.1.2, the flare-SEP relationship has been studied by many researchers. Saldanha *et al*. (2008) studied the progressive

spectral hardening in January 2005 solar flare events and confirmed that the progressive spectral hardening in these flares are related to solar energetic particle (SEP) events. Grigis and Benz (2008) studied the spectral hardening in large solar flares and proposed that the hardening during the decay phase is caused by continuing particle acceleration with longer trapping in the accelerator before escape. Grayson *et al*. (2009) studied 37 magnetically well-connected flares (W30°-W90°) observed by RHESSI and found that 12 out of 18 flares with SHH behavior produced SEP events and none of 19 flares without SHH behavior produced SEPs. However, all these studies are based on temporal evolution of spectra, while no study has been carried out in detail to estimating the evolution of the spectral index (hardness parameter) over time and its relation with spectral index of the associated SEP event. Therefore I studied hard X-ray spectra of the flares in greater detail in context to their relationship with the SEPs. I employed the RHESSI observations for this investigation and the results are presented in Chapter 5.

In chapter 5, I also investigated the flare-SEP relationship for 12 major solar flares. I obtained a correlationship of r=0.67 between hardest flare spectral index and hardest proton spectral index for these events (neglecting 20-January-2005 event). The study shows a good relationship between the hardness of the flare spectra seen on the Sun and the hardest proton spectra observed at the earth. My current result is new in contrast to previously known for electrons, as well as soft-hard-hard nature of X-ray spectra because it suggests that proton (ions) acceleration is in simultaneous to electrons at the same site, and the source for SEP is in the solar corona.

Krucker *et al*. (2007) compared the hard X-ray (HXR) photon spectra observed by the *RHESSI* with the spectra of the electrons in the associated solar impulsive particle events and found that the HXR photon power-law spectral index and the in situ observed electron spectral index measured above 50 keV show a good linear fit (r= 0.83) for prompt events and a weak correlation (r=0.43) for delayed events.

My results are consistent with earlier studies (section 5.1.2) suggesting that there exists a good relationship between solar flares and SEP events. It can be concluded from the investigations carried out in this chapter

that the flare, CME and SEP events may be considered as a combined event as regards to Sun-Earth connection.

Prediction of Solar Activity:

Owing to the space weather impact of solar eruptive phenomena, I have predicted the maximum amplitude of cycle 24 using the long term data of sunspot numbers and *aa* indices from year 1868 to 2008 and employing the 'precursor technique' of Jain (1997). . I predict the maximum amplitude for cycle 24 to be 92.8±19.6 (1-sigma accuracy), which is expected to peak in October 2012 ± 4 months (1-sigma accuracy). My results suggest that cycle 24 will be about 40%, 41% and 22% weaker than cycle 21, 22 and 23, respectively. In their overall performance during the course of last few solar cycles, precursor methods have clearly been superior to extrapolation methods (Petrovay, 2010). He stated that the current cycle 24 will probably mark the end of the Modern Maximum, with the Sun switching to a state of less strong activity and therefore it will be an important testbed for solar cycle prediction methods for our understanding of the solar dynamo. Many investigators have used different "precursor techniques", and their predictions for the maximum amplitude for solar cycle 24 appear to be varying between 75 (Svalgaard, Cliver, and Kamide, 2005) and 190 (Li, Gao, and Su, 2005).

I propose the following two hypotheses to explain the expected low amplitude of cycle 24. First, a given sunspot cycle is an extended sunspot cycle composed of two sunspot cycles, one main and the second sympathetic. The latter begins two-three years after the main cycle, and it produces a rather stronger geomagnetic activity. While comparing the geomagnetic activity during the descending phase of cycles 21, 22 and 23, I observed that the *aa* index $(aa_n^*)_{dsc}$ was 27.06, 24.56, and 18.4 respectively indicating that the magnitude of the sympathetic cycle has been decreasing since cycle 21. The weak geomagnetic activity during the descending phase of solar cycle 23 is an indicator of low amplitude of solar cycle 24. My estimate of aa^* during the sunspot maximum year for cycle 24 is 21.5 ± 3.8. This predicted value of *aa** is an indication of weak geomagnetic activity relative to the observed 31(in 1989) and 25.4 (in 2000) for cycle 22 and 23

respectively. I propose that the sympathetic cycle plays an important role in governing the amplitude, length and activity of the next main cycle.

My second hypothesis is based on long term periodicities of sunspots over and above a 11-year primary sunspot cycle. The ~200-year periodicity (Nordemann, Rigozo, and de Faria, 2005; Ma and Vaquero, 2009 and many previous studies) is well known and I propose that the low amplitude in cycle 24 may be an epoch of this periodicity, which previously occurred in 1816, approximately 196 years ago. I would like to mention that the prediction along with the hypothesis has already been published (Bhatt *et al*. 2009b). The recently updated (4-April-2011) “Solar Cycle 24 Prediction” project Homepage (NASA MSFC team) states that the current cycle 24 maybe the smallest sunspot cycle in nearly 200 years which supports my hypothesis.

Future Prospects:

The solar eruptions such as flares/CMEs/SEPs are the most powerful explosions in the solar system, and they endanger astronauts and spacecraft. These eruptions have a significant impact on the Earth’s environment. Owing to this Sun-Earth connection, they are of the utmost importance and of scientific interest in order to understand this difficult process of connection.

X-ray emission from solar flares can be studied with the instruments such as SOXS and RHESSI. However, the nature of the flare emission below 10 keV is still not clear. Thus it is extremely important to characterize the soft X-ray emission below 10 keV. This is possible with the development of high spectral resolution instruments. The development of high resolution instruments can give precise information on the line emission and hence the elemental abundance can be studied in greater detail.

In recent years, the flare- CME relationship is fairly better understood in view that the both phenomena have comparable energy budgets and impulsive acceleration phases. However, there are many unaddressed questions viz. origin and initiation of the CMEs in general and is it precursor or a follow-up event with the associated flare event? After about 100 years of study of solar flares/SEPs we are not able to understand the physical process that links these two phenomena and the location and time of the acceleration

of the particles. Great efforts have been made to probe into these events in recent years and as of now, many questions remain unanswered such as: how is the energy built-up in the corona and by which mechanism does it store the energy for a long time? Further, how all these eruptive phenomena are suddenly released?

I believe that in near future, the advanced observations of these most explosive solar events will be possible with the development of new and highly sophisticated instrumentation. Also, they will allow accurate measurements of weaker events in the light of increased sensitivity of the instruments.

REFERENCES

Aarnio, A.N., Stassun, K.G., Hughes, W.J. & McGregor, S.L.: 2011, Sol. Phys. **268**, 195

Adams, W.G.: 1892, Phil. Trans. London (A). **183**, 131

Akasofu.-I. & Chapman, S.: 1972, Solar Terrestrial Physics, Oxford University Press

Antiochos, S. K., Sturrock P. A.: 1978, Astrophys. J. **220**, 1137

Aschwanden, M. J.: 2006, Physics of the Solar Corona (2nd edition, Chichester, UK: Praxis Publishing Ltd)

Aschwanden, M. J.: 2007, Astrophys. J. **661**, 1242

Aschwanden, Markus J.; Stern, Robert A.; Güdel, Manuel: 2008, ApJ. **672**, Issue 1, 659

Babcock, H.W., 1961, Astrophys. J. **133**, 572

Barbieri, L. P. & Mahmot, R.E.: 2004, Space Weather. **2**, S09002

Barnard, L. & Lockwood, M.: 2011, JGR. **16**, A05103

Basu, S., Antia, H.M., 2003, ApJ. **585**, 553

Benz, A.: 1993, Plasma Astrophysics, Kluwer Academic Publishers

Benz, A.O.: 2008, Living Rev. Sol. Phys. **5**, 1

Bhatt, N.J., Jain, R. & Aggarwal, M.: 2009a, J. Astrophys. Astr. **30**, 71

Bhatt, N.J., Jain, R. & Aggarwal, M.: 2009b, Sol. Phys. **260**, 225

Broun, J.A.: 1861, Proc. Roy. Soc. Edinburgh, **22**, 511

Brown, J.C.: 1971, Sol. Phys. **18**, 489

Brown, J. C.: 1974, Proc-1974-Newkirk, 395

Brueckner, G. E., Howard, R. A., Koomen, M. J., Korendyke, C. M., Michels, D. J., Moses, J. D., Socker, D. G., Dere, K. P., Lamy, P. L., Llebaria, A. and 5 coauthors: 1995, Sol. Phys. **162**, Issue 1-2, 357

Burkepile, J. T., Hundhausen, A. J., Stanger, A. L., St. Cyr, O. C., & Seiden, J. A.: 2004, JGR(Space Physics). **109**, 3103

Burnight, T.R.: 1949, Physical Rev. **76**, 165

Campbell, W.H.: 1997, Introduction to Geomagnetic Fields, Cambridge University Press

Caspi, A., Lin, R. P.: 2010, Astrophys. J. Lett. **725,** 161

Carmichael, H.: 1964, Proc-1964-Hess, 451

Chapman, S.: 1935, Terr. Mag. Atmos. Phys. **40**, 349

Chapman, S.: 1952, Annali di Geofisica. **5**, 481

Chapman, G. A., Dobias, J. J., Arias, T.: 2011, ApJ. **728,** Issue 2, article id. 150

Chen, J.; Howard, R. A.; Brueckner, G. E.; Santoro, R.; Krall, J.; Paswaters, S. E.; St. Cyr, O. C.; Schwenn, R.; Lamy, P.; Simnett, G. M.: 1997, Astrophysical Journal Letters.[Astrophys. J. Lett.] **490**, L191

Chen, A-Q. & Zong, W.G.: 2009, Research in Astron. Astrophys. **9,** No.4, 470

Chen, P.F.: 2011, Living Rev. Sol. Phys. **8**, 1

Choudhuri, A. R, Chatterjee, P & Jiang, J.: 2007, Physical Review Letters, **98**, 13, id. 131103.

Chupp, E.L., Forrest, D.J., Higbie, P.R., Suri, A.N., Tsai, C., Dunphy, P.P.: 1973, Nature. **241**, Issue 5388, 333

Clilverd, M. A., Clark, T. D. G., Clarke, E. & H. Rishbeth.: 1998, J. Atmos. Sol. Terr. Phys. **60**, 1047

Colaninno, R.C. & Vourlidas, A.: 2009, ApJ. **698,** 852

Craig, I. J. D., Brown, J. C.: 1976, Astron. Astrophys. **49**, 239

Culhane, J.L., Phillips, A.T., Inda-Koide, M., Kosugi, T., Fludra, A., Kurokawa, H., Makishima, K., Pike, C.D., Sakao, T., Sakurai, T.: 1994, Sol. Phys. **153**, 307

Dabas, R.S., Sharma, K., Das, R.M., Pillai, K.G.M., Chopra, P., Sethi, N.K.: 2008, Sol. Phys. **250**, 171

de Meyer, F.: 2003, Sol. Phys. **217**, 349

Delaboudinière, J.-P., Artzner, G. E., Brunaud, J., Gabriel, A. H., Hochedez, J. F., Millier, F., Song, X. Y., Au, B., Dere, K. P., Howard, R. A. and 18 coauthors:1995**,** Sol. Phys. **162**, 291

Demetrescu, C. & Dobrica, V.: 2008, JGR. **113**, A02103

Dennis, B.R., Zarro, D.M.: 1993, Sol. Phys. **146**, 177

Dennis, B. R., Phillips, K. J. H., Schwartz, R. A., Tolbert, A. K., Hudson, H. S.: 2003, Team R, SPD. **34**, 1809

Dere, K. P., Landi, E., Mason, H. E., Monsignori Fossi, B. C., Young, P. R.: 1997, Astron. Astrophys. Suppl. **125**, 149

Desai, U. D., Pantazis, J., & Shah, K.: 1995, Astrophys. Space Sci. **231**, 487

Dibyendu Nandy, , Andrés Muñoz-Jaramillo & Petrus C. H. Martens.: 2011, Nature. **471,** 80, 3 March 2011

Dikpati, M., G.de Toma, and P. A.Gilman.: 2006, Geophys. Res. Lett., **33**, L05102.

Dryer, M.:1982, SSR. **33**, 233

Duhau, S.: 2003, Sol. Phys. **213**, 203

Dungey, J.W.: 1961, Phys. Rev. Lett. **6**, 47

Drake, J.F.: 1971, Sol. Phys. **16,** 152

Feynman, J., & Crooker, N. U.: 1978, Nature. **275**, 626

Frost, K. J. & Dennis, B. R.:1971, ApJ. **165**, 655

Gan, W. Q., Li, Y. P., Chang, J., McTiernan, J. M.: 2002, Sol. Phys. **207**,137

Gold, T.:1959, J. Geophys. Res. **64**, 1219

Gonzalez, W. D., Joselyn, J. A., Kamide, Y., Kroehl, H. W., Rostoker, G., Tsurutani, B. T. & Vasyliunas, V. M.: 1994, JGR. **99**, A4, 5771

Gosling, J. T.:1993, JGR. **98**, 18937

Grayson, J.A., Krucker, S., Lin, R.P.: 2009, ApJ. **707,** 1588

Grigis, P.C. & Benz, A. O.: 2008, ApJ. **683**, Issue 2, 1180

Hale, G.E., Ellerman, F., Nicholson, S.B. and Joy, A.H.: 1919, Astrophys. J., **49**, 153

Hanuise, C., Cerisier, J.C., Auch`ere, F., Bocchialini, K., Bruinsma, S., Cornilleau-Wehrlin, N., Jakowski, N., Lathuill`ere, C., Menvielle, M., Valette, J.-J., Vilmer, N., Watermann, J. & Yaya, P.: 2006, Annales Geophysicae. **24**, 129

Hathaway, D.H., Wilson, R.M.: 2006, Geophys. Res. Lett. **33**, L18101

Hathaway, D. H.:2010, Living Rev. Solar Phys., **7**, 1

Hey, J.S.: 1983, The Radio Universe, 3rd Edition, Oxford: Pergamon

Hirayama, T.: 1974, Sol. Phys. **34**, 323

Huber, A. C., Pantazis, J. A., & Jordanov, V. T.: 1995, Nucl. Instrum. Methods **B99**, 665

Hudson, H.S., Peterson, L.E. & Schwartz, D.A.: 1969, Astrophys. J. **157**, 389

Hudson, H., Haisch, B. & Strong, K. T.: 1995, JGR. **100**, 3473

Hudson, H.S., Canfield, R.C. & Kane, S.R.:1978, Sol. Phys. **60**, 137

Hudson, H. S.: 1991, Bull. Am. Astron. Soc. **23**, 1064

Jackman, C.H., Deland, M.T., Labow, G.J., Fleming, E.L., Weisenstein, D.K., Ko, Malcolm K.W., Sinnhuber, M., Russel, J.M.: 2005, JGR. **110**, A09S27

Jackson, J.D.:1962, Classical Electrodynamics (J. Wily & Sons, New York)

Jain, R.: 1986, Mon. Not. R. Astr. Soc. **223**, 877

Jain, R.: 1997, Sol. Phys. **176**, 431

Jain, R., Rao, A. R., Deshpande, M. R., Dwivedi, B. N., Manoharan, P. K., Seetha, S., Vahia, M. N., Vats, H. O., and Venkatkrishnan, P.: 2000a, Bull. Astron. Soc. India. **28**,117

Jain, R., Dave, H. H., Vadher, N. M., Shah, A. B., Ubale, G. P., Shah, V. M., Solanki, C. M., Kayasth, S. L., Patel, V. D., Shah, K. J., and Deshpande, M. R.: 2002a, Characterization and Response of Si PIN and CZT Detectors, PRL-GSAT-2-SOXS-0180, PRL Technical Document.

Jain, R., Dave, H. H., Vadher, N. M., Shah, A. B., Ubale, G. P., Shah, V. M., Solanki, C. M., Kayasth, S. L., Patel, V. D., Pabari, J., Shah, K. J., Panchal, G. A., and Deshpande, M. R.: 2002b, SOXS – LOW-ENERGY PAYLOAD 121 Configuration Design Review (CDR) Document of SOXS Low Energy Detector (SLED) Package, PRL-GSAT-2-SOXS-0181, PRL Technical Document.

Jain, R., Dave, H. H., Vadher, N. M., Shah, A. B., Ubale, G. P., Shah, V. M., Shah, K. J., Kumar, S., Kayasth, S. L., Patel, V. D., Trivedi, J., and Deshpande, M. R.: 2003, Pre-Flight Characterization and Response of the SLD/SOXS Payload, PRL-GSAT-2-SOXS-0185, PRL Technical Document.

Jain, R., Dave, H. H., Shah, A. B., Vadher, N. M., Shah, V. M., Ubale, G. P., Manian, K. S. B., Solanki, C. M., Shah, K. J., Sumitkumar, Kayasth, S. L., Patel, V. D., Trivedi, J. M. & Deshpande, M. R..: 2005, Sol Phys. **227**, 89

Jain, R., Joshi, V., Sakurai, T. & Upadhyay, N.:2006a, J. Astrophys. Astr. **27,** 339

Jain, R., Pradhan, A. K., Joshi, V., Shah, K. J., Trivedi, J. J., Kayasth, S. L., Shah, V.M., Deshpande, M.R.: 2006b, Sol. Phys. **239,** 217

Jain, R.; Aggarwal, M. & Sharma, R.: 2008, J. Astrophys. Astr. **29**, 125

Jain, R & Bharti, L.:2009, Asian Journal of Physics. **17,** Issue 3 & 4, 319

Jain, R., Aggarwal, M. & Kulkarni, P.: 2010, Research in Astron. Astrophys. **10**, No. 5, 473

Jain, R., Awasthi, A. & Rajpurohit, A. & Aschwanden, M. J.: 2011, Sol. Physics. **270**, Issue 1, 137

Jordanov, V. T., Pantazis, J. A., and Huber, A. C.: 1996, Radiation **22/3**, 37

Joselyn, J.A., Anderson, J.B., Coffey, H., Harvey, K., Hathaway, D., Heckman, G., Hildner, E., Mende, W., Schatten, K., Thompson, R., Thomson, A.W.R., White, O.R.: 1997, EoS Trans. AGU **78**, 205

Kaiser, M. L., Kucera, T. A., Davila, J. M., St. Cyr, O. C., Guhathakurta, M., & Christian, E.: 2008, SSR. **136**, 5

Kane, R. P.: 1997, Geophys. Res. Lett. **25**, 3121

Kane, R.P.: 1978, Nature. **274**, 139

Kane, R.P.: 1999, Sol. Phys. **189**, 217

Kane, R.P.: 2005, JGR. **110**, A02213

Kane, R.P.: 2007, Sol Phys. **243**, 205

Kay, H. R. M., Harra, L. K., Matthews, S. A., Culhane, J. L., & Green, L. M.: 2003, A&A. **400**, 779

Kiplinger, A. L.: 1995, ApJ. **453**, 973

Klimchuk, J. A.: 2001, in Proc. the Chapman Conference on Space Weather, ed. H. S. P. Song, & G. Siscoe, AGU, Geophysical Monograph Series. **125**, 143

Kopp, R.A. & Pneuman, G.W.: 1976, Sol. Phys. **50**, 85

Koskinen, H. E. J.; Huttunen, K. E. J.: 2006, SSR. **124**, Issue 1-4, 169

Kraft, S., Bavdaz, M., Castelletto, B., Peacock, A., Scholze, F., Ulm, G., Gaghardi, M. A., Nenonen, S., Tuomi, T., Juvonen, M., and Ranyamaki, R.: 1998, Nucl. Instrum. Methods. **A418**, 337

Krieger, A. et al: 1972, Sol. Phys. **22**, 150

Krucker, S., Kontar, E.P., Christe, S. & Lin, R.P.: 2007, ApJ. **663**, L109

Kuvvetli, I., Budtz-Joergensen, C. C.,Westergaard, N. J., Jonasson, P., van Pamelen, M. A., Reglero, V., Eyles, C. J., and Neubert, T.: 1999, in X. Oswald, H. Siegmund and K. A. Flanagan (eds.), EUV, X-Ray, and Gamma-Ray Instrumentation for Astronomy, Proc. SPIE, **3765**, 370

Lachish, U.: 1999, in R. B. James and R. C. Schirato (eds.), Hard X-Ray, Gamma-Ray, and NeutronDetector Physics, Proc. SPIE, **3768**, 374

Lachish, U.: 2001, IEEE Trans. Nucl. Sci. **48**

Landi, E., Chiuderi Drago, F.: 2003, Astrophys. J. **589**, 1054.

Landi, E., Phillips, K. J. H.: 2005, Astrophys. J. Suppl. **160**, 286.
Landi, E., Zanna, D. G., Young, P. R., Dere, K. P., Mason, H. E., Landini, M.: 2006, Astrophys. J. Suppl. **162**, 261.
Landi, E.; Klimchuk, J. A.: 2010, ApJ. **723**, Issue 1,320
Li, K.-J., Gao, P.-X., Su, T.-W.: 2005, Chin. J. Astron. Astrophys. **5**, 539
Lin, R.P. & Hudson, H.S.:1976, Sol. Phys. **50**,153
Lin, R. P. et al.: 2002, Sol. Phys. **210**, 3
Low, B.C.: 1996, Sol. Phys. 167, 217
Lukianova, R., Alekseev, G. & Mursula, K.: 2009, JGR. **114**, A02105
Ma, L.H., Vaquero, J.M.: 2009, New Astron. **14**, 307
MacQueen, R.M.: 1980, Philos. Trans. Royal Soc. London A297, 605
Marsch, E.:2006, Proceedings of ILWS workshop, Goa available at: http://cdaw.gsfc.nasa.gov/publications/ilws_goa2006/111_Marsch.pdf
Matteson, J. L., Coburn, W., Duttweiler, F., Heindl, W. A., Huszar, G. L., Leblanc, P. C., Pelling, M. R., Peterson, L. E., Rothschild, R. E., and Skelton, R. T.: 1997, CdZnTe Arrays for Astrophysics Applications, Proc. SPIE, **3115**, 160
Mayaud, P. N.: 1972, JGR. **77**, 6870
McTiernan, J. M., Fisher, G. H. & Li, Peng.: 1999, ApJ. **514**, Issue 1, 472
Mierla, M., Inhester, B., Antunes, A., Boursier, Y., Byrne, J. P., Colaninno, R.; Davila, J., de Koning, C. A., Gallagher, P. T., Gissot, S. and 19 coauthors: 2010, Annales Geophysicae, **28**, Issue 1, 203
Moon, Y.-J., Choe, G. S., Wang, H., Park, Y. D., Gopalswamy, N., Yang, G., & Yashiro, S.: 2002, ApJ. **581**, 694
Moon, Y.-J., Choe, G. S., Wang, H., Park, Y. D., & Cheng, C. Z.: 2003, Journal of Korean Astronomical Society. **36**, 61
Moos, N.A.F.: 1910, Magnetic observations made at the government observatory, Bombay, for the period 1846 to 1905, and their discussion, Part II: the phenomenon and its discussion, Bombay
Narita, T., Bloser, P. F., Grindlay, J. E., Sudharsanan, R., Reiche, C., and Stenstrom, C.: 1997, in F. Patrick Doty, Richard B. Hoover (eds.), Hard X-Ray and Gamma-Ray Detector Physics and Applications, Proc. SPIE. **3446**, 218
Neupert, W. M.: 1968, ApJ. **153**, L59

Nordemann, D.J.R., Rigozo, N.R., de Faria, H.H.: 2005, Adv. Space Res. **35**, 891

Ohl, A.I.: 1966, Soln. Dann. **12**, 84

Ohl, A.I.: 1971, Geomagn. Aeron. **11**, 549

Parker, E. N.: 1958, ApJ. **128**, 664

Parkinson, J.H.: 1973, Astron. & Astrophys. **24**, 215

Parks, G.K. & Winckler, J.R.:1969, ApJ. **155,** L117

Peterson, L.E. & Winckler, J.R.: 1959, JGR. **64**, 697

Petrovay. K.: 2010, Living Rev. Solar Phys. **7**, 6

Petschek, H. E.: 1964, The Physics of Solar Flares, Proceedings of the AAS-NASA Symposium held 28-30 October, 1963 at the Goddard Space Flight Center, Greenbelt, MD. Edited by Wilmot N. Hess. Washington, DC: National Aeronautics and Space Administration, Science and Technical Information Division, 1964., 425

Philip, Judge.: 2008, ApJ. **683,** L87

Phillips, K. J. H., Sylwester, J., Sylwester, B., Landi, E.: 2003, Astrophys. J. Lett. **589**, 113.

Phillips, K. J. H.: 2004, ApJ. **605,** 921

Phillips, K. J. H., Rainnie, J. A., Harra, L. K., Dubau, J., Keenan, F. P., Peacock, N. J.: 2004, Astron. Astrophys. **416,** 765

Reames, D.V.: 1999, Space. Sci. Rev. **90**, 413

Reames, D.V.: 2004, Adv. Space Res. **34**, 381

Rosner, R.; Tucker, W. H.; Vaiana, G. S.: 1978, ApJ.Part 1, **220**, 643

Russell, C. T.: 1975, Sol. Phys. **42**(1), 259

Saint-Hilaire, P., Benz, A. O.: 2005, Astron. Astrophys. **435**, 743

Saldanha, R., Krucker, S., & Lin, R. P.: 2008, ApJ. **673**, 1169

Scharmer, G. B. et al.: 2002, Nature. Vol. **420**, Issue 6912, 151

Schwabe, H., 1844, “Sonnen-Beobachtungen im Jahre 1843”, Astron. Nachr., **21**(495), 233

Schwartz, R. A., Csillaghy, A., Tolbert, A. K., Hurford, G. J., McTiernan, J. & Zarro, D.: 2002, Sol. Phys. **210**, 165

Schatten, K.: 2005, Geophys. Res. Lett. **32**, L21106

Schwenn, R.:2006, Living Rev. Solar Phys. **3**, 2

Sello, S.: 2003, Astron. Astrophys. **410**, 691

Sharma, M. R., Umapathy, C. N., Kulkarni, R., Kumar, Jain, A. K. & Sreekumar, P.: 2000, GSAT-2 Spacecraft Preliminary Design Review (PDR) Document for Solar X-ray Spectrometer – Part 2, ISRO-ISAC-GSAT-2-RR-0155, Technical Document.

Sheeley, N. R., Walters, J. H., Wang, Y.-M., Howard, R. A.: 1999, JGR. **104**, A11, 24739

Shibata, K.: 1995, Proc-1995- Watanabe, 85

Smith, D. M., et al.: 2002, Sol. Phys. **210**, 33

Sturrock, P.A.: 1966, Nature, **5050**, 695

Sugiura, M.:1964, Ann. Int. Geophys. Year, **35**, 9, Pergamon Press, Oxford

Sugiura, M. & Chapman, S.: 1960, The average morphology of geomagnetic storms with sudden commencement, Abandl. Akad. Wiss. Göttingen Math. Phys. Kl., Sondernheft Nr.4, Göttingen

Sui, L., Holman, G. D., Dennis, B. R.: 2005, Astrophys. J. **626**, 1102

Švestka, Z.:1976, Solar Flares, vol. 8 of Geophysics and Astrophysics Monographs, D. Reidel Publishing company, Boston, U.S.A

Svalgaard, L., Cliver, E.W., Le Sager, P.: 2004, Adv. Space Res. **34**

Svalgaard, L., Cliver, E.W., Kamide, Y.: 2005, Geophys. Res. Lett. **32**, L01104

Spiegel, E. A., & Zahn, J.-P. 1992, A&A. **265**, 106

Temmer, M., Veronig, A.M., Kontar, E.P., Krucker, S. & Vršnak, B.: 2010. ApJ. **712**, 1410

Thompson, R.J.: 1993, Sol. Phys. **148**, 383.

Thomas, R.J. & Teske, R.G.: 1971, Sol. Phys. **16,** 431

Tousignant, O., Hamel, L.-A., Courville, J.-F., Paki, P., Macri, J. R., Larson, K., Mayer, M., McConnell, M. L., and Ryan, J. M.: 1997, in Richard B. Hoover, F. Patrick Doty (eds.), Hard X-Ray and Gamma-Ray Detector Physics, Optics, and Applications, Proc. SPIE, **3115**, 214

Tsuneta, S.: 1996, ApJ. **456**, 840

Tsuneta, S.: 1997, ApJ. **483**, 507

Umapathy, C. N., Sharma, M. R., Kulkarni, R., Kumar, and Solanki, C. M.: 2003, GSAT-2 Spacecraft Design Document on the Processing Electronics for Low Energy Detector System-SOXS, ISROISAC-GSAT-2-RR-0365, Technical Document.

Usoskin, I.G.: 2008, Living Rev. Solar Phys., **5**, 3

Viswanatha, N.: 2000, GSAT-2 Spacecraft Preliminary Design Review Document (PDR) – Mechanisms, ISRO-ISAC-GSAT-2-RR-0160, Technical Document.

Vrˇsnak, B., Sudar, D., & Ruˇzdjak, D.: 2005, A&A. **435**, 1149

Veronig, A., Temmer, M., Hanslmeier, A., Otruba, W., & Messerotti, M.: 2002a, A&A. **382**, 1070

Veronig, A., Vršnak, B., Dennis, B. R., Temmer, M., Hanslmeier, A. & Magdalenić, J.: 2002b, Astronomy and Astrophysics, **392**, 699

Vourlidas, A., Subramanian, P., Dere, K. P., Howard, R. A.:2000, ApJ. **534**, Issue 1, 456

Vestine, E.H., Laporte, L., Lange. I. & Scott, W.E.: 1947, The geomagnetic field, its description and analysis, Carnegie Institution of Washington Publication 580, Washington D.C.

Vršnak, B.; Sudar, D.; Ruždjak, D.: 2005, A & A, **435**, 1149

Vrˇsnak, B., 2008, Ann. Geophys., **26**, Issue 10, 3089

Waldmeier, M.: 1935, Astron. Mitt. Zurich **14**(133), 105

Wang, J.L., Gong, J.C., Liu, S.Q., Le, G.M., Sun, J. L.: 2002, Chin. J. Astron. Astrophys. **2**, 557

Wilson, R.M.: 1990, Sol. Phys. **125**, 143.

Wilson, R.M., Hathaway, D.H.: 2006, NASA/TP-2006-214711, available at http://trs.nis.nasa.gov/archive/00000741/

Wilson, R.M., Hathaway, D.H.: 2008a, NASA/TP-2008-215249, 20 pp., February 2008, http://trs.nis.nasa.gov/archive/00000773/

Wilson, R.M., Hathaway, D.H.: 2008b, NASA/TP-2008-215413, 90 pp., June 2008, http://trs.nis.nasa.gov/archive/00000782/

Wilson, R.M., Hathaway, D.H.: 2009, NASA/TP-2009-215687, February 2009, http://solarscience.msfc.nasa.gov/papers.shtml

Wu, S.T.:1982, SSR. **32,** No. 1-2, 115

Xu, T., Wu, J., Zhen, S., Li, Q.: 2008, Chin. J. Astron. Astrophys. **8**, 337

Yermolaev, Yu. I. & Yermolaev, M. Yu.: 2010, Izvestiya, Atmospheric and Oceanic Physics, **46**, Issue 7, 799

Zhang, J., Dere, K.P., Howard, R.A., Kundu, M.R., White, S.M.: 2001, ApJ. **559**, Issue 1, 452

Other referred websites:

Hartland Observatory, Monthly Magnetic Bulletin, March 2011 available at: http://www.geomag.bgs.ac.uk/data_service/data/bulletins/had/2011/had_mar11.pdf

U.S. Geological Survey website: http://geomag.usgs.gov/operations.php#sensors

“The Weekly” report by NOAA/Space Weather Prediction Center available at: http://www.swpc.noaa.gov/weekly/pdf2008/prf1688.pdf

GOES databook available at http://goes.gsfc.nasa.gov/text/GOES-N_Databook/databook.pdf

User Guide SWPC NOAA available at: http://www.swpc.noaa.gov/weekly/Usr_guide.pdf

http://wdc.kugi.kyoto-u.ac.jp/dstdir/dst2/onDstindex.html

“Solar Cycle 24 Prediction”, project homepage, NASA Marshall Space Flight Center. http://solarscience.msfc.nasa.gov/predict.shtml (updated 4th April 2011)

Appendix A

Plots of Flare spectra

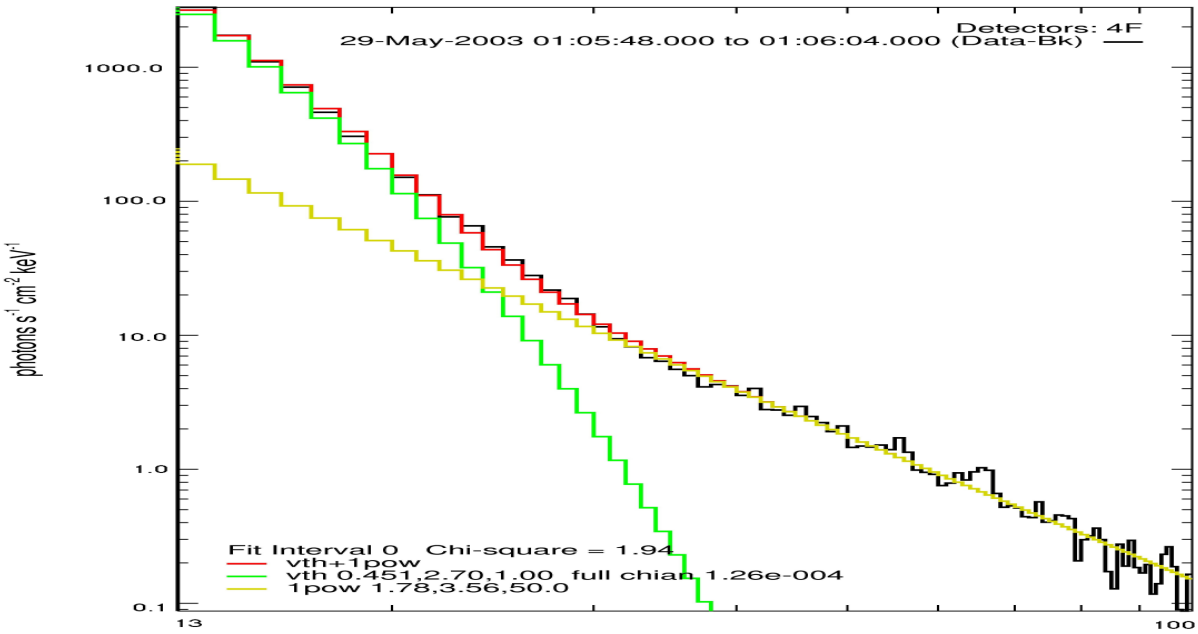

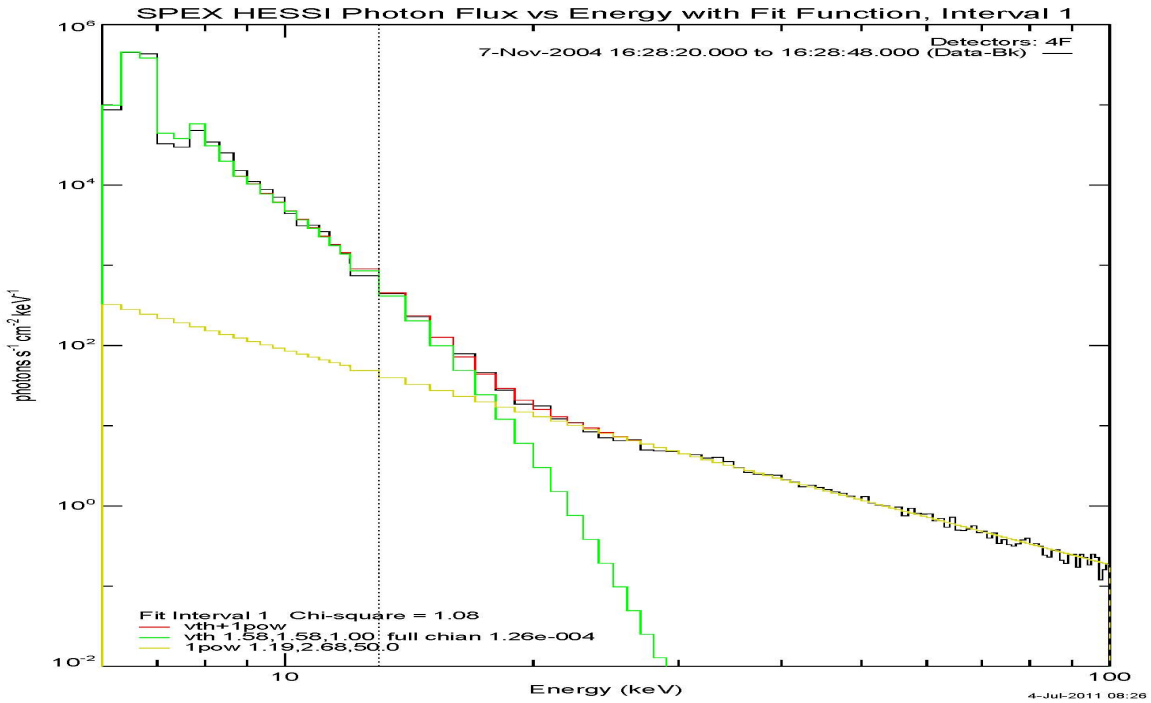

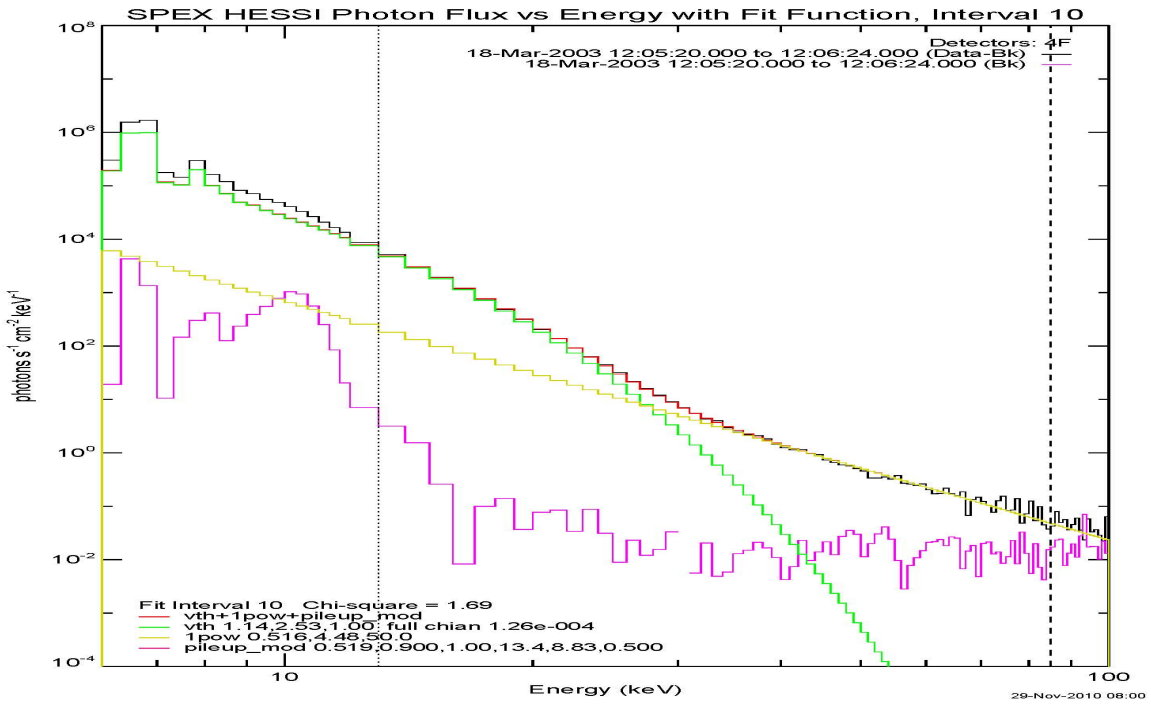
SPEX HESSI Photon Flux vs Energy with Fit Function, Interval 10
Detectors: 4F
18-Mar-2003 12:05:20.000 to 12:06:24.000 (Data-Bk)
18-Mar-2003 12:05:20.000 to 12:06:24.000 (Bk)
photons s-1 cm-2 keV-1
Energy (keV)
Fit Interval 10 Chi-square = 1.69
vth+1pow+pileup_mod
vth 1.14,2.53,1.00 full chian 1.26e-004
1pow 0.516,4.48,50.0
pileup_mod 0.519,0.900,1.00,13.4,8.83,0.500
29-Nov-2010 08:00

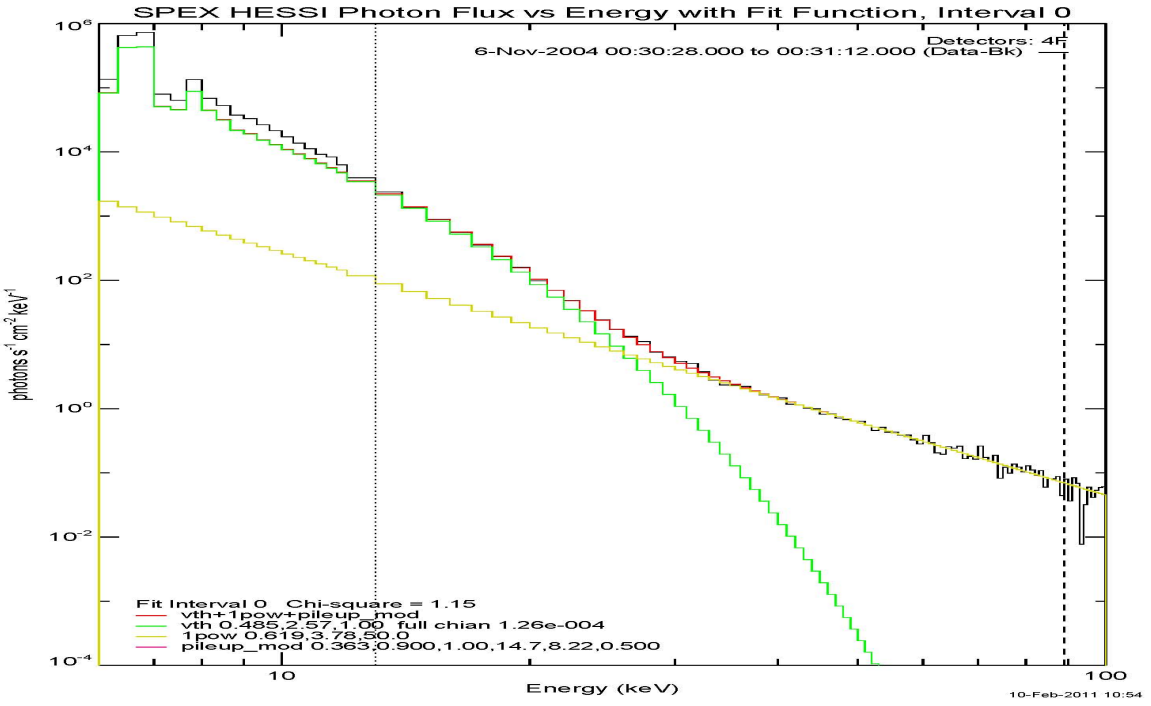
SPEX HESSI Photon Flux vs Energy with Fit Function, Interval 0
Detectors: 4F
6-Nov-2004 00:30:28.000 to 00:31:12.000 (Data-Bk)
photons s-1 cm-2 keV-1
Energy (keV)
Fit Interval 0 Chi-square = 1.15
vth+1pow+pileup_mod
vth 0.485,2.57,1.00 full chian 1.26e-004
1pow 0.619,3.78,50.0
pileup_mod 0.363,0.900,1.00,14.7,8.22,0.500
10-Feb-2011 10:54

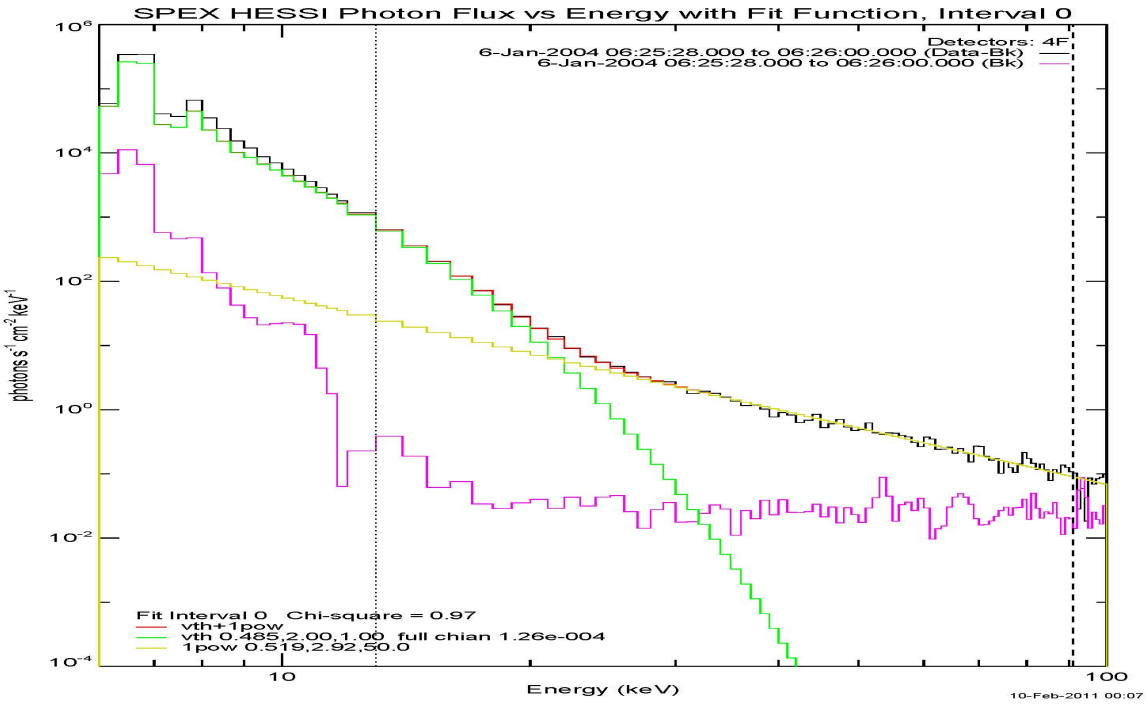
SPEX HESSI Photon Flux vs Energy with Fit Function, Interval 0
Detectors: 4F
6-Jan-2004 06:25:28.000 to 06:26:00.000 (Data-Bk)
6-Jan-2004 06:25:28.000 to 06:26:00.000 (Bk)
Fit Interval 0 Chi-square = 0.97
vth+1pow
vth 0.485,2.00,1.00 full chian 1.26e-004
1pow 0.519,2.92,50.0
photons s-1 cm-2 keV-1
Energy (keV)
10-Feb-2011 00:07

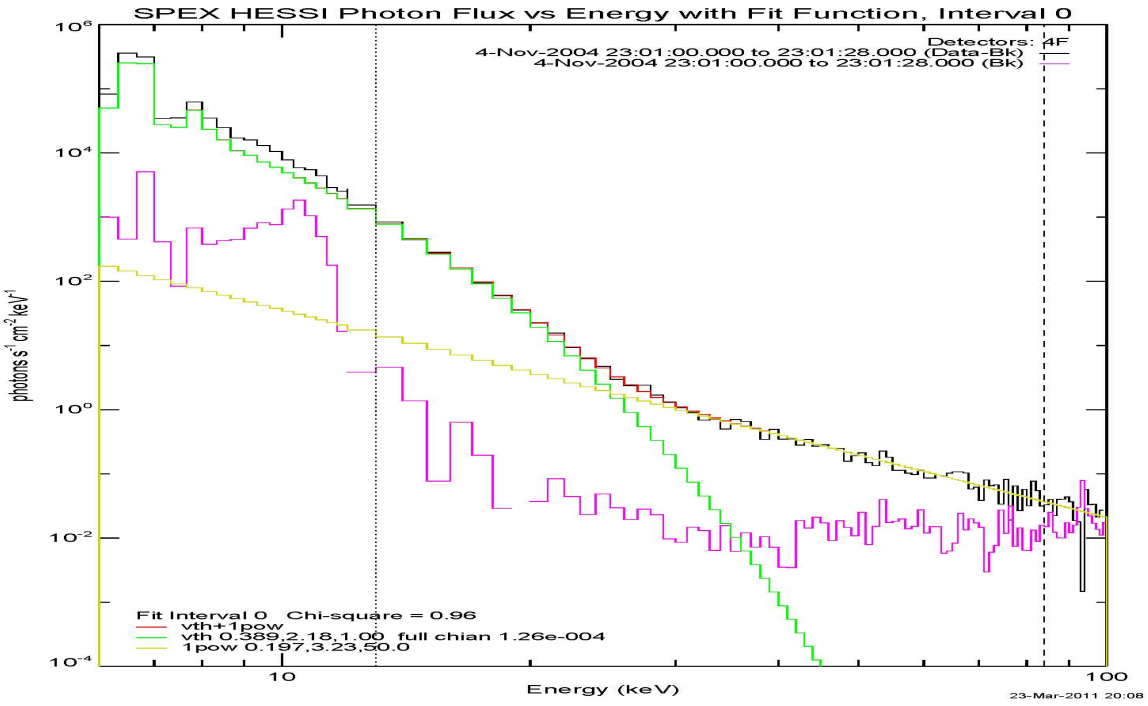
SPEX HESSI Photon Flux vs Energy with Fit Function, Interval 0
Detectors: 4F
4-Nov-2004 23:01:00.000 to 23:01:28.000 (Data-Bk)
4-Nov-2004 23:01:00.000 to 23:01:28.000 (Bk)
Fit Interval 0 Chi-square = 0.96
vth+1pow
vth 0.589,2.18,1.00 full chian 1.26e-004
1pow 0.197,3.23,50.0
photons s-1 cm-2 keV-1
Energy (keV)
23-Mar-2011 20:08

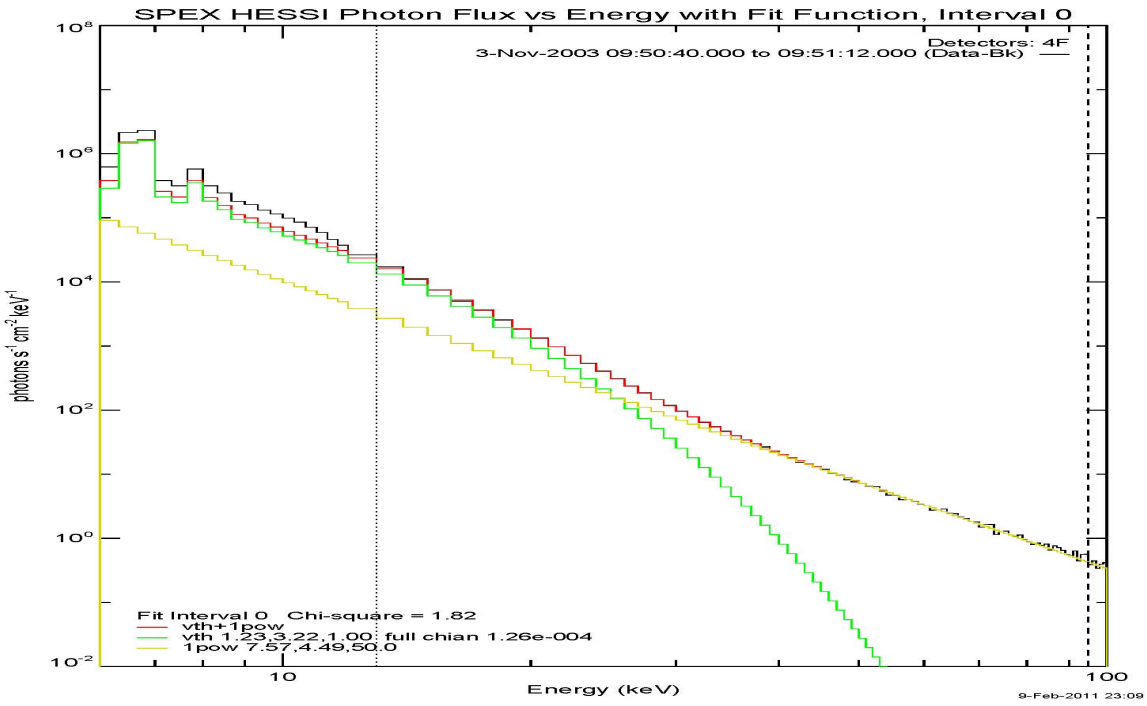
SPEX HESSI Photon Flux vs Energy with Fit Function, Interval 0
Detectors: 4F
3-Nov-2003 09:50:40.000 to 09:51:12.000 (Data-Bk)
photons s-1 cm-2 keV-1
Fit Interval 0 Chi-square = 1.82
vth+1pow
vth 1.23,3.22,1.00 full chian 1.26e-004
1pow 7.57,4.49,50.0
Energy (keV)
9-Feb-2011 23:09

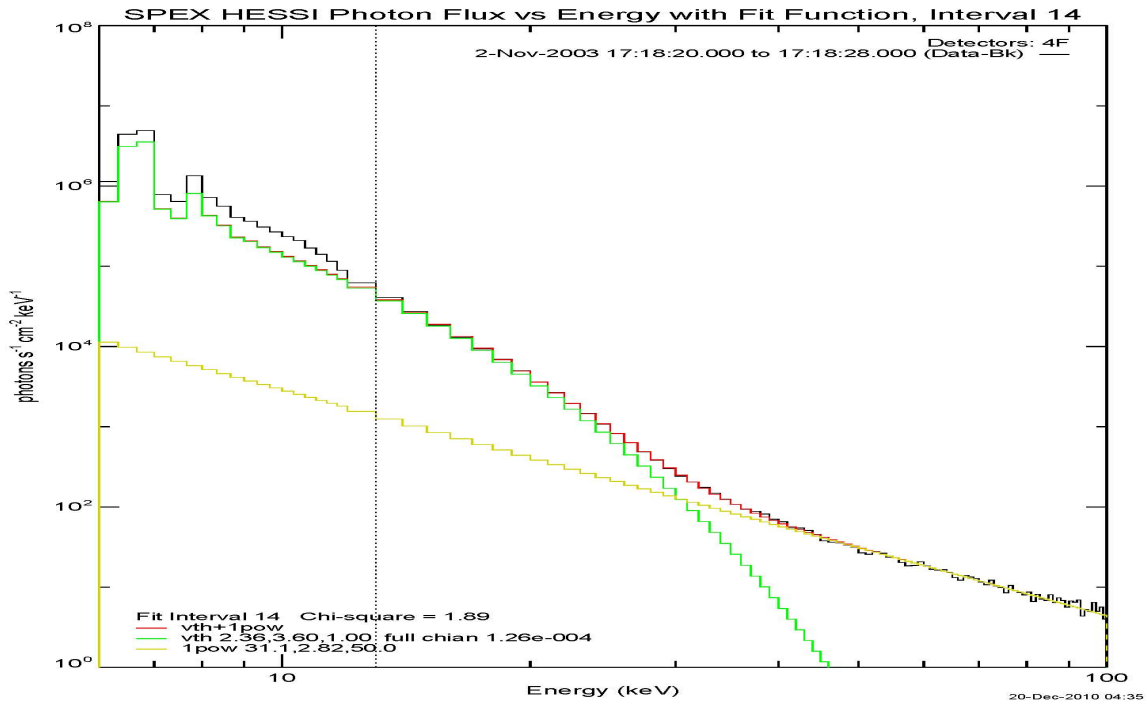
SPEX HESSI Photon Flux vs Energy with Fit Function, Interval 14
Detectors: 4F
2-Nov-2003 17:18:20.000 to 17:18:28.000 (Data-Bk)
photons s-1 cm-2 keV-1
Fit Interval 14 Chi-square = 1.89
vth+1pow
vth 2.36,3.60,1.00 full chian 1.26e-004
1pow 31.1,2.82,50.0
Energy (keV)
20-Dec-2010 04:35

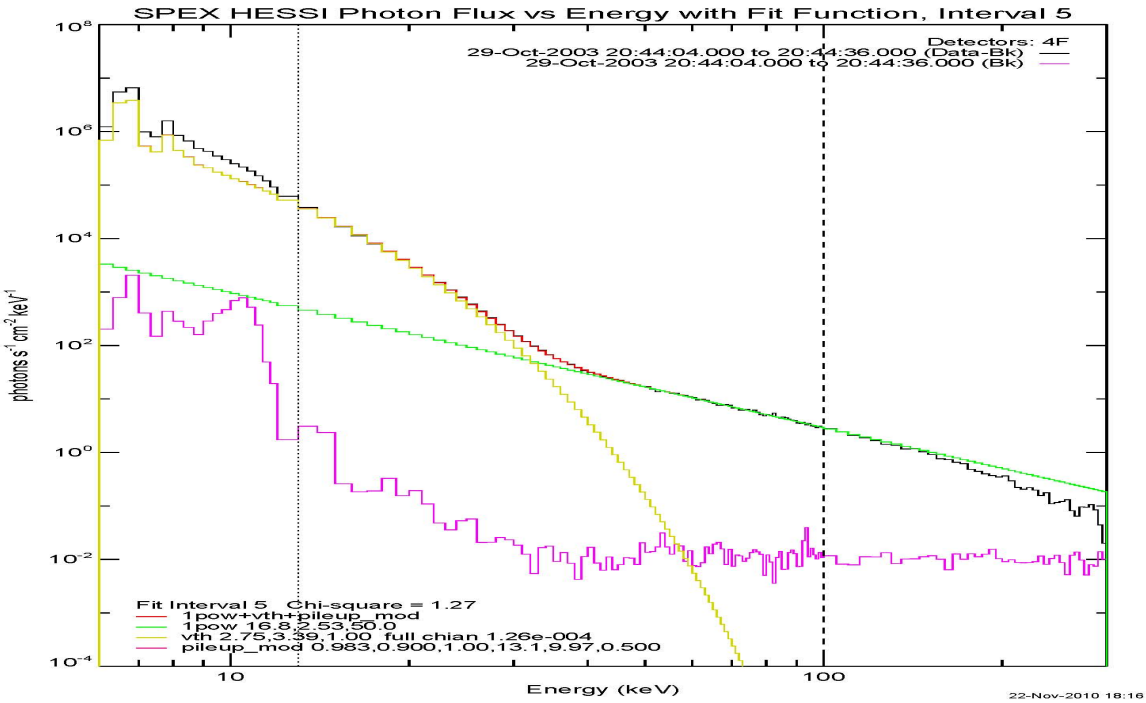
SPEX HESSI Photon Flux vs Energy with Fit Function, Interval 5
Detectors: 4F
29-Oct-2003 20:44:04.000 to 20:44:36.000 (Data-Bk)
29-Oct-2003 20:44:04.000 to 20:44:36.000 (Bk)
photons s-1 cm-2 keV-1
Energy (keV)
Fit Interval 5 Chi-square = 1.27
1pow+vth+pileup_mod
1pow 16.8,2.53,50.0
vth 2.75,3.39,1.00 full chian 1.26e-004
pileup_mod 0.983,0.900,1.00,13.1,9.97,0.500
22-Nov-2010 18:16

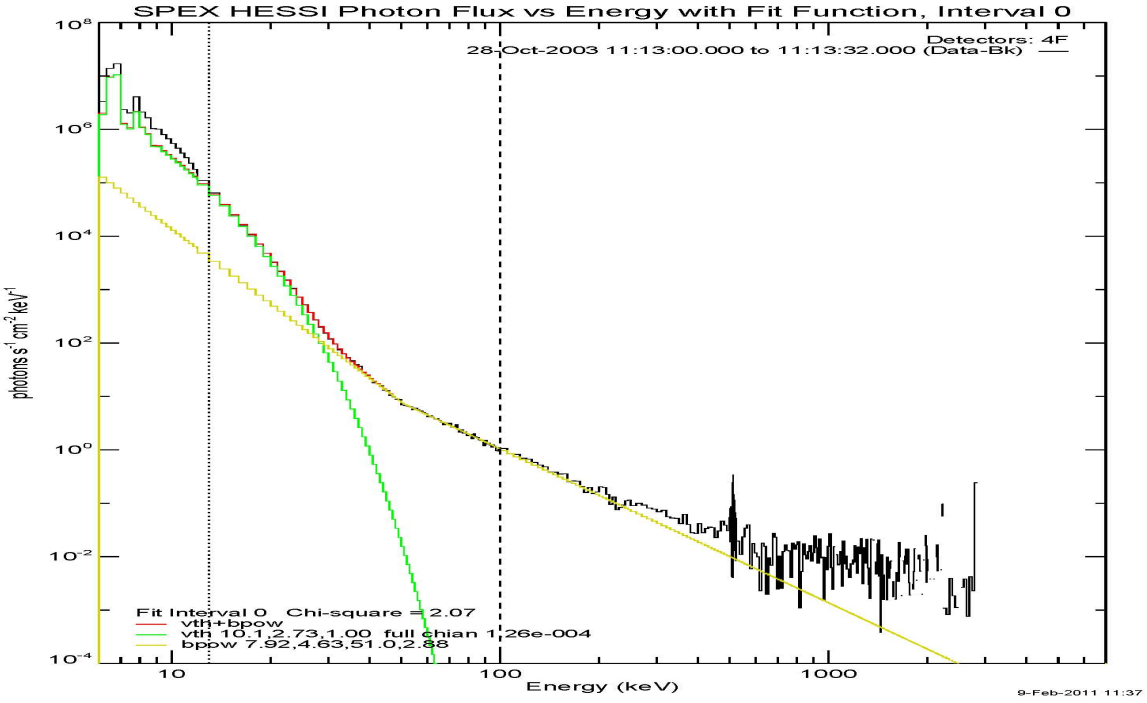
SPEX HESSI Photon Flux vs Energy with Fit Function, Interval 0
Detectors: 4F
28-Oct-2003 11:13:00.000 to 11:13:32.000 (Data-Bk)
photons s-1 cm-2 keV-1
Energy (keV)
Fit Interval 0 Chi-square = 2.07
vth+bpow
vth 10.1,2.73,1.00 full chian 1.26e-004
bpow 7.92,4.63,51.0,2.88
9-Feb-2011 11:37

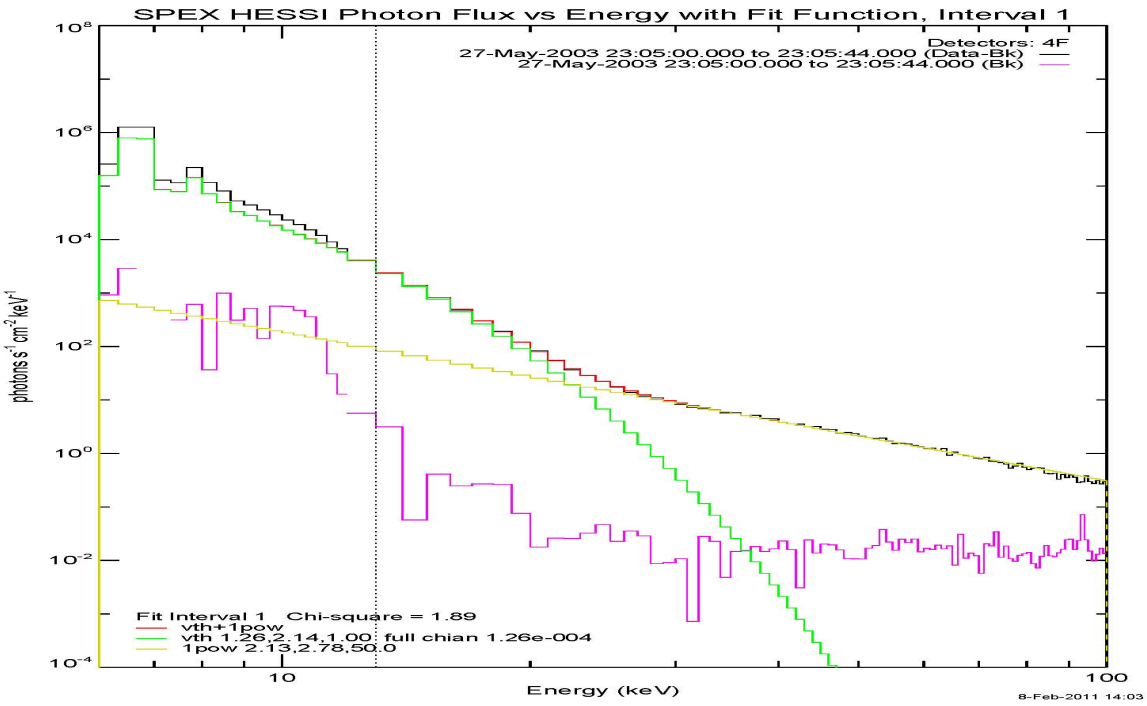
SPEX HESSI Photon Flux vs Energy with Fit Function, Interval 1
Detectors: 4F
27-May-2003 23:05:00.000 to 23:05:44.000 (Data-Bk)
27-May-2003 23:05:00.000 to 23:05:44.000 (Bk)
Fit Interval 1 Chi-square = 1.89
vth+1pow
vth 1.26,2.14,1.00 full chian 1.26e-004
1pow 2.13,2.78,50.0
photons s-1 cm-2 keV-1
Energy (keV)
8-Feb-2011 14:03

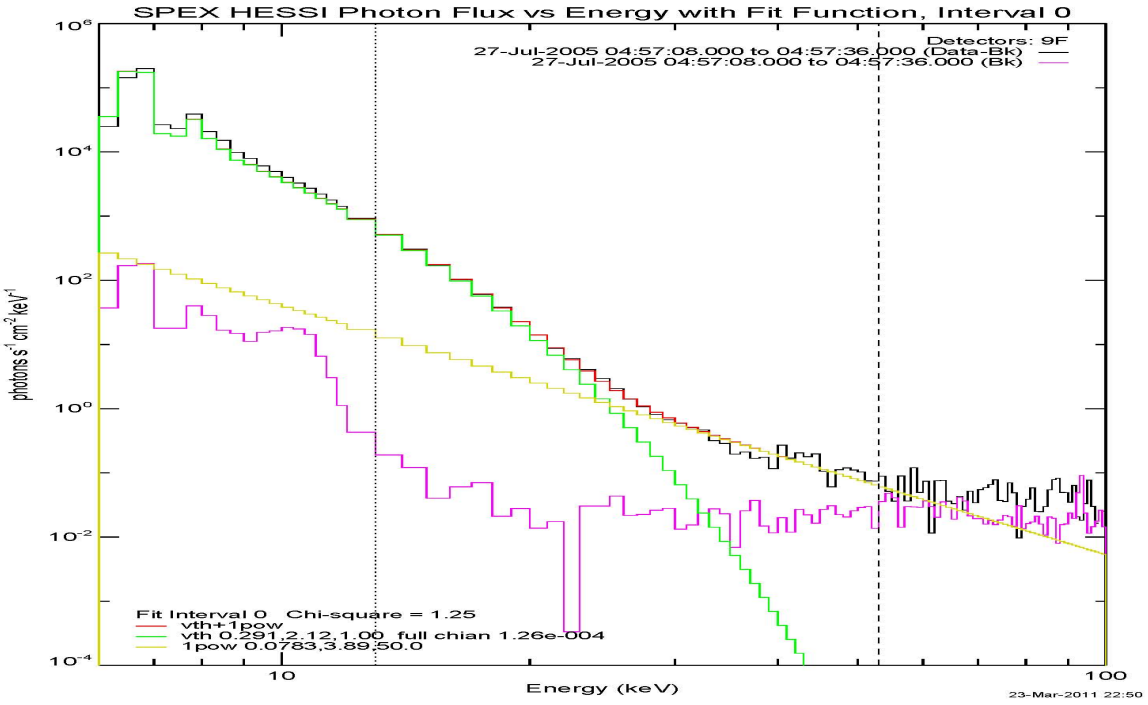
SPEX HESSI Photon Flux vs Energy with Fit Function, Interval 0
Detectors: 9F
27-Jul-2005 04:57:08.000 to 04:57:36.000 (Data-Bk)
27-Jul-2005 04:57:08.000 to 04:57:36.000 (Bk)
Fit Interval 0 Chi-square = 1.25
vth+1pow
vth 0.291,2.12,1.00 full chian 1.26e-004
1pow 0.0783,3.89,50.0
photons s-1 cm-2 keV-1
Energy (keV)
23-Mar-2011 22:50

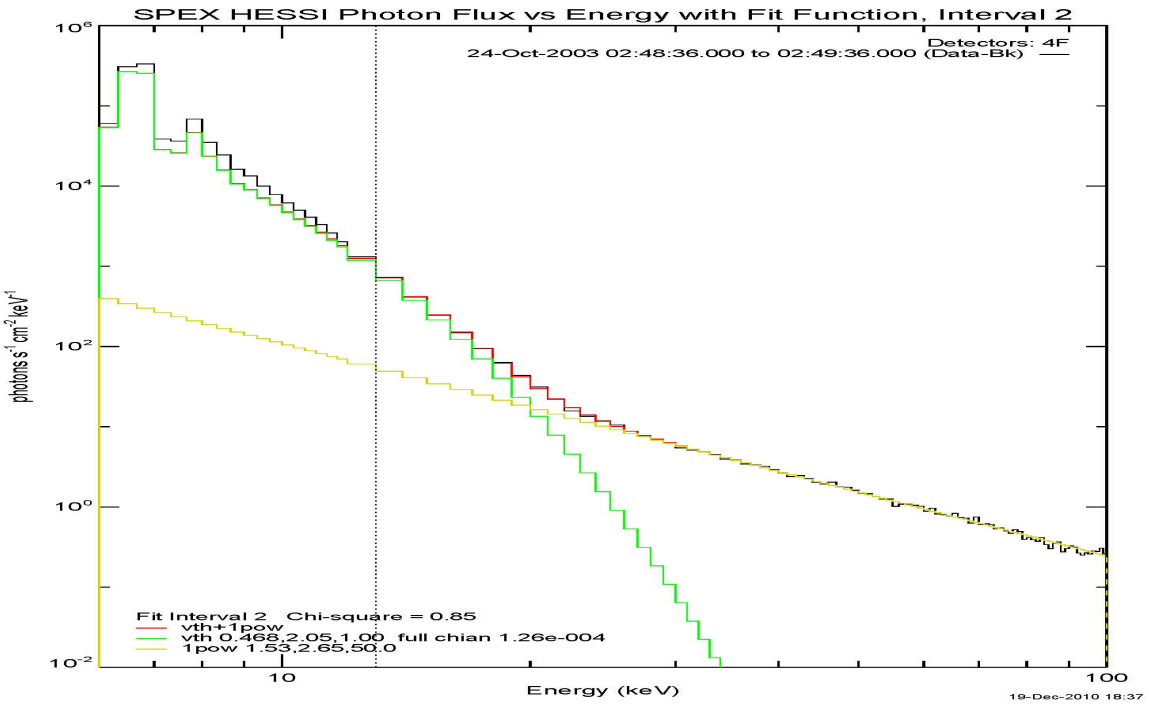
SPEX HESSI Photon Flux vs Energy with Fit Function, Interval 2
Detectors: 4F
24-Oct-2003 02:48:36.000 to 02:49:36.000 (Data-Bk)
Fit Interval 2 Chi-square = 0.85
vth+1pow
vth 0.468,2.05,1.00 full chian 1.26e-004
1pow 1.53,2.65,50.0
photons s-1 cm-2 keV-1
Energy (keV)
19-Dec-2010 18:37

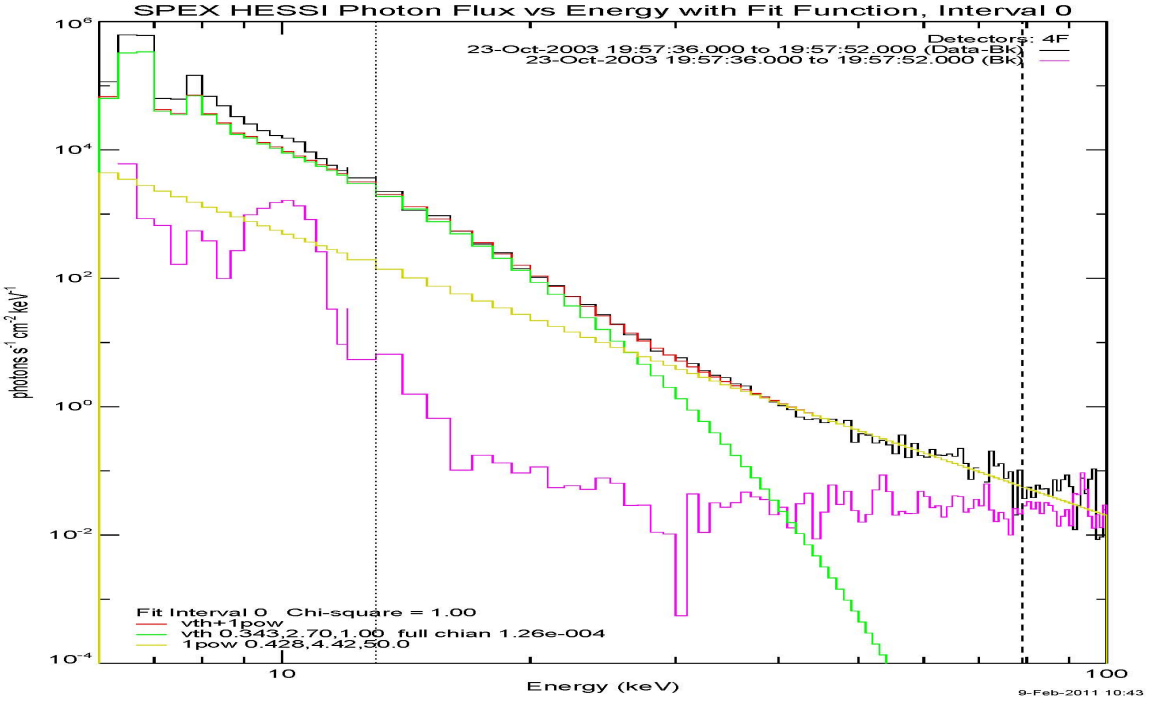
SPEX HESSI Photon Flux vs Energy with Fit Function, Interval 0
Detectors: 4F
23-Oct-2003 19:57:36.000 to 19:57:52.000 (Data-Bk)
23-Oct-2003 19:57:36.000 to 19:57:52.000 (Bk)
Fit Interval 0 Chi-square = 1.00
vth+1pow
vth 0.343,2.70,1.00 full chian 1.26e-004
1pow 0.428,4.42,50.0
photons s-1 cm-2 keV-1
Energy (keV)
9-Feb-2011 10:43

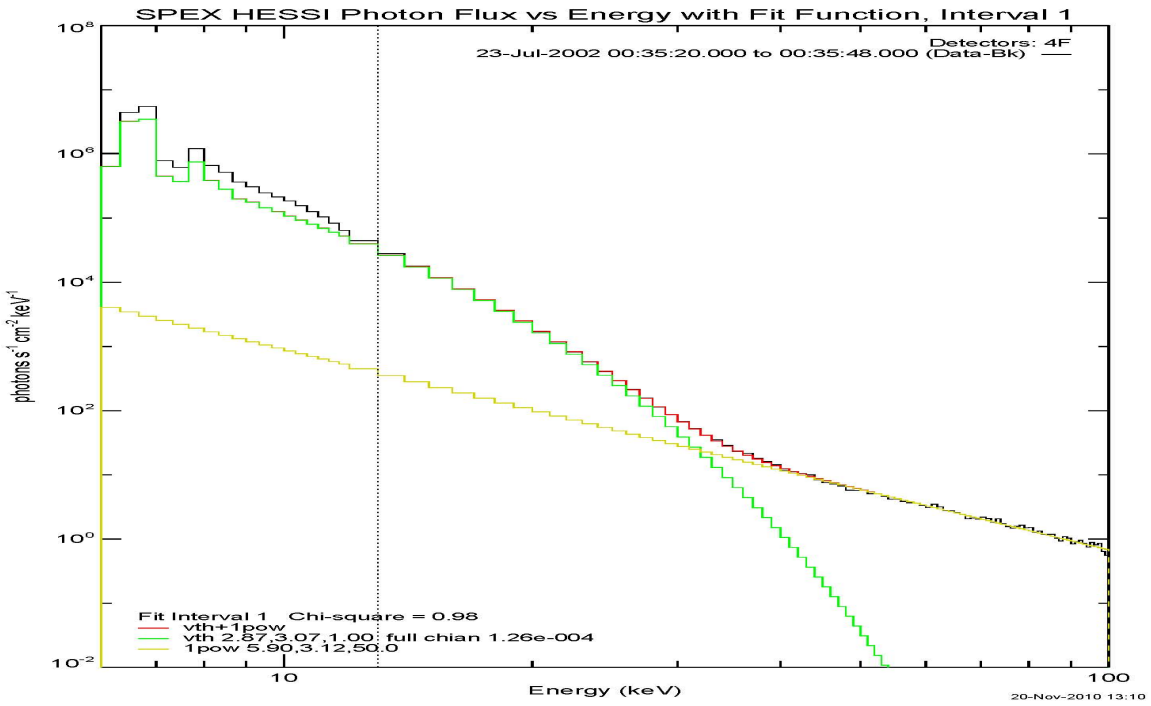
SPEX HESSI Photon Flux vs Energy with Fit Function, Interval 1
Detectors: 4F
23-Jul-2002 00:35:20.000 to 00:35:48.000 (Data-Bk)
photons s-1 cm-2 keV-1
Energy (keV)
Fit Interval 1 Chi-square = 0.98
vth+1pow
vth 2.87,3.07,1.00 full chian 1.26e-004
1pow 5.90,3.12,50.0
20-Nov-2010 13:10

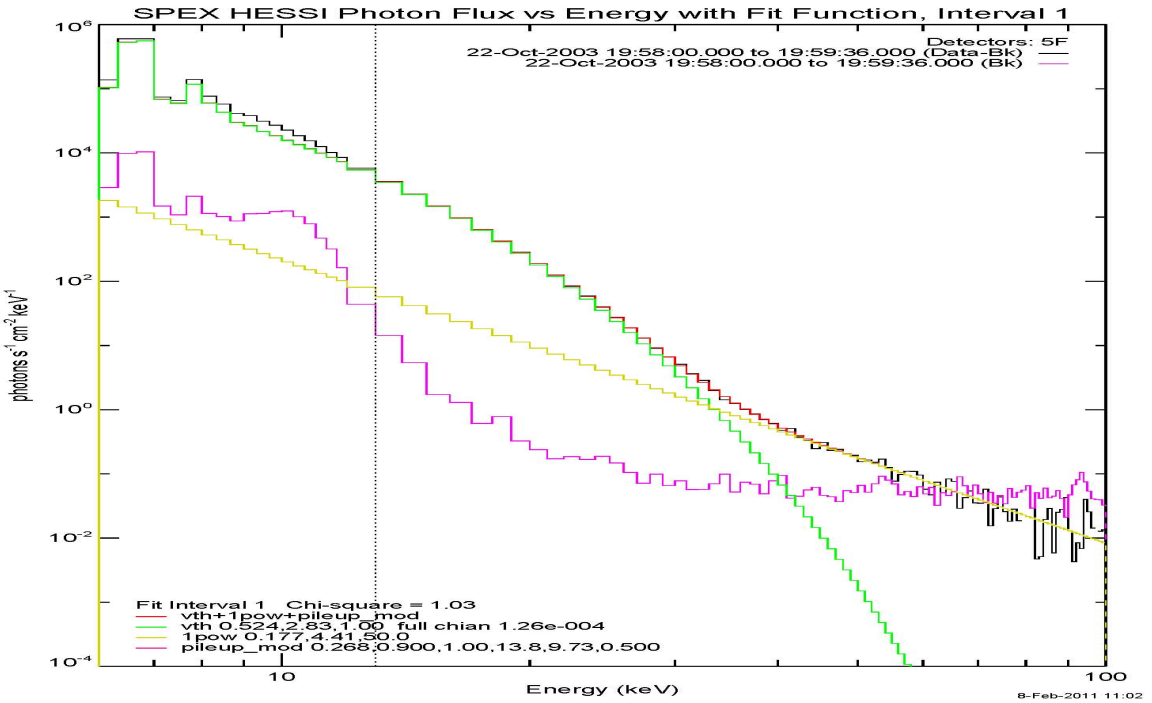
SPEX HESSI Photon Flux vs Energy with Fit Function, Interval 1
Detectors: 5F
22-Oct-2003 19:58:00.000 to 19:59:36.000 (Data-Bk)
22-Oct-2003 19:58:00.000 to 19:59:36.000 (Bk)
photons s-1 cm-2 keV-1
Energy (keV)
Fit Interval 1 Chi-square = 1.03
vth+1pow+pileup_mod
vth 0.524,2.83,1.00 full chian 1.26e-004
1pow 0.177,4.41,50.0
pileup_mod 0.268,0.900,1.00,13.8,9.73,0.500
8-Feb-2011 11:02

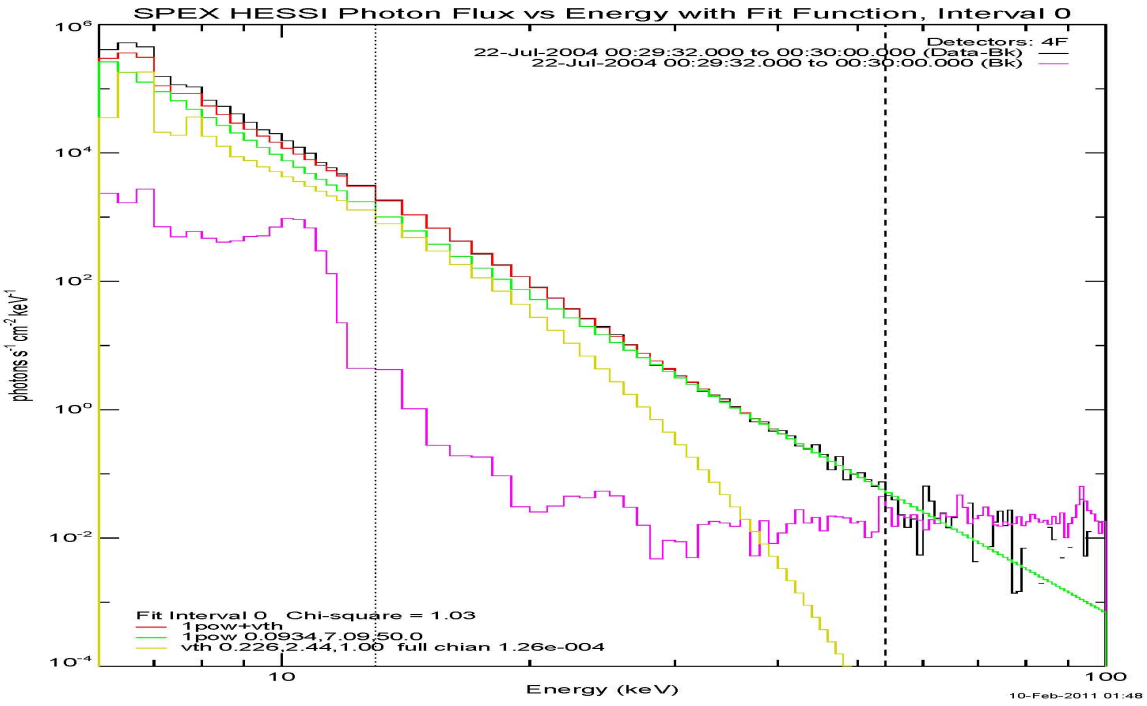
SPEX HESSI Photon Flux vs Energy with Fit Function, Interval 0
Detectors: 4F
22-Jul-2004 00:29:32.000 to 00:30:00.000 (Data-Bk)
22-Jul-2004 00:29:32.000 to 00:30:00.000 (Bk)
Fit Interval 0 Chi-square = 1.03
1pow+vth
1pow 0.0934,7.09,50.0
vth 0.226,2.44,1.00 full chian 1.26e-004
photons s-1 cm-2 keV-1
Energy (keV)
10-Feb-2011 01:48

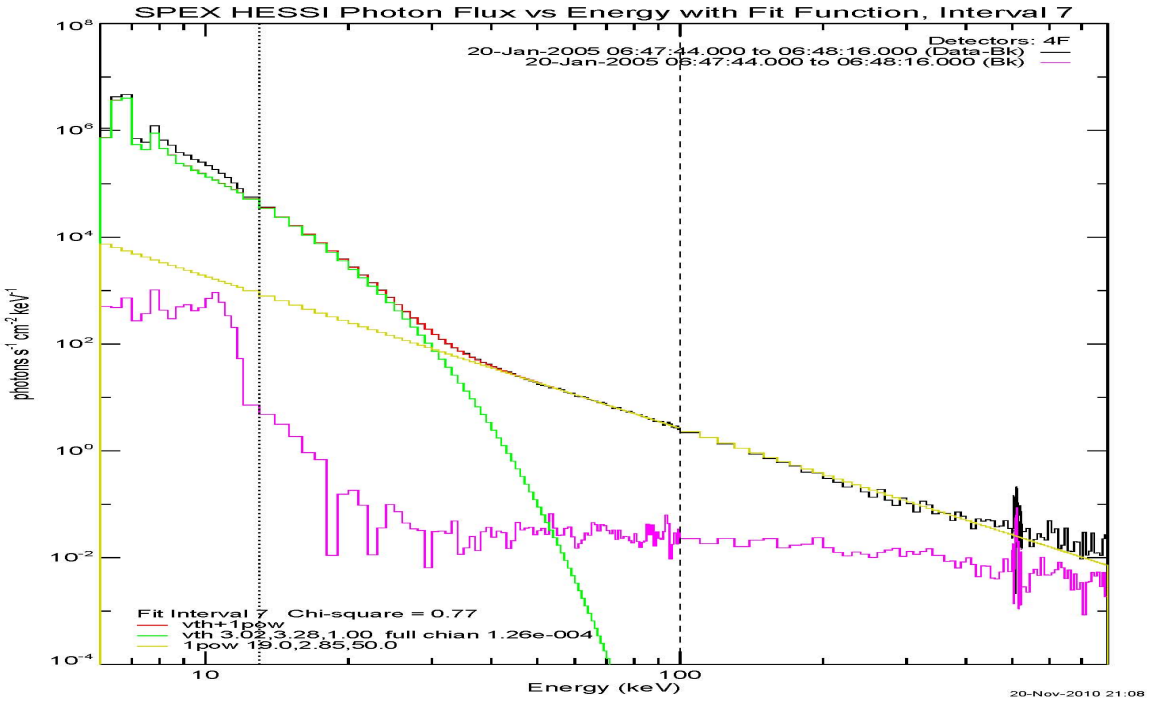
SPEX HESSI Photon Flux vs Energy with Fit Function, Interval 7
Detectors: 4F
20-Jan-2005 06:47:44.000 to 06:48:16.000 (Data-Bk)
20-Jan-2005 06:47:44.000 to 06:48:16.000 (Bk)
Fit Interval 7 Chi-square = 0.77
vth+1pow
vth 3.02,3.28,1.00 full chian 1.26e-004
1pow 19.0,2.85,50.0
photons s-1 cm-2 keV-1
Energy (keV)
20-Nov-2010 21:08

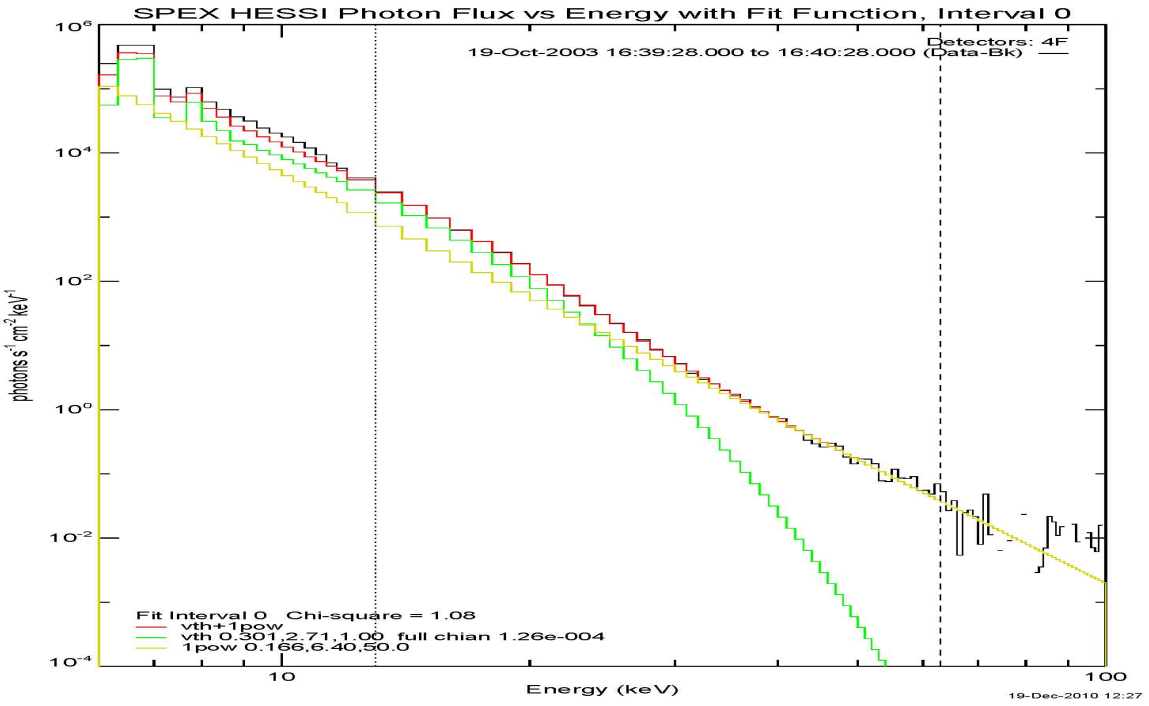
SPEX HESSI Photon Flux vs Energy with Fit Function, Interval 0
Detectors: 4F
19-Oct-2003 16:39:28.000 to 16:40:28.000 (Data-Bk)
photons s-1 cm-2 keV-1
Energy (keV)
Fit Interval 0 Chi-square = 1.08
vth+1pow
vth 0.301,2.71,1.00 full chian 1.26e-004
1pow 0.166,6.40,50.0
19-Dec-2010 12:27

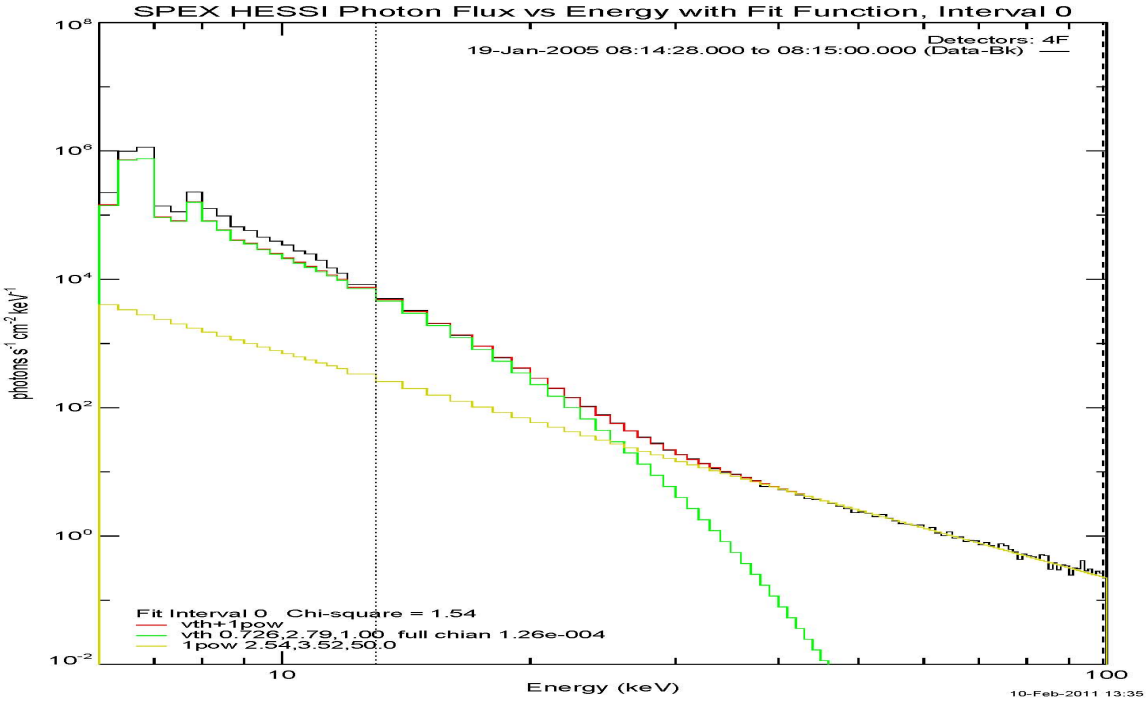
SPEX HESSI Photon Flux vs Energy with Fit Function, Interval 0
Detectors: 4F
19-Jan-2005 08:14:28.000 to 08:15:00.000 (Data-Bk)
photons s-1 cm-2 keV-1
Energy (keV)
Fit Interval 0 Chi-square = 1.54
vth+1pow
vth 0.726,2.79,1.00 full chian 1.26e-004
1pow 2.54,3.52,50.0
10-Feb-2011 13:35

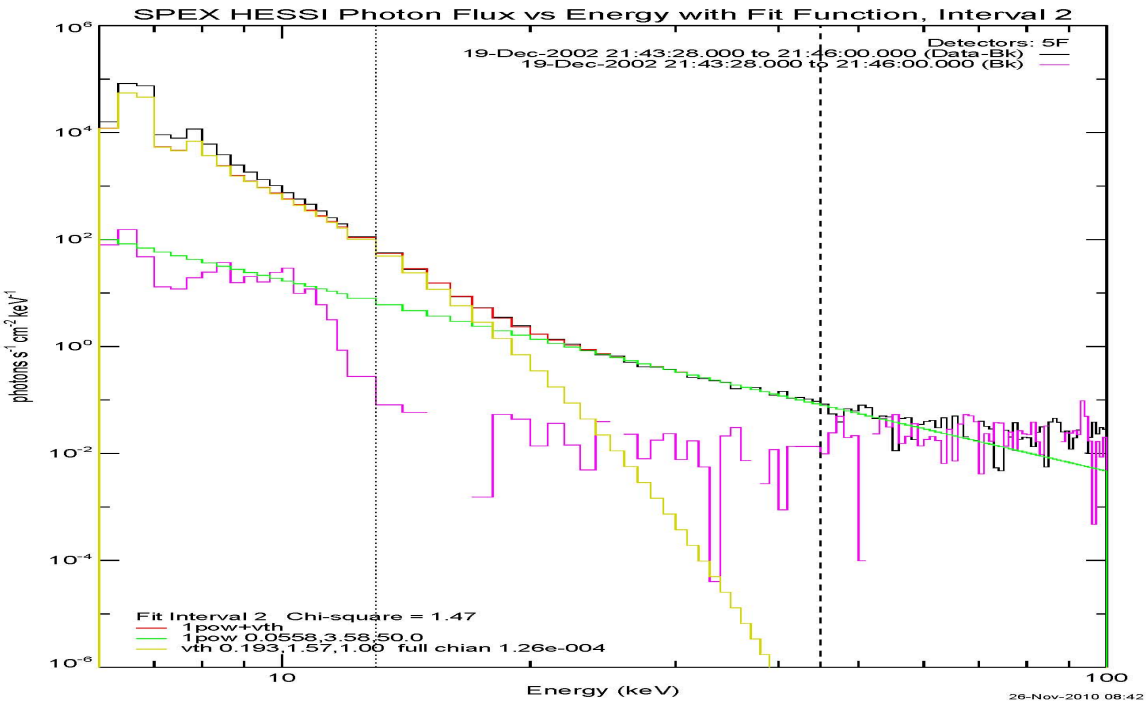
SPEX HESSI Photon Flux vs Energy with Fit Function, Interval 2
Detectors: 5F
19-Dec-2002 21:43:28.000 to 21:46:00.000 (Data-Bk)
19-Dec-2002 21:43:28.000 to 21:46:00.000 (Bk)
photons s-1 cm-2 keV-1
Energy (keV)
Fit Interval 2 Chi-square = 1.47
1pow+vth
1pow 0.0558,3.58,50.0
vth 0.193,1.57,1.00 full chian 1.26e-004
26-Nov-2010 08:42

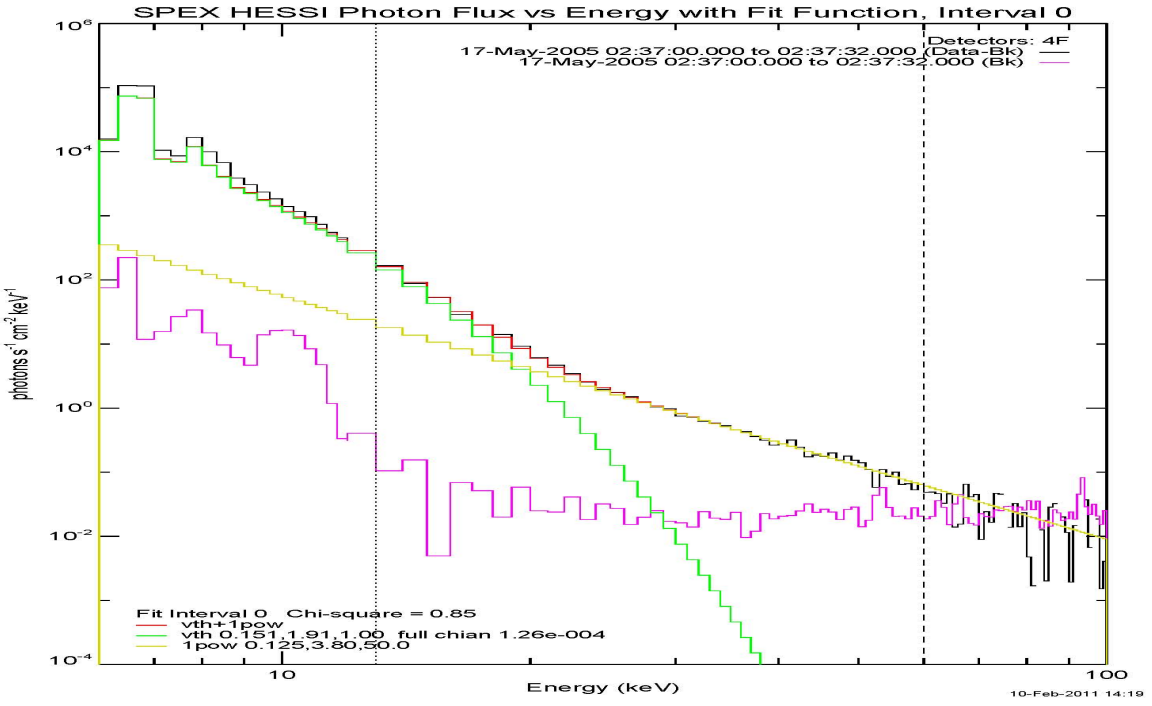
SPEX HESSI Photon Flux vs Energy with Fit Function, Interval 0
Detectors: 4F
17-May-2005 02:37:00.000 to 02:37:32.000 (Data-Bk)
17-May-2005 02:37:00.000 to 02:37:32.000 (Bk)
photons s-1 cm-2 keV-1
Energy (keV)
Fit Interval 0 Chi-square = 0.85
vth+1pow
vth 0.151,1.91,1.00 full chian 1.26e-004
1pow 0.125,3.80,50.0
10-Feb-2011 14:19

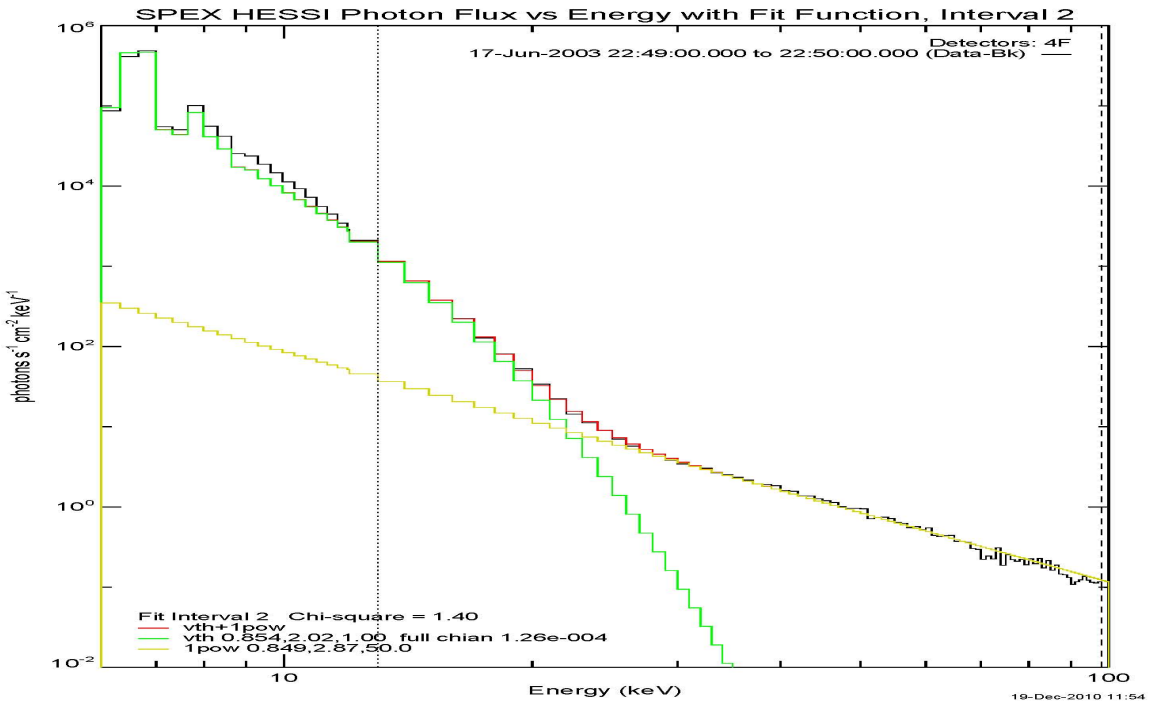
SPEX HESSI Photon Flux vs Energy with Fit Function, Interval 2
Detectors: 4F
17-Jun-2003 22:49:00.000 to 22:50:00.000 (Data-Bk)
Fit Interval 2 Chi-square = 1.40
vth+1pow
vth 0.854,2.02,1.00 full chian 1.26e-004
1pow 0.849,2.87,50.0
photons s-1 cm-2 keV-1
Energy (keV)
19-Dec-2010 11:54

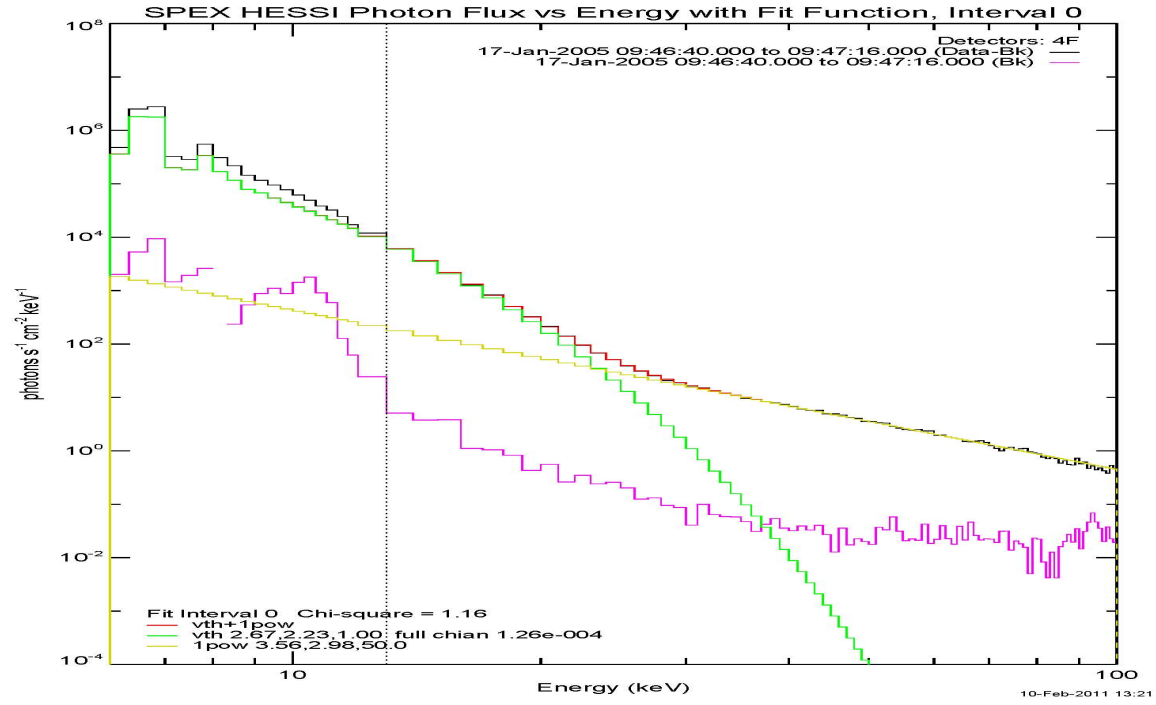
SPEX HESSI Photon Flux vs Energy with Fit Function, Interval 0
Detectors: 4F
17-Jan-2005 09:46:40.000 to 09:47:16.000 (Data-Bk)
17-Jan-2005 09:46:40.000 to 09:47:16.000 (Bk)
Fit Interval 0 Chi-square = 1.16
vth+1pow
vth 2.67,2.23,1.00 full chian 1.26e-004
1pow 3.56,2.98,50.0
photons s-1 cm-2 keV-1
Energy (keV)
10-Feb-2011 13:21

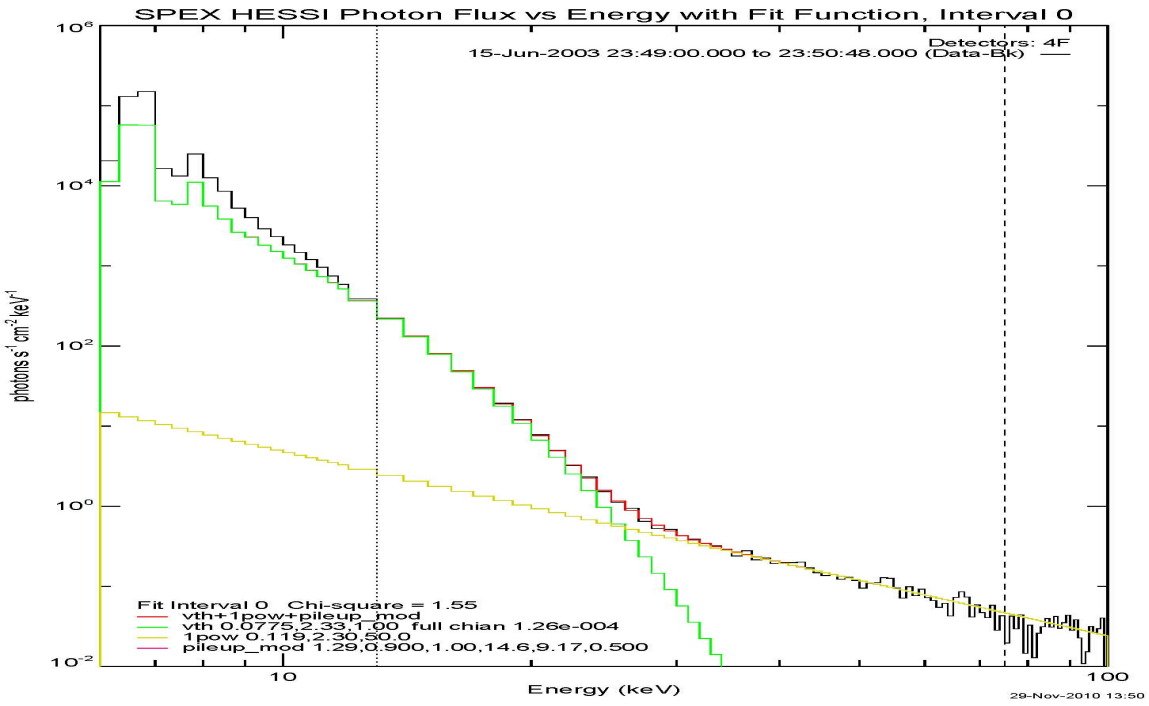
SPEX HESSI Photon Flux vs Energy with Fit Function, Interval 0
Detectors: 4F
15-Jun-2003 23:49:00.000 to 23:50:48.000 (Data-Bk)
photons s-1 cm-2 keV-1
Energy (keV)
Fit Interval 0 Chi-square = 1.55
vth+1pow+pileup_mod
vth 0.0775,2.33,1.00 full chian 1.26e-004
1pow 0.119,2.30,50.0
pileup_mod 1.29,0.900,1.00,14.6,9.17,0.500
29-Nov-2010 13:50

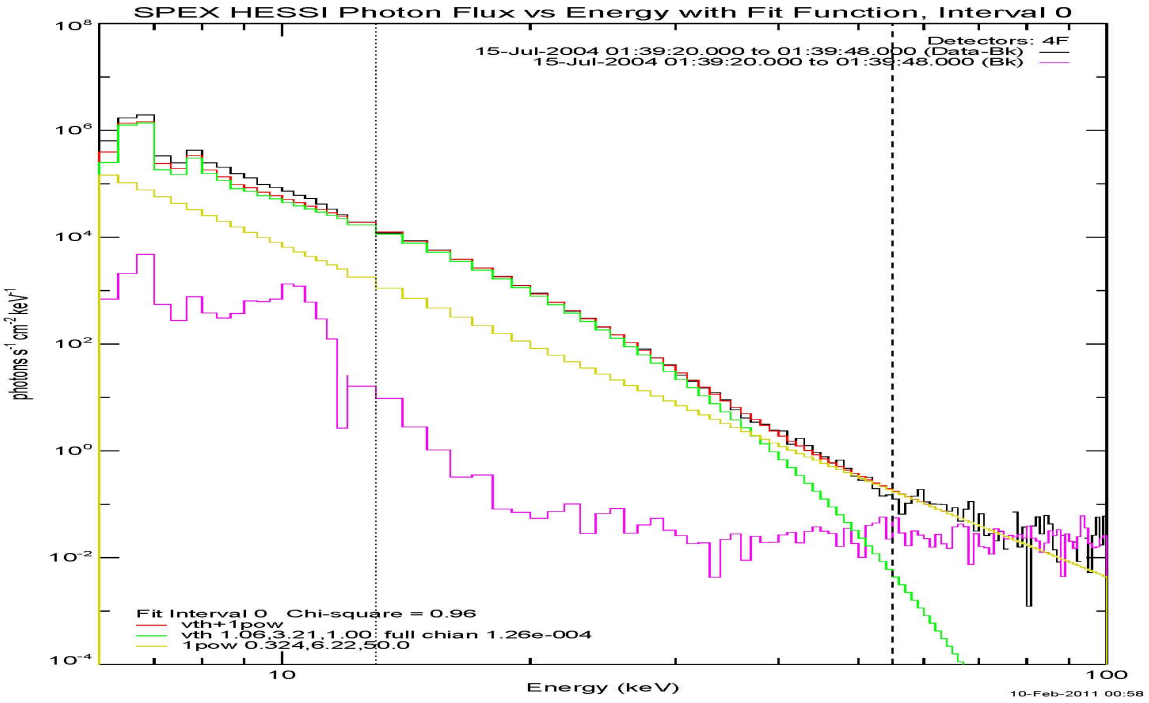
SPEX HESSI Photon Flux vs Energy with Fit Function, Interval 0
Detectors: 4F
15-Jul-2004 01:39:20.000 to 01:39:48.000 (Data-Bk)
15-Jul-2004 01:39:20.000 to 01:39:48.000 (Bk)
photons s-1 cm-2 keV-1
Energy (keV)
Fit Interval 0 Chi-square = 0.96
vth+1pow
vth 1.06,3.21,1.00 full chian 1.26e-004
1pow 0.324,6.22,50.0
10-Feb-2011 00:58

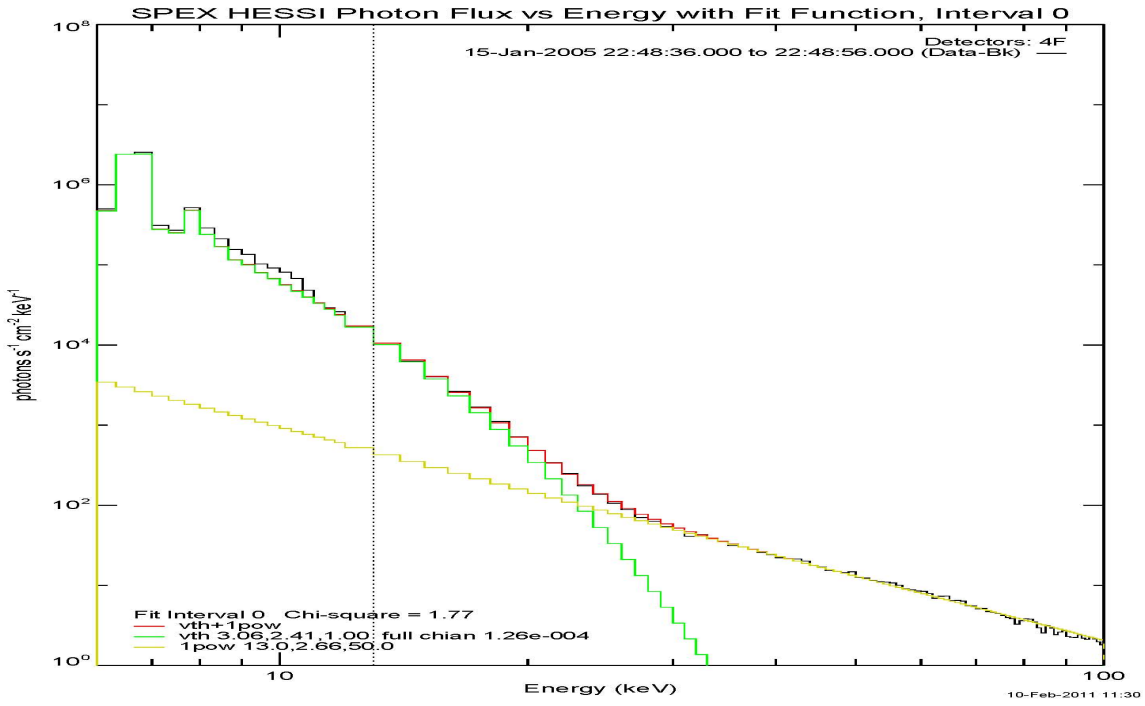
SPEX HESSI Photon Flux vs Energy with Fit Function, Interval 0
Detectors: 4F
15-Jan-2005 22:48:36.000 to 22:48:56.000 (Data-Bk)
photons s-1 cm-2 keV-1
Energy (keV)
Fit Interval 0 Chi-square = 1.77
vth+1pow
vth 3.06,2.41,1.00 full chian 1.26e-004
1pow 13.0,2.66,50.0
10-Feb-2011 11:30

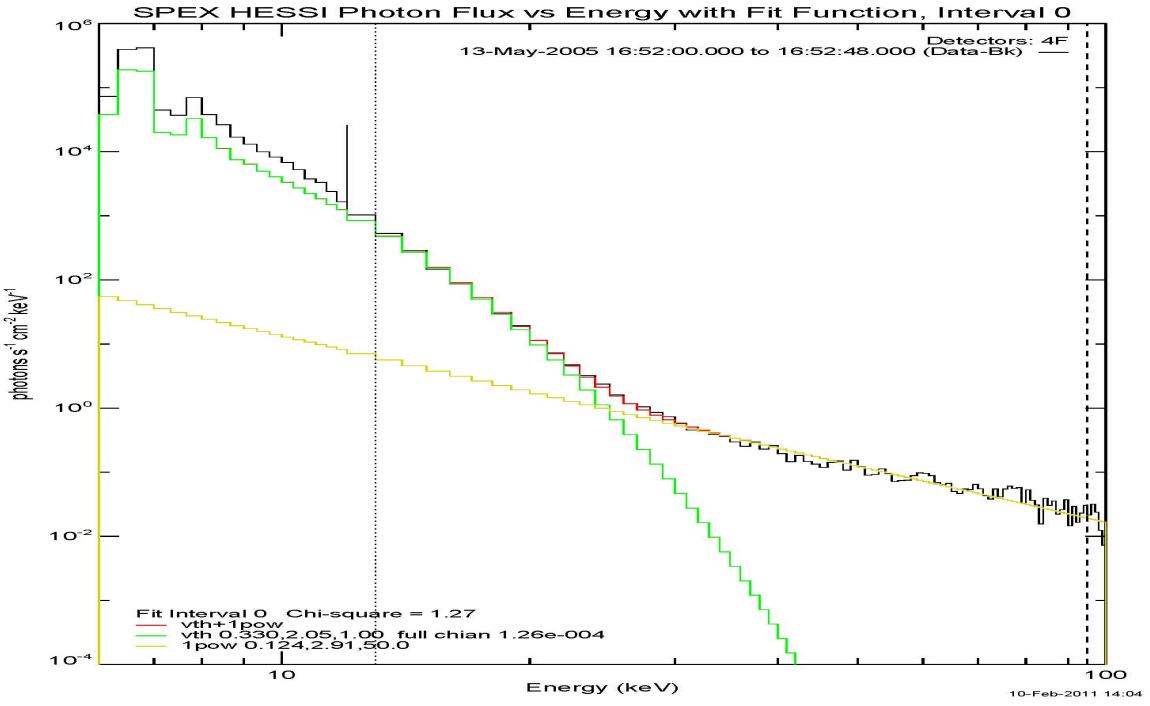
SPEX HESSI Photon Flux vs Energy with Fit Function, Interval 0
Detectors: 4F
13-May-2005 16:52:00.000 to 16:52:48.000 (Data-Bk)
photons s-1 cm-2 keV-1
Energy (keV)
Fit Interval 0 Chi-square = 1.27
vth+1pow
vth 0.330,2.05,1.00 full chian 1.26e-004
1pow 0.124,2.91,50.0
10-Feb-2011 14:04

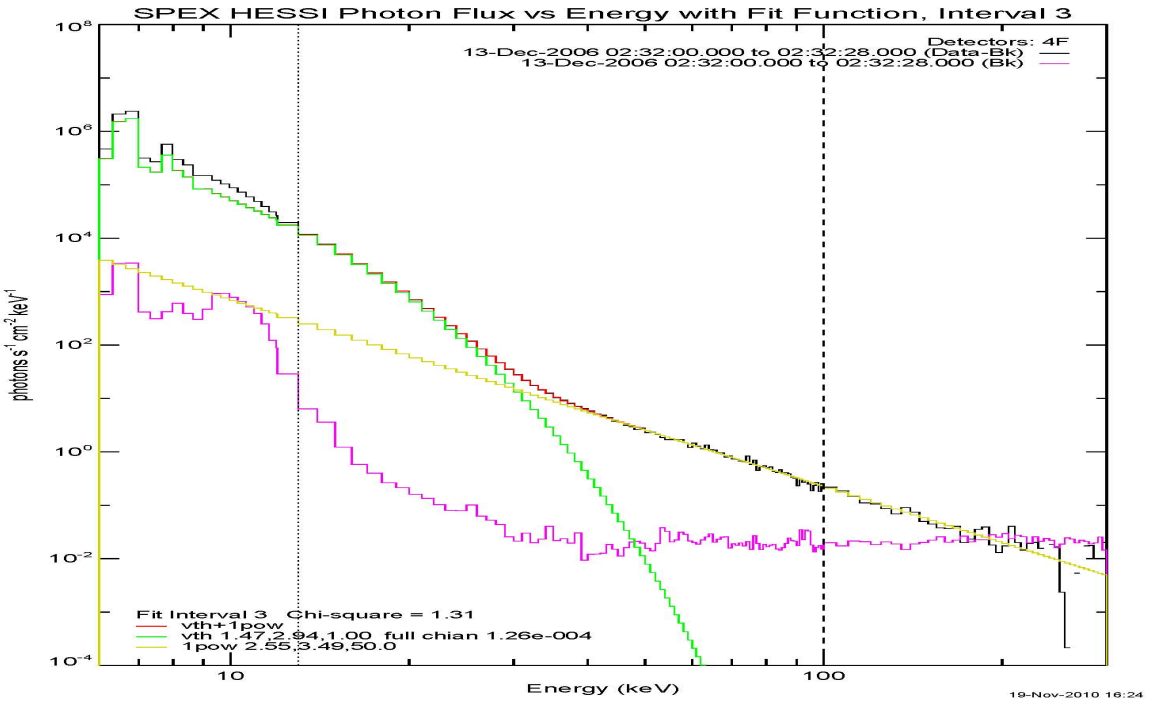
SPEX HESSI Photon Flux vs Energy with Fit Function, Interval 3
Detectors: 4F
13-Dec-2006 02:32:00.000 to 02:32:28.000 (Data-Bk)
13-Dec-2006 02:32:00.000 to 02:32:28.000 (Bk)
Fit Interval 3 Chi-square = 1.31
vth+1pow
vth 1.47,2.94,1.00 full chian 1.26e-004
1pow 2.55,3.49,50.0
photons s-1 cm-2 keV-1
Energy (keV)
19-Nov-2010 16:24

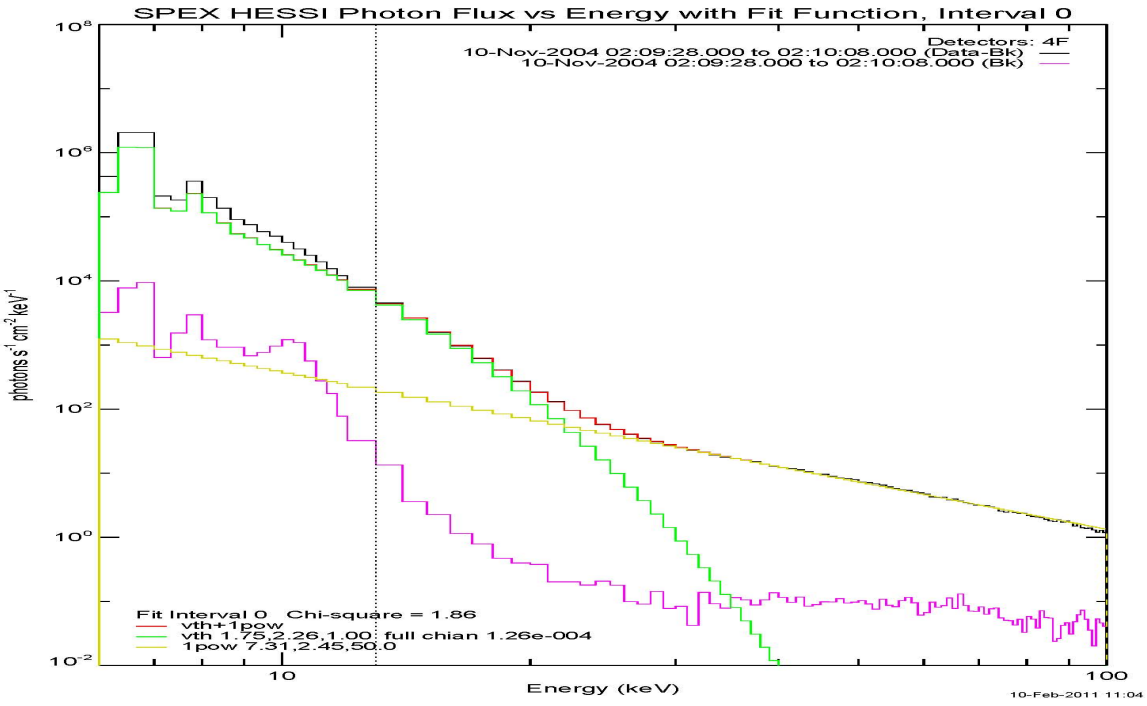
SPEX HESSI Photon Flux vs Energy with Fit Function, Interval 0
Detectors: 4F
10-Nov-2004 02:09:28.000 to 02:10:08.000 (Data-Bk)
10-Nov-2004 02:09:28.000 to 02:10:08.000 (Bk)
Fit Interval 0 Chi-square = 1.86
vth+1pow
vth 1.75,2.26,1.00 full chian 1.26e-004
1pow 7.31,2.45,50.0
photons s-1 cm-2 keV-1
Energy (keV)
10-Feb-2011 11:04

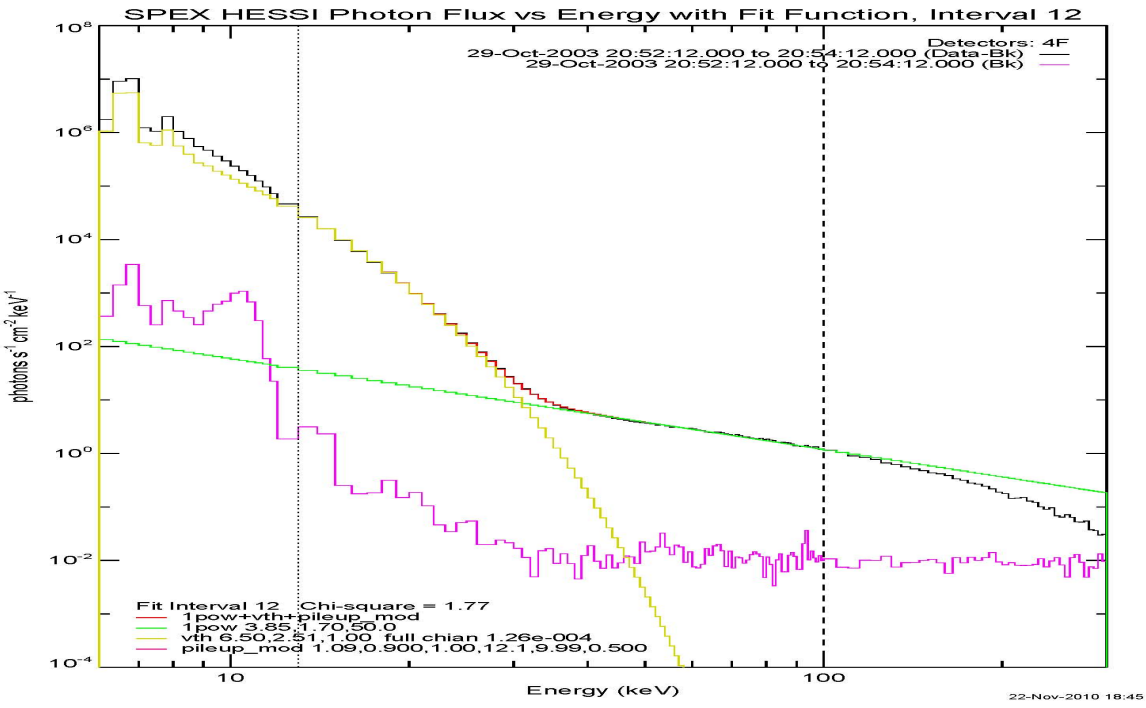
SPEX HESSI Photon Flux vs Energy with Fit Function, Interval 12
Detectors: 4F
29-Oct-2003 20:52:12.000 to 20:54:12.000 (Data-Bk)
29-Oct-2003 20:52:12.000 to 20:54:12.000 (Bk)
photons s-1 cm-2 keV-1
Energy (keV)
Fit Interval 12 Chi-square = 1.77
1pow+vth+pileup_mod
1pow 3.85,1.70,50.0
vth 6.50,2.51,1.00 full chian 1.26e-004
pileup_mod 1.09,0.900,1.00,12.1,9.99,0.500
22-Nov-2010 18:45

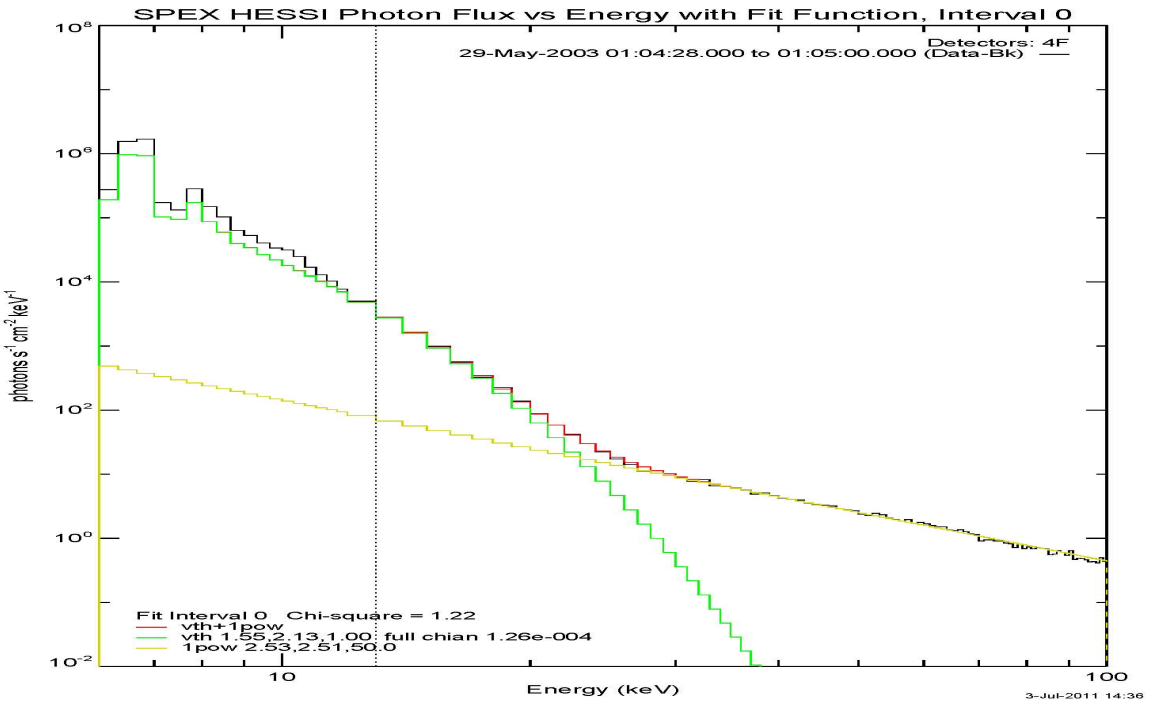
SPEX HESSI Photon Flux vs Energy with Fit Function, Interval 0
Detectors: 4F
29-May-2003 01:04:28.000 to 01:05:00.000 (Data-Bk)
photons s-1 cm-2 keV-1
Energy (keV)
Fit Interval 0 Chi-square = 1.22
vth+1pow
vth 1.55,2.13,1.00 full chian 1.26e-004
1pow 2.53,2.51,50.0
3-Jul-2011 14:36

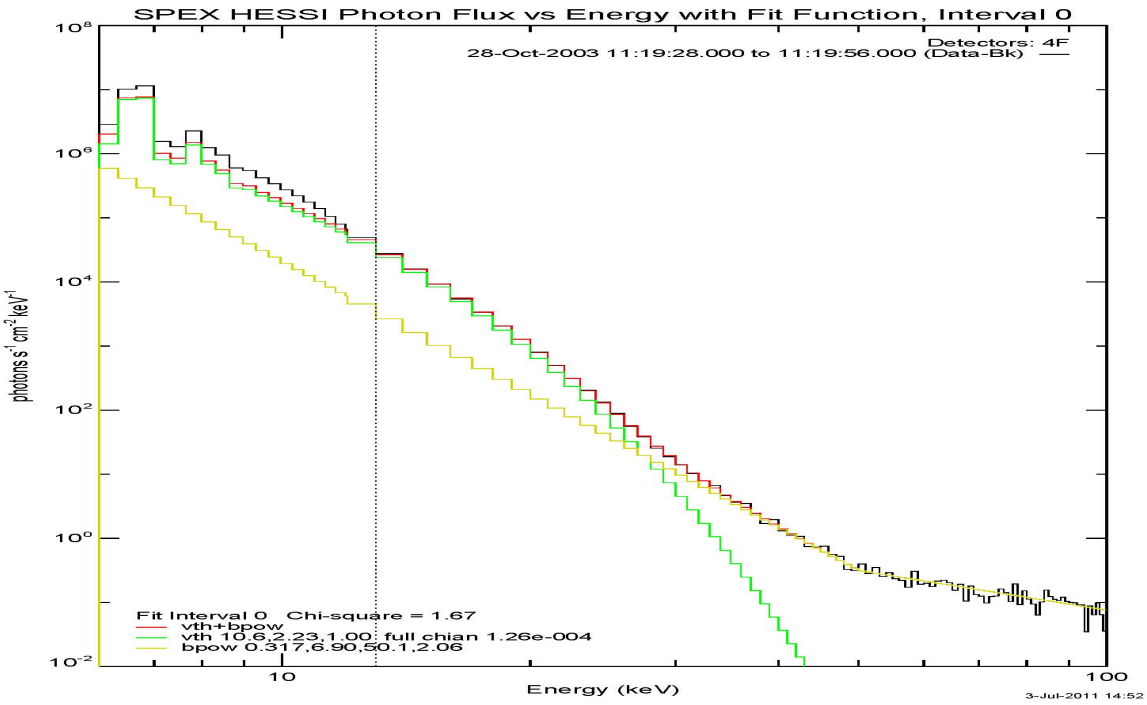
SPEX HESSI Photon Flux vs Energy with Fit Function, Interval 0
Detectors: 4F
28-Oct-2003 11:19:28.000 to 11:19:56.000 (Data-Bk)
photons s-1 cm-2 keV-1
Fit Interval 0 Chi-square = 1.67
vth+bpow
vth 10.6,2.23,1.00 full chian 1.26e-004
bpow 0.317,6.90,50.1,2.06
10
100
Energy (keV)
3-Jul-2011 14:52

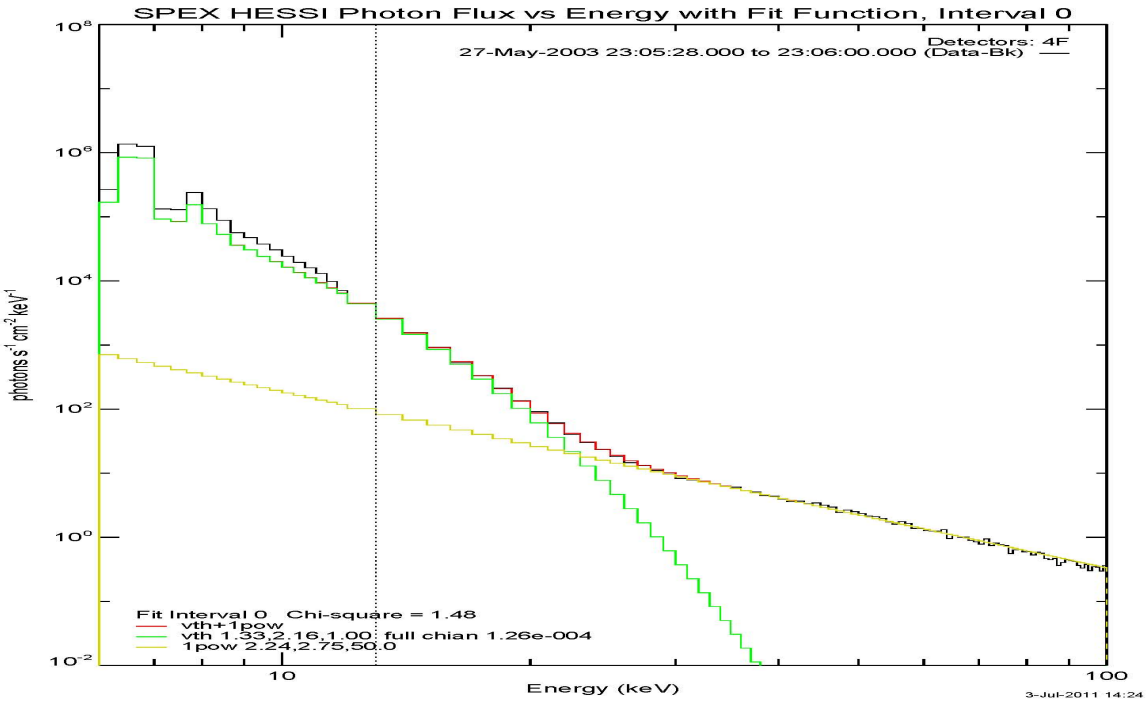
SPEX HESSI Photon Flux vs Energy with Fit Function, Interval 0
Detectors: 4F
27-May-2003 23:05:28.000 to 23:06:00.000 (Data-Bk)
photons s-1 cm-2 keV-1
Fit Interval 0 Chi-square = 1.48
vth+1pow
vth 1.33,2.16,1.00 full chian 1.26e-004
1pow 2.24,2.75,50.0
10
100
Energy (keV)
3-Jul-2011 14:24

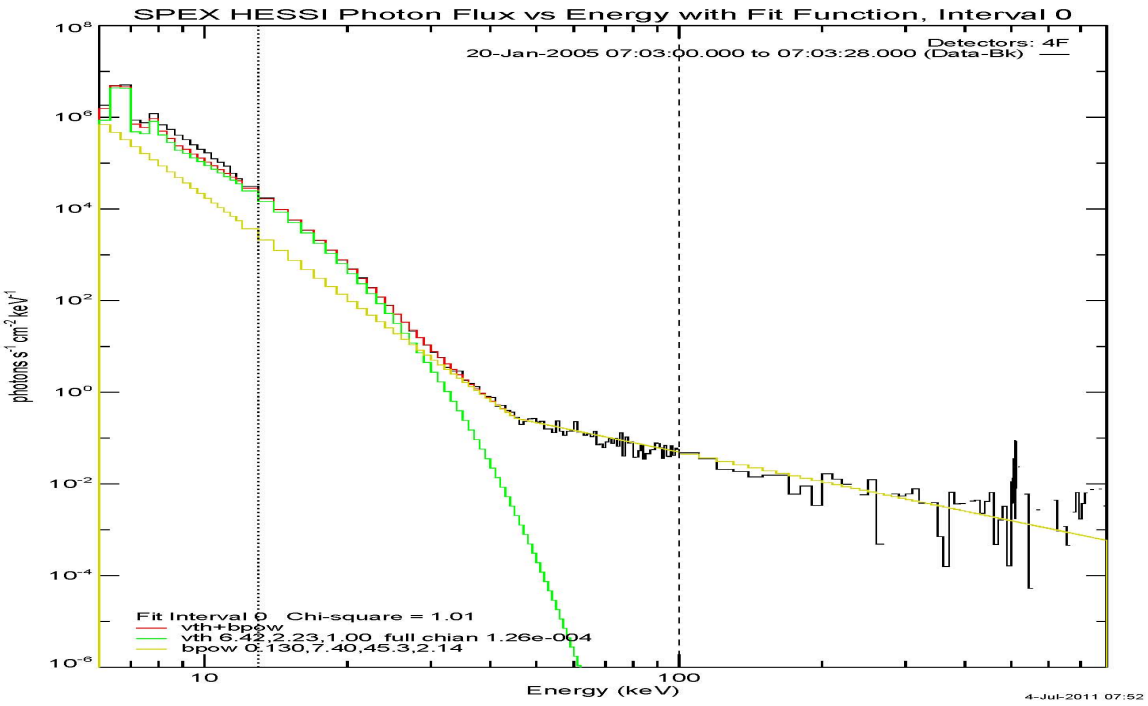
SPEX HESSI Photon Flux vs Energy with Fit Function, Interval 0
Detectors: 4F
20-Jan-2005 07:03:00.000 to 07:03:28.000 (Data-Bk)
photons s-1 cm-2 keV-1
Fit Interval 0 Chi-square = 1.01
vth+bpow
vth 6.42,2.23,1.00 full chian 1.26e-004
bpow 0.130,7.40,45.3,2.14
10
100
Energy (keV)
4-Jul-2011 07:52

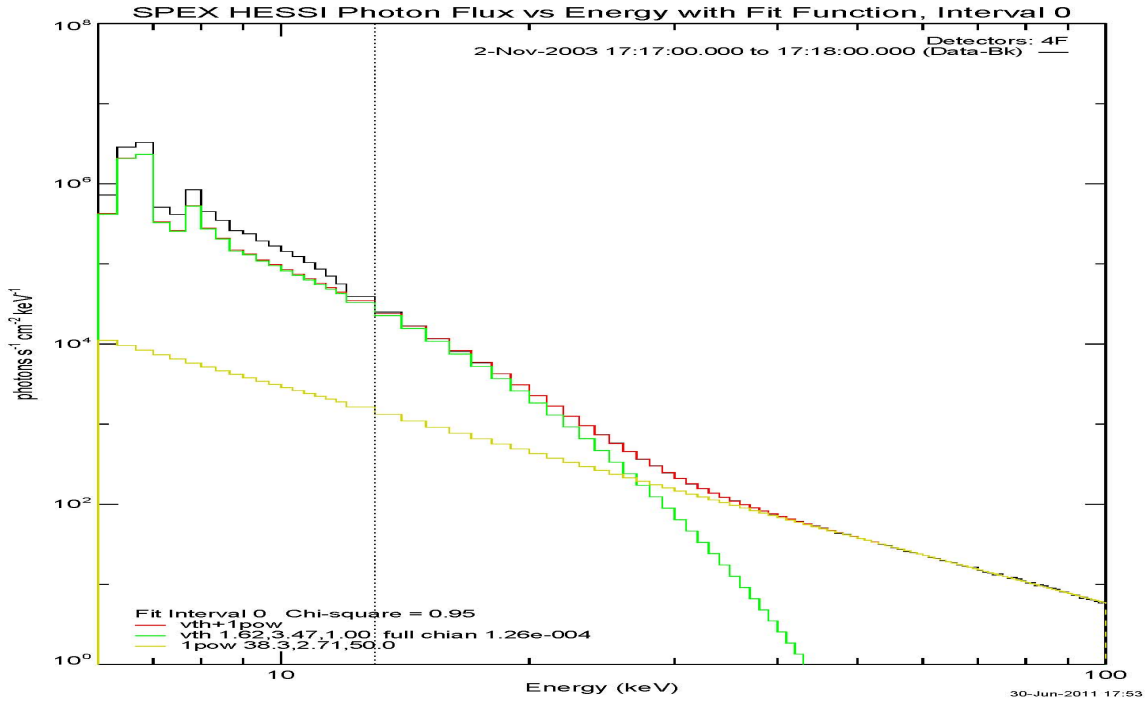
SPEX HESSI Photon Flux vs Energy with Fit Function, Interval 0
Detectors: 4F
2-Nov-2003 17:17:00.000 to 17:18:00.000 (Data-Bk)
photons s-1 cm-2 keV-1
Fit Interval 0 Chi-square = 0.95
vth+1pow
vth 1.62,3.47,1.00 full chian 1.26e-004
1pow 38.3,2.71,50.0
10
100
Energy (keV)
30-Jun-2011 17:53

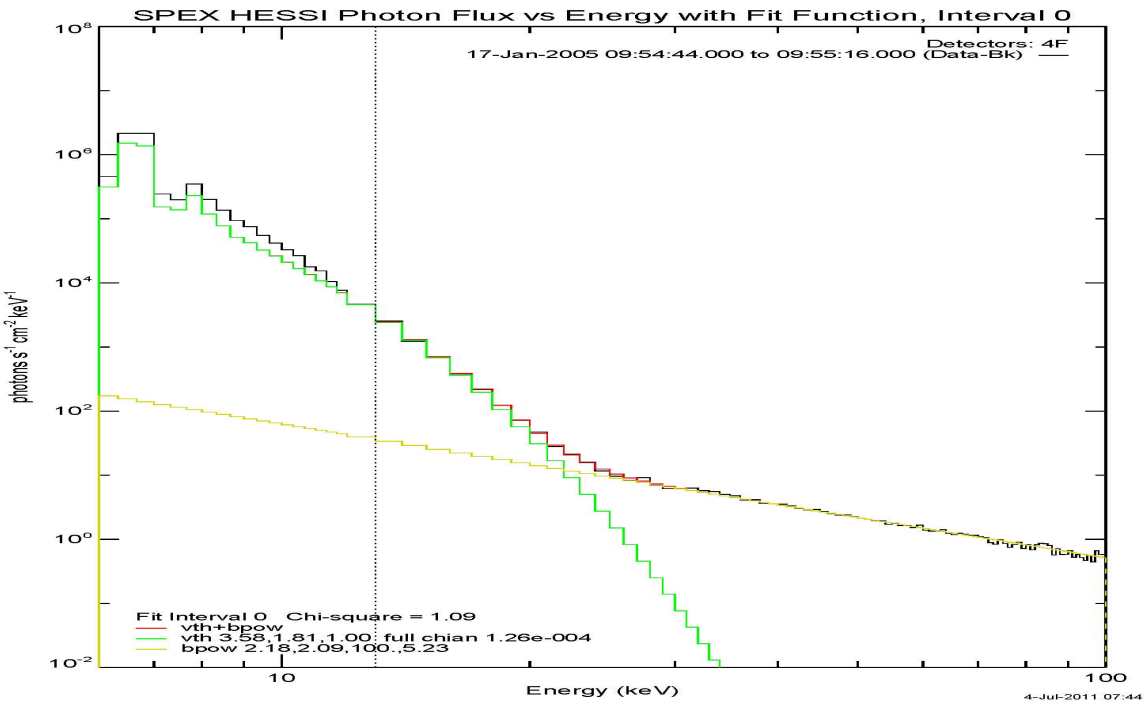
SPEX HESSI Photon Flux vs Energy with Fit Function, Interval 0
Detectors: 4F
17-Jan-2005 09:54:44.000 to 09:55:16.000 (Data-Bk)
photons s-1 cm-2 keV-1
Fit Interval 0 Chi-square = 1.09
vth+bpow
vth 3.58,1.81,1.00 full chian 1.26e-004
bpow 2.18,2.09,100.,5.23
10
100
Energy (keV)
4-Jul-2011 07:44

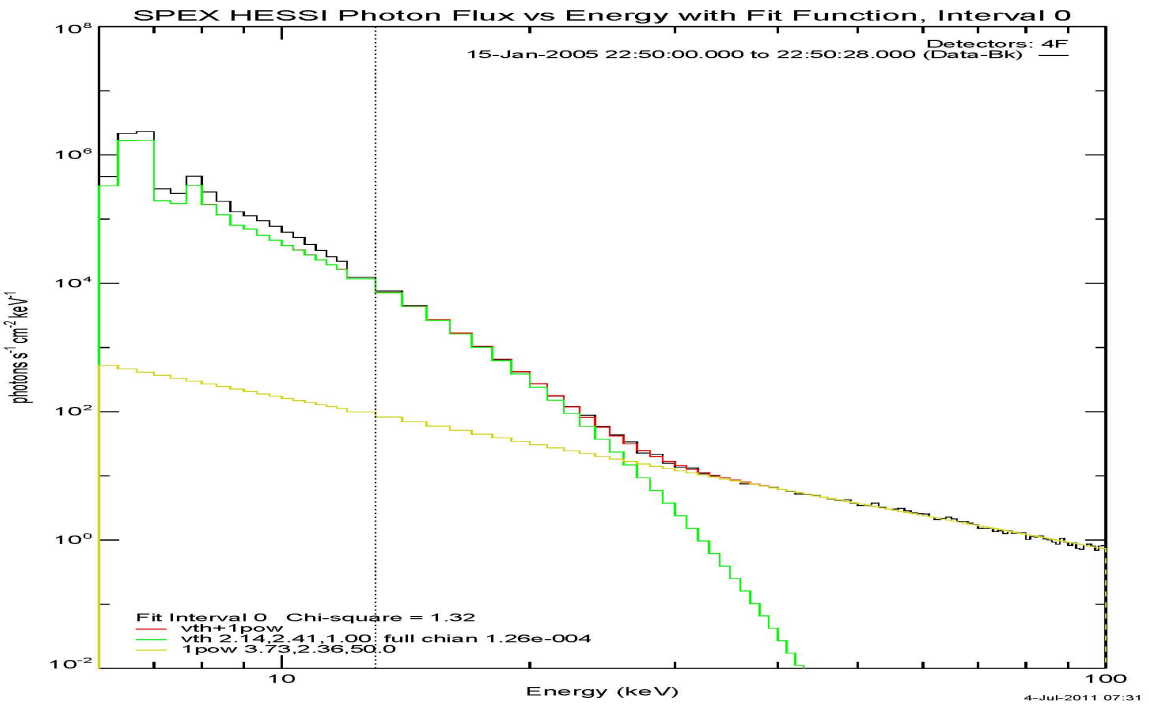
SPEX HESSI Photon Flux vs Energy with Fit Function, Interval 0
Detectors: 4F
15-Jan-2005 22:50:00.000 to 22:50:28.000 (Data-Bk)
photons s-1 cm-2 keV-1
Fit Interval 0 Chi-square = 1.32
vth+1pow
vth 2.14,2.41,1.00 full chian 1.26e-004
1pow 3.73,2.36,50.0
10
100
Energy (keV)
4-Jul-2011 07:31

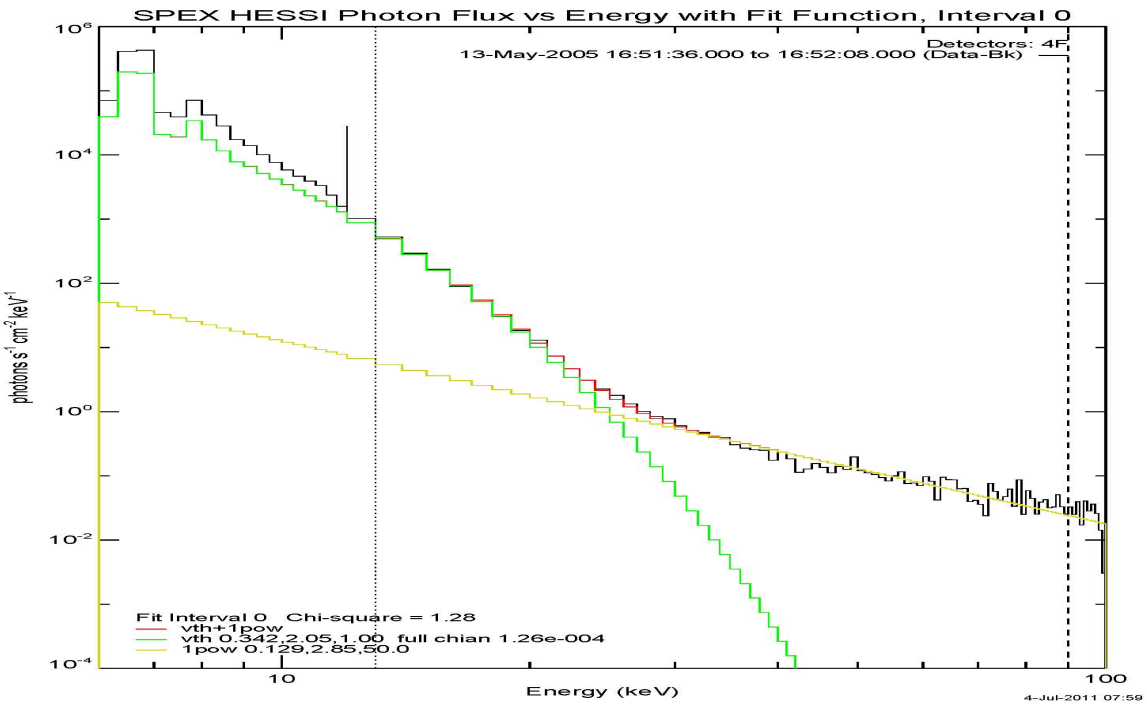
SPEX HESSI Photon Flux vs Energy with Fit Function, Interval 0
Detectors: 4F
13-May-2005 16:51:36.000 to 16:52:08.000 (Data-Bk)
Fit Interval 0 Chi-square = 1.28
vth+1pow
vth 0.342,2.05,1.00 full chian 1.26e-004
1pow 0.129,2.85,50.0
photons s-1 cm-2 keV-1
Energy (keV)
4-Jul-2011 07:59

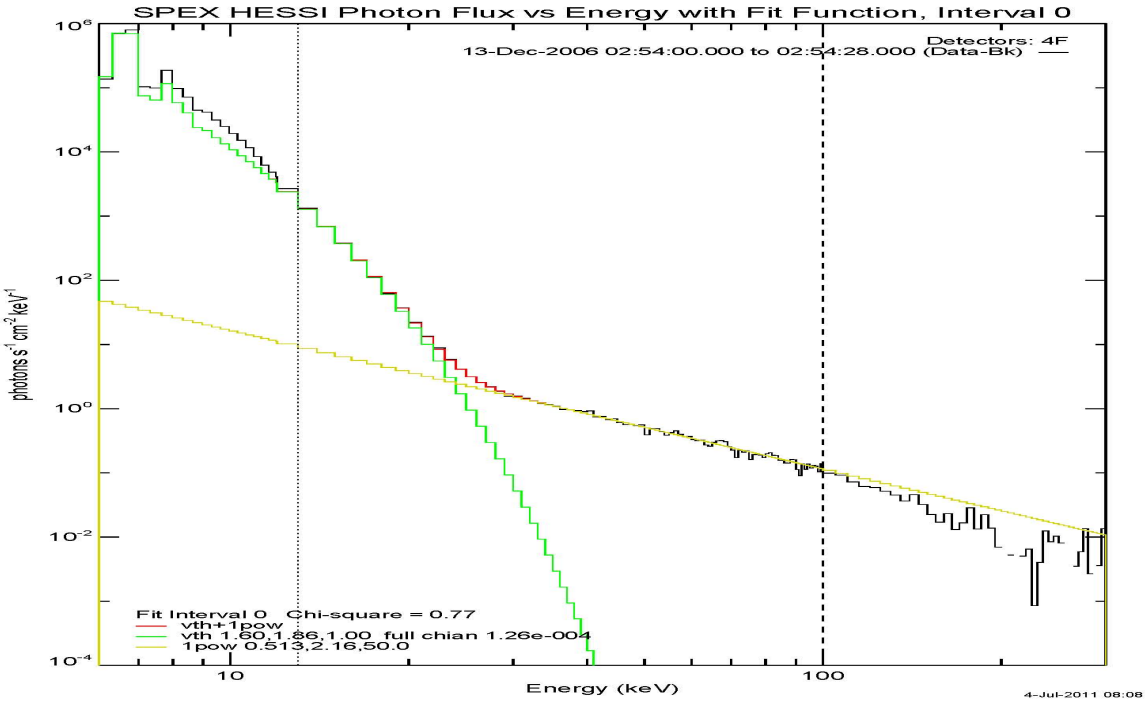
SPEX HESSI Photon Flux vs Energy with Fit Function, Interval 0
Detectors: 4F
13-Dec-2006 02:54:00.000 to 02:54:28.000 (Data-Bk)
Fit Interval 0 Chi-square = 0.77
vth+1pow
vth 1.60,1.86,1.00 full chian 1.26e-004
1pow 0.513,2.16,50.0
photons s-1 cm-2 keV-1
Energy (keV)
4-Jul-2011 08:08

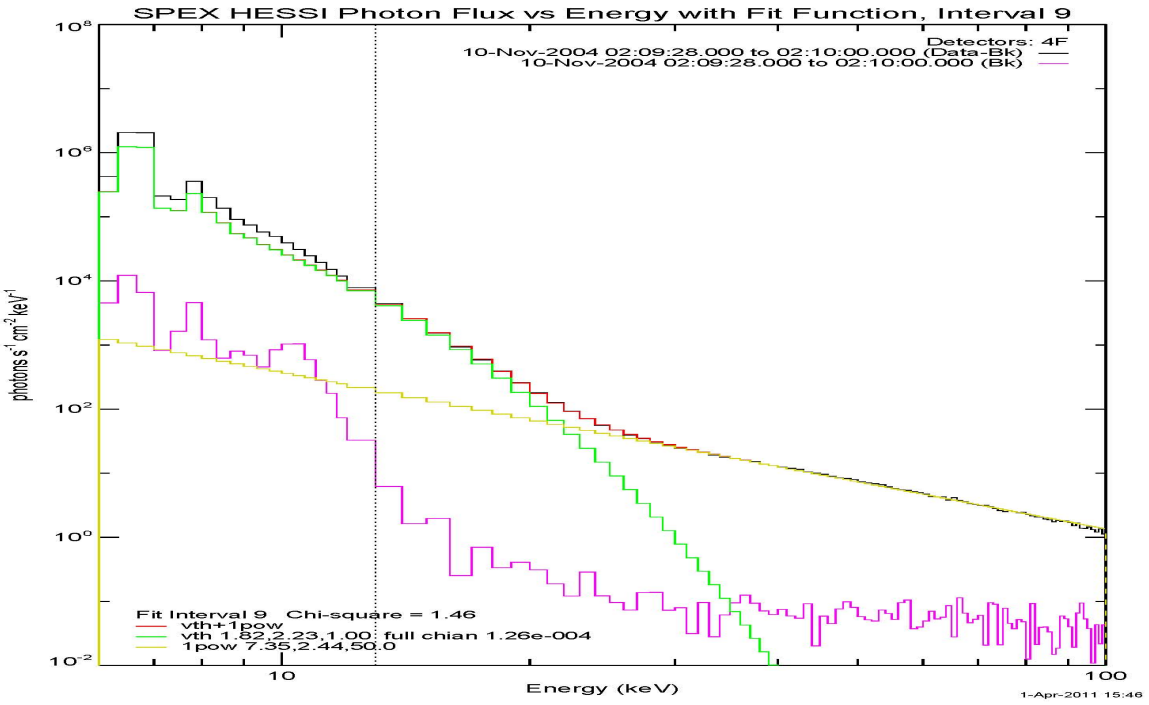
SPEX HESSI Photon Flux vs Energy with Fit Function, Interval 9
Detectors: 4F
10-Nov-2004 02:09:28.000 to 02:10:00.000 (Data-Bk)
10-Nov-2004 02:09:28.000 to 02:10:00.000 (Bk)
photons s-1 cm-2 keV-1
Fit Interval 9 Chi-square = 1.46
vth+1pow
vth 1.82,2.23,1.00 full chian 1.26e-004
1pow 7.35,2.44,50.0
Energy (keV)
1-Apr-2011 15:46

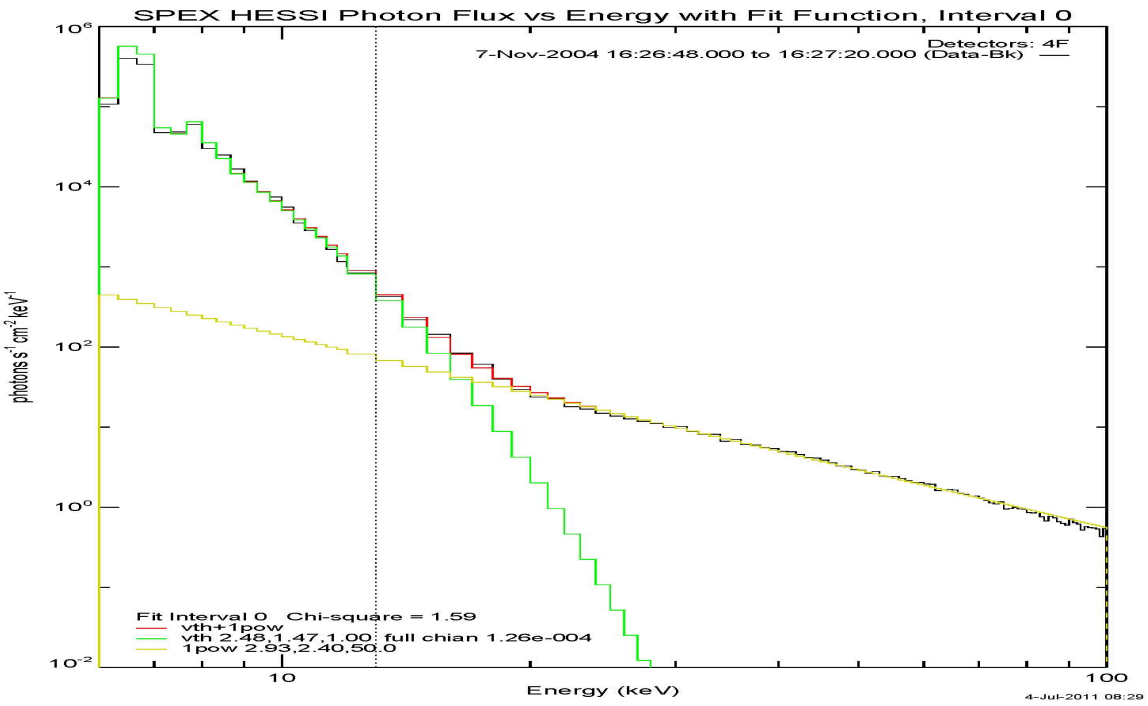
SPEX HESSI Photon Flux vs Energy with Fit Function, Interval 0
Detectors: 4F
7-Nov-2004 16:26:48.000 to 16:27:20.000 (Data-Bk)
photons s-1 cm-2 keV-1
Fit Interval 0 Chi-square = 1.59
vth+1pow
vth 2.48,1.47,1.00 full chian 1.26e-004
1pow 2.93,2.40,50.0
Energy (keV)
4-Jul-2011 08:29

SEP spectra

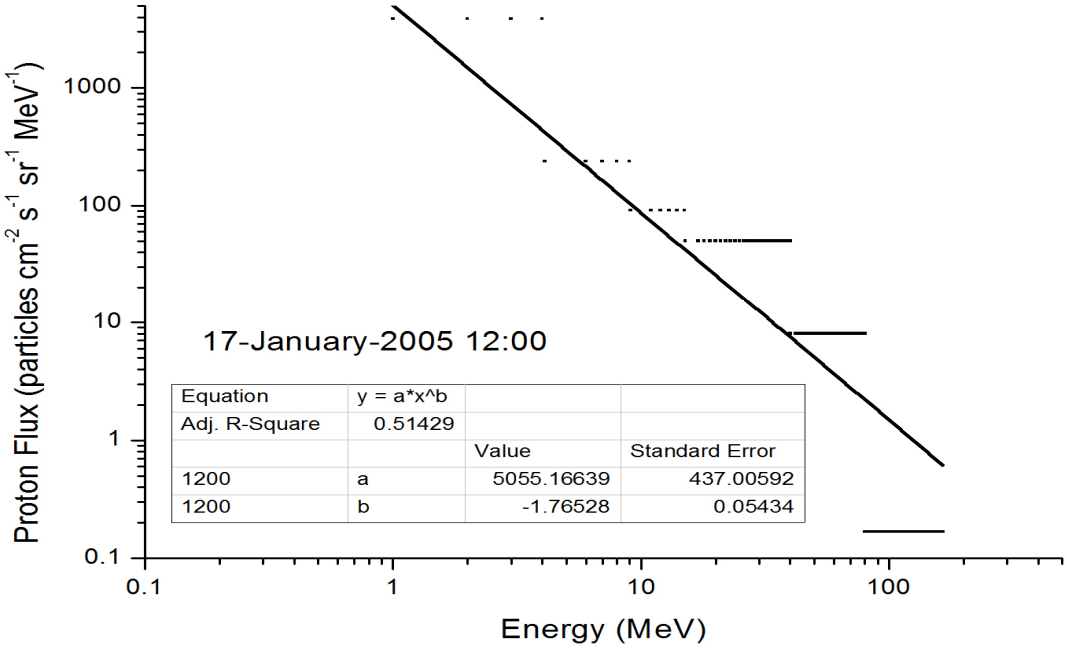

Equation	y = a*x^b		
Adj. R-Square	0.51429		
		Value	Standard Error
1200	a	5055.16639	437.00592
1200	b	-1.76528	0.05434

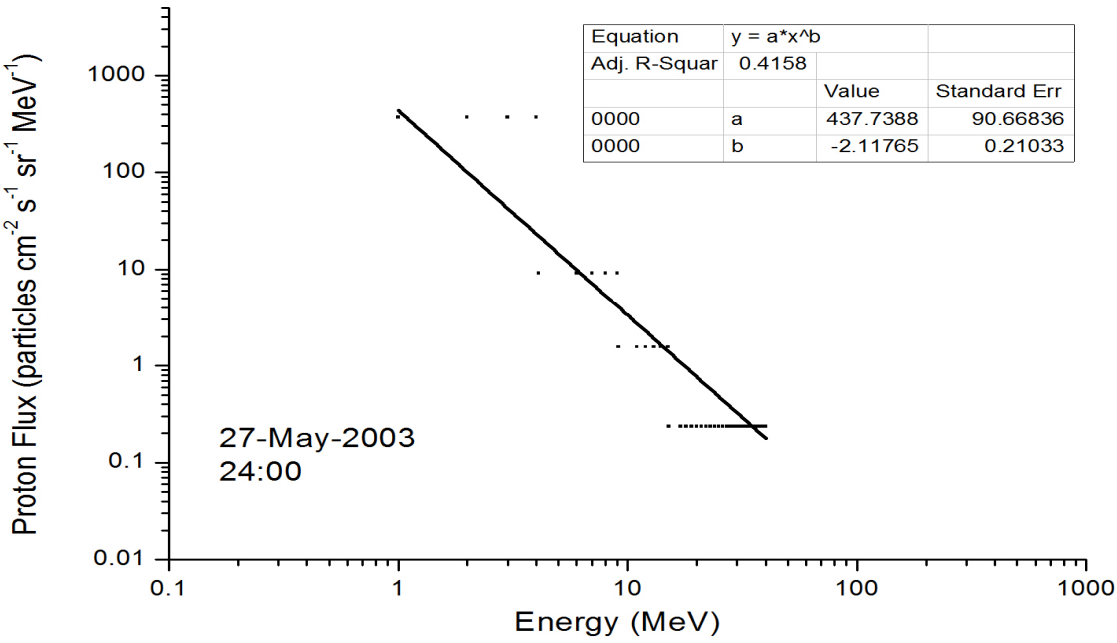

Equation	y = a*x^b		
Adj. R-Squar	0.4158		
		Value	Standard Err
0000	a	437.7388	90.66836
0000	b	-2.11765	0.21033

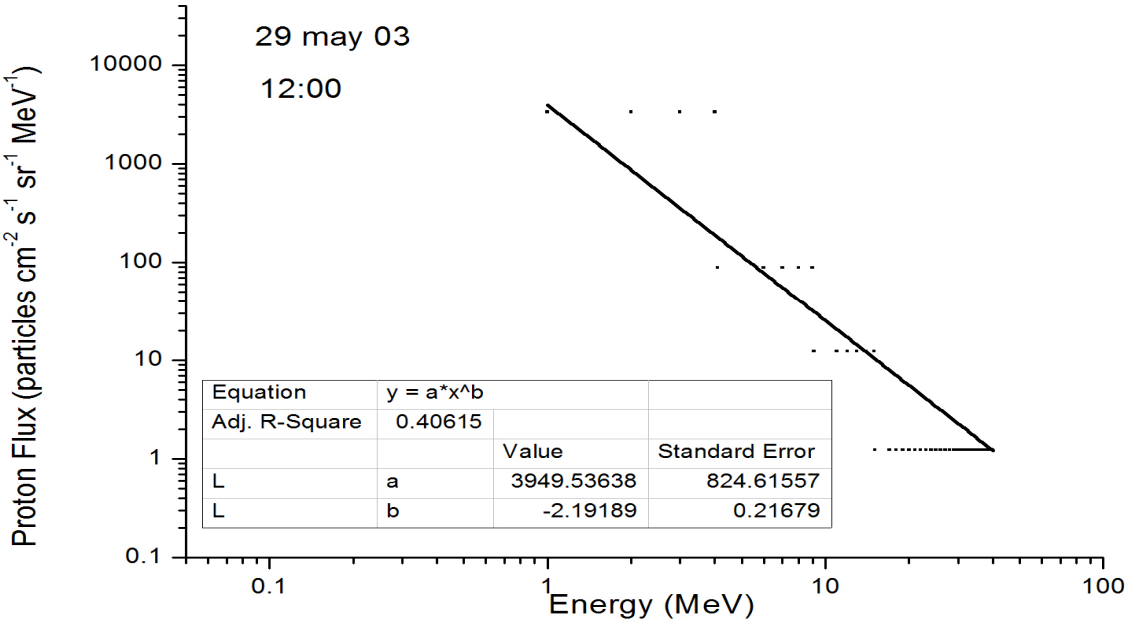
29 may 03
12:00
Proton Flux (particles cm-2 s-1 sr-1 MeV-1)
Energy (MeV)
10000
1000
100
10
1
0.1
0.1
1
10
100
Equation y = a*x^b
Adj. R-Square 0.40615
Value Standard Error
L a 3949.53638 824.61557
L b -2.19189 0.21679

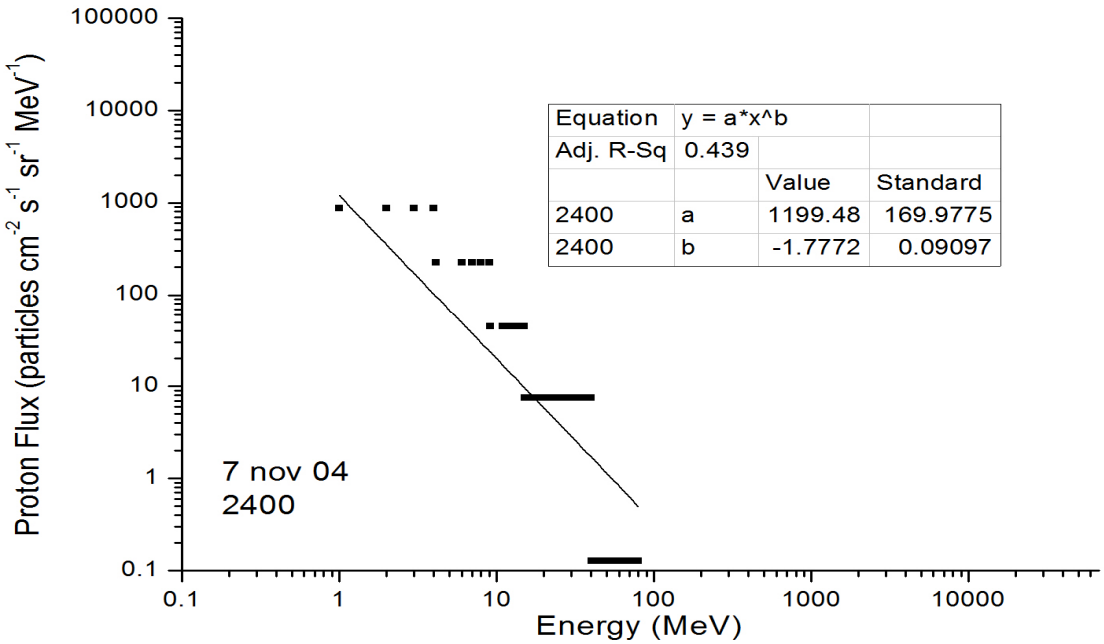
Proton Flux (particles cm-2 s-1 sr-1 MeV-1)
Energy (MeV)
100000
10000
1000
100
10
1
0.1
0.1
1
10
100
1000
10000
Equation y = a*x^b
Adj. R-Sq 0.439
Value Standard
2400 a 1199.48 169.9775
2400 b -1.7772 0.09097
7 nov 04
2400

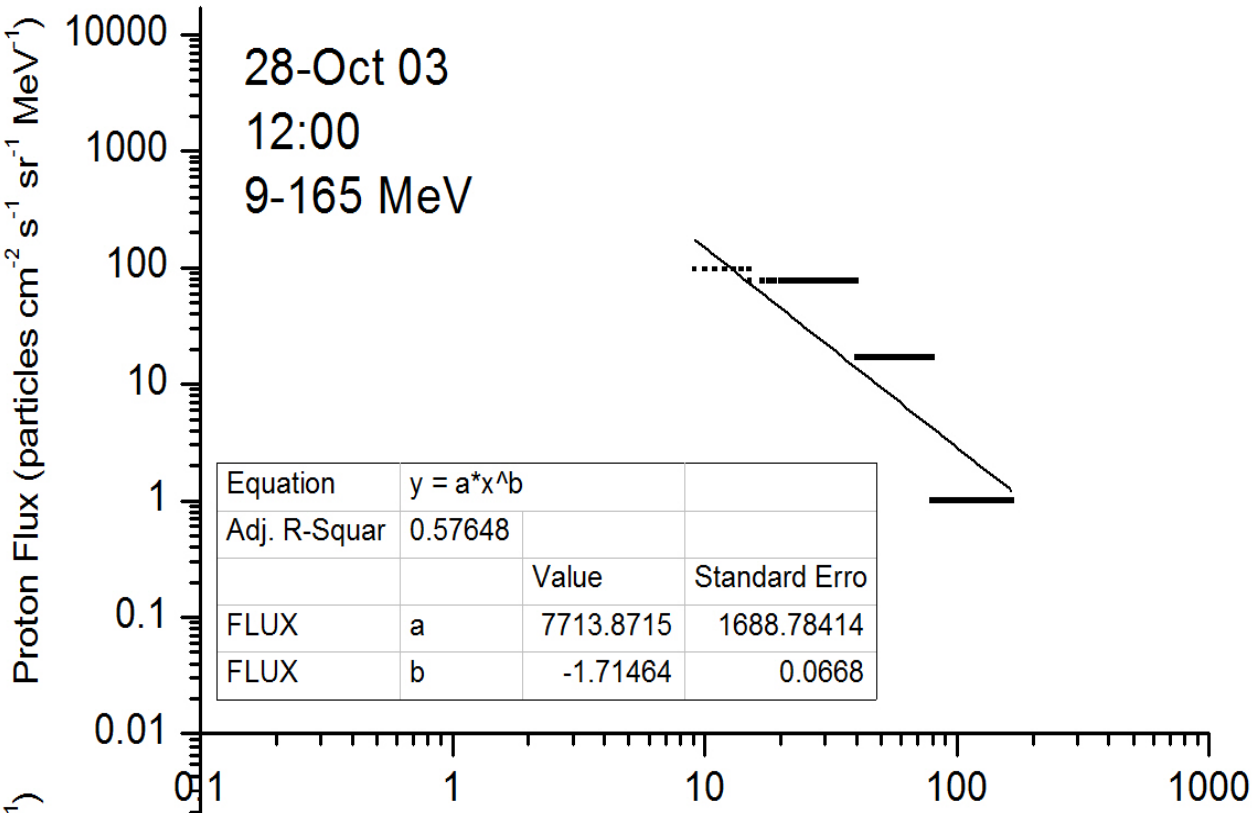
28-Oct 03
12:00
9-165 MeV
Proton Flux (particles cm-2 s-1 sr-1 MeV-1)
10000
1000
100
10
1
0.1
0.01
0.1
1
10
100
1000
Equation y = a*x^b
Adj. R-Squar 0.57648
Value Standard Erro
FLUX a 7713.8715 1688.78414
FLUX b -1.71464 0.0668

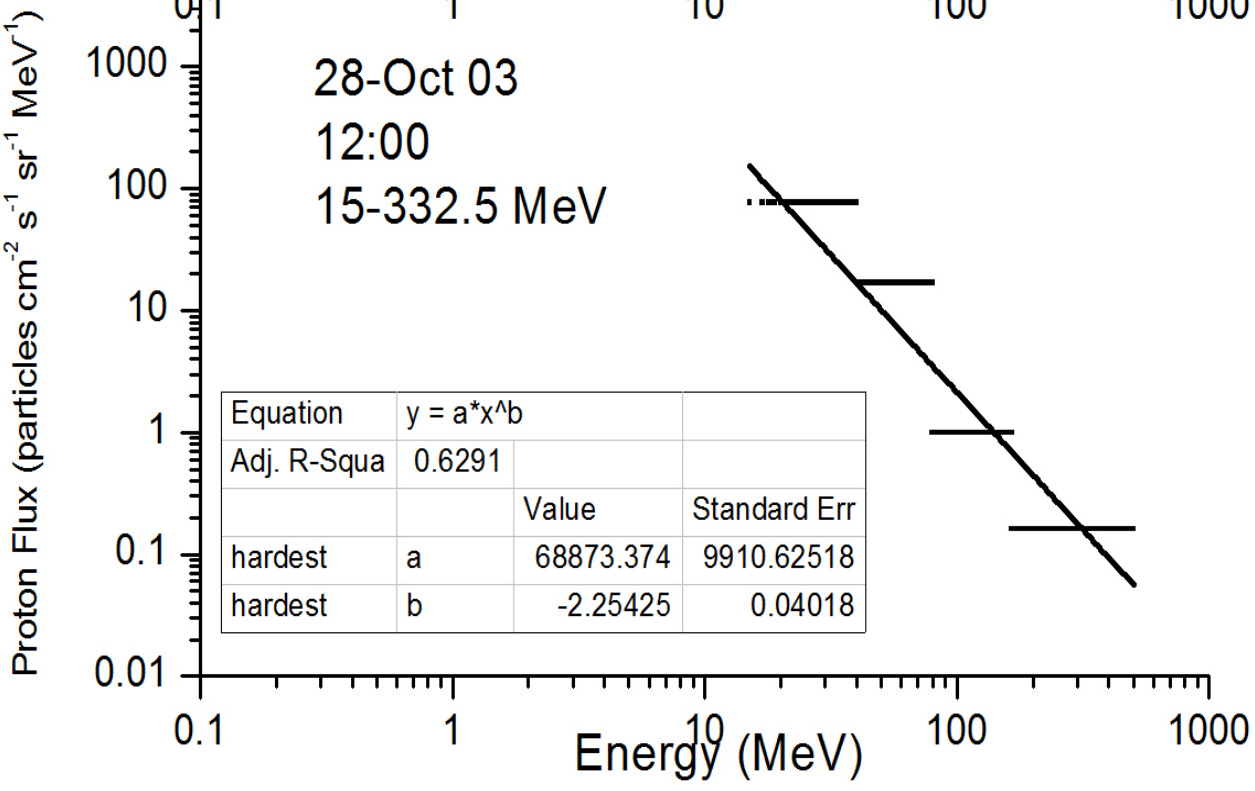
28-Oct 03
12:00
15-332.5 MeV
Proton Flux (particles cm-2 s-1 sr-1 MeV-1)
1000
100
10
1
0.1
0.01
0.1
1
10
100
1000
Energy (MeV)
Equation y = a*x^b
Adj. R-Squa 0.6291
Value Standard Err
hardest a 68873.374 9910.62518
hardest b -2.25425 0.04018

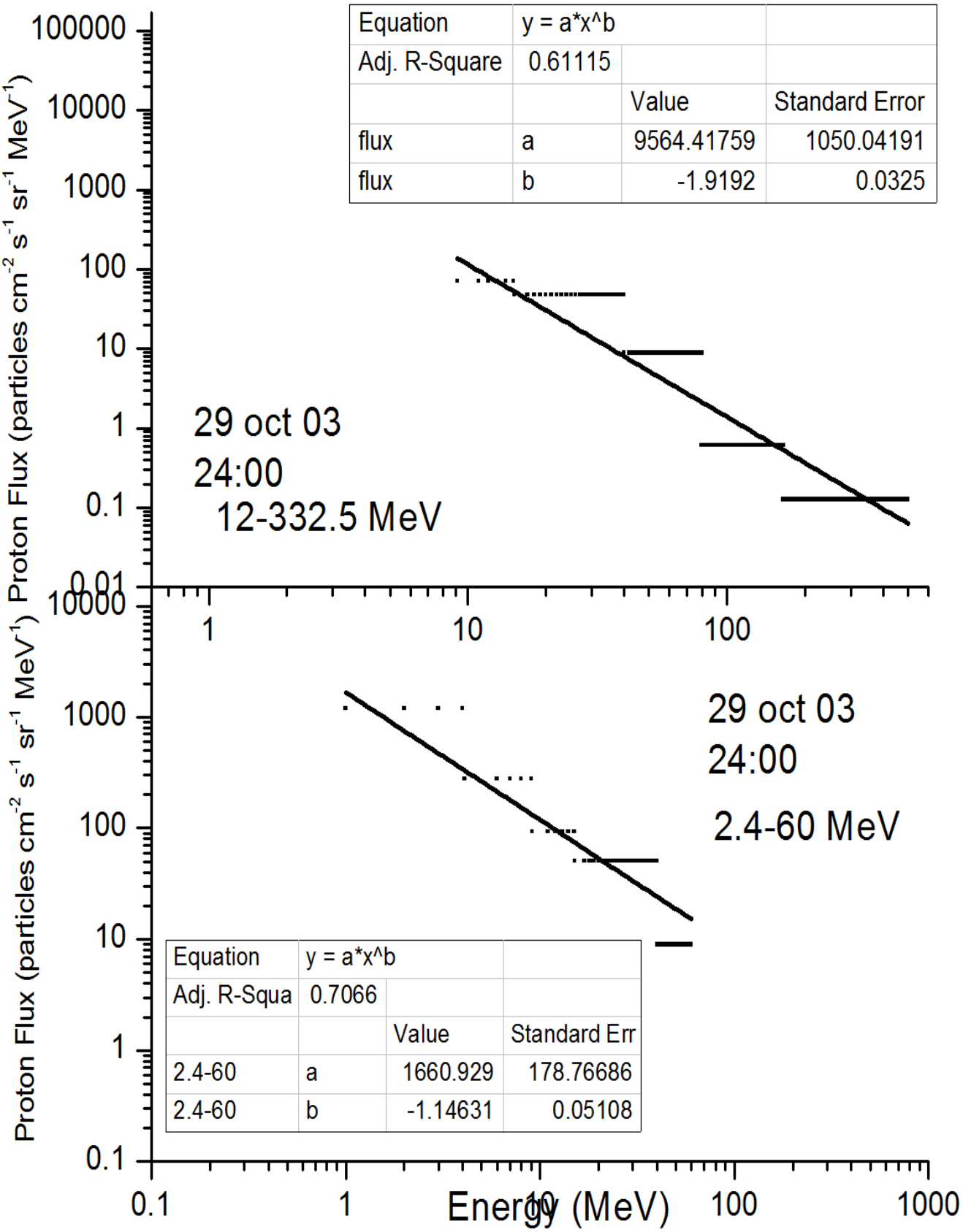
Equation y = a*x^b
Adj. R-Square 0.61115
Value Standard Error
flux a 9564.41759 1050.04191
flux b -1.9192 0.0325
29 oct 03
24:00
12-332.5 MeV
Proton Flux (particles cm-2 s-1 sr-1 MeV-1)
100000
10000
1000
100
10
1
0.1
0.01
1
10
100
29 oct 03
24:00
2.4-60 MeV
Equation y = a*x^b
Adj. R-Squa 0.7066
Value Standard Err
2.4-60 a 1660.929 178.76686
2.4-60 b -1.14631 0.05108
Proton Flux (particles cm-2 s-1 sr-1 MeV-1)
10000
1000
100
10
1
0.1
0.1
1
10
100
1000
Energy (MeV)

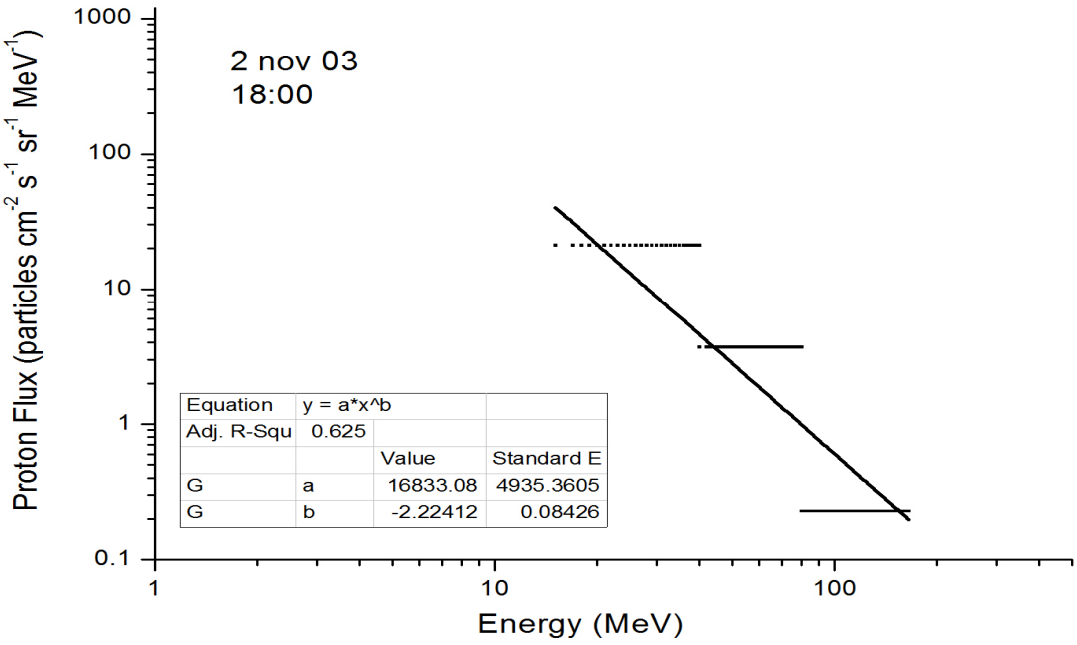
2 nov 03
18:00
Proton Flux (particles cm-2 s-1 sr-1 MeV-1)
Energy (MeV)
1000
100
10
1
0.1
1
10
100
Equation y = a*x^b
Adj. R-Squ 0.625
Value Standard E
G a 16833.08 4935.3605
G b -2.22412 0.08426

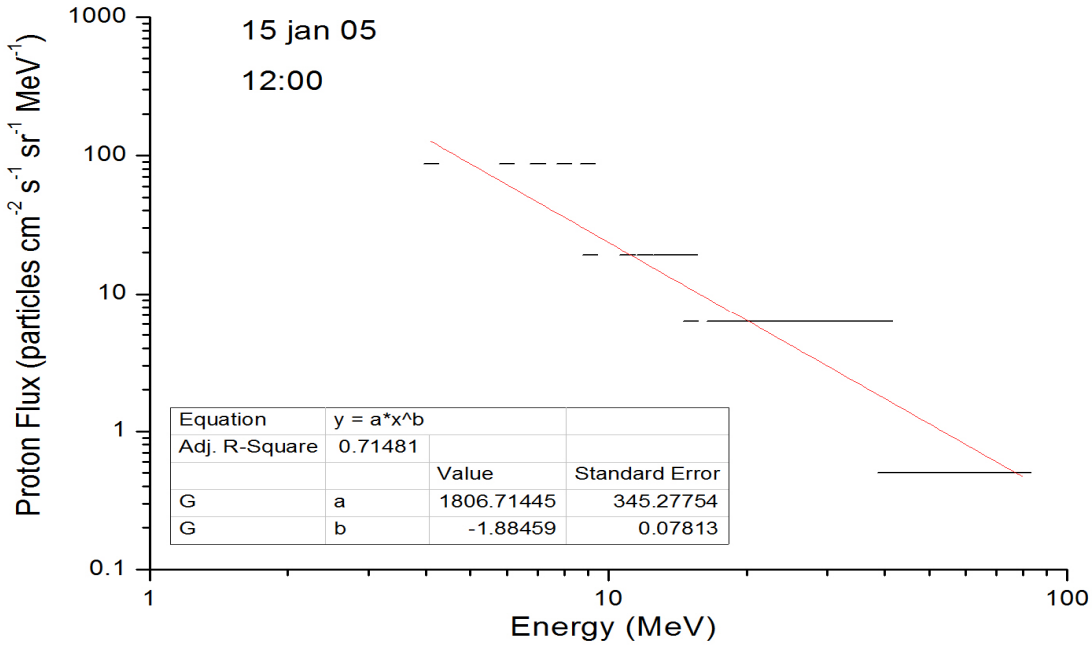
15 jan 05
12:00
Proton Flux (particles cm-2 s-1 sr-1 MeV-1)
Energy (MeV)
1000
100
10
1
0.1
1
10
100
Equation y = a*x^b
Adj. R-Square 0.71481
Value Standard Error
G a 1806.71445 345.27754
G b -1.88459 0.07813

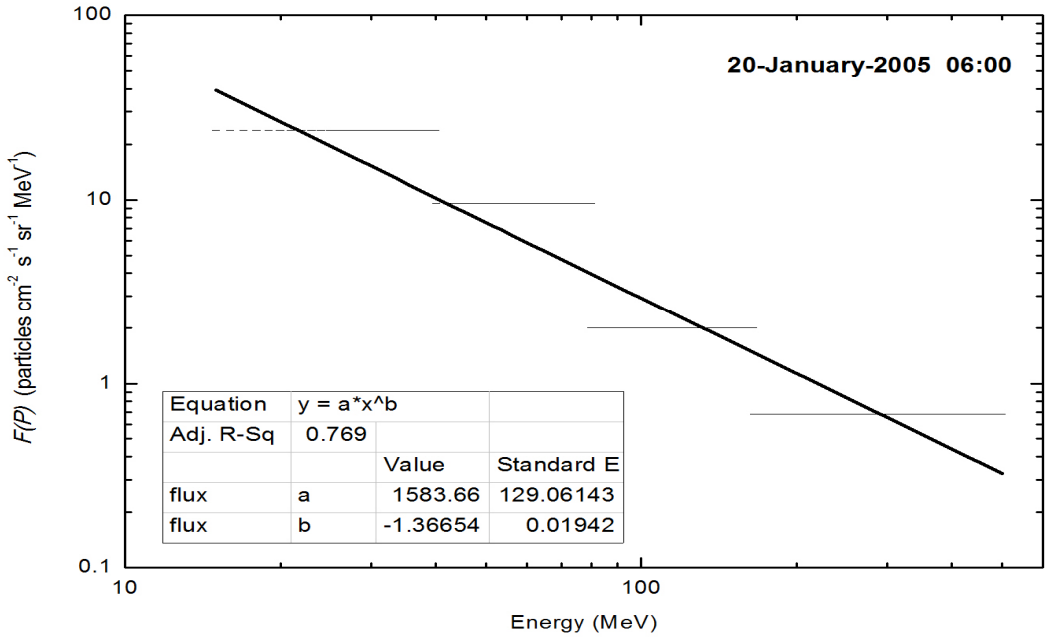
20-January-2005 06:00
F(P) (particles cm-2 s-1 sr-1 MeV-1)
Energy (MeV)
100
10
1
0.1
10
100
Equation y = a*x^b
Adj. R-Sq 0.769
Value Standard E
flux a 1583.66 129.06143
flux b -1.36654 0.01942

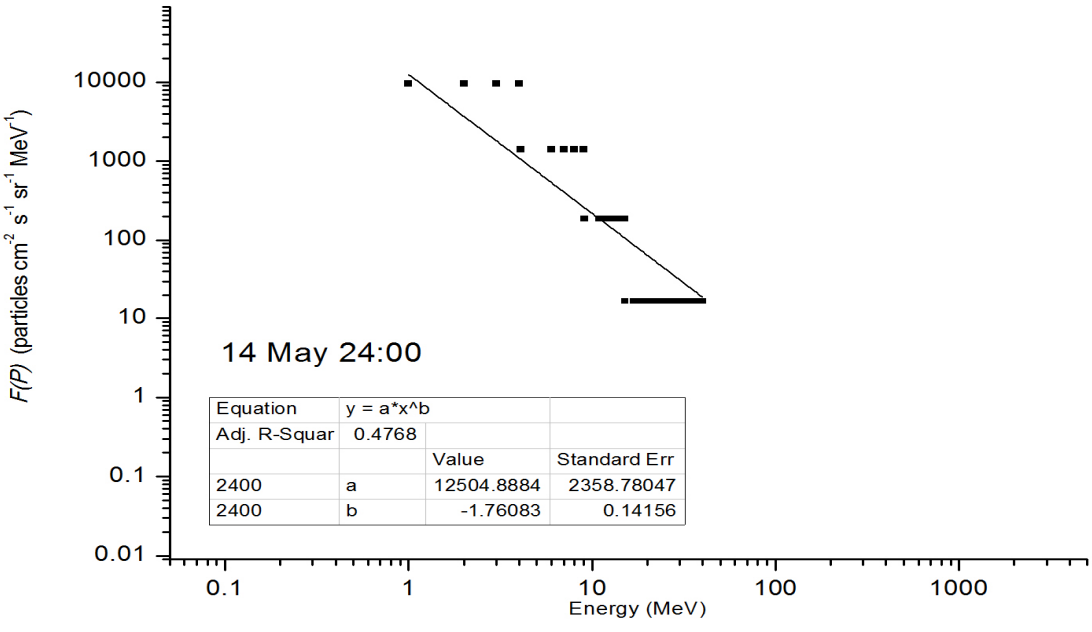
14 May 24:00
F(P) (particles cm-2 s-1 sr-1 MeV-1)
Energy (MeV)
10000
1000
100
10
1
0.1
0.01
0.1
1
10
100
1000
Equation y = a*x^b
Adj. R-Squar 0.4768
Value Standard Err
2400 a 12504.8884 2358.78047
2400 b -1.76083 0.14156